Developing new strategies to understand human kidney development and target human disease

Patricia Katherine Prado Peralta

TESI DOCTORAL UPF / 2020

Thesis supervisors:

Dr. Nuria Montserrat Pulido, ICREA Research Professor at the Institute for Bioengineering of Catalonia (IBEC)- Barcelona

Dr. Elena Garreta Bahima, Institute for Bioengineering of Catalonia (IBEC)- Barcelona

DEPARTMENT OF EXPERIMENTAL AND HEALTH SCIENCES

Universitat Pompeu Fabra
Barcelona

A mis padres, a mis hermanas y a Judit

Acknowledgements

I am really thankful to all of those who have encouraged me over these years.

Núria, moltes gràcies per haver confiat en mi des del primer moment, per a haver-me donat l'oportunitat de fer el doctorat al teu grup i, per tota la dedicació durant aquests anys. Ets un exemple de que el treball dur sempre porta recompenses i una font de coneixement inesgotable.

Elena, gràcies per ensenyar-me a treballar amb dedicació, constància i esforç i a fer les coses amb delicadesa. El teu suport i guia han sigut fonamentals durant aquests anys.

Moltes gràcies a les dues per haver contribuït a la meva formació com a professional, i també a nivell personal. Un plaer treballar amb vosaltres.

Quiero agradecer también a todos los compañeros del laboratorio, sin duda un pilar esencial en estos años. Andrés, Miriana y Lucía, compañeros de doctorado y también amigos, gracias por vuestro apoyo y todos los momentos compartidos. Carmen, muchas gracias compartir tu pasión por la ciencia, por tu paciencia, tus consejos y tu amabilidad. Carol, gracias por todos los consejos y por siempre tener la solución mágica. Gracias también Federico y Blanca por todo.

Guillem, Josele, Andrea M, Marta M, Carla, Marta H, Andrea G, muchas gracias por siempre estar ahí para animarme en los momentos más difíciles y celebrar conmigo los buenos. A todos muchas gracias por vuestro cariño, vuestro apoyo y por creer tanto en mí.

Gracias a mis padres, por siempre estar allí, por su apoyo incondicional y su amor, y por ser un ejemplo de superación a todos los niveles. Gracias Gabriela y Magali, también por vuestro amor y por ser unas hermanas maravillosas.

Judit, gràcies per la paciència, per entendre els horaris d'aquesta professió i ser el meu refugi. T'estimo.

<div align="right">Barcelona, 18 Diciembre 2020</div>

Abstract

In recent years considerable progress has been made in the development of approaches for human pluripotent stem cells (hPSCs) differentiation. An important step in this direction has been the derivation of hPSCs derived organoids to understand early steps of human organ development and disease. Here, we have developed new techniques and fundamental knowledge to generate hPSCs-kidney organoids. Towards this aim we have explored on the possibility to emulate early steps of kidney embryogenesis forcing cell to cell and cell to extracellular matrix contact as a new approach to generate hPSCs-kidney organoids with superior treats of differentiation and function. To further assess on the impact of environmental *stimuli* during kidney organoid differentiation we have interrogated on the interaction of metabolic cues in this process identifying metabolic regulators, namely Esrrα, which are responsible of kidney differentiation and human chronic kidney disease. Into the light of the current COVID19 crisis we have further exploited hPSCs-kidney organoids to understand first steps of SARS-CoV-2 infection also identifying a therapeutic compound which nowadays is in a phase II b clinical trial for COVID19 patients in more than 6 countries in the world. Based on the current developments, in the present thesis we emphasize the major achievements in the field of kidney morphogenesis, including technological advances for kidney embryonic cell culture and the use of animal models to understand kidney development. We further discuss on ongoing challenges of bringing together all this

knowledge to establish hPSCs-kidney organoids to study human kidney differentiation and disease.

Resumen

En los últimos años se han conseguido grandes avances en el desarrollo de estrategias para la diferenciación de células madre pluripotentes humanas (hPSCs). Un paso importante ha sido la derivación de organoides a partir de hPSCs enfocado a entender los eventos iniciales implicados en el desarrollo y enfermedad de los órganos humanos. En este trabajo, aportamos conocimiento fundamental y nuevas técnicas para la derivación de organoides de riñón. Con esta finalidad, hemos explorado la posibilidad de emular los eventos iniciales de la embriogénesis del riñón forzando el contacto entre célula y célula y entre célula y matriz extracelular con el fin de establecer una nueva estrategia para generar organoides de riñón con características superiores de diferenciación y función a las descritas anteriormente. Con el objetivo de profundizar en el impacto de los estímulos del entorno durante la diferenciación renal, hemos analizado el papel de las señales metabólicas en este proceso y hemos identificado el papel de reguladores metabólicos, tales como Esrrα, en la diferenciación renal así como en la enfermedad renal crónica en humanos. En el contexto de la actual crisis de la COVID19, hemos utilizado, por primera vez, los organoides de riñón para investigar los eventos iniciales implicados en la infección por SARS-CoV-2. Estos hallazgos nos han permitido identificar un compuesto terapéutico para tratar la COVID19 que actualmente está en un ensayo clínico en fase 2 en más de 6 países. En base a lo expuesto, en esta tesis hemos querido destacar los grandes avances conseguidos en el campo de la morfogénesis del riñón, incluyendo los avances técnicos en el cultivo de células embrionarias de riñón y en el uso de modelos animales

para el estudio del desarrollo renal. Así mismo, exponemos los desafíos actuales para combinar todos estos avances y aplicarlos en la derivación de organoides de riñón para estudiar la diferenciación y la enfermedad renal en humanos.

Preface

The work presented in this doctoral thesis was supported by the European Research Council (ERC) under the European Union's Horizon 2020 research and innovation programme and carried out at the "Pluripotency for Organ Regeneration" group, led by Dr. Núria Montserrat at the Institute for Bioengineering of Catalonia (IBEC) in Barcelona, Spain. This thesis has been supervised by Dr. Núria Montserrat and Dr. Elena Garreta, senior researcher in the group.

The content of this thesis provides novel insights in methodologies for kidney organoid generation and important findings regarding human kidney disease modeling. All this work has led to three publications in high impact factor journals, two revisions and one book chapter. The work presented here has also been awarded as "Best poster" in two international conferences (Summer School 2016 - Regenerative Nano - Medicine: From Advanced Delivery Systems to Electronic-Based Devices (Tel Aviv University, Israel) and 9th IBEC Symposium "Bioengineering for active aging" (Barcelona)).

The thesis complies with the procedures and regulation of the Biomedicine PhD Program of the Department of Experimental and Health Science of the University Pompeu Fabra.

Abbreviations

ACE2	Angiotensin-converting enzyme 2
AKI	Acute kidney disease
CAM	Choriallantoic membrane
CD	Collecting duct
CKD	Chronic kidney disease
CM	Cap mesenchyme
CSB	Comma-shaped body
Esrrα	Estrogen-related receptor alpha
FAO	Fatty acid oxidation
GBM	Glomerular basement membrane
hESCs	Human embryonic stem cells
hiPSCs	Human induced pluripotent stem cells
hPSCs	Human pluripotent stem cells
IM	Intermediate mesoderm
MET	Mesenchymal to epithelial transition
MM	Metanephric mesenchyme
NPCs	Nephron progenitor cells
OXPHOS	Oxidative phosphorylation

PS	Primitive streak
PTCs	Proximal tubular cells
RV	Renal vesicle
SARS-CoV-2	Severe acute respiratory syndrome coronavirus 2
SSB	S-shaped body
UB	Ureteric Bud
UE	Ureteric epithelium

TABLE OF CONTENTS

I. INTRODUCTION

1. Kidney disease and kidney development

1.1 Kidney disease

Kidney disease represents a worldwide major health problem affecting millions of people. Acute kidney injury (AKI) and chronic kidney disease (CKD) are linked to a high morbidity and mortality rate due to damage in the kidney. At the present time CKD is estimated to affect around 10% of the population and represents a frequent complication of diabetes, obesity, and cardiovascular disease so even in its earliest stages increases the risk of a premature death (O'Toole & Sedor, 2014). Nowadays around 2-5% of CKD affected patients will evolve to End Stage Renal Disease (ESRD) Furthermore, the shortage of kidney donor for force to the vast majority of the patients to undergo dialysis therapy, accounting between 1% and 2% of health-care budgets (Wouters et al., 2015). Even when renal transplantation is possible it has a low succeed rate because of the high percentage of rejections and the loss of function within the first years after transplantation. Therefore, there is an urgent demand for improved public awareness, prevention strategies, early detection, education and subsequent management of CKD in clinical practice (Zoccali et al., 2018).

1.2 Mammalian kidney embryonic development

The kidneys are bilateral organs that eliminate nitrogenous waste, regulates the volume, composition, and pressure of the blood and the density of the bones. The evolution of the kidney reflects the need of land-adaptive vertebrates to conserve water, excrete waste, and maintain electrolyte homeostasis within a variety of challenging environments. (Dressler 2006; Little & McMahon, 2012).

Kidney function requires the coordinate development of specific cell types within a unique architectural framework. The functional unit of the kidney, the nephron, accounts for around 2 million in human (Bertram et al., 2011) and about 15,000 in mice (Merlet-Bénichou et al., 1999). During kidney development in mammals the nephrons pattern and segment into compartmentalized epithelial segments assembled over a period of fetal and perinatal life. The cellular composition of the nephron sustains for their unique functions during all the adult life. As such, the blood is filtered by the glomerulus, at the proximal end of the nephron, and the filtrate is modified in a tubular epithelium and finally the urine is delivered to the collecting duct for disposal (Davidson, 2008).

The mammalian kidney development is characterized by the formation of three successive pair of kidneys. The metanephros, or permanent kidney, is the last of the three excretory organs to form. The developing kidneys are termed: the pronephros, mesonephros, and metanephros. The pronephros is rudimentary, whereas the mesonephric duct or the so-called mesonephric kidney gives rise to the mesonephric tubules, which open into the mesonephric duct. The metanephros gives rise to the adult kidney. The permanent kidney begins to form at 5 weeks gestation in humans and becomes functional toward the end of the first trimester (Gregory R Dressler, 2006; Rimoin et al., 2013) .

The mammalian kidney arises from the intermediate mesoderm (IM), an early embryonic germ layer that derives from the primitive streak (PS) which is located between the lateral and paraxial mesoderm(s). The IM appears soon after gastrulation, in humans by embryonic day (E) 22 (~E 8.0 in mice). The IM further specifies into two different embryonic tissues: the ureteric bud (UB) and the metanephric

mesenchyme (MM). Reciprocal inductive interactions between UB and MM subsequently lead to the formation of the collecting duct system and the nephrons. Specifically, the UB gives rise to all the epithelial epithelium of the collecting ducts (CDs), and the MM differentiates to the stroma and to the cap mesenchyme (CM). The CM is the embryonic tissue from where all the epithelial cells along the nephron will arise (from the glomerulus through the connecting segment). After birth the mammalian kidney is characterized by a significant cellular complexity with more than 30 different cell types, including epithelial, endothelial, and stromal components (J. Park et al., 2018).

1.2.1 Mouse kidney development

Patterning of the mesoderm

During gastrulation, that is at E 7.5 in the mice, PS, a transient midline structure in the embryo, serves as a conduit through which epiblast cells fated to become mesoderm and endoderm ingress to establish the embryonic germ layers (Lawson et al., 2001) (Figure 1a). In the mouse embryo, prior to any morphological indication of urogenital development, the activation of specific marker genes is the first indication that the lateral plate mesoderm and subsequent IM are differentiated from surrounding cells. At this stage LIM homeobox protein 1 (Lhx1) (Tsang et al., 2000), Odd-skipped related 1 (Osr1 (James & Schultheiss, 2003), and Paired-box transcription factor (Pax) 2 and Pax8 (Bouchard et al., 2002) are essential for IM specification. During mouse kidney development the specification of the IM occurs as cells migrate through the (PS). From E8.5 to E10.5 the IM patterns into anterior-posterior axis (Barak et al., 2005) (Figure 1a).
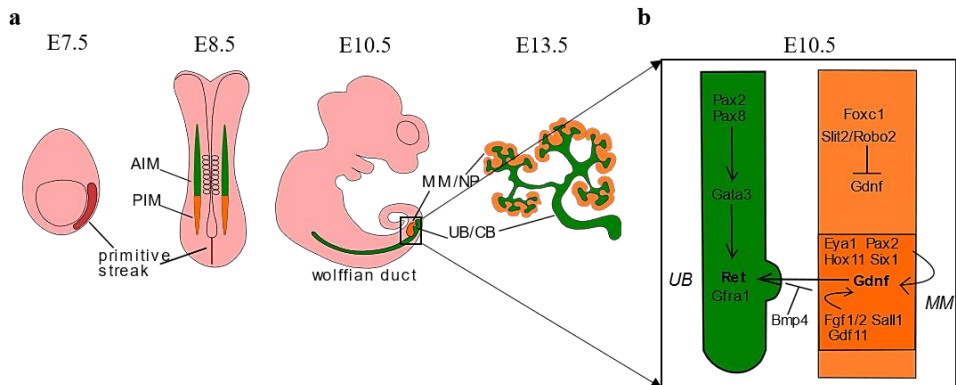
3

Figure 1. (**a**) **Schematic representation of mouse kidney embryonic development at the indicated embryonic days (E).** Primitive streak (labelled in red) gives rise to both anterior intermediate mesoderm (AIM) and posterior intermediate mesoderm (PIM). The AIM further epithelializes into the wolffian duct while the PIM gives rise to the metanephric mesenchyme (MM). An outgrowth of the wolffian duct forms the ureteric bud (UB) that further develops into collecting duct (CD) and the ureter. The MM gives rise to the nephron progenitors (NPs) that will form the nephrons. (**b**) **Key molecular pathways involved in early metanephric kidney development.** At E10.5 reciprocal inductive interactions between the MM and the UB promote the branching of the UB into the MM. Genes such Eya1, Pax2, Hox11, Six1, Sall1, Fgf 1/2, upregulate Gdnf production. Gdnf is secreted from the MM and binds to Ret receptor and Gfrα1 coreceptor and promote UB outgrowth. Ret expression is regulated by Gata3 that in turn is regulated by Pax2/8. The ectopic bud outgrowth is prevented by Bmp4 that surrounds the wolffian duct. Slit2 and Robo2 signaling downregulate the expression of Gdnf in the anterior part of the MM. Illustrations reproduced and adapted from: (**a**) (Takasato and Little 2016) and (**b**) (Davidson 2008).

At E8.5 the mouse kidney development begins with the formation of the pronephric duct, or primary nephric duct. As the pronephric duct extends down the trunk it induces the formation of mesonephric tubules from the adjacent IM (known as nephrogenic cord). At this stage at the caudal end of the nephric duct lies the MM, a region of cells morphologically distinct from the surrounding mesoderm. The formation

of the adult kidney, or metanephros, begins at E10.5 when the UB protrudes from the pronephric duct and outgrowths into the surrounding metanephric mesenchyme (MM). Reciprocal inductive signals between UB and MM, the two main progenitor populations of the kidney, are essential for survival and differentiation of both the mesenchymal and epithelial components in the early kidney (GROBSTEIN, 1956) (Figure 1b). At E11.5 the UB forms a T-shaped bifurcation and begins to undergo consecutives cycles of branching and elongation to generate the collecting duct system (Cebrián et al., 2004). As this process occurs, each UB tip is surrounded by a subset of MM clusters, the so-called CM from where all the epithelial segments of the nephron are formed (including glomerular and tubular epithelial cells) (Bard et al., 2001). These mesenchymal cell aggregates undergo a mesenchymal-to-epithelial transition (MET) to form the renal vesicles (RV) at E12.5. From this moment each RV proliferates to give rise to comma-shaped bodies (CSBs) and S-shaped bodies (SSBs) that fuse with the collecting duct epithelium (Boyle et al., 2008) (Figure 2). Each embryonic SSB subsequently patterns along the proximal-distal axis being segmented into podocyte progenitors and the precursors of the proximal and distal tubule segments. The distal segment of each SSB fuses with the collecting duct epithelium, forming a single, continuous epithelial tubule (Gregory R Dressler, 2006) (Figure 2). The proximal end of each SSB forms the glomerulus and comprises a capillary tuft surrounded by the podocytes. Initial branching is dichotomous, with each new UB tip inducing a new CM aggregate. Dichotomous branching starts to slow at approximately E15.5 in the mouse (Cebrián et al., 2004). In mice, new nephrons continue to be induced at the tips of the growing buds until five days post-birth. At the perinatal stage the youngest nephrons form

arcades that drain into a single collecting tubule (Gregory R Dressler, 2006).

UB branching

The pioneer work from Grobstein (1956) (GROBSTEIN, 1956) showed that the formation of nephrons requires a primary induction event from the UB to the CM. At E10.5, the initiation of kidney development is marked by the UB outgrowth (Figure 1b). The tyrosine kinase receptor Ret, its ligand glial-derived neurotrophic factor (Gdnf), and the coreceptor Gfrα1 are essential for promoting UB outgrowth. Ret is expressed in the nephric duct, while Gdnf is localized in the MM, and Gdnf receptor alpha 1 (Gfrα1) in both the nephric duct and the surrounding mesenchyme. The released Gdnf and Gfrα1 activates Ret and promote cell migration, invasion, and proliferation of the UB (Shakya et al., 2005). The Ret/Gdnf signaling is regulated positively by various transcription factors and proteins and by specific inhibitors. HOX family genes are essential for anterior-posterior patterning, and it is known that Hox11 genes control early metanephric induction by its interaction with the pax-eya-six regulatory cascade (Wellik et al., 2002). Eyes absent homolog 1 (Eya1) (P. X. Xu et al., 1999) together with Sina occulis (Six) 1 (P.-X. Xu et al., 2003) transcription factors are essential for MM specification. Wilms tumor suppressor gene (Wt)1 (Kreidberg et al., 1993) and Sal-like (Sall) 1 (Nishinakamura et al., 2001a) are expressed by the MM and regulate Gdnf expression and UB outgrowth (Figure 1b). UB grow is also sustained via Fibroblast grow factors (Fgf), such Fgf1 and Fgf2, that also promote MM survival (Poladia et al., 2006). Importantly, Pax 2 (Brophy et al., 2001) is expressed in both the UB and early MM condensates and acts ensuring high levels of Gdnf, and together with Pax8 regulate the expression of Gata3 transcription

factor that is required for Ret proper expression in the nephric duct (Grote et al., 2006). Regarding the negative regulators, the transcription factors FoxC1/C2 (Kume et al., 2000), and Robo2/Slit2 pathway (Grieshammer et al., 2004), downregulated the expression of Gdnf in the anterior part of the MM to prevent ectopic UB outgrowth. Lateral branching is prevented by the action of Bone morphogenic (Bmp) 4 that acts in the UB trunk. protein acts in the UB trunk preventing lateral branching (Cain & Bertram, 2006; Miyazaki et al., 2000) (Figure 1b).

Nephron induction

The process of MET initiates at E11.5 with the appearance of small cluster of CM, the so-called pre-tubular aggregates (PTs), on either side of each unbranched UB tip. During MET the cells in the PTs become polarized subsequently forming the RVs in which the apical and basolateral sides of the forming tubules can be distinguished at this stage (Figure 2a). This transition is accompanied with lumen formation and tubule development (Rak-Raszewska et al., 2015). Specific inductive signals drive this transition and, among them, several Wnt proteins act as the main factors driving MET (Herzlinger et al., 1994). At this stage, the mesenchymal aggregates express Wnt4, and the UB express Wnt11 and Wnt9a (Carroll et al., 2005; Shan et al., 2010). Ret signaling, activates Wnt11, which is required in a positive feed-back loop to maintain the expression of Gdnf in the MM (Kispert et al., 1996). Wnt9b secreted by the stalk region of the ureter induces canonical β-catenin signaling in the MM, activating a molecular cascade that involves early markers of nephron formation such Pax8, Fgf8, Lhx1, and Wnt4 (Carroll et al., 2005) (Figure 2b). Wnt4a acts in an autocrine manner to maintain and propagate the inductive response that promotes the formation and differentiation of the RV (J.-S. Park et al., 2007).

The induction of nephrogenesis is crucial, but it is also critical to maintain the precursor pool to avoid the conversion of the entire mesenchymal population into nephrons (Schedl, 2007) . Not all cells of the MM aggregate and become epithelial, some cells will remain as mesenchymal interstitial stromal cells between the developing tubules. Signaling coming from these interstitial stromal cells is essential for nephron formation and UB branching (Gregory R Dressler, 2006) (further information is found in the subsection "***Renal stromal cells***" below).

The maintenance of the progenitors in a proliferative and undifferentiated state requires the transcription factor Six2 (Self et al., 2006). The Six2 positive (+) cells also express transcription factors which include Pax2 and Sall1. All these genes are essential for both, the maintenance of the MM multipotent progenitor fate and for the ulterior self-organization and later differentiation (Osafune et al., 2006; Torres et al., 1995). At this stage Bmp7 is also required for suppressing tubulogenesis and for promoting survival of the CM (Dudley et al., 1999) .

Nephron patterning

By E12.5 the mesenchymal aggregates form the RVs with an end still in contact with ureteric epithelium (UE). A single cleft elongates from each RVs and form the CSBs (Figure 2c). Further morphological changes will generate a second cleft and CSBs become S-shaped by E13.5 (Figure 2d). The SS-nephron is a transitional nephron stage with an additional level of patterning which includes proximal, medial, and distal segments that will further differentiate in glomerulus, proximal tubule, intermediate tubule (comprising the loop of Henle) and the distal

tubule (Gregory R Dressler, 2006) (Figure 2e). The are key molecular mechanisms driving the patterning process in the developing nephron.

Then Wnt-β catenin signaling induces Fgf8, which is required for the activation of Lhx1, that controls the expression of POU-domain transcription factor Brn1 and Delta-like protein 1 (DLL1) in presumptive distal nephron precursors (Grieshammer et al., 2005; Kobayashi et al., 2005) (Figure 2c). Therefore, Brn1 commits the cells to becoming distal tubules, and together with Irx genes control the fate of intermediate tubule cells, giving rise to the Henle's loop in mammals (Nakai et al., 2003; Reggiani et al., 2007). The distal part of the future nephron also presents high levels of E-cadherin (Mugford et al., 2009), indicating changes in the expression of cell-cell adhesion molecules. The proximal tubule specification requires the activation of Notch signaling pathway, *via* its ligand Dll1 in the future proximal tubule of the nephron (Cheng et al., 2007; Leimeister et al., 2003) (Figure 2d). The proximal segment of SSBs give rise to the glomeruli, the most complex segment of each individual nephron. Each glomerulus is composed of endothelial, mesangial and podocyte cells. Wt1 expression is restricted to the presumptive podocyte layer and acts suppressing Pax2 expression which seems essential for podocyte maturation (Ryan et al., 1995). The developing podocyte precursors release vascular endothelial growth factor (Vegf) that attracts endothelial cells that contribute to the formation of the mature glomerulus (Eremina et al., 2003). At this stage endothelial cells produce factors, including the platelet-derived growth factor (Pdgf), that supports the differentiation of mesangial cells the supportive cells providing (Lindahl et al., 1998)structure and elasticity to the capillary tuft (Figure 2d). The glomerular basement membrane (GBM) generated by the podocytes separates the endothelial and

mesangial cells from the urinary space. Importantly, the foot processes of the podocytes create the slit diaphragm, a unique type of tight junction which defines the specific pore size essential for the selection of the molecules that will traverse the filtration barrier and enter the urinary space. Importantly, there is a specific complex of proteins, including Nephrin (Boute et al., 2000), Podocin (Roselli et al., 2002), CD2AP (Barletta et al., 2003), and Neph1(Shih et al., 1999), that are essential for maintaining the slit diaphragm and foot process function, and therefore, to maintain the integrity of the filtration barrier. The urinary space is surrounded by the parietal glomerular epithelium and exits into the proximal tubule (Quaggin & Kreidberg, 2008; Schell et al., 2014). By the end of kidney development, by E18.5, the different nephron segments (vascular loop, podocytes, Bowman's capsule, proximal convoluted tubule, intermediate segments with Henle's loop, distal convoluted tubule and collecting duct) are in change of particular physiological functions such as blood filtration, pH regulation, and the reabsorption of solutes (Figure 2e).

Renal stromal cells

During kidney development, in addition to the UB and CM, there is another important source of metanephric regulatory signals, these are the renal stromal cells. These mesenchymal cells do not undergo MET and are found in a disperse manner between the forming nephrons. This cell population is critical for the regulation of the Nephron progenitor cells (NPCs) and UB development. Together with NPCs, renal stromal cells secrete Gdnf in the MM to promote UB branching (Magella et al., 2018). Additionally, the renal stromal cells produce retinoic acid (RA) which in turns upregulate expression of Ret in the UB and therefore contribute to UB branching (Rosselot et al., 2010). Another function of the renal

stromal cells during kidney embryonic development is to control NPCs expansion via FAT4 protocadherin expression which binds to DCHS1/2 cadherin-related protein in MM while restricting NPCs self-renewal (Bagherie-Lachidan et al. 2015; Mao, et al 2015). Finally, renal stromal progenitor cells give rise to all the cell types that comprise the mural cell layer of both the renal blood and lymphoid vessels along with other relevant cell types such as glomerular mesangial cells or pericytes. All these cells comprise the renal interstitium whose function, a part providing structural support to kidney through the production of the extracellular matrix (ECM) production is to fulfill important endocrine functions with the identification of interstitial renin- and erythropoietin-producing cells (Zeisberg & Kalluri, 2015).
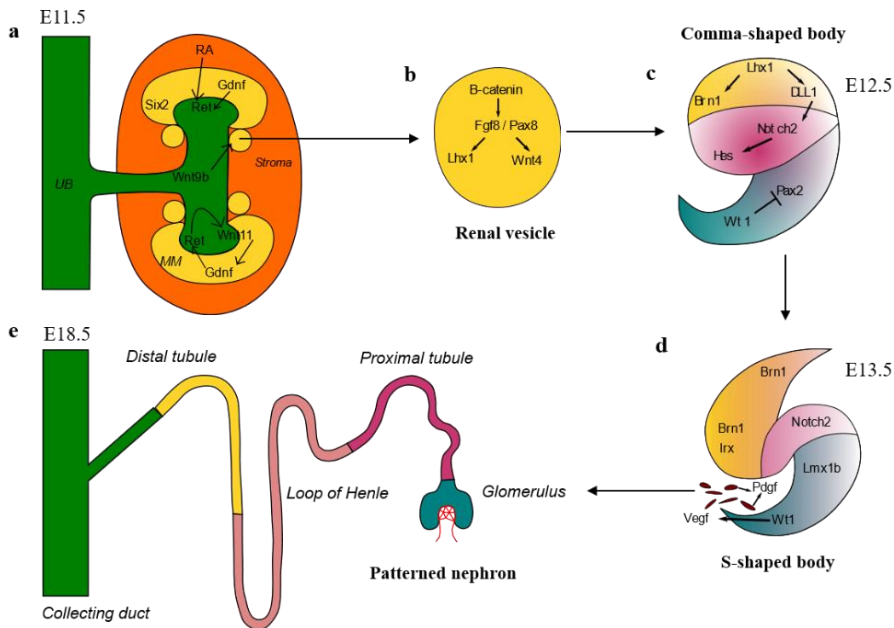
Figure 2. Key events driving nephron induction and patterning. (a) At E11.5 the UB has branched, forming a T-shaped structure. Each UB tip is surrounded by the cap mesenchyme (CM). Reciprocal signaling between the CM and UB, as well as signals coming from the surrounding stromal cells (RA), maintain the UB branching and promote the formation of the pre-tubular aggregates from the CM. Pre-tubular aggregates (PTAs) formation respond to Wnt9b action and Pax8, Fgf8 and Wnt4 are early markers of this CM condensates. Wnt4 initiates the mesenchymal-to-epithelial transition (MET) and induces the formation of the renal vesicle (RV) **(b)** that further gives rise to a Comma-shaped body **(c)** and then a S-shaped body **(d)**. Wnt-β catenin signaling activates Lhx1 that controls the expression of Brn1 and Dll1 in the presumptive distal precursors of the nephron, while the proximal nephron development depends on Notch signaling. Angioblasts invade the proximal cleft of the S-shaped body and contribute to the glomerular capillary. The distal portion of the S-shaped body fuses with the collecting duct and the nephron patterning events along the proximal-distal axis result in the formation of a patterned nephron **(e).** Illustrations reproduced and adapted from: (a) (Davidson 2008) and (b,c,d,e) (Schedl 2007).

2. Study of kidney development

Developmental biology aims to uncover fundamental aspects of organ formation. This complex process, so-called morphogenesis, involves the interaction of genetic programs that work in concert with diffusible gradients and changes in the properties of the physical microenvironment. For many decades, the understanding of kidney development has been possible thanks to the possibility to isolate and grow *ex vivo* developing kidneys from many different species. As early as 1952, Moscona and Moscona (MOSCONA & MOSCONA, 1952) developed *in vitro* culture systems to dissociate and re-aggregate cells from organ rudiments of the early chick embryo. Further work in the field of developmental biology paved the way to monitor early steps of organ re-assembly *ex vivo* leading to seminal discoveries in the field of kidney development. Nowadays, our understanding of kidney morphogenesis largely relays on those first studies from where tissue

dissociation and organotypic culture condition techniques have provided key information for the establishment of culture systems to understand human kidney development.

2.1 Kidney organogenesis study

The culture of whole developing and post-natal organs has been a major field of study since the early 1950s. A key advancement in the field was established by Grobstein (1956) who first defined an *in vitro* culture method that sustained the culture the mouse metanephric kidney (GROBSTEIN, 1956). This study and further experiments showed that kidney organogenesis has the great advantage to occur in *ex vivo* culture, which allows the study, in a dish, of many aspects of its development, particularly branching morphogenesis of the collecting duct system and nephrogenesis. Additionally, over the last decades, important advances in fields like microscopy, live imaging, cell biology and specially genetics have been extremely valuable for increase the knowledge of embryonic development processes. More recently, genetic analyses show the conservation of genetic hierarchies across divergent species, showing the common origin of the embryonic kidney in all vertebrates, despite adult kidneys are specifically adapted to species-specific needs (Gregory R Dressler, 2006).

Traditionally, mice have been the primary model to study kidney due to the similar structural organization between the mouse and human kidney. However, mammalian kidney complexity also makes challenging the study of its development. To overcome this issue, it is crucial that among the different animal species, each kidney is comprised of similar cell types and performs common renal functions.

2.2 Animal models and cell sources to study kidney development and disease

The three separates kidney types that arise during embryogenesis make kidney development in amniotes unique (Davidson, 2008). The acquisition of extra kidney structures seems to respond to the transition from a freshwater proto-vertebrate to a dry terrestrial environment (H. W. Smith, 2011). In lower vertebrates with freshwater larvae, the pronephric kidney regulates water excretion and prevents early dead by edema. The mesonephric kidney responds to increased demands on waste extraction and fluid homeostasis, associated with bigger animals. The unique ability of the metanephric kidney of conserving water, is what allowed the transition of the amniote to the dry land (Vize et al., 1997). Despite their differences, each type of kidney present similar types of cells and regulates common renal functions, what means that genes driving the development of one kidney type are also re-employed in the other. Therefore, other nonmammalian vertebrate species, such as frog, fish and chick, that present simpler kidneys, have been key for the study of the inductive signals and cellular processes at the single nephron level, and investigate genetic mechanisms and cell processes that shape kidney development.

2.2.1 Amphibians

In contrast with mammals, amphibians present a kidney that is less complex and with a faster development. The study of inductive cell signaling events and morphogenesis in amphibians such *Xenopus* is possible due to the fact that analogous genetic networks regulate

mammalian and amphibian nephric organ development (Krneta-Stankic et al., 2017).

Xenopus present several advantages that complement the mammalian models in the study of nephrogenesis. *Xenopus* female develops the eggs externally and in a large number (100-500), enabling easy manipulation and visualization during all the development (FOX, 1963; Krneta-Stankic et al., 2017). As previously mentioned, all vertebrates in early stages present primitive embryonic kidneys that eventually will be replaced by more complex adult kidneys (pro-, meso-, metanephros). The mammalian pronephros are nonfunctional and will be replaced by the mesonephros, and finally by the metanephros, the adult kidneys (Saxén & Sariola, 1987).

Xenopus embryos develop the pronephros as fully functional kidneys after 2-3 days of fertilization, and each pronephros consists of a single nephron with structural and functional similarities with the mammalian nephron (Wessely & Tran, 2011). Therefore, amphibian pronephros can be divided in three domains: the glomus (responsible for blood filtration), the tubules and the duct (responsible for filtering and eliminating waste products) (Brändli, 1999).

The conservation of the genetic mechanism that specify early kidney development, make the *Xenopus* one of the most excellent model systems for genetic screens and tissue transplantations assays. Experiments showing the ability of isolated mesodermal explants from presumptive pronephric regions to form glomus tissue and nephric tubules in culture has been key to study pronephric development (Brennan et al., 1998; Vize et al., 1995). The *Xenopus* embryo has been used to demonstrate the *in vitro* induction of nephric tubules in isolated

animal cap explants (mass of undifferentiated cells) when treated when specific doses of Activin A and RA (Moriya et al., 1993; Osafune et al., 2002). These experiments have been critical to assess the role of these morphogens in the differentiation and proliferation of mesodermal tissues. These experiments have been also fundamental to assess the role of Notch signaling in proximal-distal patterning of pronephros in where Notch-1 seems to regulate the decision between pronephric duct and tubule cell fate in *Xenopus* (McLaughlin et al., 2000).

Importantly, it has been showed that *in vitro*-induced pronephros are capable of restoring the function of native pronephros in host *Xenopus* embryos in which the kidney rudiments were removed (T. C. Chan et al., 1999). Moreover, *Xenopus* embryos and tissue explants are a good tool for high-throughput drug screening and for drug development, and given that the embryos develop outside of the mother the formation of the pronephric tubules can be visualized *in vivo* (Kyuno et al., 2008; Schmitt et al., 2014; Tomlinson et al., 2012). Live imaging experiments in *Xenopus* kidneys has allowed to visualize the cellular movements during nephrogenesis, such the convergent extension movements during tubule formation (Lienkamp et al., 2012).

Therefore, *Xenopus* is a simple and fully functional model of nephrons and pronephros. These great advantages also offer the possibility to use this animal model in *ex vivo* organ culture assays modulating the environmental factors and assessing the impact in tissue development.

2.2.2 Zebrafish

Zebrafish is another lower vertebrate with freshwater larvae, like *Xenopus*, presenting a pronephric kidney that plays a critical role in water excretion and prevents embryo early death by edema (Iain A Drummond, 2005). Zebrafish pronephros consists of a single midline glomerulus filter from the dorsal aorta and drains into two, mediolateral pronephric tubules that empty into converging ducts (Iain A Drummond, 2005).

Zebrafish as model of vertebrate organogenesis presents several advantages that made it an ideal tool for studies of kidney development and disease. Zebrafish embryos are transparent and grow outside the mother, facilitating the observation and manipulation. What is more, they present highly fecundity and rapid development, being free-swimming larvae after 2.5 days (Kimmel et al., 1995), this allow the study of cellular processes and genes controlling kidney development in a short period of time. Additionally, despite being simple in form, zebrafish pronephric glomerulus presents different cell types that are normally presented in higher vertebrates (endothelial cells, podocytes and polarized tubular epithelial cells) (I A Drummond et al., 1998).

These characteristics together with the advances in gene targeting strategies, make zebrafish the ideal tool for mutagenesis screens, and a perfect *in vivo* system to model mammalian diseases affecting glomerular and tubular development.

Taking advantage of the common features between zebrafish pronephric podocytes and mammalian podocytes several defects on glomerulus formation have been studied. Experiments using mutant embryos with defects on their vasculature, support the idea that Vegf secreted by the podocyte acts attracting and assembling the glomerular

capillary tuft (Majumdar & Drummond, 2000). The relevance of degradation and remodeling of the GBM in the capillary tuft formation has been assessed with zebrafish mutants that fail to express specific matrix protease (Serluca et al., 2002). Remarkably, zebrafish podocytes also show slit diaphragms between their foot processes, being one of the major characteristics of mammalian glomerulus blood filter (Reiser et al., 2000). As previously mentioned, specific proteins such Nephrin and Podocin are key for maintaining the filtration barrier integrity. Therefore, defects on the formation of the slit diaphragm result in proteinuria or filtration on high molecular weight proteins (Roselli et al., 2002; Ruotsalainen et al., 1999). Glomerular filtration assays taking advantage of zebrafish homologs of Podocin and Nephrin offer a model of study of human proteinuria (Iain A Drummond, 2005).

This animal model also enables to study defects on kidney tubule, such polycystic kidney disease, one of the most common human genetic diseases (Calvet & Grantham, 2001). Several studies have identified genes that when mutated resulted in cystic pronephroi, including: Polycistin (Pc) 1 and Pc2 (mediate calcium entry) (Nauli et al., 2003), Nek8 (member of the serine/threonine kinases) (Liu et al., 2002) or Nphp proteins (regulate function of basal bodies and/or cilia) (Otto et al., 2003) or Hnf1-β (regulate other cyst-associated genes) (Sun & Hopkins, 2001).

The fact that genes mutated in human diseases are also key for the development and function of the zebrafish pronephros, together with the amenability of this model system to genetic manipulation strategies, makes this animal model an excellent system to study genes function and cell-cell interactions that underline kidney development and disease.

2.2.3 Chicken

In avian embryos the regulation of the ion and water homeostasis relies on the developing metanephric kidneys and on the chorioallantoic membrane (CAM) (Bolin & Burggren, 2013). Early in development, the embryo depends on the CAM to regulate ion and water balance, but as the development proceeds, the mesonephric kidney, later replaced by the metanephric kidney, assumes increasingly important roles in water balance, ion regulation and nitrogenous waste excretion (Gabrielli & Accili, 2010).

The CAM comprises amniotic and allantoic compartments that serves as sources/sinks for both fluid and electrolytes (Graves et al., 1986). During avian embryo development, the kidneys develop in a similar manner that in mammals and reptiles, showing successive nephron types change as the embryo develops. First, the pronephros emerges from the surrounding mesoderm, and it is quickly replaced by the mesonephros that start to grow around E3. Around E15 the mesonephros degenerates as it is replaced by the metanephros (definitive kidney) (Friedmann, 1960). The avian metanephric kidney present nephrons with extended tubular loops and large glomeruli ("mammalian-type" of nephron), and also nephrons with shorter loops and smaller glomeruli ("reptilian-type" of nephron) (Narbaitz & Kacew, 1978).

The avian kidney has been extensively used to study the mechanism governing kidney development. (Garreta et al., 2020).By the 1940s, different researchers demonstrated that growing tissue removed from the avian limb rudiment would rearrange and pattern *in vitro* (RUDNICK, 1946) and *in ovo* (SAUNDERS, 1947) . In addition, disaggregated and reaggregated chick embryonic kidneys became proper

kidney epithelial tubules surrounded by mesenchyme-derived stroma in culture (MOSCONA & MOSCONA, 1952) These experiments pinpointed that cell reaggregation could result in self-reassembly of tissue-like structures, whereby cells organized autonomously into pre-patterned structures. Paul Weiss and A. Cecil Taylor (1960) showed that when chick embryonic cells from different organs at advanced stages of development were reaggregated and grafted into a highly vascularized "neutral environment", as the CAM, the resulting "cell-masses" formed well-organized organs *ex vivo* (Weiss & Taylor, 1960). Interestingly, in that study the authors highlighted the phenomenon of self-organization as the major cause driving morphogenesis instead of "external inductions", which was the major trend explaining development at that time (Weiss & Taylor, 1960).

Chick embryo has been used in induction experiments to study the role of specific morphogens during kidney development. In the context of signals driving IM specification, it has been showed that in the chick embryo the specification of Pax2-positive IM requires contact with axial mesoderm (Mauch et al., 2000). The role of Bmps as potent ventralizing factors has been studied in *Xenopus*, zebrafish, and chicken, showing that this proteins act during gastrulation to determine the size and location of the IM along the medial-lateral axis (James & Schultheiss, 2005; Kishimoto et al., 1997). Another experiment in chick embryos showed that Bmps are also required after gastrulation to drive specific events of metanephric development, such nephric duct formation (Obara-Ishihara et al., 1999).

Renal function in mammals and birds share many similarities, most importantly in the development and maturation of the kidney, being

a key model to use in the investigation of different of this organ development and function. Despite differences in organ morphology between the different types of kidneys presents in vertebrates, all the cited studies collectively show that many parallels do exist at the cellular and molecular level between all these different model systems. Nevertheless, the study of the metanephric kidney relays on the use of mammalian animal models.

2.2.4 Mouse models

The use of murine models for the study of mammalian kidney development has experienced incredible advances in the last decades. This has been possible thanks to the progression in techniques such, organ culture, gene targeting (allowing the creation of transgenic knockin and kockout animals), and the isolation of embryonic stem cells in culture.

Kidney in vitro culture

Kidney culture methods set up had as central event Clifford Grobstein (1956) studies, who is considered the "father of kidney organ culture". In his pioneering studies, Grobstein separated mouse embryonic kidney rudiments at E11.0, isolating the mesenchyme from the UB epithelium leading to the observation that none of them developed separately (GROBSTEIN, 1956). This seminal experiment showed the necessity of inductive signals between these progenitor

tissues for the proper development of the kidney while providing an *ex vivo* culture platform study kidney organogenesis (Figure 3).
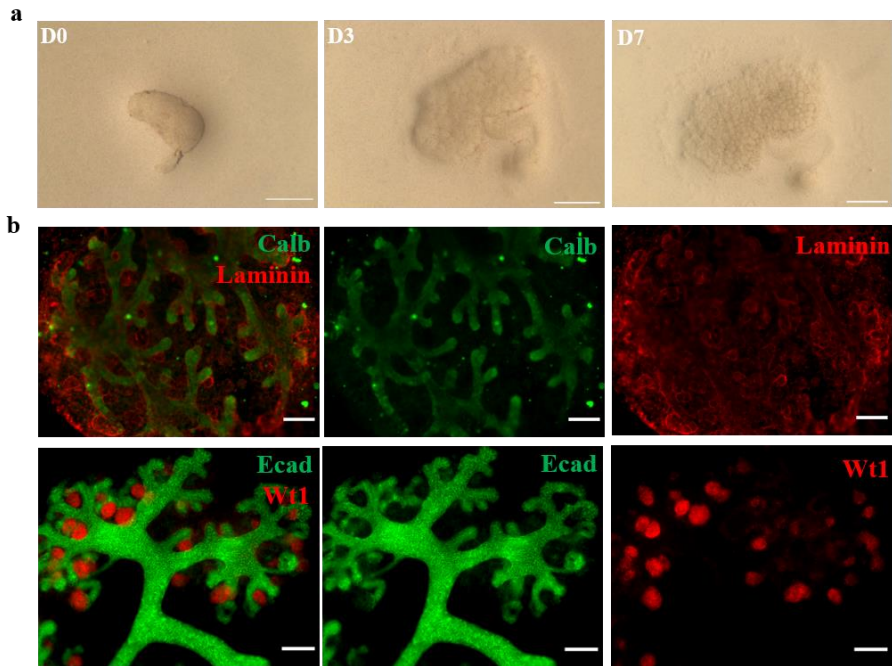

Figure 3. *In vitro* culture of E11.5 mouse embryonic kidneys (a) Bright-field images of E11.5 mouse kidney grown in culture for 0, 3 and 7 days. Scale bar: 0.5 mm.**(b)** Immunofluorescence of E11.5 mouse kidneys after 7 days in culture and stained for different renal markers to show maturation. Calbidin (Calb) is a marker of the UB (*green*) and Laminin a marker of the basement membrane (*red*) (upper panel). Ecad is a marker of the UB (green) and distal tubule and Wt1 a marker of podocytes and CM (red) (lower panel). Scale bar: 100 µm.

Grobstein assay and its ulterior variants allowed the study of the basic mechanisms of renal development. Of importance, the work of Saxen and colleagues (1987) (Saxén & Sariola, 1987) showed that it was possible to culture mouse embryonic isolated MM under a specific inducing condition. In this regard, it was shown that the MM is competent to respond to inductive signals from several embryonic

tissues, including the embryonic spinal cord (eSC) (Saxén & Sariola, 1987). This seminal discovery demonstrated that nephrogenesis induction is permissive rather than instructive, as renal MM is already committed to generate renal epithelial tubules regardless of the origin of the inductive signals.

Importantly, the *in vitro* culture of mice developing kidney culture has helped to study other transcription factors and signaling pathways that can act as mesenchymal inducers. Chemicals as lithium has been studied as putative inducers of MM. Lithium chloride by inhibiting Glycogen Synthase Kinase-3 (GSK-3) disrupts the Wnt/β-catenin signaling and allows MM formation (J A Davies & Garrod, 1995; Halt & Vainio, 2012). Inhibition of GSK-3 implies the cytoplasmic stabilization of β-catenin which leads to the activation of target genes (Kuure et al., 2007). Further studies using lithium chloride, bromoindirubin-3'-oxime (BIO), or 6-[[2-[[4-(2,4-dichlorophenyl)-5-(5-methyl-1H-imidazol-2-yl)-2-pyrimidinyl]amino]ethyl]amino]-3-pyridinecarbonitrile (CHIR99021) showed that by inactivating GSK-3, they act preventing MM apoptosis and enhancing tubulogenesis (Ye et al., 2012). Other molecules can also interfere with the Wnt signaling and act blocking kidney development. Experiments with the inhibitor of Wnt production 2 (IWP2) and the inhibitor of Wnt response 1 (IWR1) showed inhibition of correct kidney formation (Voronkov & Krauss, 2013). These studies reinforce the relevance of Wnt/β-catenin signaling in tubulogenesis.

Mouse transgenic models

The combination of genetic models and the different systems to culture *ex vivo* the mouse developing kidney has allowed to start elucidating on the role of specific genes during embryogenesis.

Several knock-out or loss-of-function mouse models have confirmed the relevance of specific genes during UB outgrowth and MM induction. Mutants for Pax2 (G R Dressler et al., 1990; Rothenpieler & Dressler, 1993), Wt1 (Kreidberg et al., 1993) or Sall1 (Nishinakamura et al., 2001b) showed how UB failed to grow while the MM stayed uninduced. Regarding factors involved in UB growth and branching, mutants of Ret receptor (Shakya et al., 2005) or regulator factors such Wnt11, Fgf, Egf, resulted in kidney agenesis or impaired UB branching (Jamie A Davies, 2002). In the same manner, defects in negative regulators also affects UB branching. This was demonstrated in Bmb4-null embryos which showed ectopic UBs (Miyazaki et al., 2000). It has been also reported that in transgenic animal models for genes driving MET and nephron patterning events, as Wnt9b mutants (Carroll et al., 2005), there is failure to form PTAs and as consequence to undergo tubulogenesis. Also, that mice deficient for Notch2 (Cheng et al., 2007) lack glomeruli and proximal tubules. Studies of genes involved in podocyte formation such as Vegf, showed that when Vegf expression is blocked or genetically abrogated, the formed glomeruli lack capillary tuft and present important vascular defects (Kitamoto et al., 1997; Sison et al., 2010).

All these studies show that *in vitro* kidney culture is a valuable tool, however it presents important limitations. Kidneys is a complex three-dimensional (3D) organ, therefore when cultured in two-

dimensions (2D) on the top of culture filters the morphology of the UB branching is not equal as *in vivo*. This limitation showed the need for developing 3D culture techniques.

3D culture approaches

It has been reported that the culture of UB in ECM compounds such Matrigel or collagen IV, together with the addition of growth factors, results in a branching pattern similar to the *in vivo* UB (Meyer et al., 2004). Similarly, the Davies group developed a variant of the Grobstein assay, the so-called dissociation-reaggregation assay (Figure 4a,b). In their work, the authors isolated mouse kidney MMs and UBs between E11.5 and E13.5 and further dissociated the embryonic tissues into singe-cell suspensions which were then reaggregated and cultured using standard organotypic culture conditions. To reduce cell apoptosis, the authors transiently cultured the kidney reaggregates with Rho kinase inhibitors observing that the kidney structures formed present normal morphology, expressed correct differentiation markers and were attached at their distal ends with the UB (Unbekandt & Davies, 2010). With this work the authors were able to stablish a 3D culture method for the generation of kidney tissues alike to the normal mouse embryonic kidneys (Figure 4a,b)

The dissociation-reaggregation assay opened the door to the generation of chimeric kidney rudiments *ex vivo* by mixing different cell types and testing their nephrogenic potential (Figure 4c). By mixing cells genetically modified before reaggregation these works also asses the contribution of the specific genes to nephron formation (Junttila et al., 2015; Unbekandt & Davies, 2010).
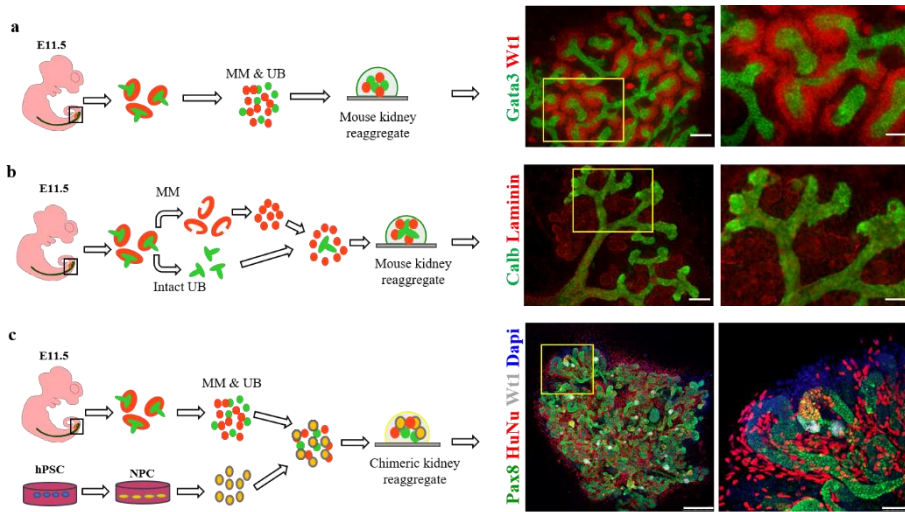
Figure 4. Kidney disaggregation-reaggregation assays for the study of kidney development *ex vivo*. (a) E11.5 mouse kidneys are dissociated into single cell suspensions and further reaggregated and cultured *ex vivo*. Representative immunofluorescence images of the generated mouse kidney reaggregates showing MM (Wt1, *in red)* and UB (Gata 3, *in green*) positive structures. Notice the formation of multiple small branching UBs rather than the single normal-tree arrangement. Scale bar: 100 µm, 50µm. **(b)** Dissociated mouse MM is combined with intact mouse UB and cultured *ex vivo*. Representative immunofluorescence images of the generated mouse kidney reaggregate showing MM (laminin, in red) and UB (Calbidin, in green) positive structures. Nephrons are arranged around one single-collecting duct. Scale bar: 100 µm, 50 µm. **(c)** hPSC-NPCs are combined with cell suspensions from dissociated E11.5 mouse kidneys and cultured for 5 days to assess the *ex vivo* capacity of hPSC-NPCs to further engraft into nascent tubular or glomerular developing structures. Representative immunofluorescence images of chimeric kidney reaggregates showing nascent nephron structures (Pax8, *in green*) in where human cells (HuNu, in red) engraft in both glomerulus- or tubular-like structures (Wt1, in white). Magnified area shows human cells (HuNu, *in red*) in the proximal segment of a developing nephron structures (Pax 8, *in red*) a nascent glomerular-like structure. Scale bar: 250 µm, 50µm

Mouse embryonic stem cells

As early as during 1964 Kleinsmith and Pierce showed on a rare type of tumor, called teratocarcinoma which contained cells that were both pluripotent and self-renewing (KLEINSMITH & PIERCE,

1964). Pluripotent means the capacity of an individual cell to give rise to all other cell types of the body and the germline. This property is normally restricted to a brief window in early development. Self-renewal refers to the intrinsic ability to produce identical daughter cells while retaining the ability for differentiation. As such, it is the defining feature of a stem cell. The study of teratocarcinoma stem cells led to the definition of culture conditions sustaining for their propagation *ex vivo* while preserving their pluripotent capacities, that is with no spontaneous differentiation. In 1981 Martin Evans, Matt Kaufman and Gail Martin found that cells from early mouse embryos exposed to the same culture environment as the one defined by Kleinsmith and Pierce could suspend embryonic stem cells developmental progression and continue to multiply while remaining pluripotent (Evans & Kaufman, 1981). From that moment mouse embryonic stem cells (mESCs) provided a crucial tool for manipulating mouse embryos to study mouse genetics, development and physiology. In this regard, mESCs have not only revolutionized experimental mammalian genetics but, with the advent of equivalent human ES cells (hESCs), have now opened new *vistas* to understand renal differentiation in the Petri dish. In this regard, the strategy to developing an *in vitro* differentiation method for the generation of renal cells has been to recapitulate embryonic kidney development.

With regards to kidney differentiation, almost all mouse differentiation protocols use embryoid bodies (EBs) as an intermediate step to generate renal progenitor cells. Kim and Dressler were the first authors to use a combination of Activin A, Bmp7, and RA to differentiate mouse PSCs into renal cells (D. Kim & Dressler, 2005). By a first step inducing EBs from undifferentiated mESCs the authors committed the

initial mESCs cultures into cells expressing markers for IM and early derivatives of the MM, such as Pax2, Wt1, Lim1, Gdnf, Cadherin-6, and Eya1. In addition, the authors injected the resulting cells into developing kidneys and observed their integration into tubules, along with the expression of proximal tubule markers. Following this work, Morizane and colleagues used mouse induced pluripotent stem cells (miPSCs) generated from mouse fibroblasts which upon EB induction were further committed into cells expressing Six2, Wt1, Pax2, Nephrin, and KSP (the last one being a tubular specific marker) (Morizane et al., 2009). During the entire process, Activin A, Gdnf, and Bmp7 or only Activin-A were added to the differentiation media. When the three nephrogenic factors were used, the authors found that the miPSC could differentiate into MM-like cells, while the sole use of Activin A enabled for the generation of tubular-like cells (Chow et al., 2020).

2.2.5 Human pluripotent stem cells

NPCs can be isolated from the mouse embryonic kidney and it has been recently described on the possibility to identify cell culture conditions for their expansion *in vitro* raising the prospect of nephrogenesis *in vitro* (Brown, et al 2015). Nevertheless, access to NPCs from human embryonic kidney is not affordable and rises important ethical concerns. An alternative to recreate NPCs stands in the identification of human cell sources with renal differentiation potential. In this regard, human pluripotent stem cells (hPSCs) due to their inherent functional properties represent a unique cell source to virtually generate any cell type of our body. Profiting from this characteristic both hESCs (Thomson et al. 1998) and human induced pluripotent stem cells (hiPSCs) (Takahashi et al. 2007) are being used to phenocopy early steps

28

of tissue specification and differentiation. This has resulted in the establishment of cell culture procedures which recapitulate developmental signals by culturing hPSCs in front of cell culture media containing soluble factors or chemical compounds emulating the biochemical signaling that hPSCs encounter during tissue development. These approaches are largely relaying in the use of other external stimuli as the presentation of ECM proteins promoting differentiation or the use of supportive cells that act as producers of paracrine signaling in these culture systems.

3. Derivation of kidney organoids from hPSCs

3.1 Major milestones in the field of kidney organoid derivation

Accumulated findings on the genetic mechanisms and cell processes that shape kidney development using animal models such as chick and mouse have been crucial when providing a correct understanding of early kidney embryogenesis. Because most of our knowledge on kidney development is derived from these model organisms, it is expected that a better knowledge of how human kidney development proceeds will result in our comprehension on species-related differences and to envision new strategies to regenerate the human kidney. Despite the difficulty in accessing human embryos and their ethical use, the field has recently been able to investigate human embryonic kidney samples. These works have started to shed light on differences between human and mouse kidneys. (Lindström, et al. 2018). With the advance of powerful tools such as single-cell RNA-sequencing (scRNA seq) it is now possible to start performing a thorough

characterization of the multiple cell types encountered in the human kidney as well as the proportion of a specific cell population with respect to the others. When generating this data sets from mouse and kidney organs at different stages during embryonic development the resolution of differentiation state and spatial distribution at single cell level may help to improve our understanding on kidney development. To date different reports have defined culture conditions for the isolation and expansion of embryonic kidney cells (reviewed in Shankland et al. 2007; Romagnani, et al 2013a; Romagnani and Anders 2013b;). An alternative methodology for the generation of unlimited quantities of kidney-related cell types is the differentiation of hPSCs. In the last few years independent research groups have described for the first time the possibility of generating different kidney populations from hPSCs. In this regard, Song and colleagues were the first to describe on the derivation of podocyte progenitor cells from hiPSCs. In their work the authors showed that hiPSCS-derived podocytes were efficiently integrated in mouse metanephric tissues. Yet, the question of which embryonic progenitor cells during development are equivalent to Song's iPSC-immature podocytes remained to be answered (Song et al., 2012). In this regard, the recent work from Nishinakamura laboratory has shown on the derivation of podocyte-like cells using a hiPSCs reporter cell line to monitor the expression of Nphs1, this line was previously described by the same group (Sharmin et al., 2016). In this recent work the authors first employed mouse embryonic NPCs to define the experimental conditions to be used in Nphs1-GFP hiPSCs line, which consisted in the use of Wnt signaling to induce MET and podocyte differentiation, together with the inhibition of Tgf-β signaling to support the domination of the RV proximal domain which resulted in the suppression of other

nephron lineages. This approach enabled successful induction of human podocytes from PSCs with >90% purity exhibiting global gene expression signatures comparable to those of adult human podocytes (including foot process–like and slit diaphragm–like structures), and showed functional responsiveness to drug-induced injury (Yoshimura et al., 2019). In another approach, the group from Melissa Little has recently isolated 3D human glomeruli from iPSC-derived kidney revealing improved podocyte-specific gene expression, maintenance *in vitro* of polarized protein localization, and an improved glomerular basement membrane matrisome compared to 2D cultures. Importantly, in that same work the authors also showed that organoid-derived glomeruli retain marker expression in culture for 96 h, allowing for toxicity screening (Hale et al., 2018).

Other protocols on the development of renal cell types were also described by Narayanan and colleagues who described on generation of renal epithelial cells from hESCs. The differentiated stem cells exhibited markers characteristic of renal proximal tubular cells and their precursors generating tubular structures *in vitro* and *in vivo* (Narayanan et al., 2013). By the same time, Mae and colleagues differentiated, for the first time, monolayers of hESCs towards IM making use of a reporter hiPSC line in which GFP was targeted into Osr1. In their work Mae and colleagues first performed a screen of ~40 different growth factors and identified that Bmp7 was the most potent inducer of Osr1 expression. Then the authors set up a straightforward methodology to generate IM-like cells out of different cell lines using monolayer cell culture or EBs, nonetheless the generated cells also showed signatures of other kidney mature cell types and limited tubular structures. To further explore on the identification of chemically defined medium sustaining for the

31

derivation of IM-differentiated iPSCs the same group pursued the identification of two retinoid-like molecules inducing IM derivation from iPSCs and further showed that the resulting IM-like cells exhibit the capability to differentiate into multiple kidney cell types, also developing 3D renal-tubule-like structures in *ex vivo* organ culture settings (Mae et al., 2013).

Into the quest of straight forward procedures to generate kidney progenitor cells the Izpisua Belmonte laboratory did show on the possibility to generate, for the first time, UB progenitors from both hESCs and from hiPSCs derived from patients affected by polycystic kidney disease (PKD). Making use of a two-step protocol the authors first induced mesodermal specification by Bmp4 and Fgf2. Then IM anteriorization was induced exposing the cells to RA, Activin A and Bmp2. After only 4 days in culture UB progenitor cells expressed Hoxb7, Ret and Gfra1. Moreover, when UB-like-hiPSC-derived cells were co-cultured with dissociated E11.5 mouse metanephric cells, UB-like-hiPSC-derived cells only integrated into cytokeratin 8 (Ck8) + UB-like structures, suggesting, for the first time, the induction of UB lineage-committed IM cells *ex vivo* (Xia, et al 2013). Another strategy was described by the Little group which developed different procedures for the generation of well-characterized kidney progenitor cells from both hESCs and hiPSCs into IM first generating posterior primitive streak cells. To achieve this, the authors generated a reporter hESC line for monitoring the expression of Mixl1 (a gene transiently expressed in the primitive streak during embryogenesis) by knock-in GFP into the Mixl1 *locus*. In this manner it was possible to individually generate UB cells or simultaneously generate MM and UB derivatives from hPSCs. Making use of re-aggregation assays the authors assessed the differentiation

potential of both hPSCs derived MM and cells (M. Takasato et al., 2014). Interestingly, Lam and colleagues followed a different approach to efficiently generate Pax2+Lhx1+ IM cells that spontaneously form tubular-like structures. Furthermore, the generated cells generated in the study of Lam and colleagues efficiently integrated into mouse metanephric cultures and differentiated into multipotent NPCs exhibiting a CM-like signature, including Six2, Sall1 and Wt1 markers (Lam et al., 2014). In the same manner, Taguchi and colleagues reported on the derivation of both mESCs- and hiPSCs- which showed the ability to reconstitute 3D nephron-like structures (including both glomerulus- and renal tubule-like structures *in vitro*). These co-cultures made use of embryonic spinal cords as an external inducing source for kidney differentiation *ex vivo* (Taguchi et al., 2014).

Based upon these findings, Imberti and colleagues derived NPCs from hiPSCs following a two-step protocol by first exposing hiPSCs to RA, RhoA and PI3K inhibitors and Activin A to induce IM generation. Next IM-committed hiPSCs were treated with Fgf2, Bmp7 and Gdnf for 13 additional days to generate MM-derived hiPSCs. Although other authors had already demonstrated the possibility of generating MM-derived hPSCs, in this work Imberti and colleagues demonstrated for the first time that hiPSC-derived renal progenitors robustly engrafted into damaged tubuli restoring renal function (Imberti et al., 2015). Other approaches to recapitulate MM derivation were also reported by the group of Bonventre, which showed on the generation of Six2+Sall1+Wt1+Pax2+ NPCs with 90% efficiency after 9 days. More importantly, the authors proved that NPCs form hPSCs-derived kidney organoids (kidney organoids) in both 2D and 3D settings after 21–28 days, containing epithelial nephron-like structures expressing markers of

podocytes (Podxl, Nphs1), proximal tubules (Cdh2, Ltl), loops of Henle (Ecad, Umod) and distal tubules (Ecad, Brn1) mimicking nephron development. Importantly, the organoid culture system was used to study the mechanisms of proximal and/or distal tubular toxicity by exposing kidney organoids to chemical agents routinely used in animal models *in vivo* (Morizane et al., 2015). Along this same line, another work from the same laboratory, showed that kidney stem cells derived from hPSC can be induced to form spheroids mirroring tissue-specific epithelial physiology. In this work, Freedman and colleagues were able to knock out Podxl , polycystic kidney disease (Pkd) 1 or Pkd2 genes by clustered regularly interspaced short palindromic repeat (CRISPR)/CAS9 RNA-guided nucleases CRISPR/Cas9, proving for the first time the feasibility of 3D renal-derived structures to model human kidney disease (Freedman et al. 2015).

Then, the laboratory of Melissa Little went one step further in the generation of kidney organoids containing individual nephrons (~100 nephrons/organoid) that further segmented into distal and proximal tubules, early loops of Henle and glomeruli containing podocytes elaborating foot processes. In this work the authors performed bulk RNA seq for transcriptomically profile the extent of kidney organoid differentiation also comparing the matureness of the generated organoids with human embryonic kidneys and demonstrated that upon 25 days of differentiation kidney organoids transcriptomically resembled the first trimester gestational kidney (Takasato et al. 2015).

Into the light of all these findings our group hypothesized that enhancing cell-to-cell contact by the aggregation of IM-hPSCs cells soon after their derivation would result in the generation of kidney organoids

with superior characteristics of renal differentiation. Following this logic our procedure resulted in the generation of kidney organoids with augmented differentiated features which were confirmed by an exhaustive analysis using both immunohistochemistry and bulk RNA seq, the later showing that our procedure led to the generation of kidney organoids which upon 16 days in culture transcriptomically matched the second trimester human gestational kidney (Garreta et al., 2019). Indeed, both these works benefit from already available organ-specific datasets and the use of KeyGenes (Roost et al., 2015) a machine-learning algorithm that accurately predicts the identity score of the different cell types present in organoids confirming the differentiation progression of kidney organoids towards the first (Takasato et al. 2015) or the second trimester kidneys, respectively (Garreta et al., 2019). All in all, these procedures highlight on the utility of hPSCs as unique cells sources to understand on the growth factor signaling required across kidney embryogenesis (Takasato and Little 2015). As a result, all these different approaches broadly use the same signaling pathways and arrive to different stages of differentiation in a remarkably congruent time frame supporting on the relevance of kidney organoids as a model human nephrogenesis (Little & Combes, 2019).

3.2 Major drawbacks in the field of kidney organoid derivation

Besides all the advances mentioned above, the kidney organoid field is already facing important drawbacks, which include the lack of a well-defined nephron progenitor population able to support nephrogenesis within the short lifespan of kidney organoids (~35 days in culture). In this regard, it is well known that nephrogenesis within the

mammalian kidney depends on the reciprocal interactions between the UB and the surrounding Six2+ CM, however, the majority of the protocols for the derivation of kidney organoids first differentiate kidney progenitor through the formation of NPCs that are then induced to epithelialize using a pulse of the GSK3 inhibitor CHIR (an analog of Wnt9b, the natural epithelialization stimulus in the mammalian embryonic kidney). Importantly, this single epithelialization induction differs from the process of differentiation in the native developing kidney, where cells at numerous stages of differentiation co-exist within the organ as recently described by McMahon laboratory (Lindström, et al. 2018). Following this logic, the laboratory of Oxburgh has recently shown that the asynchronous mixing of hPSCs-derived NPCs with epithelializing nephrons over time results in the generation of heterochronic organoids in where the proximal and distal nephron components preferentially derive from different cell populations. Furthermore, the resulting organoids were well vascularized when engrafted under the kidney capsule (Kumar Gupta et al., 2020). Thus, further studies exploiting this approach may increase our understanding on how to develop new venues to define new differentiation procedures sustaining for the derivation of NPCs supporting nephrogenesis. This basic knowledge will be of major benefit when envisioning new prospects for renal replacement applications.

Another area of intense research stands in the definition of new approaches to provide a vascular compartment to kidney organoids. In this regard, *in vivo* vascularization (host-derived vascularization) of either hiPSC-derived nephron progenitor cell aggregates (Bantounas et al., 2018; Sharmin et al., 2016) or kidney organoids (Tanigawa et al., 2018; van den Berg et al., 2018) has been partially achieved after

organoid transplantation under the kidney capsule of immunodeficient mice profiting from the high vascularization capacity of this tissue. In a different approach, our group has shown on the possibility to engraft kidney organoids onto the chick CAM showing host vascularization, but also the formation of capillary loop stage glomeruli-like structures with endothelial cells of human origin in close contact to podocyte-like cells (Garreta et al., 2019). Another recent study has designed a 3D printed chamber at the millimeter scale to culture hPSC-derived kidney organoids under constant fluid flow that sufficed for the expansion of endothelial progenitors within the organoids and a higher degree of vascularization compared to the static culture conditions (Homan et al., 2019). Altogether, these findings indicate that the formation of functional vascular networks upon transplantation likely rely on the synergistic modulation of the microenvironment together with the formation of the proper interactions between the host vasculature and the endothelial-committed cells that do exist in hPSCs-derived organoids *prior* transplantation. This last point will benefit from recent findings showing on the generation of kidney organoids with enhanced endothelial cell compartment such as the recent findings reported from the Xia laboratory on the definition of a new procedure protocol to generate vascularized organoids by modulating Wnt signaling (Low et al., 2019). In their work the authors took advantage of WNT signaling modulation to control the relative proportion of proximal versus distal nephron segments for the production of Vegfa , the major factor responsible for the maintenance of the glomerular vasculature (Eremina et al., 2003; Sison et al., 2010). More importantly, in the work from Low and colleagues made use of scRNA seq to further identify a subset of NPCs as a potential source of renal vasculature which was further

supported by the revelation of Six1+Cd31+ (Sall1+Cd31+) cells (Low et al., 2019). In this regard, recent work from McMahon laboratory has shown on the utility of single-nucleus droplet-based sequencing of the human fetal kidney for the identification of nephron, interstitial, and vascular cell types that together generate the renal corpuscles identifying factors predicting precursors or mature podocytes which express Fbln2, Bmp4, or Ntn4, in conjunction with recruitment, differentiation, and modeling of vascular and mesangial cell types into a functional filter (A. D. Kim et al., 2019). *In vitro* studies using primary cells from fetal kidneys proved that these factors exhibit angiogenic or mesangial recruiting potential also exerting inductive properties consistent with a key organizing role for podocyte precursors in kidney development. It will be interesting to challenge developing hPSCs kidney organoid to boost these processes.

Another technical challenge, regardless of the approach used to induce vascularization, is to recapitulate embryonic branching morphogenesis in kidney organoids. As predicted from mice (Costantini & Kopan, 2010), recent analysis in the human fetal kidney would suggest that the collecting duct tips should be marked by Ret expression (Lindström, et al. 2018; Menon et al. 2018; Hochane et al. 2019). Nonetheless, there is no study showing Wnt9b expression in kidney organoids nor any evidence for the existence of UE. In this regard, the Melissa Little group referred to the Gata3+Ecad+ structures encountered in kidney organoids as collecting duct (Takasato, et al. 2015), however, in that same work RNA seq analysis did not reveal Wnt9b or Ret expression. Recently, the same group has referred to those structures as connecting segment (Little & Combes, 2019), which refers to the region of the nephron which bridges to the collecting duct epithelium (Little et

al., 2007). Nonetheless, the same group did not find that this presumptive connective segment derives from Six2+ cells as happens in mouse (Georgas et al., 2011) suggesting that this epithelium may arise from an UE during the time course of organoid formation. In this regard, the work from the Nishinakamura laboratory has been the only one providing a comprehensive overview on the distinct origins and developmental processes of the ureteric bud (Taguchi & Nishinakamura, 2017). Towards this aim the authors took advantage of the Hoxb7-GFP transgenic mouse line in order to establish a kidney reconstruction assay by modifying previously reported methods (Auerbach & Grobstein, 1958; Ganeva et al., 2011; GROBSTEIN, 1953). Through the reaggregation of E11.5 MMs, including NPs and SPs with a wolffian duct or UB from E9.5, E10.5, and E11.5 E the authors were able to show that UB or WD from the E11.5 embryo would robustly branch in front of WD from E10.5 and E9.5. Importantly, the authors employed the best culture condition supporting WD-acquired branching capacity in order to further define the biochemical cocktail inducing the maturation of WD progenitors into UB-like cells. This information allowed for the derivation of novel culture procedures for the differentiation of mESCs into induced UB which effectively reconstructed the higher-order structure of the embryonic kidney by their assembly with NPCs and isolated renal embryonic stromal cells. Then the authors translated these findings to applying the different procedures using hiPSCs. All in all, the work of Nishinakamura showed that reassembled organoids developed the inherent architectures of the embryonic kidney, including the peripheral progenitor niche and internally differentiated nephrons that were interconnected by a ramified UE. Thus, exploiting the selective induction on hPSCs together with the reassembly of the different cell

types will be a powerful approach to recapitulate organotypic architecture in hPSC-derived organoids and to further assess on the role of human UB branching epithelium as an organizer of tissue geometry and cell viability during human embryonic kidney development. A summary of recent published reports on the generation of hPSC-derived kidney progenitors and kidney organoids is compiled in **Table 1**.

Table 1. Main methodologies for the derivation of hPSCs-renal cells and hPSCs-kidney organoids. *This table provides a comparison between the main protocols published for the derivation of hPSCs-renal cells (A) and hPSCs-kidney organoids (B) including schematic explanation of the protocol differentiation (steps, duration, growth factors, cytokines and cell lines used); renal cell types and renal structures obtained, and functional/validation and in vivo assays performed to assess the maturation and functionality of the derived renal cells generated.*

A) hPSCs-derived renal cells

Protocol	Renal differentiation protocol	hPSC-derived renal cells	Functional and validation assays	*In vivo* validation
Song et al. (2012)	**(d0-d3) EB formation:** 10 ng/ml Activin A + 15 ng/ml Bmp7 + 0.1 µM RA **(d3-d11) Glomerular podocytes:** 10 ng/ml ActivinA + 15 ng/ml Bmp7 + 0.1 µM RA Cell lines used: Human iPSC (human kidney mesanglial cells)	Derivation of hiPSC-derived podocytes showing protein localization of mesodermal and podocyte markers: Wt1, Pax2, Nephrin, Podocin and Synaptodin.	Contractile response to angiotensin II and endocytosis of FITC-labeled albumin.	Efficient integration into WT1-positive glomerular aggregates in mouse metanephric tissues.
Narayanan et al. (2013)	**(d0-d20) Proximal tubular cells:** 10 ng/ml Bmp2 + 2.5 ng/ml Bmp7 + 10 ng/ml Activin A + 0.1 µmol/l RA Cell lines used: Human ESCs	Derivation of renal PTCs expresing Aqp1 and other markers of renal epithelial cells and PTCs, showing expression patterns comparable to human PTCs.	Integration into CK18-positive tubular epithelia when injected into the cortex of kidney explants from newborn mice. Response to PTH and GGT activity *in vitro* and under bioreactor conditions.	Formation of tubular-like structures in subcutaneous implants into immunodeficient mice.
Mae et al. (2013)	**(d0-d2) Mesoderm:**100 ng/ml Activin A + 3µM CHIR +/- 10µM Y27632 **(d2-d10) Early intermediate mesoderm:** 100 ng/ml Bmp7 + 3µM CHIR **(d10-d17) Intermediate mesoderm:** 10 ng/ml Tgfβ1 Cell lines used: Human iPSCs (201B6, 201B7, 253G1 and 253G4) and human ESCs (H9, khES1 and khES3)	Generation of IM cells expressing Osr1 (90% postive cells) that differentiate into multiple cell types of IM-derived organs. Renal-like cells expressing specific markers of proximal tubule (Ltl/Aqp1), glomerulus (Pna, Podxl), epithelial markers (Cytokeratin, Ecad) and UB (Dba/Sall4).	Integration into mouse metanephric tissues and formation of tubule-like cells after co-cultuting of Osr1+ with mouse metanephric cells.	Detection of cells positive for renal markers such Aqp1, Ltl, Ecad and Dba, after transplanting Osr1+ cells into the epididymal fat pads of immunodeficient mice.

Table 1. (Continued)

Xia et al. (2013)	**(d0-d2) Mesoderm progenitors:** 30 ng/ml Bmp4 and 50 ng/ml Fgf2 **(d2-d4) Intermediate Mesoderm - Ureteric bud progenitors:** 1µM RA + 10 ng/ml Activin A + 100 ng/ml Bmp2 Cell lines used: Human ESCs and human iPSCS (dermal fibroblasts)	Derivation of UB progenitors expressing Hoxb7, Ret and Gfra1 markers rather than markers from MM.	Integration into Ck-8 + UB-like structures when co-cultured with dissociated E11.5 mouse metanephric kidneys.	N/A
Lam et al. (2014)	**(d0-d2) Mesoderm:** 5µM CHIR **(d2-d4) Intermediate Mesoderm:** 100ng/ml Fgf2 + 1µM RA **(d4-d7) Cap mesenchyme:** 100 ng/ml Fgf9 + 10 ng/ml Activin A Cell lines used: Human ESCs and human iPSCs (foreskin and dermal fibroblasts)	Generation of Pax2+ Lhx1+ IM cells . Upon growth factor withdrawal, IM cells give rise to tubular structures expressing Ltl/N-cadherin /Ksp. With the addition of Fgf9 and Activin A, the IM cells differentiates into CM nephron progenitors expressing Six2/Sall1/Wt1.	IM cells of d3 (Pax2+ Lhx1+) and d9 (Ltl+ KSP+) reaggregated with dissociated cells from wild-type E12.5 mouse embryonic kidney. Human d3 cells integrated into mouse metanephric interstitium, and human d9 cells in both mouse metanephric interstitium and within organized laminin-bounded structures containing mouse cells. CHIR treatment to Six2+ cells resulted in changes in cell morphology and formation of tubular-like structures (mimicking in vivo tubulogenesis) Re-aggregation assays of Six2+ cells with mouse embryonic kidney showed organization into clusters Ltl+ cells.	Ltl+ Ksp+ tubular structures injected beneath the kidney capsule of a immunodeficient mice, resulted in human growths expressing Aqp1

Table 1. (Continued)

Takasato et al. (2014)	Strategy A: (d0-d2) **Posterior Primitive Streak:** 30 ng/ml Bmp4 + 10 ng/ml Activin A **(d2-d6) Intermediate mesoderm:** 200 ng/ml Fgf9 + 1µg/ml heparin **(d6-d17) Metanephric mesenchyme and ureteric bud epithelium:** 200 ng/ml FGF9 + 50 ng/ml BMB7 + 0.1 µM RA + 1 µg/ml heparin	Derivation of PS cells (Mixl1+, Lhx1+) that differentiate into IM (Osr1+, Pax2+, Lhx1+) that simultaneously generate both MM (Six2+, Wt1+, Gdnf+, Hoxd11+) and UE cells (C-Ret/Hoxb7) Prolonged differentiation showed UE structures (Ecad+) and surrounded by MM cells	N/A	Reaggregation assays of dissociated mouse embryonic kidneys (E12.5-13.5) with d12-13 hESC-derived renal cells. Integration only into MM and UE
	Strategy B: (d0-d2) **Posterior Primitive Streak**: 8µM CHIR **(d2-d12) Intermediate mesoderm**: 200 ng/ml Fgf9 + 1µg/ml heparin **(d12-d18) Metanephric mesenchyme and ureteric bud epithelium**: no growth factors Cell lines used: Human ESCs and human iPSCs	Faster induction of kidney markers and more prolonged expression of MM genes. Identification of Gata3 co-expressing with Pax2+ UE with MM condensed tightly around the UE tips. Presence of Foxd1+ renal stroma cells. Later differentiation showed Ecad+ UE structures surrounded by clumps of MM (Wt1+, Six2+, Pax2+). The MM expressed early nephron/renal vesicles such Cdh6 and Jag1. hESC-derived kidney cells (d18) enzymatically dissociated into single cells, pelleted and cultured following standard culture conditions for embryonic mouse kidney rudiments.Within 4 days, detection of Ecad+ tubules expressing UE markers (Pax2+, Aqp2+) and proximal tubule markers (Aqp1+, Slc3a1+).	N/A	Reaggregation assays of dissociated mouse embryonic kidneys (E12.5-13.5) with d12-13 hESC-derived renal cells. Integration into all major compartments of the developing kidney including UE, early nephron/renal vesicles and nephron progenitor mesenchyme

43

Table 1. (Continued)

Imberti et al. (2015)	**(d0-d6) Intermediate mesoderm:** 0.1 µM RA + 5 µM LY294002 + 10 ng/ml Activin A (from d2 to d4) **(d6-d19) Metanephric mesenchyme:** 50 ng/ml Bmp7 + 10 ng/ml Fgf2 + 15 ng/ml Gdnf Cell lines used: Human iPSCs (SC101 A1)	Generation of IM cells expressing Wt1, Pax8, Pax2, Six2 and SALL1 that progressively acquired renal progenitor phenotype expressing markers of nephrogenic zone(NCAM), and markers of MM and glomerular cells (CD133,CD24). It was also assessed the expression of Claudin1 (glomerulus), and AQP1 and GGT1 (proxima tubule)	N/A	D12 MM-derived were intravenously infused into cisplatin-induced AKI mouse model. It was observed a robustly engraftment of the MM-derived cells into the damaged tubuli and restorment of renal function

B) *hPSCs-derived kidney organoids*

Protocol	Kidney organoid derivation protocol	Cell types within the kidney organoid	Functional and validation assays	*In vivo* validation
Taguchi et al. (2014)	**(d0-d1) EB formation :** 0.5 ng/ml Bmp4 + 10 µM Y27632 **(d1-d2) Epiblast:** 1 ng/ml Actvin A + 20 ng/ml Fgf2 **(d2-d8) Posterior nascent mesoderm:** 1 ng/ml Bmp4, 10 µM CHIR **(d8-d10)Posterior intermediate mesoderm:** 10 ng/ml Activin A + 3 ng/ml Bmp4 + 3µM CHIR + 0.1 µM RA + 10 µM **(d10-d13) Metanephric mesenchyme:** 5ng/ml Fgf9 + 1 µM CHIR + 10 µM Y27632 *d14 NPCs co-cultured with mouse embryonic spinal cord (E11.5-E12.5)* Cell lines used: human iPSCs (from dermal fibroblasts)	Derivation of 3D neprhon-like structures showing roubust tubulogenesis and clustered podocyte formation. Formation of well-specified nephron components: glomeruli (Wt1+, Nephrin+), proximal tubule (Cadherin6+) and distal tubule (Ecad+).	N/A	N/A

Table 1. (Continued)

Morizane et al. (2015)	**(d0-d4) Late primitive streak**: 8 µM CHIR for ESCs, 10 µM CHIR + 5 ng/ml Noggin for iPSCs **(d4-d7) Posterior Intermediate mesoderm:** 10 ng/ml Activin A **(d7-d9) Metanephric mesenchyme:** 10 ng/ml Fgf9 *d9 NPCs aggregation into spheroids* **(d9-d11) Pretubular aggregates:** 3 µM CHIR + 10 ng/ml Fgf9 **(d11-d14) Renal vesicle:** 10 ng/ml Fgf9 **(d14-d21) Nephrogenesis:** no growth factors Cell lines used: Human ESCs (H9) and human iPSCs (dermal fibroblasts).	Derivation of kidney organoids with epithelial nephron structures expressing markers of podocytes (Wt1+, Podxl+, Nphs1+), proximal tubule (Ltl+, Aqp1+), loops of Henle (Ecad+, Umod+) and distal tubules (Ecad+), mimicking nephron development.	Kidney organoids exposed to DAPT (Notch inhibitor) supressessed proximal tubular formation. Kindey organoids exposed to cisplantin and gentamicin (chemical agents used in animal models *in vivo*), enabled assessment of proximal and/or distal tubular toxicity	N/A
Freedman et al. (2015)	**(d0-d3) Sandwiched spheroid colonies:** 10 µM Y27632, matrigel *d3 hPSC-derived spheroids directly differentiated into kidney organoid s* **(d3-d16) Tubular organoid differentiation:** 12 µM CHIR for 36h, then retrieved, media replacement every 3 days thereafter Cell lines used: Human ESCs (H9 and WA09) and human iPSCs (foreskin and dermal fibroblasts)	Derivation of nephron-like organoids containing cell populations with characteristics of proximal tubules (Ecad+, Ltl+), podocytes (Wt1+, Podxl+, Synpo+) and endothelium (Cd31+,vWF+). All major components of the developing proximal nephron are represented within each organoid in a kidney-like architecture.	Kidney organoids showed selective uptake of dextran and methotrexate cargoes in tubules, and expression of Kim1 after nephrotoxic chemial injury (cisplatin and gentamicin). CRISPR/Cas9 knockout of Podxl and Pkd1, Pkd2 genes for human kidney disease modeling.	Tubular organoids dissociated and implated into kidneys of neonatal immunodeficient mice. After 3 weeks, observation of Hna+ epithelial structures within mouse kindey cortex, with expression of Ltl at similar intensities as neighboring mouse tubules.
Takasato et al. (2015)	**(d0-d7) Intermediate Mesoderm:** 8 µM CHIR for 2-5d (CHIR exposure time determine anterior and/or posterior commitment) + 200 ng/ml Fgf9 + 1 µg/ml heparin for 2-5d. *d7 IM cells aggregated into spheroids* **(d7-d25) Nephrogenesis:** 5 µM CHIR for 1h, then 200 ng/ml Fgf9 + 1 µg/ml heparin for 5d and then non growth factor for another 6-13d. Cell lines used: Human iPSCs (CRL1502, clone C32)	Derivation of kidney organoids with nephrons associated with collecting duct network sorrounded by renal interstitum and endothelial cells. Within each organoids identification of early podocytes (Wt1+, Nphs1+), proximal tubules (Ltl+, Ecad+), early loops of Henle (Umod+), distal tubules (Ecad+), collecting ducts (Pax2+, Gata3+, Ecad+) and endothelial network (Cd31+, Kdr+, Sox17+).	Proximal tubule endocytosis capacity by the selective uptake of dextran from the media. Specific acute apoptosis in mature proximal tubules after cisplatin treatment. RNA seq of kidney organoids, clustered kideny organoids at d11 and d18 with first trimester human fetal kidney. TEM analysis showed the presence podocyte-like cells aligned on a basement membrane and developing primary and secondary cell processes.	N/A

45

Table 1. (Continued)

Taguchi et al. (2017)	**NPC induction** (Modification of the previous reporter protocol (Taguchi et al. 2014)) **(d0-d1) EB formation:** 10µM Y27632 + 1ng/ml Activin A + 20 ng/ml Fgf2 **(d1-d7) Posterior nascent mesoderm:** 10 µM CHIR + 10 µM Y27632 **(d7-d9) Posterior intermediate mesoderm:** 10 ng/ml AA + 3 ng/ml BMP4 + 3µM CHIR + 0.1 µM RA + 10 µM Y276321 ng/ml BMB4, 10 µM CHIR99021 **(d9-d12) Metanephric mesenchyme:** 5 ng/ml FGF9 + 1 µM CHIR + 10 µM Y27632	NPCs not cultured in 3D	Reconstitution assays of induced NPCs and UB cells from mESCs with primary stromal progenitors generated murine organoids with nephrons interconnected by branched epithelium. These assays were NOT characterized with human cells in this report. Evaluation of Pax2 knockout hiPSCs for NPCs or UB differentiation elucidated the role of this transcription factor into MET of WD precursors.	N/A
	UB lineage induction **(d0-d2.5) Nascent mesoderm:** 10 µM Y27632 + 10 ng/ml AA + 1 ng/ml Bmp4 for 24h and 1 ng/ml Bmp4 + 10 µM CHIR for 36h **(d2.5-d4.5) Anterior Intermedia Mesoderm:** 0.1 µM RA + 100 ng/ml FGF9 + 100 nM LDN193189 + 100 µM SB431542 for 24h **(d4.5-d6.25) Committed Wolfian Duct progenitor:** 0.1 µM RA + 100 ng/ml FGF9 + 5 µM CHIR + 30 nM LDN193189 for 18h *d6.25 Reaggregatio of sorted Crcr4+/Kit+ WB cells* **(d6.25-d12.5) Ureteric Bud maturation:** 10 µM Y27632 + 0.1 µM RA + 1 µM CHIR (first 24h) 3 µM CHIR (last 48h) + 5 ng/ml FGF9 (first 48h) + 100 ng/ml FGF1 + 2 ng/ml Gdnf (last 48h) + 10 nM LDN193189 + 10 % GFR matrigel for 36h Cell lines used: Human iPSCs (201 B7 from dermal fibroblasts)	Derivation of UB branching organoids, ureteric epithelium showed tips with cells expressing Sox9 and stalk regions with cells expressing Ck8. Detailed analysis of the tip region identified the typical ampulla or dichotomous bifurcation with cells expressing Pax2/Ecad.		N/A

Table 1. (Continued)

Garreta et al. (2019)	**(d0-d3) Posterior primitive streak**: 8 µM CHIR **(d3-d4) Intermediate mesoderm**: 10 ng/ml Activin A + 200 ng/ml Fgf9 + 1 µg/ml heparin *d4 IM cells eaggregated into spheroids* **(d4-d7) Nephron progenitor cells**: 3 µM CHIR + 200 ng/ml Fgf9 + 1 µg/ml heparin **(d7-d11) Renal vesicle**: 200 ng/ml Fgf9 + 1 µg/ml heparin **(d11-d20) Nephrogenesis**: no growth factors Cells lines used: Human ESC (ES[4], H1, H9) and human iPSCs (CBiPSsv-4F-40 from CD133+ cord blood cells)	Derivation of nephron-like kidney organoids (d20) segmented into proximal tubules (Ltl+, Aqp1+, Slc3a1+), loops of Henle (Ecad+, Umod+), distal tubules (Ecad+) and glomeruli expressing (Podxl+, Podocin+, Nphs1+, Wt1+).	TEM analysis indicated presence of podocyte-like cells with deposition of a basement membrane and developing primary and secondary cell processes. Presence of brush borders and high mitochondrial content in epithelial tubular-like cells. Comparative RNA seq analysis clustered kidney organoids with second trimester human fetal kidney. Reagregation with mouse embryonic kidney cells showed human cells integration into mouse nascent nephron. Assessnemt of nephron patterning with β- catenin induction (distalization) or Notch disruption (loss of glomeruli and proximal tubuli). Exposition to cell culture medium promoting OXPHOS enhanced proximal tubular differentiation. Acceleration of kidney organoid differentiation when cultured in a soft-environtment (mimicking *in vivo* microenvironment).	Implantation of kidney organoid into the chick CAM promoted vascularization (Cd34+ cells) and enhanced nephron maturation of nephron. Implanted organoid showed ability to respond to injected cisplatin through chick vasculature. Assessment of increased levels of Kim1 and Caspase 3 in proximal tubule structures.
Low et al. (2019)	**(d0-d4) Primitive Streak (4d)**: 10 µM CHIR **(d0-d7) Intermediate Mesoderm**: no growth factors **(d7-d9) Nephron progenitor cells**: 50 ng/ml Fgf9+ 3 µM CHIR *d10-d12 NPCs reaggregated into spheroids* **(d10/12-d24) Nephrogenesis**: 50 ng/ml Fgf9 + 10 µM y27632 (only for 24h) + /- 10 µM CHIR (determines proportion of proximal-versus-distal segments) Cell lines used: Human ESCs (H9 and H1) and human iPSCs (GM10287 from fibroblasts)	Derivation of kidney organoids (d24) densely packed showing multiple nephron components, including podocytes (Npsh1+), proximal tubules (Ltl+), medial tubules (Jag1+) and distal tubules (Ecad+). Identification of a vascular network (Cd31+, Cd34+) spreading alongside nephron structure of the entire kidney organoids.	Introduction of HUVECs into the kidney organoids showed that the exogenous endothelial cells formed a vascular network, intetrated with the resident vascular network. VEGF receptor inhibitors comprised organoid vascular networks without afecting nephron structures. sc RNA seq identified a subset of NPCs with vascular progenitor-like property that further differentiate into more mature endothelial cells. Patterning CHIR treatments showed kidney organoids full of tubules in presence of CHIR, and the absence of it resulted in high glomerulus-to-tubule ratio.	Implantation of kidney organoids into a immunocompromised mice showed structural and functional maturation. Formation of glomerular capillary tufts of human origin, development of glomerular filtration barrier and size-selective dextran handling.

47

Table 1. (Continued)

Yoshimura et al. (2019)	**Nephron progenitors:** derived following Taguchi et al. 2017 protocol, sorting of NPCs Itga8+/Pdgra- population and aggregation into spheroids **(d0-d1) Pretubular aggregates:** 3 µM CHIR + 10 µM Y27632 **(d1-d3)** **Proximalized renal vesicle:** 10 µM Fgf9 + 5 µM Iwr1 + 5 µM SB431542 + 10 µM RA **(d3-d9/d12) Podocytes:** 2 µM IWR1 + 5 µM SB431542 Cell lines: Human iPSCs (201 B7 from fibroblasts)	Derivation of podocytes with 90% purity expressing Wt1, Nephrin, Neph1 and Podocin at d12, and showign foot process-like and slit diaphragm-like strcutures.	RNA seq analysis indicated similar gene expression profile to human adult podocytes. Induced podocytes also showed higher protein expression levels of podocyte-related proteins than inmortalized podocytes or podocytes derived from convectional kidney organoids. PAN treatment induced podocytes injury as *in vivo*. TEM showed protrusions of the basolateral domain expressing NPHS1 on their surface membrane. Slit diaphragm–like structures were also detected.	N/A
Kumar Gupta et al. (2020)	NPCs derived following Morizane et al. 2015 protocol and aggregated into spheroids at d9 **Direct differentiation of kidney organoids** **(d0-d9):** 100 ng/ml Bmp7 + 100 ng/ml Fgf9 + 1 µg/ml heparin for 4 d and without growth factors for 5d. **Organoids with heterochronic recombination** **(d0-d2):** 100 ng/ml Bmp7 + 100 ng/ml Fgf9 + 1 µg/ml heparin *d2 aggregates dissociated and reaggregated with new differentiated NPCs* **(d2-d11):**100 ng/ml Bmp7 + 100 ng/ml Fgf9 + 1 µg/ml heparin for 4 d and without growth factors for 5d. Cell lines used: Human ESCs (H9) and human iPSCs	Derivation of kidney organoids showing proximal tubuli (Ltl+), distal tubuli (Brn1+, Ecad+), collecting duct (Ecad+, Gata3+, Dba+), podocytes (Podxl+, Wt1+), endothelial network (Cd31+) and pericytes (Pdgfrβ+). Heterocronic kidney organoids showerd the double number of structures stained for each molecular marker and less remnant undifferentiated NPCs expressing Six2 when compared with control organoids.	Systemic perfused FITC-IB4 labeled endotelial vascular cells in close contact with kidney organoid podocytes. Systemic perfusion of dextran showed its accumulation in kidney organoids tubules.	Engrafted heterocronic organoids under the kidney capsules of immunocompromised mice showed enhanced maturation and functional vascularization.

4. hPSCs-Kidney organoids to understand human disease

As mentioned in the previous sections in the last decades different organisms have been extremely helpful to model kidney disease and development prior to the advent of the organoid technology. As an example, immunodeficient mice such as the nude and severe combined immunodeficiency (SCID) have been commonly used as recipients of human cells or tissues as these are permissive to foreign cells due to a lack of host immunity. Other example includes the use of humanized mice which have been shown to be re-populated with human immune cells by human hematopoietic stem cells upon transplantation

For many diseases, mice models have been instrumental in understanding the mechanisms underlying pathogenesis. Yet, their utility CKD has been limited because they fail to recapitulate important functional, structural, and molecular features of advanced human kidney disease. For these reasons, the use of human kidney organoids is envisioned as a new model system to generate functional renal cell types suitable and to explore on the effect of prevalent systemic conditions compromising kidney function.

4.1 The importance of metabolism in kidney function in health and disease

The kidney is a highly metabolically active organ that uses the 20% of the cardiac output to develop its activities. Renal epithelial tubular cells (PTCs) due to absorption functions contains one of the highest mitochondrial density in the body (Bhargava P., and Schnellmann RG., 2017; Li S. and Susztak K., 2018) and account for

almost the total of the renal mass. To afford with the energy requirements sustaining their physiological functions, PTCs use fatty acid oxidation (FAO) for the generation of ATP. Therefore, mitochondrial metabolism is key, since any imbalance in its functioning can lead to the development of kidney diseases including AKI, CKD and renal fibrosis (He L., et al., 2017). Indeed, it is being shown that during AKI both mouse and human PTCs exhibit structural damage which correlates with kidney function. In this regard, CKD is defined by more than 40% decline in estimated glomerular filtration rate (eGFR) for more than 3 months and is characterized by PT cell atrophy almost independent of disease etiology. Furthermore, PTCs atrophy strongly correlates with kidney function in CKD (Chang-Panesso and Humphreys, 2017) (Kang et al., 2015; Li et al., 2012).

To date, several approaches have been proposed to explore molecular pathways that drive such structural and functional changes in AKI and CKD. Comprehensive genome-wide kidney tissue transcriptomics analysis has identified molecular hallmarks of this complex process both in patient samples and mouse models (Beckerman et al., 2017; Qiu et al., 2018; Woroniecka et al., 2011). These studies have highlighted a correlation between a large number of transcripts and kidney fibrosis. Cellular metabolism, such as genes in lipid metabolism, FAO and oxidative phosphorylation (OXPHOS) showed strong correlation with disease state both in human and mouse CKD models (Chung et al., 2019; Kang et al., 2015). Conversely, pharmacological, or genetic approaches that enhance FAO and mitochondrial biogenesis are being envisioned as putative treatments to restore kidney damage (Gomez et al., 2015; Tran et al., 2011).

It is well known that mitochondrial biogenesis is orchestrated by specific nuclear transcription factors that regulate the expression of genes encoding mitochondrial proteins (Ploumi C., et al., 2016). Peroxisome proliferator-activated receptor gamma coactivator 1-α (Pgc1α) and Estrogen-related receptor α (Esrrα) are key components of the regulatory network that controls mitochondrial biogenesis. Pgc1α was discovered as a coregulator of Peroxisome proliferator-activated receptor γ (Ppparγ) expressed in the brown fat at low temperatures that mediates adaptive thermogenesis (Puigserver P. et al., 1998). However, there have been discovered many new aspects of Pgc1α's role, such as, its implication in mitochondrial functions. When Pgc1α is induced, mitochondrial biogenesis is enhanced, which leads to an increase in the number of mitochondria, and therefore promotes OXPHOS. However, during this process reactive oxygen species (ROS) can also be generated. Importantly, and to avoid these toxic effects, Pgc1α can also induce the transcription of ROS-detoxification-enzymes such as Sod2, Gpx1, Ucp2. In this way, it is being shown that PTCs can obtain more energy without suffering from oxidative damage *in vivo* (Li S. and Susztak K., 2018). Moreover, Pgc1α can interact with other transcriptional factors such as Ppar α/β involved in the regulation of oxidation and FAO enzymes, and with Retinoid X receptors (Rxrs) for FAO regulation as well. On the other hand, Pgc1α is also being described to bind to the Nuclear respiratory factor (Nrfs) for the electron transport chain (Etc) assembly and with the mitochondrial transcription factor A (Tfam) needed for the transcription and replication of mitochondrial DNA. Finally, the interaction of PGC1α with Errs is essential for the regulation of angiogenic growth factors and mitochondrial biogenesis (Lin J et al., 2005; Handschin C. et al., 2006). Indeed, Errα is mainly expressed in

metabolically active tissues such as heart, brown adipose tissue, liver, and kidney with a preferential use of fatty acids as fuel.

During both AKI and CKD, Pgc1α levels are decreased and lipid droplets accumulate. During AKI, nutrient or oxygen deficit in PTCs lead to a loss of kidney function (Bonventre JV., and Yang L., 2011) that if prolonged evolves into CKD (Izquierdo-Lahuerta A., et al., 2016). As PTCs can only rely on FAO for energy obtention PTCs dedifferentiate as a strategy to lower energy requirements, but when energy depletion persists over time it can lead to a loss of mitochondrial function and cause several metabolic diseases such as diabetic kidney disease or kidney fibrosis. Studies suggest that FAO, and not mitochondrial density or Pgc1α levels, is determinant for CKD development and kidney fibrosis (Li SY. and Susztak K., 2018; Kang HM., et al., 2015). Moreover, tubule epithelial expression of Pgc1α is essential for the recovery of the damaged kidney. Its overexpression can reduce the expression of profibrotic genes and revert Notch-induced renal fibrosis (Lynch MR., et al., 2017). Pgc1α levels can also attenuate the physiological changes of AKI, and it has been associated with an improvement of the renal function after ischemia. Therefore, although Pgc1α and Pprα are dispensable for basal metabolism, their increase is associated with a protective phenotype in the kidney leading to the investigation of its role as a potential target for therapeutic interventions aiming to ameliorate AKI and CKD effects (Fontecha-Barriuso M., et al., 2020). Whereas much more attention has been raised on the role of Pgc1α linking metabolism and function in kidney development and disease, the role of other Pgc1α co-factors as Errα is totally elusive opening new venues to target kidney disease through the regulation of PTCs metabolism.

4.1.1 Boosting metabolism to generate hPSCs derivatives and organoids.

In the renal field PTCs metabolism and toxicity has historically relied on various PT cell lines, such as LLC-PK1, MDCK, and HK2 (Rezzani et al., 2002; Gunness et al., 2010); nonetheless, these cell lines are not adequate for use as predictive models. Other alternatives have relayed in the use of primary PTCs (Pizzonia et al., 1991; Baer et al., 1997; Qi et al., 2007) or commercial PT cells (e.g., ATCC, Lonza, and Biopredic). Besides these advances one major challenge with PT derived cells is their limited capacity to be expanded in culture, even when ectopically expressing telomerase reverse transcriptase (Wieser et al., 2008). All these issues seem to be now overcome with the advent of hPSCs-kidney organoids and the possibility to isolate PT-like cells from these 3D cultures.

Biologically, coupling of metabolism and cell state makes perfect sense as it harmoniously couples energy production and utilization with cellular function. Indeed, in the last decade, several works have also started to assess on the relevance of metabolism in cell function taking advantage of metabolomics for the examination and identification of endogenous biochemical reaction products. In this regard Yanes and colleagues questioned the molecular framework that controls pluripotency and differentiation demonstrating that hPSCs present a unique metabolic signature characterized by the presence of highly unsaturated endogenous molecules (Yanes et al., 2010). Importantly, they suggested that this highly unsaturated metabolome reacts to pro-oxidative events that influence cell fate and postulated that stem cell redox status is regulated during differentiation. These observations agree

with previous studies postulating that intracellular oxidative state regulate the balance between self-renewal and differentiation (J. Smith et al., 2000). The same group was pioneer to analyze the metabolome in the iPSCs context comparted to ESCs and to their somatic cells of origin (Panopoulos et al., 2012). Cellular bioenergetics confirmed their previous findings, showing that somatic cells convert from an oxidative state to a glycolytic state in pluripotency, and therefore confirming that the inhibition of oxidative pathways is relevant for maintaining pluripotency (Yanes et al., 2010). Additionally, their data suggested that changes in cell metabolism are critical for somatic cell reprograming, showing a correlation between the bioenergetic state of somatic cells and their reprogramming efficiency. These and further studies, established the strong link between oxidative metabolism and pluripotency regulation, demonstrating the metabolic shift towards oxidative phosphorylation during cell differentiation and towards a glycolytic metabolism during cell reprogramming (Wanet et al., 2015). In this regard our laboratory has recently hypothesized that the presentation of a cell culture regime boosting a cellular specific metabolic profile in the time course of organoid derivation would result in the generation of that specific cell type. To that aim, we challenged kidney developing organoids in front of a specific culture regime promoting OXPHOS and showed that this regime promoted the generation of kidney organoids with higher numbers of PTCs which in turn exhibited a significant increased respiratory capacity (Garreta et al., 2019). As cell metabolism captures the biochemical phenotype of any given cell and connects the biochemical extracellular microenvironment (i.e., availability of nutrients, such as glucose and oxygen) with the functional cellular need (i.e., pluripotency exit, differentiation, among others) in the next years it

will be important to further explore on the direct crosstalk between metabolism and epigenetics as a new approach to guide hPSCs differentiation and organoid generation.

4.2 hPSCs-kidney derived organoids to understand SARS-Cov-2 infection and target COVID19 disease.

Early in December 2019 a novel coronavirus—severe acute respiratory syndrome coronavirus 2 (SARS-CoV-2)—emerged in humans in Wuhan, China, and has since disseminated globally(Q. Li et al., 2020; Zhu et al., 2020). As of December 12, 2020, the confirmed case count of coronavirus disease 2019 (COVID-19) had surpassed 68 million with 1,5 million of confirmed deaths.

Based on full-genome sequence analysis, SARS-CoV-2 shows high homology to SARS-related coronaviruses identified in horseshoe bats (P. Zhou et al., 2020). The coronaviruses are a large family of single-stranded RNA (ssRNA) viruses associated with respiratory diseases in humans. Most of the coronaviruses provoke non-severe clinical symptoms, except severe acute respiratory syndrome coronavirus (SARS-CoV) (R. D. Smith, 2006), Middle East respiratory syndrome coronavirus (MERS-CoV) (O'Keefe, 2016) , and now SARS-CoV-2. All these diseases are linked to a high mortality rate. In this regard, SARS was a new illness firstly identified in 2003 and associated to a novel coronavirus identified as SARS pathogen (SARS-CoV) (Drosten et al., 2003). From December 2019, several studies have demonstrated that SARS-CoV-2 share multiple similarities with SARS-CoV, including a high conservation in the receptor binding domain (RBD) thereby suggesting a common host cell receptor (Andersen et al., 2020; Lu et al., 2020; Zhu et al., 2020). Indeed, nowadays accumulated evidence show

that the surface unit of the spike protein (S) of SARS engages the angiotensin-converting enzyme 2 (ACE2) as the entry receptor. This step is followed by TMPRSS2 protease priming which is required for fusion and internalization of the ACE2-viral spike complex priming (Hoffmann et al., 2020; Letko et al., 2020; Walls et al., 2020). . Upon the fusion of viral and cellular membranes viral particles entry into the cells and SARS-CoV infection is established (Bourgonje et al., 2020; Imai et al., 2005; Kuba et al., 2005; W. Li et al., 2003). Furthermore, nowadays other recent studies have suggested that SARS-CoV-2 strike protein directly binds to human ACE2 with even higher affinity that Spike protein from SARS-CoV (Walls et al., 2020; Wan et al., 2020; Wrapp et al., 2020).

ACE2 is a homologue of angiotensin-converting enzyme (ACE) and has an essential role in the renin-angiotensin-aldosterone system (RAAs), being involved in the regulation of vasoconstriction, renal sodium reabsorption and potassium secretion, aldosterone synthesis, blood pressure elevation, and induction of inflammatory and pro-fibrotic pathways (Ferrario et al., 2005; Tikellis & Thomas, 2012). The most common symptoms of patients infected with SARS-CoV-2 are fever and cough (Chen et al., 2020) and this can be explained by ACE2 expression in alveolar epithelial type II cells (Y. Zhao et al., 2020), which are key for lung gas exchange (Dobbs, 1989) . The injury of these cells during SARS-CoV-2 infection explains the severe lung injury associated with this disease, however, it has been observed a multi-organ dysfunction in COVID-19 patients (Guan et al., 2020; Huang et al., 2020). Importantly, different works have shown ACE2 expression in multiple extrapulmonary tissues including heart, kidneys, blood vessels, and intestine (Crackower et al., 2002; Danilczyk & Penninger, 2006; Ding et

al., 2004; Gu et al., 2005; Hamming et al., 2004; Zhang et al., 2020), overall showing the wide distribution of ACE2 across the human body. Multi-organ damage and dysfunction associated with SARS-CoV-2 includes myocardial dysfunction (Bonow et al., 2020), gastrointestinal and liver (Fan et al., 2020) disorders, and AKI (Z. Li et al., 2020). In this regard, it has been postulated that SARS-CoV-2 cell entry and pathological events mainly occurs in the cells of the respiratory tracts and further dissemination of the infection is related to local ACE2 expression. In the renal context, previous works have already shown that ACE2 is strongly expressed in kidney proximal tubules (Danilczyk & Penninger, 2006). Since ACE2 exists both in membrane-bound and soluble circulating forms, one proposed therapy for COVID19 disease would be administering the soluble form of ACE2 (sACE2). In this manner sACE2 would act as a decoy to interfere with the binding of SARS-CoV-2 to the full-length ACE2 that is membrane bound.

The study of ACE2-SARS-Cov-2 interactions and downstream molecular cascades upon virus-cell interactions has mainly relayed in the use of animal models, animal cells from humans or primates (including Caco-2 or VeroE6 cell lines, respectively) or simple cell cultures using human immortalized cells. The mentioned models of study present several limitations such species barriers and the potential lack of the specific target cells. In this regard, kidney organoids represent a more physiological *in vitro* approach in where to study the ACE2-SARS-CoV-2. Eventually, these model systems are providing rapid and effective toolsets to interrogate and target ACE2-SARS-CoV-2 interactions as well as to explore therapeutic compounds blocking or disrupting these processes.

In this regard, two early works have generated human bronchial organoids for human for SARS-CoV-2 research (Han et al., 2020; Suzuki et al., 2020). Briefly, the authors showed that their organoids were permissive to the SARS-CoV-2 infection and could evaluate antiviral effects of COVID-19 candidate therapeutic compounds, including camostat (Suzuki et al., 2020). As mentioned above besides the lung damage caused by pneumonia, SARS-CoV-2 affects several organs like the kidney (Z. Li et al., 2020), liver (Fan et al., 2020), and the cardiovascular system (Zheng et al., 2020). For this reason we have recently led the first study showing that the supernatant of SARS-CoV-2 infected kidney organoids differentiated from hESCs can efficiently infect Vero E6 cells, showing that the kidney organoids produce infectious progeny virus (Monteil, Kwon, et al., 2020). In the same line, the work from Zhao and colleagues has demonstrated that human liver ductal organoids are permissive to SARS-CoV-2 infection and support replication (B. Zhao et al., 2020). Interestingly, virus infection impaired the bile acid transporting functions of cholangiocytes (B. Zhao et al., 2020). This effect might be the reason for the bile acid accumulation and consequent liver damage in patients with COVID-19. Importantly, the intestine is another viral target organ (Z. Zhou et al., 2020) and two independent laboratories have recently reported that human intestinal organoids, which were established from primary gut epithelial stem cells, support SARS-CoV-2 replication (Lamers et al., 2020; J. Zhou et al., 2020b).

To further explore on the amenability of the organoid technology to identify treatments for COVID19 treatment in our study we have also explored on how SARS-CoV-2 can directly infect human blood vessel organoids differentiated from human induced pluripotent stem cells

(Monteil, Kwon, et al., 2020). These findings were confirmed lately by Varga and colleagues who detected the presence of viral elements within endothelial cells and an accumulation of inflammatory cells in human samples (Varga et al., 2020). Taken together, our study together with the observations made by Vargas and colleagues suggested that SARS-CoV-2 infection induces endotheliitis in several organs as a direct consequence of virus involvement. Still, while true that hPSCs organoids can reproduce the pathology of COVID-19 in specific tissues on which they are modeled, they still cannot reproduce the systemic symptoms associated with whole body responses to the viral infection. A summary of the *in vitro* and *in vivo* models that are being used in SARS-CoV-2 research is compiled in **Table 2**.

Table 2. *In vitro* and *in vivo* models of study described for SARS-CoV-2 research. *This table provides an overview of the different models that are being used in COVID-19 research and their major findings.*

Cell lines				
Type		Source	Main outcomes	Work
Primary human airway epithelial cells		Commercial cell lines (Lonza, PromoCell, etc.)	These cells show the ability to isolated SARS-CoV-2 and to present cytopathic effect after SARS-CoV-2 infection, mimicking infected human lung cells.	Zhu et al. (2020)
Vero E6 cells	Wild type cells	Obtained from kidney epithelial cells of an African green monkey (1963)	The high expression of ACE2 make these cells the most common clone used to replicate and isolate the SARS-CoV-2.	P. Zhou et al. (2020)
	TMPRSS2-overexpressing cells		Cuture supernatants of TMPRSS2-overexpressing cells present viral RNA copies > 100 times higher than in wild type Vero E6 cells.	Matsuyama et al. (2020)
Caco-2 cells		Immortalized cell line of human colorectal adenocarcinoma cells	These cells showed effective replicate SARS-CoV-2.	J. M. Kim et al. (2020)
Calu-3 cells		Human lung cancer cell line	In the assesment of the capacity of SARS-CoV-2 S pseudovirions to transduce human cells, SARS-CoV-2 S pseudovirions showed an onver 500-fold increase un luciferase activities in Calu-3 cells.	Ou et al. (2020)
HEK293T cells		Human embryionic kidney cells	After SARS-CoV-2 inoculation, HEK293T cells showed modest viral replication	Harcourt et al. (2020)
Huh7 cells		Human liver cells	In the assesment of the capacity of SARS-CoV-2 S pseudovirions to transduce human cells, Huh7 cells showed aroun 10-fold increase in luciferase activities.	Ou et al. (2020)

Organoids			
Type	Source	Main outcomes	Work
Human bronchial organoids	Derived from comercially available human bronchial epithelial cell lines	SARS-CoV-2 infection of these bronchial organoids lead to the detection of intracellular viral genome, progeny virus, cytotoxicity, pyknotic cells, and increases of the type I interferon. Treatment with camostat (inhibitor of TMPRSS2) reduced the viral copy number to 2% of the group of control.	Suzuki et al. (2020)
Human lung organoids	Derived from human ESCs	Alveolar type II cells present in the lung organoids, express ACE2 and allow SARS-CoV-2 infection. Treatment with imatinib and mycophenolic acid (inhibitors of SARS-CoV-2 entry) decreased SARS-CoV-2 infection of lung organoids.	Han et al. (2020)
Human kidney organoids	Derived from human ESCs	Supernatant of SARS-CoV-2 infected human kidney organoids, could effectively infect Vero E6 cells, indicating that kidney organoids produce infectious progeny virus.	Monteil, Kwon, et al. (2020)
		Treatment of kidney organoids with remdesivir in combination with human recombinant soluble ACE2, enhance their anti-viral efficacies and improved the therapeutic windows agains SARS-CoV-2.	Monteil, Dyczynski, et al. (2020)
Human liver ductal organoids	Derived from primary bile ducts isolated from human liver biopsies	SARS-CoV-2 infection damages the barrier and bile acid transporting functions of cholangiocytes, by modulating the the expression of genes driving tight junction formation and bile acid transportation.	Zhao et al. (2020)
Human intestinal organoids	Established from primary gut epithelial stem cells	Enterocytes of human intestinal organois were easily infected by SARS-CoV and SARS-CoV-2, and productoin of infectious viral particles was detected.	Lamers et al. (2020) and J. Zhou et al. (2020)
Human blood vessel organoids	Engineered from human induced pluripotent stem cells	Infection of blood vessel organoids showed active replication SARS-CoV-2.	Monteil, Kwon, et al. (2020)

Animals models				
Origin			**Observations**	**Work**
Mice	Wild type mice		SARS-CoV-2 can use all ACE2 proteins, except for mouse ACE2, as host receptor for infection.	P. Zhou et al. (2020)
	Transgenic mice expressing human ACE2		Infection with SARS-Cov-2 lead to animal weight lost, interstitial pneumonia and detection of viral antigens in bronchial epithelial cells, macrophages and alveolar epithelia. These phenomena was not observed in wild type mice infected with SARSR-CoV-2.	Bao et al. (2020)
Syrian hamster			Hamsters infection with SARS-CoV-2 lead to fast breathing, weight lost, alveolar damage, high lung viral load and spleen and lymphoid atrophy.	Chan et al. (2020)
Ferrets			SARS-CoV-2 infected ferrets showed elevated body temperature and virus replication. Viral antigens were found in nasal turbinate, trachea, lungs, and intestine together with acute broncholitis in infected lungs.	Y. Il Kim et al. (2020)
Cats			In cats infected with SARS-CoV-2 the virus replicated in the mose and troat leading to inflammation of the respiratory tract. It was shown that cats are suspectible to airbone transmission. Replication in the upper respiratory tract was associated with high tramission, and replication in the lower respiratory tract with lung disease.	Shi et al. (2020)
Cynomolgus macaques			Cynomolgus macaques are permissive to SARS-CoV-2 infection, incubated the virus for prolonged time and showed COVID19-like disease. SARS-CoV-2 presented efficient replication in respiratory epithelial cells, including nasal cavity, bronchi, bronchioles, and alveoli.	Rockx et al. (2020)
Rhesus macaques			After SARS-CoV-2 infection, the macaques showed high viral loads in the upper and lower respiratory tract, and presented humoral and cellular immune responses, and viral pneumonia. Rhesus macaques have been used to assess adenovirus-vectored vaccine, DNA vaccine candidates expressing different froms of S protein, and remdesivir therapeutic effects.	van Doremalen et al. (2020), Williamson et al. (2020) and Yu et al. (2020)

II.   OBJECTIVES

II. OBJECTIVES

This thesis has been focused in four aims:

1. To generate a procedure for the generation of hPSCs-kidney organoids forcing cell-to-cell contact and cell to ECM interactions as a new approach to promote differentiation.

2. To provide a vascular component to hPSCs-kidney organoids taking advantage of the chick CAM.

3. To interrogate for the impact of experimentally-induced metabolic challenges as a new approach to favor the generation of renal cells during hPSCs-kidney differentiation.

4. To underscore on the impact of metabolic-induced changes in the generation of hPSCs-kidney organoids to model early stages of kidney disease.

5. To generate a platform for the interrogation of early steps of SARS-CoV-2 infection taking advantage of hPSCs-kidney organoids.

III.   RESULTS

III. RESULTS

Paper I: Garreta, E., **Prado, P***., Tarantino, C., Oria, R., Fanlo, L., Martí, E., Zalvidea, D., Trepat, X., Roca-Cusachs, P., Gavaldà-Navarro, A., Cozzuto, L., Campistol, J. M., Belmonte, J. C. I., Pozo, C. H. del, & Montserrat, N. (2019). Fine tuning the extracellular environment accelerates the derivation of kidney organoids from human pluripotent stem cells. *Nature Materials*. **(*sharing first co-authorship).**

Paper II: Dhillon, P., Park, J., Hurtado del Pozo, C., Li, L., Doke, T., Huang, S., Zhao, J., Kang, H. M., Shrestra, R., Balzer, M. S., Chatterjee, S., **Prado, P**., Han, S. Y., Liu, H., Sheng, X., Dierickx, P., Batmanov, K., Romero, J. P., Prósper, F., … Susztak, K. (2020). The Nuclear Receptor ESRRA Protects from Kidney Disease by Coupling Metabolism and Differentiation. *Cell Metabolism*.

Paper III: Monteil, V., Kwon, H., **Prado, P**., Hagelkrüys, A., Wimmer, R. A., Stahl, M., Leopoldi, A., Garreta, E., Hurtado Del Pozo, C., Prosper, F., Romero, J. P., Wirnsberger, G., Zhang, H., Slutsky, A. S., Conder, R., Montserrat, N., Mirazimi, A., & Penninger, J. M. (2020). Inhibition of SARS-CoV-2 Infections in Engineered Human Tissues Using Clinical-Grade Soluble Human ACE2. *Cell*, *181*(4), 905-913.e7.

1. Paper I

Garreta, E., **<u>Prado, P</u>**., Tarantino, C., Oria, R., Fanlo, L., Martí, E., Zalvidea, D., Trepat, X., Roca-Cusachs, P., Gavaldà-Navarro, A., Cozzuto, L., Campistol, J. M., Belmonte, J. C. I., Pozo, C. H. del, & Montserrat, N.

Fine tuning the extracellular environment accelerates the derivation of kidney organoids from human pluripotent stem cells.

Nature Materials (2019)

(*sharing first co-authorship)

nature
materials

Fine tuning the extracellular environment accelerates the derivation of kidney organoids from human pluripotent stem cells

Elena Garreta[1,11], Patricia Prado[1,11], Carolina Tarantino[1], Roger Oria [2,3], Lucia Fanlo[4], Elisa Martí[4], Dobryna Zalvidea[2], Xavier Trepat[2,3,5,6], Pere Roca-Cusachs[2,3], Aleix Gavaldà-Navarro[7], Luca Cozzuto[8], Josep M. Campistol[9], Juan Carlos Izpisúa Belmonte[10], Carmen Hurtado del Pozo[1] and Nuria Montserrat [1,5,6]*

The generation of organoids is one of the biggest scientific advances in regenerative medicine. Here, by lengthening the time that human pluripotent stem cells (hPSCs) were exposed to a three-dimensional microenvironment, and by applying defined renal inductive signals, we generated kidney organoids that transcriptomically matched second-trimester human fetal kidneys. We validated these results using ex vivo and in vitro assays that model renal development. Furthermore, we developed a transplantation method that utilizes the chick chorioallantoic membrane. This approach created a soft in vivo microenvironment that promoted the growth and differentiation of implanted kidney organoids, as well as providing a vascular component. The stiffness of the in ovo chorioallantoic membrane microenvironment was recapitulated in vitro by fabricating compliant hydrogels. These biomaterials promoted the efficient generation of renal vesicles and nephron structures, demonstrating that a soft environment accelerates the differentiation of hPSC-derived kidney organoids.

Kidney organoids have been produced from human pluripotent stem cells (hPSCs) by specific induction of the metanephric mesenchyme (MM) lineage (including nephron progenitor cells, NPCs)[1–7], or by the simultaneous induction of MM- and ureteric bud (UB)-like progenitors[8,9], the two progenitor cell populations that give rise to the adult kidney during development. Recently, NPCs and UB progenitors were separately induced and then aggregated together into three-dimensional (3D) spheroids that generated kidney organoids with higher-order architecture[10]. For kidney organoids generated from human embryonic stem cells (hESCs), CRISPR/Cas9 technology can be used to recapitulate the molecular features of kidney diseases[4]. Human kidney organoids can also be used as unprecedented in vitro models to screen for nephrotoxicity[3,4,9]. Besides the importance of these findings, major concerns related to the lack of vascularization and insufficient maturation still require further investigation to advance the field of hPSC-derived kidney organoids (kidney organoids). Biophysical cues have been shown to regulate cell behaviour, including the stemness and differentiation of different stem cell populations. Recently, application of fluid flow enhanced hPSC-derived podocyte-like cell differentiation in monolayer culture[11], and the modulation of adherent forces in kidney organoids, resulted in changes in the functional performance of proximal tubular epithelial-like cells within kidney organoids[12].

Efficient generation of kidney organoids in 3D culture

During mammalian kidney development, the posterior primitive streak (PPS) and anterior primitive streak (APS) give rise to the intermediate mesoderm (IM) and definitive endoderm, respectively. The posterior IM generates the MM, whereas the anterior IM forms the UB. The PPS can be generated from hPSCs using a combination of growth factors (including BMP4)[1,7,8], or by exposing undifferentiated cells to varying doses and durations of the Wnt signalling agonist CHIR99021 (CHIR), a widely used inhibitor of glycogen synthase kinase 3 (GSK3β)[1–5,8,9]. Building upon these observations, we asked whether PPS cells could be generated by exposing hPSCs to a high dose of CHIR (8 μM) in two-dimensional monolayer culture over three consecutive days (Supplementary Fig. 1a; Methods). This treatment regimen was sufficient to induce PPS-committed cells that were positive for the PPS marker BRACHYURY (referred to as T), at $82.2 \pm 2.6\%$ efficiency (Supplementary Fig. 1b,c). PPS-committed cells upregulated the expression of PPS genes in comparison with APS genes (Supplementary Fig. 1d). Subsequent exposure of PPS-committed cells to a combination of FGF9 and activin A (20:1) for an additional day resulted in acquisition of the early IM marker PAX2 at $85.0 \pm 1.4\%$ efficiency (Supplementary Fig. 2a–c; Methods). Accordingly, messenger RNA levels for the posterior IM markers *OSR1* and *HOXD11* and the anterior IM marker *GATA3* were also upregulated at this stage (Supplementary Fig. 2d).

We next reasoned that increasing the time that IM-committed cells are exposed to 3D culture, which increase cell-to-cell and cell-to-extracellular matrix interactions, would generate kidney organoids at higher efficiencies than previously reported[3,8,9]. Therefore, 3D spheroids were generated by the self-aggregation of IM cells and maintained under 3D organotypic culture until day 16 (Fig. 1a; see Methods). Treatment of IM-committed 3D spheroids (day 0) with CHIR (3 μM) for 3 d (from day 0 to day 3), while maintaining FGF9 signalling (from day 0 to day 7), resulted in the formation of numerous renal vesicles (RVs) on day 8 (Supplementary Fig. 3a,b), which were analysed by immunofluorescence for RV-associated markers, including PAX2, WT1, LHX1, PAX8, HNF1β, ECAD and BRN1 (Supplementary Fig. 3a,c,d). Remarkably, SIX2-positive cells were absent on day 8, indicating the lack of MM progenitors at this stage (Supplementary Fig. 3d). In addition, downregulation of the epithelial-to-mesenchymal markers *TWIST* and *SNAIL* and upregulation of *WNT4* and *ECAD* coincided with initiation of the mesenchymal-to-epithelial transition, which is essential for nephrogenesis (Supplementary Fig. 3e). RV-stage organoids were then differentiated in the absence of growth factors (from day 7 to day 16). This resulted in the derivation of kidney organoids with multiple nephron-like structures that were segmented into typical nephron components, including proximal tubules (LTL$^+$ AQP1$^+$/SLC3A1$^+$), loops of Henle (ECAD$^+$ UMOD$^+$), distal tubules (UMOD$^-$ ECAD$^+$), and glomeruli (PODXL$^+$/PODOCIN$^+$/NEPHRIN$^+$/NEPH1$^+$/WT1$^+$ PODXL$^+$ LTL$^-$/PODOCIN$^+$ LTL$^-$) (Fig. 1b, Supplementary Fig. 4a–g). In addition, quantitative PCR (qPCR) and immunofluorescence analyses confirmed that isolated LTL$^-$ and LTL$^+$ cell fractions from day 16 organoids expressed markers of glomerular and proximal tubular identity, respectively (Supplementary Fig. 5a–f). Similarly, markers representative of the major steps of differentiation were analysed by qPCR (Supplementary Fig. 6). Our methodology was quite robust, as kidney organoids from two commercial hESC lines and one human induced pluripotent stem cell (hiPSC) line were also generated (Supplementary Fig. 7a–d, Supplementary Fig. 8).

To gain insight into the sequence of transcription regulatory events necessary to promote renal differentiation from hPSCs, we performed RNA sequencing (RNA-Seq) analysis at major stages during the differentiation process. We compared our results with transcriptional data from human fetal organs/tissues from the first and second trimesters of gestation[13,14] (Supplementary Fig. 9, Supplementary Table 1; Methods), demonstrating that our technique specifically generated renal lineages. Importantly, RNA-Seq analysis showed that day 8 RV-stage organoids transcriptionally matched human fetal kidneys at 16 weeks of gestation, whereas day 16 kidney organoids matched human fetal kidneys at 22 weeks of gestation (Fig. 1c, Supplementary Table 2; Methods). We validated these findings by analysing markers of nephron progenitors (*SIX2*, *SALL1*, *PAX2*), the proximal tubular segment (*SLC3A1*) and the glomerular compartment (*NPHS1*, *PODXL*, *SYNPO*, *WT1*) via qPCR (Fig. 1d). Additionally, immunofluorescence analysis showed that localization of late-stage nephron markers was comparable between kidney organoids and human fetal kidney samples (Supplementary Fig. 4a–g). Transmission electron microscopy (TEM) analysis was performed on day 16 kidney organoids (Fig. 1e–j). Ultrathin sections revealed the presence of primitive podocyte-like cells with deposition of a basement membrane (Fig. 1g) and developing primary and secondary cell processes (Fig. 1h). Epithelial tubular-like cells with brush borders and high mitochondrial content were also detected (Fig. 1i,j).

Kidney organoids recapitulate human kidney development

The formation of kidney organoids with segmented nephrons may depend on the existence of a transient population of NPCs responsible for the generation of nephron structures in vitro. We analysed by immunofluorescence the expression of OSR1, WT1, PAX2 and SIX2, confirming that cells exhibiting a NPC signature were present in day 5 spheroids (Supplementary Fig. 10a,b). The posterior origin of NPCs was also confirmed by the detection of *HOXD11, OSR1*, and *WT1* mRNA by qPCR (Supplementary Fig. 10c). Interestingly, the anterior IM fate was also generated at this stage, as *GATA3* mRNA was detected (Supplementary Fig. 10c). We next evaluated the ability of day 5 NPCs to form kidney chimaeric structures ex vivo, taking advantage of a faithful reaggregation assay with mouse embryonic kidney cells[15,16]. After 6 d of culture, differentiated NPCs, identified by the expression of human nuclear antigen (HuNu), integrated into nascent nephron structures that expressed WT1 in the glomerular segment and PAX8 in the nascent nephron (Fig. 2a–f; Methods). Thus, day 5 NPCs exhibited the capacity to integrate into mouse nascent nephron structures, but not into the UB compartment, suggesting that the induction of UB derivatives from hPSCs may depend on additional exogenous signals. These results challenge previous findings[9] and agreed with a recent study that identified optimal time windows and exogenous signals for selectively inducing NPC and UB lineages from mouse and human PSCs[10].

Next, we investigated the capacity of human kidney organoids to faithfully recapitulate complex nephron patterning events that have been mainly studied in the mouse model[17]. Day 8 RV-stage organoids were exposed to inhibitors of tankyrase (IWR1) and GSK3β (CHIR) to decrease or increase β-catenin signalling, respectively. CHIR treatment reduced the number of WT1$^+$ glomerulus-like structures when compared with vehicle (control) and IWR1. In contrast, the percentage of LTL$^+$ proximal tubule-like structures was unchanged (Fig. 2g,h). qPCR analysis confirmed a decrease in the expression of *WT1* and *PODXL* (proximal segment), and the induction of *WNT4* (a β-catenin target gene) in CHIR-treated organoids relative to control, whereas *PAX2* (whole nephron) remained unchanged (Fig. 2i). We next determined the effect of disrupting Notch signalling by treating day 8 RV-stage organoids with the γ-secretase inhibitor DAPT. Inhibition of Notch resulted in a severe loss of proximal tubule-like structures (LTL$^+$), together with a reduction in PODXL$^+$ glomerulus-like structures when compared with control (Supplementary Fig. 11a,b). qPCR analysis confirmed the downregulation of proximal (*WT1*) and medial (*SLC3A1*) nephron segment markers (Supplementary Fig. 11c). These findings agree with the role of Notch signalling in specifying proximal and medial identity during nephron patterning in the mouse[17], and expand previous knowledge about the effect of Notch signalling on kidney organoids[3].

The kidney is a highly metabolic organ that generates ATP through oxidative phosphorylation. Into the light of this knowledge, we hypothesized that the energy metabolism profile of cells should be taken into account to promote the differentiation of hPSCs into renal subtypes. Therefore, we exposed day 8 RV-stage organoids to either cell culture medium that promotes glycolysis in stem cells[18] (endothelial cell growth medium, EGM) or cell culture medium favouring oxidative phosphorylation (renal epithelial cell growth medium (REGM) with insulin) for 8 d. Seahorse analysis revealed that REGM increased mitochondrial respiration in kidney organoids when compared with EGM (Fig. 2j–l), promoting an oxidative phosphorylation bioenergetic phenotype. Kidney organoids under REGM conditions enhanced tubule differentiation, as shown by the development of prominent proximal tubular structures (LTL$^+$), more than with EGM (Fig. 2m,n), in agreement with previous findings[19].

Vascularization of kidney organoids

Kidney organoids have shown the presence of nascent vascular endothelial cells surrounding renal structures, but lack a proper vascular pattern[4,9]. Of note, only two independent studies have reported in vivo vascularization of either hiPSC-derived NPCs[20] or kidney organoids[21] when transplanted under the kidney capsule of immunodeficient
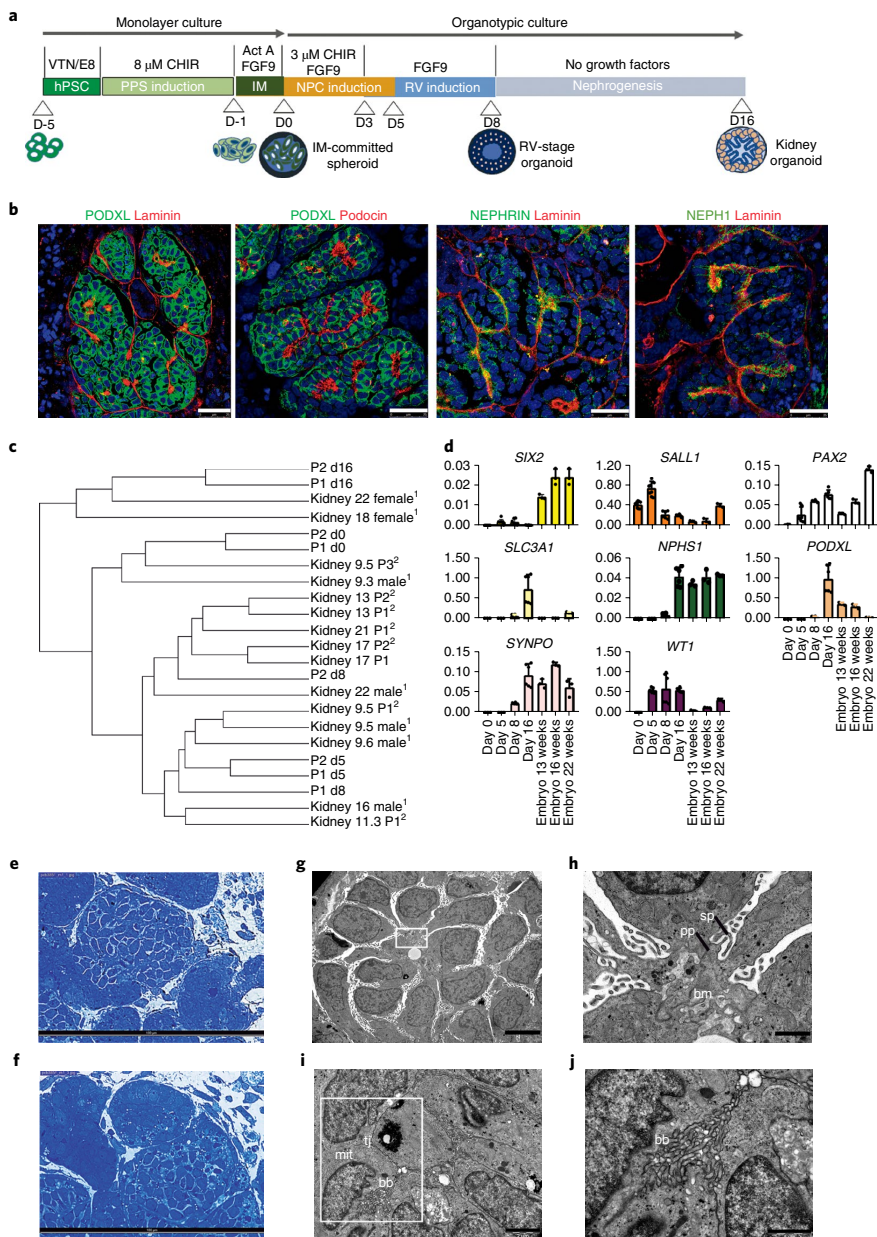
Fig. 1 | Efficient generation of kidney organoids in 3D culture. a, Schematic of the stepwise differentiation methodology for generating kidney organoids from hPSCs. **b**, Confocal microscopy images of glomerular structures in day 16 kidney organoids showing podocyte-like cells positive for PODXL, nephrin, NEPH1 and podocin, and the basement membrane protein laminin. Scale bars, 25 μm. **c**, Dendrogram representing the hierarchical clustering of day 0,5,8 and 16 kidney organoids with human fetal kidneys from 9, 13, 17 and 18 weeks of gestation (first trimester) and 22 weeks of gestation (second trimester). Data from Chuva de Sousa Lopes (SRP055513)[13] (1) and McMahon (SRP111183)[14] (2) are included in the analysis. **d**, qPCR analysis during kidney organoid differentiation and 13-, 16-, and 22-week human fetal kidneys (genes are indicated). Data are mean ± s.d. For *SIX2, WT1, SALL1* and *PAX2*, day 0, day 5, $n = 3$; day 8, day 16, $n = 2$. For *PODXL, SLC3A1, SYNPO* and *NPHS1*, day 0, day 5, $n = 1$; day 8, day 16, $n = 2$. Each sample is a pool of six organoids. Three technical replicates are shown per sample. **e,f**, Semithin sections of day 16 kidney organoids showing glomerular (**e**) and tubular-like (**f**) structures. Scale bars, 100 μm. **g–j**, TEM of day 16 kidney organoids. **g**, Immature podocytes. Scale bar, 5 μm. **h**, A magnified view of the boxed region in **g** showing a detail of podocyte-related structures including the deposition of a basement membrane (bm), and primary (pp) and secondary cell processes (sp). Scale bar, 1 μm. **i**, Epithelial tubular-like cells with brush borders (bb), high mitochondrial (mit) content and tight junctions (tj). Scale bar, 2 μm. **j**, A magnified view of the boxed region in **i** showing a detail of brush borders. Scale bar, 1 μm.
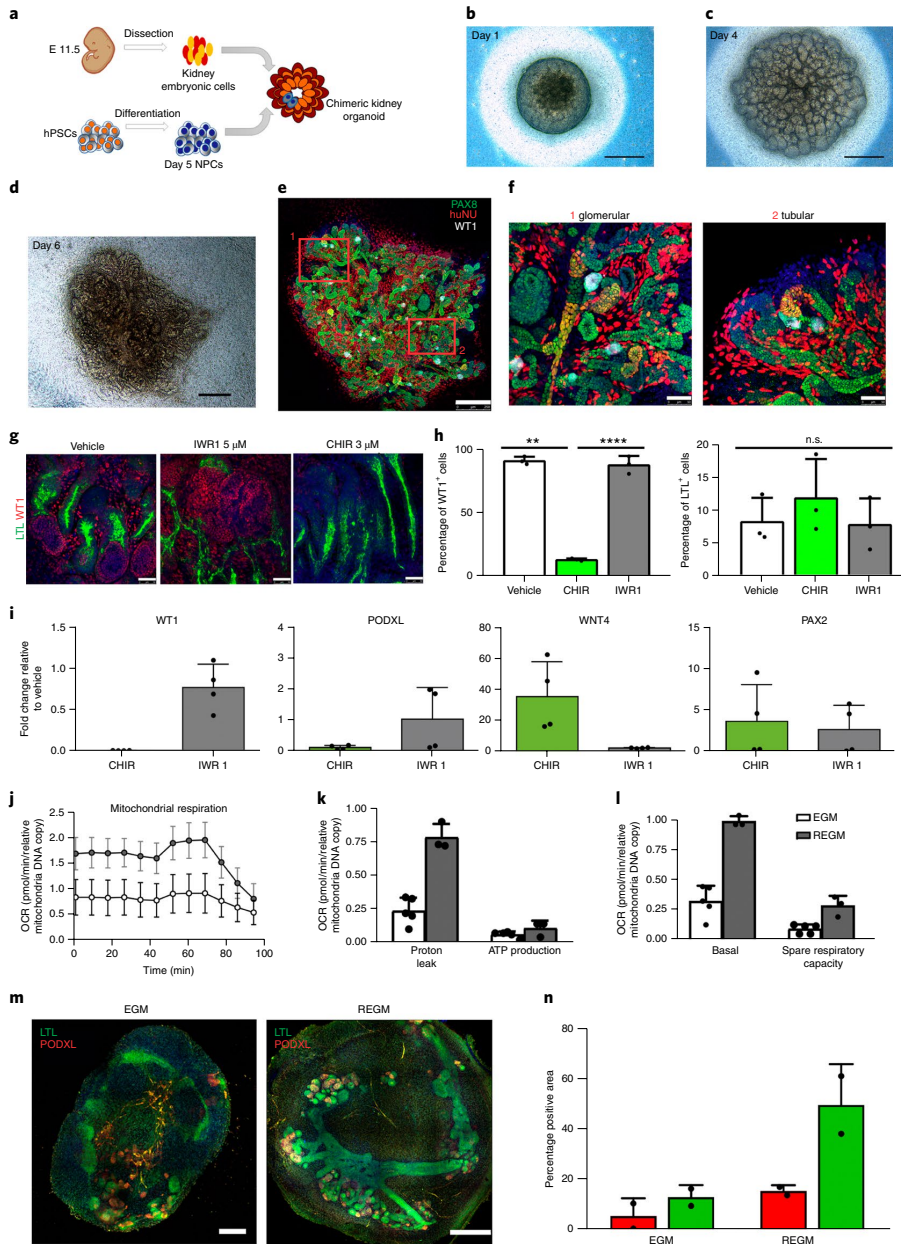
Fig. 2 | Kidney organoids model human kidney organogenesis in vitro. a, Representation of the coculture of day 5 NPCs with mouse embryonic kidney cells. **b–d**, Bright-field images of reaggregates after 1 d (**b**), 4 d (**c**) and 6 d (**d**) in culture. Scale bars, 500 μm. **e**, Immunocytochemistry for PAX8, WT1 and HuNu of the reaggregate in **d**. Scale bar, 250 μm. **f**, Magnified views of **d**. Scale bars, 50 μm. **g–i**, Modulation of β-catenin signalling in kidney organoids with IWR1 and CHIR inhibitors. **g**, Immunocytochemistry for WT1 and LTL in day 16 kidney organoids with the indicated regimens. Scale bars, 50 μm. **h**, Corresponding quantification of the percentage of WT1+ cells and LTL+ structures. Data are mean ± s.d. $n = 3$ organoids per treatment. One-way analysis of variance with Tukey´s post hoc test. For % WT1, $F_{(1.009, 2.017)} = 213.6$, $P = 0.0045$; vehicle versus CHIR, **$P = 0.0082$; CHIR versus IWR1, ****$P = 0.000034$; vehicle versus IWR1, n.s., not significant, $P = 0.9995$. For % LTL, $F_{(1.002, 2.004)} = 0.9976$, $P = 0.4232$, not significant. **i**, Corresponding qPCR analysis (genes are indicated). Data are mean ± s.d. (three technical replicates). **j–l**, Energy metabolism profile of kidney organoids maintained in EGM or REGM: kinetic oxygen consumption rate (OCR) response (**j**), inner mitochondrial membrane proton leak and cellular ATP production (**k**) and basal respiration and spare respiratory capacity (**l**). Data are normalized to mitochondrial DNA copy number/sample. Data are mean ± s.d. $n = 3$ (EGM) and $n = 2$ (REGM) organoids. **m**, Immunocytochemistry for LTL and PODXL in day 16 kidney organoids under EGM or REGM regimen. Scale bars, 200 μm (EGM) and 400 μm (REGM). **n**, Corresponding quantification of the percentage of PODXL+ and LTL+ structures. Data are mean ± s.d. $n = 2$ organoids per condition.

mice, identifying in both cases host-derived vascularization. We decided to explore an alternative approach for providing a vascular environment to kidney organoids. We made use of the chick chorioallantoic membrane (CAM), a highly vascularized extraembryonic tissue that has been used in tumour angiogenesis research[22,23] and for the grafting of biomaterials[24]. More so than other in vivo models, such as the mouse, CAM represents a naturally immunodeficient environment that offers direct, minimally invasive access to the assay site, thereby facilitating the monitoring of the experiments in situ. We implanted day 16 kidney organoids into the CAM of 7-day-old chick embryos, and then maintained them in ovo for 5 d (Fig. 3a; Methods). On day 3 of implantation, multiple blood vessels from the CAM were macroscopically distinguished throughout kidney organoids (Fig. 3b, Supplementary Video 1). The circulation of chick blood within kidney organoids was clearly observed after 5 d (Fig. 3c, Supplementary Video 2). At this stage, in vivo injection of dextran–FITC (fluorescein isothiocyanate) into the CAM allowed for live imaging of the vasculature, confirming the grafting of the organoids into the CAM (Fig. 3d, Supplementary Video 3). Compared with in vitro counterparts (Supplementary Fig. 12a), CAM-implanted kidney organoids (implanted organoids) exhibited glomeruli with an enlarged Bowman's space and tubule-like structures with enlarged lumens (Supplementary Fig. 12b,c, magnified views). Furthermore, CAM blood vessels (indicated with asterisks in Supplementary Fig. 12b,c,d) were found in close vicinity to glomerulus structures. Immunofluorescence analysis of consecutive sections confirmed the presence of chick blood vessels (labelled with *Lens culinaris* agglutinin) within implanted organoids. The latter were identified by the expression of the human marker HuNu and the presence of glomerulus-like structures (WT1⁺) (Supplementary Fig. 12e). Next, we tested the ability of implanted organoids to respond to the well known nephrotoxic agent cisplatin. Twenty-four hours after injecting cisplatin into the chick vasculature, levels of KIM-1 (a marker of renal tubule toxicity) and cleaved CASPASE 3 (a classical apoptotic marker) were upregulated in proximal tubular structures (LTL⁺), compared with specimens injected with a control solution (Supplementary Fig. 12f,g).

We next analysed semithin (Fig. 3e) and ultrathin sections (Fig. 3f–k) of implanted organoids. TEM images revealed the presence of aligned podocyte-like cells on one side of a linear basement membrane (Fig. 3f–h). Endothelial-like cells were found on the opposite side of the basal lamina (Fig. 3f) and, occasionally, chicken erythrocytes were observed within the glomerular-like structures (Fig. 3h). Podocyte-like cells exhibited multiple microvilli on the apical surface and extended primary and secondary cell processes on the basal side (Fig. 3f–i, Supplementary Fig. 12h–j). Secondary cell processes were bridged by slit diaphragm-like structures (Fig. 3g–i, Supplementary Fig. 12h–j). These features, which reflect functional differentiation, were not detected in the organoids cultured in vitro (Fig. 1g, h). Furthermore, tubular-like cells with thick brush borders and high mitochondrial content were observed (Fig. 3j,k). Immunofluorescence analysis showed apical localization of PODXL in aligned podocyte-like cells situated on the basement membrane (LAMININ⁺). Conversely, podocin and NEPH1 localized on the podocyte basal side (Fig. 3l). Likewise, CD34⁺ endothelial-like cells (stained with an antihuman specific CD34 antibody) were closely associated with NEPHRIN⁺/PODXL⁺ podocyte-like cells within glomerulus-like structures in implanted organoids (Fig. 3m, Supplementary Fig. 12k). Moreover, endothelial-like cells (CD31⁺) within glomerulus-like structures (PODXL⁺) coexpressed the human marker HuNu (Fig. 3n). In contrast, for kidney organoids cultured in vitro, CD34⁺ endothelial-like cells were not found within glomerulus-like structures (PODXL⁺) (Supplementary Fig. 12l).

Soft hydrogels enhance the formation of kidney organoids
Mirroring the exact biochemical (for example, site-specific bioactive ligands) and biophysical (for example, extracellular matrix stiffness,

fluid flow, oxygen tension) properties of a physiological environment represents an as yet unaffordable technical approach in tissue engineering. By contrast, fabrication of hydrogels with mechanical properties (for example, Young's modulus) similar to native tissues is a key methodology for guiding cellular responses and differentiation[25]. Therefore, we decided to characterize the specific mechanical properties of the CAM (by measuring the Young's modulus, Supplementary Fig. 13a; Methods), which exhibited a stiffness value of about 1 kPa (Supplementary Fig. 13b), representative of an early embryonic microenvironment[26] in which undifferentiated cells are primed for lineage commitment[27]. We next explored whether substrates mimicking a soft microenvironment may favour the generation of kidney organoids, compared with stiffer substrates. Thus, we fabricated functionalized polyacrylamide hydrogels of tunable stiffness (ranging from soft, 1 kPa, to very rigid, 60 kPa) as substrates for hPSC differentiation (Supplementary Fig. 14a; Methods). In comparison with rigid hydrogels, hPSCs grown on soft hydrogels under undifferentiated conditions formed tightly compacted hPSC colonies (ECAD⁺) (Supplementary Fig. 14b), showing reduced nuclear localization of the mechanotransduction marker Yes-associated protein (YAP) (Supplementary Fig. 14c). RNA-Seq analysis of hPSCs revealed that soft hydrogels promoted the expression of genes related to embryo and mesodermal differentiation (Supplementary Table 3), suggesting that a soft milieu may better replicate early stages of embryonic development, during which time counteracting gene regulatory networks control both pluripotency and differentiation ground states[28]. Based on these observations, we hypothesized that using soft hydrogels during the first steps of monolayer differentiation (including PPS and IM induction) may help guide hPSCs toward renal commitment. PPS induction of hPSCs differentiated on soft hydrogels resulted in higher mRNA levels of *T* and *SALL1* markers when compared with rigid conditions (Supplementary Fig. 15a,b). PPS differentiation was also analysed by RNA-Seq, showing that soft hydrogels induced the expression of genes related to transcription regulation and downregulated genes related to extracellular matrix and basement membrane (Supplementary Table 4, Supplementary Fig. 15c). Induction of PPS-committed cells into IM-committed cells (Supplementary Fig. 16a) showed that soft hydrogels promoted increased mRNA levels of the early IM marker *PAX2*, the posterior IM marker *HOXD11*, the anterior IM marker *LHX1*, and *SALL1* when compared with rigid conditions (Supplementary Fig. 16b). Upon differentiation under 3D organotypic culture, IM-committed cells derived on soft hydrogels began to develop RVs one day earlier (at day 7: Supplementary Fig. 16c), and resulted in the generation of more RVs than those derived on rigid hydrogels, as shown by quantitative analysis of PAX2⁺ RVs (Fig. 4a,b). Moreover, day 16 kidney organoids from soft conditions developed more WT1⁺ glomerulus-like and LTL⁺ tubule-like structures than those derived from rigid conditions (Fig. 4c,d), and expressed increased mRNA levels of late-stage nephron (*NPHS1, SCNN1B*) and vascularization (*ENDOGLIN, VEGFR*) markers (Fig. 4e). TEM of day 16 kidney organoids showed the presence of tubule-like structures containing epithelial cells with prominent brush borders in both soft and rigid conditions (Fig. 4f, Supplementary Fig. 17). Interestingly, soft hydrogels induced the differentiation of podocyte-like cells containing slit diaphragm-like structures between the cell processes (Fig. 4g–i), a podocyte differentiation feature that was absent in rigid conditions (Fig. 1g,h, Supplementary Fig. 17). Considering these findings, day 16 kidney organoids derived from soft hydrogels were then implanted into the CAM for 5 days (Fig. 4j). TEM revealed the presence of tubular epithelial-like cells with brush borders (Fig. 4k) and numerous glomerular structures containing podocyte-like cells above a dense basement membrane and in close vicinity to endothelial cells and chicken erythrocytes (Fig. 4l). Furthermore, induced podocyte-like cells exhibited secondary cell processes with slit diaphragm-like structures (Fig. 4m,n).
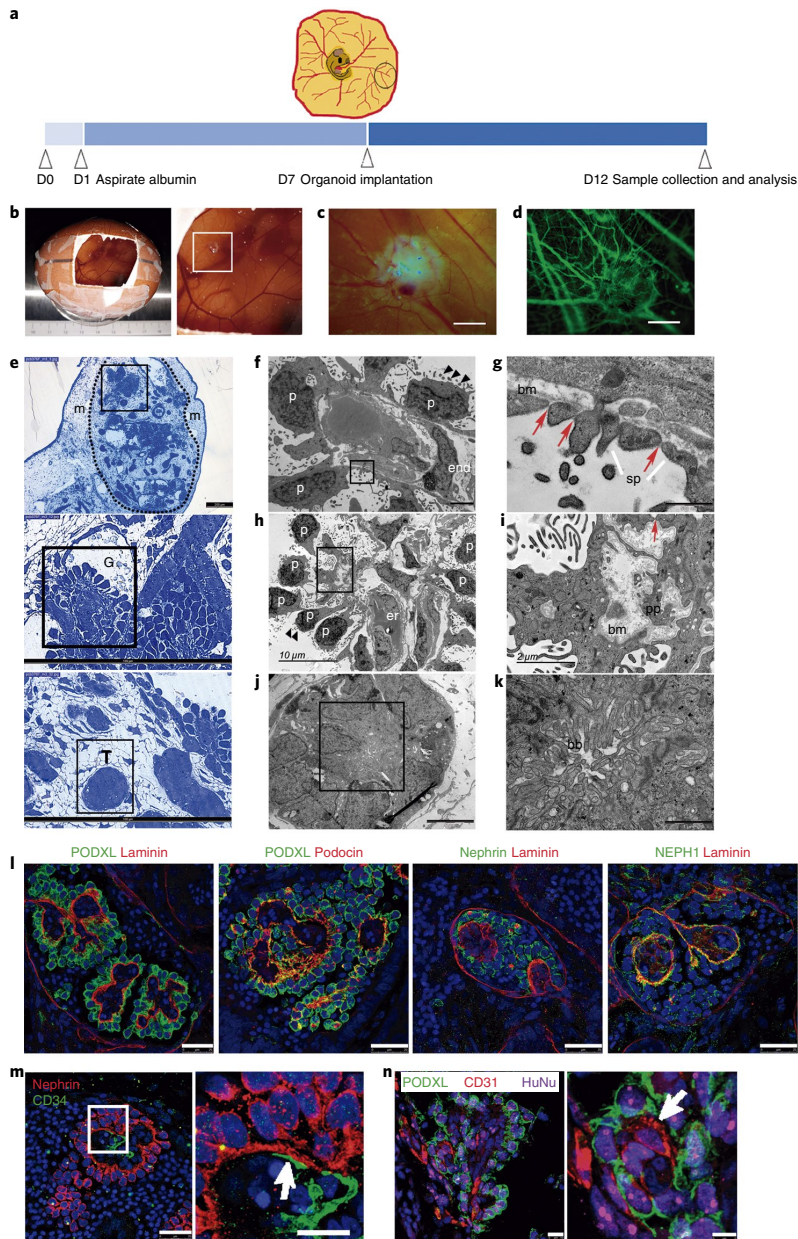
Fig. 3 | In vivo vascularization of kidney organoids using chick CAM. a, Methodology for the implantation of day 16 kidney organoids into chick CAM. **b,c**, Macroscopic views of implanted organoids maintained in ovo for 3 d (**b**) and 5 d (**c**). **d**, The implanted organoid in **c** after intravital injection of dextran–FITC through the chick vasculature. Scale bars, 1000 μm (**c,d**). **e**, Semithin sections of a kidney organoid (dashed line) implanted in the CAM mesenchyme (m) for 5 d. Magnified views of glomerular (G) and tubular (T) cells are shown. Scale bars, 200 μm, 100 μm (magnified views). **f–k**, TEM of implanted organoids. Magnified views of the boxed regions in **f,h,j** are shown in **g,i,k**, respectively. **f**, Differentiated podocytes (p) extending primary cell processes and apical microvilli (black triangles) are located on one side of the basement membrane and a vascular endothelial cell (end) is found on the opposite side. **g**, Slit diaphragm-like structures (red arrows) between secondary cell processes (sp). bm, basement membrane . **h**, Aligned podocytes showing primary cell processes and apical microvilli (black triangles). er, chicken erythrocytes. **i**, A detail of the basement membrane (bm), primary cell processes (pp) and a slit diaphragm-like structure (red arrow). **j**, Tubular-like cells. **k**, A detail of brush borders (bb). Scale bars, 2 μm (**f**), 500 nm (**g**), 10 μm (**h**), 2 μm (**i**), 5 μm (**j**), 1 μm (**k**). **l–n**, Confocal microscopy images of glomerular structures in implanted organoids. **l**, Immunohistochemistry for PODXL, nephrin, NEPH1, podocin and laminin. Scale bars, 25 μm. **m**, Immunohistochemistry for nephrin and CD34. Scale bars, 25 μm, 10 μm (magnified view). **n**, Immunohistochemistry for PODXL, CD31 and the human marker HuNu. Scale bars, 10 μm, 5 μm (magnified view). White arrows indicate endothelial-like cells in close contact with podocyte-like cells (**m,n**).
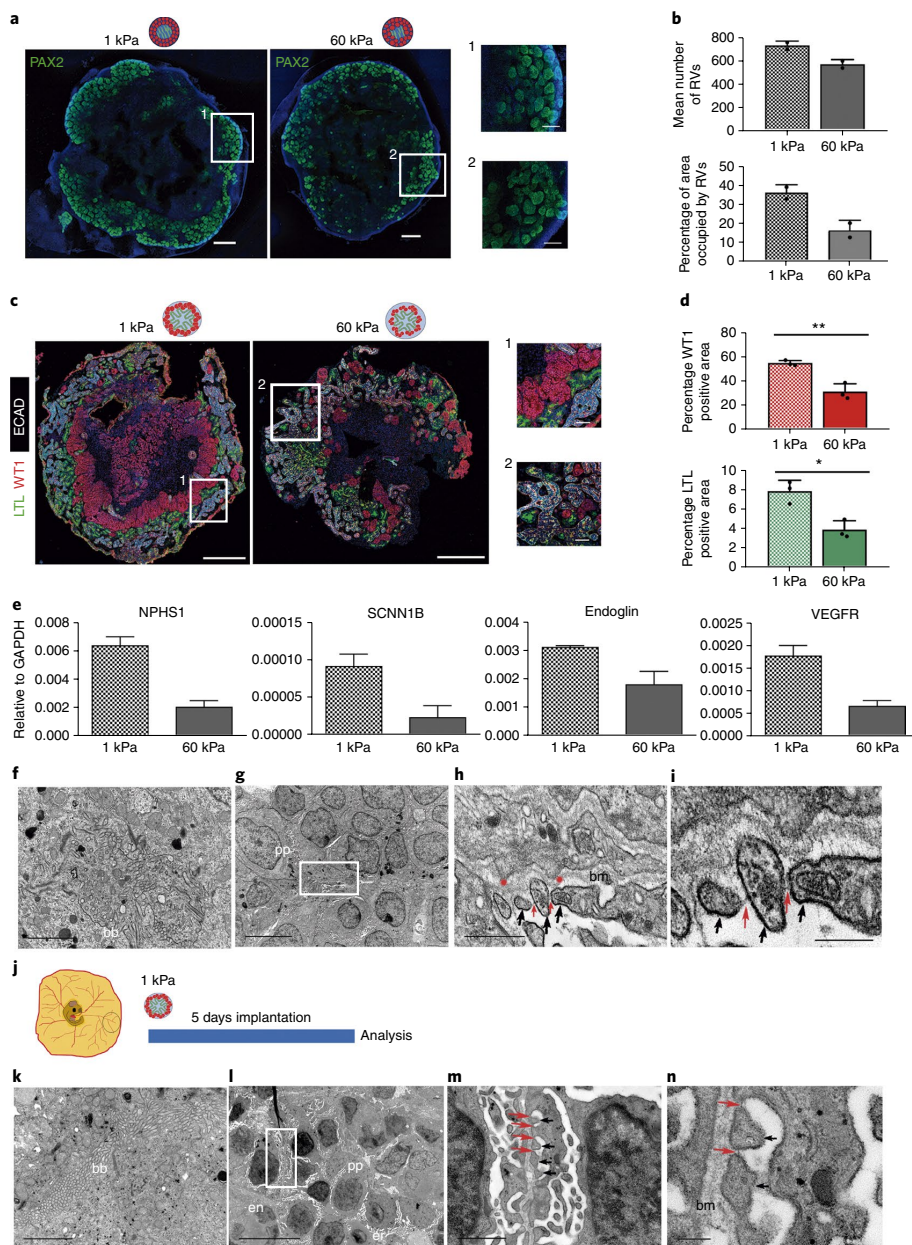
Fig. 4 | Soft hydrogels accelerate the differentiation of kidney organoids. a, Immunocytochemistry for PAX2 in RV-stage organoids generated using 1 kPa or 60 kPa hydrogels. Scale bars, 500 μm, 150 μm (magnified views). **b**, Quantification of **a**. The mean number of RVs and area percentage occupied by RVs were quantified. Data are mean ± s.d. $n = 2$ organoids per condition. **c**, Immunohistochemistry for LTL, WT1 and ECAD in day 16 kidney organoids from 1 kPa or 60 kPa. Scale bars, 500 μm and 50 μm (magnified views). **d**, Quantification of **c**. The percentages of WT1$^+$ and LTL$^+$ area were quantified. Data are mean ± s.d. $n = 3$ organoids per condition. For WT1$^+$ $t(4) = 5.8057$, **$P = 0.0044$. For LTL$^+$ $t(4) = 4.6023$, *$P = 0.0100$. Two-tailed Student's t-test. **e**, qPCR analysis of day 16 kidney organoids from 1 kPa or 60 kPa (genes are indicated). Data are mean ± s.d. (technical replicates). **f–i**, TEM of day 16 kidney organoids from 1 kPa. **f**, Epithelial tubular-like cells with brush borders (bb). **g**, Podocyte-like cells with primary cell processes (pp). **h,i**, Magnified views of **g**. Secondary cell processes (black arrows) with slit diaphragm-like structures (red arrows). Red asterisks, podocyte membrane protrusions. bm, basement membrane. Scale bars, 2 μm (**f**), 5 μm (**g**), 500 nm (**h**), 200 nm (**i**). **j**, Day 16 kidney organoids from 1 kPa were implanted into the CAM. **k–n**, TEM of implanted kidney organoids from 1 kPa. **k**, Tubular-like cells with brush borders. **l**, Aligned podocyte-like cells extending primary cell processes near endothelial (en) cells and chicken erythrocytes (er). **m,n**, Magnified views of **l**. Secondary cell processes with slit diaphragm-like structures. Scale bars, 2 μm (**k**), 10 μm (**l**), 1 μm (**m**), 200 nm (**n**).

Outlook

The methodology described here reduced the time needed to generate kidney organoids when compared with previous protocols by about 30%[1,3–5,9], leading to the generation of kidney organoids that transcriptionally resembled second-trimester human fetal kidneys. This is an improvement over previous findings, in which kidney organoids clustered with trimester 1 human fetal kidneys[9]. Furthermore, here we have shown that kidney organoids implanted into chick CAM successfully engrafted and were vascularized in ovo, providing a straightforward model for nephrotoxicity and kidney disease modelling applications. Importantly, CAM-implanted kidney organoids showed morphological features that reflect functional differentiation compared with in vitro conditions. When CAM stiffness was mimicked in vitro via compliant hydrogels, hPSCs differentiated on soft substrates (CAM-like) generated IM-committed cells that showed an accelerated formation of more RVs and nephron structures than those produced on rigid substrates. Furthermore, kidney organoids generated from soft hydrogels exhibited improved differentiation characteristics when compared with those found under stiffer conditions. These differentiation features were also enhanced after CAM transplantation. Overall, the methodology described here paves the way toward further developing biomimetic approaches that will enhance organoid differentiation (either in vitro or in vivo). These advances will enable future studies of kidney development and disease.

Online content

Any methods, additional references, Nature Research reporting summaries, source data, statements of data availability and associated accession codes are available at https://doi.org/10.1038/s41563-019-0287-6.

References

1. Taguchi, A. et al. Redefining the in vivo origin of metanephric nephron progenitors enables generation of complex kidney structures from pluripotent stem cells. *Cell Stem Cell* **14**, 53–67 (2014).
2. Lam, A. Q. et al. Rapid and efficient differentiation of human pluripotent stem cells into intermediate mesoderm that forms tubules expressing kidney proximal tubular markers. *J Am Soc Nephrol.* **25**, 1211–1225 (2014).
3. Morizane, R. et al. Nephron organoids derived from human pluripotent stem cells model kidney development and injury. *Nat. Biotechnol.* **33**, 1193–1200 (2015).
4. Freedman, B. S. et al. Modelling kidney disease with CRISPR-mutant kidney organoids derived from human pluripotent epiblast spheroids. *Nat. Commun.* **6**, 8715 (2015).
5. Toyohara, T. et al. Cell therapy using human induced pluripotent stem cell-derived renal progenitors ameliorates acute kidney injury in mice. *Stem Cells Transl. Med.* **4**, 980–992 (2015).
6. Imberti, B. et al. Renal progenitors derived from human iPSCs engraft and restore function in a mouse model of acute kidney injury. *Sci. Rep.* **5**, 8826 (2015).
7. Xia, Y. et al. Directed differentiation of human pluripotent cells to ureteric bud kidney progenitor-like cells. *Nat. Cell Biol.* **15**, 1507–1515 (2013).
8. Takasato, M. et al. Directing human embryonic stem cell differentiation towards a renal lineage generates a self-organizing kidney. *Nat. Cell Biol.* **16**, 118–126 (2014).
9. Takasato, M. et al. Kidney organoids from human iPS cells contain multiple lineages and model human nephrogenesis. *Nature* **526**, 564–568 (2015).
10. Taguchi, A., & Nishinakamura, R. Higher-order kidney organogenesis from pluripotent stem cells. *Cell Stem Cell* **21**, 730–746 (2017).
11. Musah, S. et al. Mature induced-pluripotent-stem-cell-derived human podocytes reconstitute kidney glomerular-capillary-wall function on a chip. *Nat. Biomed. Eng.* **1**, 0069 (2017).
12. Cruz, N. M. et al. Organoid cystogenesis reveals a critical role of microenvironment in human polycystic kidney disease. *Nat. Mater.* **16**, 1112–1119 (2017).
13. Roost, M. S. et al. KeyGenes, a tool to probe tissue differentiation using a human fetal transcriptional atlas. *Stem Cell Rep.* **4**, 1112–1124 (2015).
14. Lindström, N. O. et al. Conserved and divergent features of human and mouse kidney organogenesis. *J. Am. Soc. Nephrol.* **29**(3), 785–805 (2018).
15. Unbekandt, M. & Davies, J. A. Dissociation of embryonic kidneys followed by reaggregation allows the formation of renal tissues. *Kidney Int.* **77**, 407–416 (2010).
16. Davies, J. A., Unbekandt, M., Ineson, J., Lusis, M. & Little, M. H. Dissociation of embryonic kidney followed by re-aggregation as a method for chimeric analysis. *Methods Mol. Biol.* **886**, 135–146 (2012).
17. Lindström, N. O. et al. Integrated β-catenin, BMP, PTEN, and Notch signalling patterns the nephron. *eLife* **3**, e04000 (2014).
18. De Bock, K. et al. Role of PFKFB3-driven glycolysis in vessel sprouting. *Cell* **154**, 651–663 (2013).
19. Narayanan, K. et al. Human embryonic stem cells differentiate into functional renal proximal tubular-like cells. *Kidney Int.* **83**, 593–603 (2013).
20. Sharmin, S. et al. Human induced pluripotent stem cell-derived podocytes mature into vascularized glomeruli upon experimental transplantation. *J. Am. Soc. Nephrol.* **27**, 1778–1791 (2016).
21. Van den Berg, C. W. et al. Renal subcapsular transplantation of PSC-derived kidney organoids induces neo-vasculogenesis and significant glomerular and tubular maturation in vivo. *Stem Cell Rep.* **10**, 751–765 (2018).
22. Ribatti, D. Chick embryo chorioallantoic membrane as a useful tool to study angiogenesis. *Int. Rev. Cell Mol. Biol.* **270**, 181–224 (2008).
23. Cimpean, A. M., Ribatti, D. & Raica, M. The chick embryo chorioallantoic membrane as a model to study tumor metastasis. *Angiogenesis* **11**, 311–319 (2008).
24. Baiguera, S., Macchiarini, P. & Ribatti, D. Chorioallantoic membrane for in vivo investigation of tissue-engineered construct biocompatibility. *J. Biomed. Mater. Res. B* **100**, 1425–1434 (2012).
25. Vining, K. H. & Mooney, D. J. Mechanical forces direct stem cell behaviour in development and regeneration. *Nat. Rev. Mol. Cell Biol.* **18**, 728–742 (2017).
26. Przybyla, L., Lakins, J. N. & Weaver, V. M. Tissue mechanics orchestrate Wnt-dependent human embryonic stem cell differentiation. *Cell Stem Cell* **19**, 462–475 (2016).
27. Ahmed, K. et al. Global chromatin architecture reflects pluripotency and lineage commitment in the early mouse embryo. *PLoS One* **5**, e10531 (2010).
28. Theunissen, T. W. & Jaenisch, R. Mechanisms of gene regulation in human embryos and pluripotent stem cells. *Development* **144**, 4496–4509 (2017).

Author contributions

E.G. and N.M. conceived and designed the experiments. E.G., P.P., C.T. and C.H.P. performed the experiments. E.G., P.P., C.T. and R.O. characterized the cell lines and contributed to the protocol design. A.G.-N. and C.H.P. carried out the Seahorse analysis. L.C. contributed to the transcriptomic analysis. E.G., P.P., C.T., R.O., L.F., E.M., D.Z., X.T., P.R.-C., J.M.C., J.C.I.B., C.H.P. and N.M. contributed to data interpretation. E.G. and N.M. wrote the manuscript. All authors commented on the manuscript and contributed to it. N.M. oversaw the project.

Competing interests

The authors declare no competing interests.

Additional information

Methods

Culture of hPSCs. All hPSC lines were obtained after the approval of the Ethics Committee of the Center of Regenerative Medicine in Barcelona and the Comisión de Seguimiento y Control de la Donación de Células y Tejidos Humanos del Instituto de Salud Carlos III (project numbers: 0336E/7564/2016; 0336E/5311/2015; 0336E/15986/2016; 0336E/79489/2015; 00336E/20031/2014). ES[4] hESC and CBiPSsv-4F-40 were obtained from The National Bank of Stem Cells (ISCIII, Madrid). H1 and H9 hESC lines were purchased at Wicell. All the lines were maintained in Essential 8 medium (A1517001, Life Technologies) in cell culture plates coated with 5 µg ml⁻¹ vitronectin (A14700, Fisher Scientific) with 5% CO_2 at 37 °C. Cells were passaged every 4–6 d.

hPSC differentiation into renal progenitor cells and generation of 3D kidney organoids. hPSCs grown on vitronectin-coated plates were rinsed twice with PBS (1001–015, Life Technologies) and disaggregated into small cell clusters with 0.5 mM EDTA (E9884, Sigma). Cells were then seeded onto vitronectin-coated culture plates at a density of 5×10^4–1.5×10^4 cells per cm² in Essential 8 medium (day −5). After overnight culture, the differentiation was initiated by treating hPSCs with 8 µM CHIR (SML1046, Sigma) in advanced RPMI 1640 basal medium (12633-012, Life Technologies) supplemented with 2 mM L-GlutaMAX (35050–038, Life Technologies) and penicillin/streptomycin (penicillin 10,000 U ml⁻¹:streptomycin 10,000 µg ml⁻¹; 15140122, Life Technologies) for 3 d (from day −4 to day −1). Next, cultures were treated with 200 ng ml⁻¹ FGF9 (100–23B, Peprotech), 1 µ ml⁻¹ heparin (H3149-10KU, Sigma) and 10 ng ml⁻¹ activin A (338-AC-050, Vitro) for 1 d (from day −1 to day 0). Media changes were performed every day. On day 0, single-cell suspensions were obtained by dissociating cells with Accumax (07921, Stem Cell Technologies). Cells were then resuspended in advanced RPMI 1640 basal medium containing 3 µM CHIR, 200 ng ml⁻¹ FGF9 and 1 µ ml⁻¹ heparin, placed in 96-well plates (V bottom) at 5×10^5 cells per well, spun down (300 g for 3 min) and maintained in culture for 2 d without medium change. On day 2, cell spheroids were placed onto Transwells (CLS3460, Sigma) and cultured in advanced RPMI 1640 basal medium containing 3 µM CHIR, 200 ng ml⁻¹ FGF9 and 1 µg ml⁻¹ heparin for another 1 d. On day 3, CHIR was removed and organoids were maintained in advanced RPMI 1640 basal medium with 200 ng ml⁻¹ FGF9 and 1 µg ml⁻¹ heparin for another 4 d. From day 7 organoids were maintained in advanced RPMI 1640 basal medium until day 16 unless otherwise indicated, changing the medium every second day.

Immunocytochemistry. After a single wash with PBS, samples were fixed with 4% paraformaldehyde (153799, Aname) for 20 min at room temperature. Next, samples were washed twice with PBS and further blocked using Tris-buffered saline (TBS) with 6% donkey serum (S30, Millipore) and 1% Triton X-100 (T8787, Sigma) for 1 h at room temperature. Samples were then treated overnight at 4 °C with primary antibodies diluted in antibody dilution buffer consisting of TBS with 6% donkey serum and 0.5% Triton X-100. After three rinses with antibody dilution buffer, samples were treated for 4 h at room temperature with fluorescent-conjugated secondary antibodies (Alexa Fluor (A) 488-, Cy3- or A647-; 1:200). A previous blocking step with a streptavidin/biotin blocking kit (SP-2002, Vector Labs) was performed when samples were assayed for biotinylated LTL (B-1325, Vector Labs) and Alexa Fluor 488-conjugated streptavidin (SA5488, Vector Labs) was used to detect LTL⁺ cells. Nuclei were detected using 4,6-diamidino-2-phenylindole (DAPI; 1:5000, D1306, Life Technologies) for 30 min. For mounting, samples were immersed in Fluoromount-G (0100-01, Southern Biotech). Image acquisition was carried out using an SP5 Leica microscope or a Zeiss LSM780 confocal microscope. Primary antibodies and associated information are provided in Supplementary Table 5.

Electron microscopy. After fixation of samples with 2.5% glutaraldehyde containing 1% tannic acid in 0.1 M phosphate buffer (pH 7.4), samples were postfixed for 1 h at 4 °C with 1% OsO_4 in 0.1 M phosphate buffer. Graded ethanol series were performed followed by epoxy resin embedding. Toluidine blue staining was performed in semithin sections before examination using a light microscope. Then, ultrathin sections were obtained using an EM UC7 ultramicrotome (Leica Microsystems) and collected on copper grids. 4% uranyl acetate and lead citrate were then used for staining. Samples were subsequently analysed with a JEM 1230 electron microscope (JEOL).

Total RNA isolation and qPCR with reverse transcription. TRI Reagent was employed for total RNA purification following the manufacturer's recommendations (T9424, Sigma). TURBO DNase inhibitor (AM1907, Ambion) was used in order to eliminate any residual genomic DNA. Complementary DNA was synthesized from 1 µg of RNA using a Cloned AMV First-Strand cDNA synthesis kit (12328, Invitrogen). Quantitative PCR with reverse transcription (QUANTSTUDIO 5 Applied Biosystems, Thermo Fisher Scientific) was used to quantify gene expression from cDNAs (25 ng/well) using PowerUp Sybr Green Master Mix (A25742, Thermo Fisher Scientific). GAPDH or Rplp0 were used for data normalization. Primer sequences used in this study are listed in Supplementary Table 6.

Next-generation RNA sequencing. Sequencing libraries were prepared from 1 µg of total RNA (previously isolated using TRI Reagent—T9424, Sigma) using an Illumina TruSeq RNA Sample Prep Kit (catalogue no. FC-122–1001). Sequencing was carried out to produce between 50 and 60 million paired end reads/sample using the Illumina Hiseq 2500 platform. Raw sequences were inspected for their quality using FastQC (version v0.11.5)[29] and trimmed using Skewer (version 0.2.2)[30]. STAR mapper (version 2.5.3a)[31] was used to align the data to the human reference genome (GRCh38). The option '–quantMode' was employed to count the number of mapped tags within genes (annotation Gencode v26). On average, 90% of tags were univocally mapped either to the genomic or to a splice junction. Data from Chuva de Sousa Lopes (SRP055513)[13] were analysed in the same way. Read counts per genes were finally analysed using the R statistical package DESeq2[32]. Since the two experiments were performed using different techniques (RNA-Seq and DeepSAGE), we used the ComBat function from the svaseq R package[33] on rlog-transformed read counts in order to mitigate the batch effect. Scaled rlog values were then used to calculate the sample-to-sample distance and plotted as a dendrogram. Data from Little (SRP059518)[9] and McMahon (SRP111183)[14] were analysed using the same procedure. The package Keygenes[13] was used to classify every sample according to its similarity to a tissue. Keygenes compares the transcriptional profiles of test samples with that from organs or cell types from a training set. In this study, the 'fetal wo' training set was used. This training set contains transcriptional data from 17 fetal organs.

Flow cytometry. Cells were dissociated using Accumax (07921, Stem Cell Technologies) for 5 min at 37 °C. Next, cells were resuspended in PBS and incubated with LIVE/DEAD Fixable Violet stain reagent (L23105, Life Technologies) (1:1000) for 30 min in the dark. For intracellular staining, a Foxp3/Transcription Factor Staining Buffer Set (00–5523–00, Labclinics) was used according to manufacturer's instructions. Briefly, cell suspensions were fixed in the dark for 30–60 min at room temperature with Foxp3 fixation/permeabilization working solution. Permeabilization of samples was performed using the permeabilization buffer for 5 min at room temperature. Blocking was performed using 2% fetal bovine serum for 15 min. Incubations with conjugated antibodies were performed for 30 min. The antibodies used were OCT4 conjugated to Alexa Fluor 488 (560253, BD Pharmigen), brachyury conjugated to allophycocyanin (IC2085A, R&D Systems) and PAX2 (AF3364, R&D Systems) conjugated to A488 using a Lightning-Link® Rapid conjugation kit (322–0010, Innova Biosciences) following the manufacturer's instructions. Samples were then washed with permeabilization buffer and resuspended in PBS + 2% fetal bovine serum. For cell sorting experiments, kidney organoids were stained with fluorescein-conjugated LTL (FL-1321, Vector Laboratories) as described elsewhere[12]. Kidney organoids were then dissociated to single cells using Accumax (07921, Stem Cell Technologies) for 15 min followed by 0.25% (wt/vol) trypsin (25300–054, Life Technologies) for 15 min at 37 °C. SA3800 software version 2.0.4 (SONY) was used to acquire flow cytometry samples in the Sony SA3800 spectral cell analyser (SONY). FACSDiva software version 8.0.1 (BD Biosciences) was used in the FACS Aria Fusion instrument (BD Biosciences) for cell sorting experiments. FlowJo software version 10 was used to analyse the data.

Reaggregation of mouse embryonic kidney cells with hPSC-derived NPCs. These experiments were performed following approval by the Ethics Committee on Animal Research of the University of Barcelona, Spain (protocol no. OB 391/18). Reaggregation experiments were carried out as previously described in ref. [16]. In brief, embryonic kidneys from 11.5–12.5 d post conception were collected from time-mated pregnant C57BL/6J mice. Kidney rudiments were removed from mouse embryos by manual dissection under a dissecting microscope. Dissociation of kidney rudiments into single cells was performed by incubating kidneys with 0.25% (wt/vol) trypsin (25300–054, Life Technologies) for 1–2 min at 37 °C, followed by quenching of trypsin using complete medium (MEM + 10% fetal bovine serum + penicillin/streptomycin) and pipetting up and down vigorously for 30 s to disaggregate kidneys. Day 5 organoids were dissociated into single cells with Accumax (07921, Stem Cell Technologies). The resultant cell suspensions were sieved through a 40 µm pore cell strainer. Next, 7.2×10^5 mouse kidney cells were combined with 8×10^3 cells from day 5 organoids, placed in a 96-well plate (V bottom) in complete medium with 10 µM ROCK inhibitor (72304, Stem Cell Technologies), spun down (300 g for 3 min) and incubated at 37 °C, 5% CO_2 to allow aggregate formation. After overnight culture, aggregates were placed onto Transwells (CLS3460, Sigma) and maintained in complete medium at 37 °C and 5% CO_2 for 4–6 d. Medium changes were performed every 48 h.

Nephron patterning assays. For nephron patterning assays, samples were cultured in basic differentiation media supplemented with 10 µM DAPT (565770, Sigma), 3 µM CHIR (SML1046, Sigma) or 5 µM IWR1 (681669, Sigma) from day 8 to day 16. Organoids were then collected for RNA isolation and fixed with 4% paraformaldehyde for immunocytochemistry.

Seahorse analysis. Kidney organoids at day 16 of differentiation were resuspended in warm Seahorse XF Assay Medium (Seahorse Bioscience). Individual organoids were transferred to an islet plate (one organoid per well) containing 400 µl of

medium per well. After 1 h of incubation at 37 °C, plates were loaded into an XF24 respirometry machine (Seahorse Bioscience). Uncoupled and maximum OCR were assayed with oligomycin (1 μM) and FCCP (1.5 μM). To inhibit complex I- and III-dependent respiration, rotenone (1 μM) and antimycin A (1 μM) were used, respectively. OCR represents the oxygen tension and acidification of the medium as a function of time (pmol min^{-1}).

Implantation of kidney organoids onto chick CAM. Following animal care guidelines in Spain, no approval was required to perform the experiments described here. Briefly, fertilized white Leghorn chicken eggs were supplied by Granja Gibert. Eggs were placed horizontally in a humidified atmosphere at 38 °C in a Javier Masalles 240 N incubator. After 24 h, 3 ml of albumin was evacuated from the egg using a 18-gauge syringe. At embryonic day 7 (ED 7), a small window was created by cutting the egg shell using a sterile scalpel. Then, day 16 kidney organoids were implanted onto the surface of the CAM (one kidney organoid per egg) by gently scraping the upper CAM layer (avoiding bleeding or visible rupture of capillaries) at the desired implantation site. Egg windows were sealed with conventional plastic tape and incubated for 3–5 additional days (until ED 10–12).

Intravital imaging of the CAM vasculature. Under a dissecting microscope, superficial CAM veins were injected with 1 mg ml^{-1} FITC–dextran (2 MDa) (FD-2000S, Sigma) in PBS using a 30-gauge Hamilton syringe, allowing solutions to circulate for 5 min. Injected volumes were kept at 50 μl. Live imaging was performed using a MZ10 F Leica stereomicroscope equipped with a MC170 HD Leica camera.

Nephrotoxicity assay. Chick embryos (ED 14) that contained kidney organoids implanted into the CAM were intravenously injected with desired dosages of cisplatin (P4394, Sigma) using a 30-gauge Hamilton syringe, as previously reported[34]. Specimens injected with control solution (without cisplatin) were used as controls. Eggs were then sealed with conventional plastic tape and incubated overnight at 38 °C. After 24 h, CAM-implanted kidney organoids were collected and analysed.

Histological analysis and immunohistochemistry on CAM-implanted kidney organoids. CAM-implanted kidney organoids were harvested at day 5 of the implantation period, fixed in 4% paraformaldehyde at 4 °C overnight and embedded in paraffin. For histological analysis, 5 μm thick sections were stained with haematoxylin and eosin. For immunohistochemistry, antigen retrieval consisting of citrate buffer (pH 6) at 95 °C for 30 min was performed. Samples were then blocked with TBS containing 3% donkey serum and 1% Triton X-100 for 1 h at room temperature. Subsequently, primary antibodies were used overnight at 4 °C in TBS with 3% donkey serum and 0.5% Triton X-100. After three washing steps with TBS containing 3% donkey serum and 0.5% Triton X-100, samples were treated with the appropriate conjugated secondary antibodies (Alexa Fluor 488-, Cy3- or A647-; all 1:200) for 2 h at room temperature. Nuclei were stained with DAPI (1:5000, D1306, Life Technologies) for 10 min. Samples were immersed in Fluoromount-G (0100-01, Southern Biotech). Image acquisition was carried out using a SP5 Leica microscope or a Zeiss LSM780 confocal microscope. Primary antibodies and associated information are provided in Supplementary Table 5.

Determination of the Young's modulus of the chick CAM. The ball indentation method was used to assess the Young's modulus (E) of the chick CAM, as described in ref. [35]. The indentation depth (d) was calculated based on the derivative of fluorescence intensity profile using a custom-made MATLAB code. E was calculated from the indentation force (F), d and the radius of the ball indentor (R). For $d < 0.3 R$, the Hertz contact mechanics model was used to calculate E as follows: $E = [3(1 - \nu^2)F]/4R^{0.5}d^{1.5}$, where ν is the Poisson's ratio of the CAM.

Fabrication of functionalized polyacrylamide hydrogels. Glass-bottom dishes were loaded with a solution of acetic acid, 3-(trimethoxysilyl)propyl methacrylate (Sigma) and ethanol (1/1/14). Wells were next rinsed three times with 96% ethanol. Different concentrations of acrylamide and bis-acrylamide were combined with a solution containing 0.5% ammonium persulfate, 0.05% tetramethylethylenediamine (Sigma) and 2% fluorescent 200 nm far-red carboxylated nanobeads (Invitrogen). Specifically, concentrations of 5 and 0.04% of acrylamide and bis-acrylamide were used for the softer hydrogels, and 12% and 0.25% of acrylamide and bis-acrylamide for the stiffer hydrogels, resulting in a nominal Young's modulus of 1 kPa and 60 kPa, respectively, according to ref. [36]. The substrates were functionalized as previously described in ref. [37]. Briefly, a drop containing 1 mg ml^{-1} acrylic acid NHS (A8060, Sigma), 0.2% bis-acrylamide, 0.2% tetramethacrylate (408360, Sigma) and 0.05% (w/v) Irgacure 2959 was added on the surface of the hydrogel and photoactivated under exposure to ultraviolet light for 10 min. Afterwards, functionalized hydrogels were washed with HEPES and PBS and incubated overnight with 50 μg ml^{-1} vitronectin (A14700, Fisher Scientific) at 4 °C.

Quantification of immunofluorescence images. A custom-made MATLAB code was used to perform the quantification of immunofluorescence images. For quantification of number and area of RVs, the DAPI image was first smoothed with a mean filter to homogenize the intensity values of the nuclei within an RV. This image was converted into a binary image after applying an intensity threshold. The binary image was used to segment the RVs by applying a watershed algorithm. From this segmentation, a list containing the area of each RV and the number of RVs was obtained. The entire area of the organoid was identified using the same principle but reducing the threshold for the binary conversion. The percentage of area occupied by RVs was calculated by adding the area of all RVs identified divided by the entire area of the organoid. For quantification of LTL$^+$ and PODXL$^+$ structures, the percentage of area occupied by LTL$^+$ and PODXL$^+$ structures was calculated using the same procedure as described above. For quantification of WT1$^+$ cells, the DAPI image was converted into a binary image after applying an intensity threshold. The binary image was used to segment the nuclei by applying a watershed algorithm. All nuclei found were counted. The same procedure was used to identify WT1$^+$ nuclei. The positive nuclei in WT1 images were divided by the number of DAPI nuclei, giving a percentage of WT1$^+$ cells for each condition.

Human kidney material. Primary human proximal tubular cells were obtained from collaborators at Hospital Clinic de Barcelona, Spain. The procedure was approved by the ethics committee of Hospital Clinic de Barcelona (project no. 2009/5023). Primary renal proximal tubular epithelial cells were obtained in the laboratory of origin as previously described[38]. Human fetal kidney samples included in this study were provided by the Fetal Tissue Bank of Vall d'Hebron University Hospital Biobank (PT13/0010/0021), part of the Spanish National Biobanks Network, and they were processed following standard operating procedures with the appropriate approval of the Ethical and Scientific Committees (project no. 0336E/9934/2015). The gestational age of human fetal kidney samples was determined using ultrasound heel-to-toe and crown-to-rump measurements[39]. Human fetal kidney samples from 13, 16 and 22 weeks of gestation were supplied as whole tissues embedded in OCT (at −80 °C) and as frozen tissue samples for RNA extraction.

Statistics and reproducibility. Data are mean ± standard deviation (s.d.). Statistical differences between two groups were tested with a two-tailed Student's t-test or one-way analysis of variance followed by Tukey's post hoc test. Data were statistically significant if $P < 0.05$. Number of replicates ($n = x$), P values and degrees of freedom are included in the figure legends. GraphPad Prism version 6.01 software was used for statistical analysis. A table summarizing sample size, number of experiments and statistical test results (when applicable) for each figure panel is also provided as Supplementary Table 7.

For in vitro experiments, two to six organoids were analysed at the times and conditions indicated in each experiment. For ex vivo reaggregation assay, we used one to three pregnant mice (to collect embryonic kidneys from mouse embryos) per experiment. Two or three reaggregates were analysed per experiment. For implantation of organoids into chick CAM in ovo, about 6–22 chicken eggs were used per experiment and about 2–10 implanted kidney organoids were analysed per experiment.

RNA-Seq of kidney organoids during the time course differentiation was performed on six pooled kidney organoids at each time analysed from two independent experiments (Fig. 1c and Supplementary Fig. 9).

For main figures where representative immunofluorescence images are shown, at least $n = 2$ biologically independent kidney organoids were analysed from independent experiments showing similar results (Fig. 1b, $n = 2$ organoids; Fig. 2g, $n = 3$ organoids per treatment; Fig. 2m, $n = 4$ organoids per culture condition; Fig. 3l,m, $n = 2$ implanted organoids; Fig. 3n, $n = 3$ implanted organoids; Fig. 4a, $n = 2$ organoids per stiffness condition; Fig. 4c, $n = 3$ organoids per stiffness condition).

For main figures where representative TEM images are shown, $n = 2$ biologically independent kidney organoids were analysed from independent experiments showing similar results (Fig. 1e–j, Fig. 3e–k, Fig. 4f–i and Fig. 4k–n).

Macroscopic images of kidney organoids after implantation into chick CAM are representative of three independent CAM implantation experiments (Fig. 3b, $n = 6$ implanted organoids; Fig. 3c, $n = 10$ implanted organoids; Fig. 3d, $n = 3$ implanted organoids after dextran–FITC injection).

For supplementary figures, complete information on the number of independent experiments and samples analysed is provided in the corresponding figure legends.

Reporting Summary. Further information on research design is available in the Nature Research Reporting Summary linked to this article.

Code availability
MATLAB codes can be requested from the corresponding author.

Data availability
RNA-Seq data are publicly available in Gene Expression Omnibus (GEO, http://www.ncbi.nlm.nih.gov/geo) under the accession numbers GSE108349, GSE108350 and GSE108351. All remaining datasets supporting the findings described here are

available within the article and its supplementary information files. Additionally, data are available from the corresponding author upon reasonable request.

References

29. Andrews, S. FastQC: a quality control tool for high throughput sequence data. http://www.bioinformatics.babraham.ac.uk/projects/fastqc (2010).
30. Jiang, H., & Lei, R. & Ding, S. W. & Zhu, S. Skewer: A fast and accurate adapter trimmer for next-generation sequencing paired-end reads. *BMC Bioinform.* **15**, 182 (2014).
31. Dobin, A. et al. STAR: ultrafast universal RNA-seq aligner. *Bioinformatics* **29**, 15–21 (2013).
32. Love, M. I., Huber, W. & Anders, S. Moderated estimation of fold change and dispersion for RNA-seq data with DESeq2. *Genome Biol.* **15**, 550 (2014).
33. Leek, J. T. Svaseq: removing batch effects and other unwanted noise from sequencing data. *Nucl. Acids Res.* **42**, e161 (2014).
34. Kue, C. S., Tan, K. Y., Lam, M. L. & Lee, H. B. Chick embryo chorioallantoic membrane (CAM): an alternative predictive model in acute toxicological studies for anti-cancer drugs. *Exp. Anim.* **64**, 129–138 (2015).
35. Lee, D., Rahman, M. M., Zhou, Y. & Ryu, S. Three-dimensional confocal microscopy indentation method for hydrogel elasticity measurement. *Langmuir* **31**, 9684–9693 (2015).
36. Yeung, T. et al. Effects of substrate stiffness on cell morphology, cytoskeletal structure, and adhesion. *Cell Motil. Cytoskelet.* **60**, 24–34 (2005).
37. Przybyla, L., Lakins, J. N., Sunyer, R., Trepat, X. & Weaver, V. M. Monitoring developmental force distributions in reconstituted embryonic epithelia. *Methods* **94**, 101–113 (2016).
38. Montserrat, N. et al. Generation of induced pluripotent stem cells from human renal proximal tubular cells with only two transcription factors, OCT4 and SOX2. *J. Biol. Chem.* **287**, 24131–24138 (2012).
39. O'Rahilly, R. & Müller, F. Developmental stages in human embryos: revised and new measurements. *Cells Tissues Organs* **192**, 73–84 (2010).

nature research

Corresponding author(s):   Núria Montserrat

Reporting Summary

Nature Research wishes to improve the reproducibility of the work that we publish. This form provides structure for consistency and transparency in reporting. For further information on Nature Research policies, see Authors & Referees and the Editorial Policy Checklist.

Statistical parameters

When statistical analyses are reported, confirm that the following items are present in the relevant location (e.g. figure legend, table legend, main text, or Methods section).

n/a	Confirmed	
☐	☒	The exact sample size (*n*) for each experimental group/condition, given as a discrete number and unit of measurement
☐	☒	An indication of whether measurements were taken from distinct samples or whether the same sample was measured repeatedly
☐	☒	The statistical test(s) used AND whether they are one- or two-sided *Only common tests should be described solely by name; describe more complex techniques in the Methods section.*
☐	☒	A description of all covariates tested
☐	☒	A description of any assumptions or corrections, such as tests of normality and adjustment for multiple comparisons
☐	☒	A full description of the statistics including central tendency (e.g. means) or other basic estimates (e.g. regression coefficient) AND variation (e.g. standard deviation) or associated estimates of uncertainty (e.g. confidence intervals)
☐	☒	For null hypothesis testing, the test statistic (e.g. *F*, *t*, *r*) with confidence intervals, effect sizes, degrees of freedom and *P* value noted *Give P values as exact values whenever suitable.*
☒	☐	For Bayesian analysis, information on the choice of priors and Markov chain Monte Carlo settings
☒	☐	For hierarchical and complex designs, identification of the appropriate level for tests and full reporting of outcomes
☒	☐	Estimates of effect sizes (e.g. Cohen's *d*, Pearson's *r*), indicating how they were calculated
☐	☒	Clearly defined error bars *State explicitly what error bars represent (e.g. SD, SE, CI)*

Our web collection on statistics for biologists may be useful.

Software and code

Policy information about availability of computer code

Data collection	SA3800 version 2.0.4 (SONY) was used for flow citometry. FACSDiva version 8.0.1 (BD Biosciencies) was used for fluorescence-activated cell sorting. Zeiss ZEN 2012 SP5 FP1 version 14.0.11.201 and Leica LAS AF vesion 2.6.3.8173 were used for confocal microscopy. Cell^D version 3.2 and LAS EZ version 3.4.0 were used for optical microscopy. QuantStudio Real time PCR software was used for qPCR data collection.
Data analysis	FlowJo version 10 was used for flow cytometry data analysis. ImageJ version 2006.02.01 was used for image processing. MATLAB version 9.1.0.441655 (R2016b) was used. Matlab analysis procedures that were employed to calculate the young modulus of the CAM and to quantify immunofluorescence images can be made available upon request to the corresponding author. A description of the procedures is available in Methods section of the manuscript. Microsoft excel was used for qPCR and RNA-seq data analysis. Graphpad Prism version 6.01 was used for graphing and statistical analysis. FastQC version 0.11.5, Skewer version 0.2.2, STAR mapper version 2.5.3a and R statistical package DESeq2 were used for RNA-seq data analysis.

For manuscripts utilizing custom algorithms or software that are central to the research but not yet described in published literature, software must be made available to editors/reviewers upon request. We strongly encourage code deposition in a community repository (e.g. GitHub). See the Nature Research guidelines for submitting code & software for further information.

Data

All manuscripts must include a data availability statement. This statement should provide the following information, where applicable:

- Accession codes, unique identifiers, or web links for publicly available datasets
- A list of figures that have associated raw data
- A description of any restrictions on data availability

RNA-seq data are publicly available in Gene Expression Omnibus (GEO, http://www.ncbi.nlm.nih.gov/geo) under the accession numbers GSE108349, GSE108350 and GSE108351. All remaining datasets that support the findings of this study are available within the article and its supplementary information files, and from the corresponding author upon reasonable request.

Field-specific reporting

Please select the best fit for your research. If you are not sure, read the appropriate sections before making your selection.

☒ Life sciences   ☐ Behavioural & social sciences   ☐ Ecological, evolutionary & environmental sciences

For a reference copy of the document with all sections, see nature.com/authors/policies/ReportingSummary-flat.pdf

Life sciences study design

All studies must disclose on these points even when the disclosure is negative.

Sample size	No statistical methods were used to determine sample size. A minimum of two independent experiments were carried out. For in vitro experiments, 2-6 organoids were analyzed at the time points and conditions indicated in the manuscript for each experiment. Sample size was determined based on previous studies in the field. For ex vivo reaggregation assay, we used 1-3 pregnant mice (to collect embryonic kidneys from mice embryos) per experiment. A number of 2-3 reaggregates were analyzed per experiment. Sample size was determined based on previous studies in the field. For in vivo implantation of organoids, a number of about 6-22 chicken eggs were used per experiment. A number of 2-10 implanted kidney organoids were analyzed per experiment from a total of six experiments. Sample size was determined based on previous studies using tumoral cell lines in the chick CAM. model. All sample sizes, statistical tests and P values are indicated in the figure legends or described in the "Statistics and reproducibility" section of the manuscript.
Data exclusions	No data were excluded from the analyses.
Replication	All experimental findings were reproduced independently at least two times. All attempts at replication were successful. To ensure the reproducibility of our methodology for generating kidney organoids, we used three different human embryonic stem cell (hESC) lines and one human induced pluripotent stem cell line. The number of times that each experiment was repeated is indicated in the figure legends or described in the "Statistics and reproducibility" section of the manuscript.
Randomization	Cells/organoids were chosen at random for measurements within each condition.
Blinding	Blinding was not used during data collection and analysis in experiments that did not involve direct comparisons between groups. Blinding was used for quantitative measurements comparing different conditions in which data analysis was carried out using a custom made code (Fig. 2g,h; Fig. 2m,n; Fig. 4a,b; Fig.4c,d).

Reporting for specific materials, systems and methods

Materials & experimental systems

n/a	Involved in the study
☒	☐ Unique biological materials
☐	☒ Antibodies
☐	☒ Eukaryotic cell lines
☒	☐ Palaeontology
☐	☒ Animals and other organisms
☒	☐ Human research participants

Methods

n/a	Involved in the study
☒	☐ ChIP-seq
☐	☒ Flow cytometry
☒	☐ MRI-based neuroimaging

Antibodies

Antibodies used	Antibodies and other staining reagents used for immunocytochemistry/immunohistochemistry: OCT4 (Santa Cruz, Cat# sc-5279, clone C-10, Lot# L2216, Dilution 1:25); Nanog (R&D Systems, Cat# A F1997, polyclonal, Lot# KKJ0616121, Dilution 1:25); YAP (Santa Cruz, Cat# sc-101199, clone 63.7, Lot# I0315, Dilution 1:200); Brachyury (R&D Systems, Cat# AF2085, polyclonal, Lot# KQP031611, Dilution 1:100); PAX2 (R&D Systems, Cat# AF3364, polyclonal, Lot# XOT0215072, Dilution 1:20); SALL1 (R&D Systems, Cat# PP-K9814-00, clone K9814, Lot# A-3, Dilution 1:100); WT1 (Abcam, Cat# ab89901, clone CAN-R9(IHC)-56-2, Lot# GR177328-54, Dilution 1:100); OSR1 (Abnova, Cat# H00130497-M04, clone 3F3, Lot# DB041-3F3, Dilution 1:25); LHX1 (Developmental Studies Hybridoma Bank, Cat# 4F2-s, clone 4F2, Dilution 1:50); SIX2 (Proteintech, Cat# 11562-1-AP, polyclonal, Dilution 1:500); PAX8 (Proteintech, Cat# 10336-1-AP, polyclonal, Dilution 1:500); ECAD (BD Bioscience, Cat# 610181, clone 36/E-cadherine, Lot# 7187865, Dilution 1:50); PODXL (R&D Systems, Cat# BAF1658, polyclonal, Lot# JLV0112111, Dilution 1:25); HNF1β (Santa Cruz, Cat# sc-7411, clone C-20, Lot# B0116, Dilution 1:100); BRN1 (Santa Cruz, Cat# sc-6028-R, clone C-17, Lot# J2512, Dilution 1:200); NEPHRIN (R&D Systems, Cat# AF4269, polyclonal, Lot# ZMU0114031, Dilution 1:300); KIM1 (R&D Systems, Cat# AF1750, polyclonal, Lot# JTB0317031, Dilution 1:300); cleaved Caspase-3 (Cell Signalling, Cat# 9661S, clone D175, Lot# 45, Dilution 1:200); CD34 (Abcam, Cat# ab8536, cloneQBEND-10, Lot# GR49632-21, Dilution 1:200); CD31 (Abcam, Cat# ab28364, polyclonal, Lot# GR31176844-16, Dilution 1:50); HuNu (Abcam, Cat# ab191181, clone 235-1, Lot# GR3185051-2, Dilution 1:100); Uromodulin (UMOD) (R&D Systems, Cat# AF5144, polyclonal, Lot# CBRF0114081, Dilution 1:50); Aquaporin 1 (AQP1) (Santa Cruz, Cat# sc-20810, clone H-55, Lot# C1815, Dilution 1:50); SLC3A1 (Sigma, Cat# HPA038360, polyclonal, Lot# R35388, Dilution 1:100); Laminin (Sigma, Cat# L9393, polyclonal, Lot# 028M4890V, Dilution 1:50); PODOCIN (Sigma, Cat# P0372, polyclonal, Lot# 064M4780, Dilution 1:50); NEPH1 (Santa Cruz, Cat# sc-373787, clone F-6, Lot# A0313, Dilution 1:50); SGLT2 (Abcam, Cat# ab37296, polyclonal, Lot# GR320725-7, Dilution 1:100); Sodium potassium ATPase (NaK) (Abcam, Cat# ab209299, clone ED1845Y, Lot# GRZ64184-1, Dilution 1:200); Biotinylated Lotus Tetragonolobus Lectin (LTL) (Vector Laboratories, Cat# B-1325, Lot# ZC2428, Dilution 1:200); Biotinylated Lens Culinaris Agglutinin (LCA) (Vector Laboratories, Cat# B-1045, Lot# ZC1221, Dilution 1:500); Alexa Fluor 488-conjugated streptavidin (Vector Laboratories, Cat# SA5488, Lot# ZD0313, Dilution: 1:50); Antibodies and other staining reagents used for flow cytometry: Fluorescein labeled LTL (Vector Laboratories, Cat# FL-1321, Lot# ZC0914, Dilution: 1:500); OCT4 conjugated to Alexa Fluor-488 (BD Pharmigen, Cat# 560253, Lot# 7110598, Dilution: 20 μl/test); Alexa Fluor 488 Mouse IgG1k isotype control (BD Pharmigen, Cat# 557721, Lot# 7082749, Dilution: 5 μl/test); Brachyury conjugated to allophycocyanin (APC) (R&D Systems, Cat# IC2085A, Lot# ADUQ0216041, Dilution: 10 μl/test); Goat IgG APC-conjugated antibody (R&D Systems, Cat# IC108A, Lot# AAOE0516031, Dilution: 10 μl/test); PAX2 conjugated to A488 using the Lightning-Link® Rapid conjugation kit (322-0010, Innova Biosciences) (R&D Systems, Cat# AF3364, Lot# XOT0215072, Dilution: 1:200); Normal Goat IgG Alexa Fluor® 488-conjugated Control (R&D Systems, Cat# IC108G, Lot# ABWO41607, Dilution: 5 μl/test); LIVE/DEAD Fixable Violet stain reagent (Life Technologies, Cat# L23105, Dilution: 1:1000) Information of all antibodies / staining reagents is provided in the Methods section or Supplementary information of the manuscript.
Validation	Antibody validations for the species and assay used were performed by antibody suppliers as described in the manufacture's web page, or were published in previous studies. Relevant articles are: Xia Y, Nivet E, Sancho-Martinez I, Gallegos T, Suzuki K, Okamura D, Wu MZ, Dubova I, Esteban CR, Montserrat N, Campistol JM, Izpisua Belmonte JC. Directed differentiation of human pluripotent cells to ureteric bud kidney progenitor-like cells. Nat Cell Biol. 2013 Dec;15(12):1507-15. doi: 10.1038/ncb2872. Epub 2013 Nov 17. PubMed PMID: 24240476. (OCT4, OSR1, SIX2: human, immunofluorescence). Martí M, Mulero L, Pardo C, Morera C, Carrió M, Laricchia-Robbio L, Esteban CR, Izpisua Belmonte JC. Characterization of pluripotent stem cells. Nat Protoc. 2013 Feb;8(2):223-53. doi: 10.1038/nprot.2012.154. Epub 2013 Jan 10. PubMed PMID: 23306458. (OCT4, Nanog, Brachyury: human, immunofluorescence). Elosegui-Artola A, Andreu I, Beedle AEM, Lezamiz A, Uroz M, Kosmalska AJ, Oria R, Kechagia JZ, Rico-Lastres P, Le Roux AL, Shanahan CM, Trepat X, Navajas D, Garcia-Manyes S, Roca-Cusachs P. Force Triggers YAP Nuclear Entry by Regulating Transport across Nuclear Pores. Cell. 2017 Nov 30;171(6):1397-1410.e14. doi: 10.1016/j.cell.2017.10.008. Epub 2017 Oct 26. PubMed PMID: 29107331. (YAP: human, immunofluorescence) Morizane R, Lam AQ, Freedman BS, Kishi S, Valerius MT, Bonventre JV. Nephron organoids derived from human pluripotent stem cells model kidney development and injury. Nat Biotechnol. 2015 Nov;33(11):1193-200. PubMed PMID: 26458176; PubMed Central PMCID: PMC4747858. (SALL1, LHX1, SIX2, PAX8, PODXL, HNF1β, BRN1, KIM1, LTL: human, immunofluorescence) Takasato M, Er PX, Chiu HS, Maier B, Baillie GJ, Ferguson C, Parton RG, Wolvetang EJ, Roost MS, Chuva de Sousa Lopes SM, Little MH. Kidney organoids from human iPS cells contain multiple lineages and model human nephrogenesis. Nature. 2015 Oct

22;526(7574):564-8. doi: 10.1038/nature15695. Epub 2015 Oct 7. Erratum in: Nature. 2016 Aug 11;536(7615):238. PubMed PMID: 26444236. (SIX2, ECAD, NEPHRIN, Caspase-3, LTL: human, immunofluorescence).

Sharmin S, Taguchi A, Kaku Y, Yoshimura Y, Ohmori T, Sakuma T, Mukoyama M, Yamamoto T, Kurihara H, Nishinakamura R. Human Induced Pluripotent Stem Cell-Derived Podocytes Mature into Vascularized Glomeruli upon Experimental Transplantation. J Am Soc Nephrol. 2016 Jun;27(6):1778-91. doi: 10.1681/ASN.2015010096. Epub 2015 Nov 19. PubMed PMID: 26586691; PubMed Central PMCID: PMC4884101. (CD31: human, immunofluorescence).

Cai G, Lai B, Hong H, Lin P, Chen W, Zhu Z, Chen H. Effects of cryopreservation on excretory function, cellular adhesion molecules and vessel lumen formation in human umbilical vein endothelial cells. Mol Med Rep. 2017 Jul;16(1):547-552. doi: 10.3892/mmr.2017.6664. Epub 2017 May 31. PubMed PMID:28586042; PubMed Central PMCID: PMC5482135. (CD34: human, immunofluorescence).

Lei P, Ding D, Xie J, Wang L, Liao Q, Hu Y. Expression profile of Twist, vascular endothelial growth factor and CD34 in patients with different phases of osteosarcoma. Oncol Lett. 2015 Jul;10(1):417-421. Epub 2015 May 20. PubMed PMID: 26171042; PubMed Central PMCID: PMC4487166. (CD34: human, immunofluorescence).

Cruz NM, Song X, Czerniecki SM, Gulieva RE, Churchill AJ, Kim YK, Winston K, Tran LM, Diaz MA, Fu H, Finn LS, Pei Y, Himmelfarb J, Freedman BS. Organoid cystogenesis reveals a critical role of microenvironment in human polycystic kidney disease. Nat Mater. 2017 Nov;16(11):1112-1119. doi: 10.1038/nmat4994. Epub 2017 Oct 2. PubMed PMID: 28967916; PubMed Central PMCID: PMC5936694. (NEPHRIN, PODXL, LTL, Fluorescein labeled LTL: human, immunofluorescence).

Lindström NO, Tran T, Guo J, Rutledge E, Parvez RK, Thornton ME, Grubbs B, McMahon JA, McMahon AP. Conserved and Divergent Molecular and Anatomic Features of Human and Mouse Nephron Patterning. J Am Soc Nephrol. 2018 Mar;29(3):825-840. doi: 10.1681/ASN.2017091036. Epub 2018 Feb 15. PubMed PMID: 29449451; PubMed Central PMCID: PMC5827611. (Pax2, WT1, SLC3A1, Uromodulin: human, immunofluorescence).

Vedula EM, Alonso JL, Arnaout MA, Charest JL. A microfluidic renal proximal tubule with active reabsorptive function. PLoS One. 2017 Oct 11;12(10): e0184330. doi: 10.1371/journal.pone.0184330. eCollection 2017. PubMed PMID: 29020011; PubMed Central PMCID: PMC5636065. (SGLT2: human, immunofluorescence).

Kang KJ, Lee MS, Moon CW, Lee JH, Yang HS, Jang YJ. In Vitro and In Vivo Dentinogenic Efficacy of Human Dental Pulp-Derived Cells Induced by Demineralized Dentin Matrix and HA-TCP. Stem Cells Int. 2017; 2017:2416254. doi:10.1155/2017/2416254. Epub 2017 Jun 28. PubMed PMID: 28761445; PubMed Central PMCID: PMC5518496. (HuNu: human, immunofluorescence).

Jilani SM, Murphy TJ, Thai SN, Eichmann A, Alva JA, Iruela-Arispe ML. Selective binding of lectins to embryonic chicken vasculature. J Histochem Cytochem. 2003 May;51(5):597-604. PubMed PMID: 12704207. (Biotinylated Lens Culinaris Agglutinin: chicken, immunofluorescence).

Yamaguchi S, Morizane R, Homma K, Monkawa T, Suzuki S, Fujii S, Koda M, Hiratsuka K, Yamashita M, Yoshida T, Wakino S, Hayashi K, Sasaki J, Hori S, Itoh H. Generation of kidney tubular organoids from human pluripotent stem cells. Sci Rep. 2016 Dec 16;6: 38353. doi: 10.1038/srep38353.PubMed PMID: 27982115; PubMed Central PMCID: PMC5159864. (Aquaporin 1: human, immunofluorescence).

Fagerberg L, Hallström BM, Oksvold P, Kampf C, Djureinovic D, Odeberg J, Habuka M, Tahmasebpoor S, Danielsson A, Edlund K, Asplund A, Sjöstedt E, Lundberg E, Szigyarto CA, Skogs M, Takanen JO, Berling H, Tegel H, Mulder J, Nilsson P, Schwenk JM, Lindskog C, Danielsson F, Mardinoglu A, Sivertsson A, von Feilitzen K, Forsberg M, Zwahlen M, Olsson I, Navani S, Huss M, Nielsen J, Ponten F, Uhlén M. Analysis of the human tissue-specific expression by genome-wide integration of transcriptomics and antibody-based proteomics. Mol Cell Proteomics. 2014 Feb;13(2):397-406. doi: 10.1074/mcp.M113.035600. Epub 2013 Dec 5. PubMed PMID: 24309898; PubMed Central PMCID: PMC3916642. (PODOCIN: human, immunofluorescence).

Wong KG, Ryan SD, Ramnarine K, Rosen SA, Mann SE, Kulick A, De Stanchina E,Müller FJ, Kacmarczyk TJ, Zhang C, Betel D, Tomishima MJ. CryoPause: A New Method to Immediately Initiate Experiments after Cryopreservation of Pluripotent Stem Cells. Stem Cell Reports. 2017 Jul 11;9(1):355-365. doi: 10.1016/j.stemcr.2017.05.010. Epub 2017 Jun 8. PubMed PMID: 28602613; PubMed Central PMCID: PMC5511100. (Brachyury conjugated to allophycocyanin (APC): human, flow cytometry).

Eukaryotic cell lines

Policy information about cell lines

Cell line source(s)	Human pluripotent stem cell lines:
	All the human pluripotent stem cell lines used in this study were obtained after the approval of the Ethics Committee of the CMRB and the approval of the Comisión de Seguimiento y Control de la Donación de Células y Tejidos Humanos del Instituto de Salud Carlos III (project numbers: 0336E/7564/2016; 0336E/5311/2015; 0336E/15986/2016; 0336E/79489/2015; 00336E/20031/2014). ES[4] hESC and CBiPSsv-4F-40 were obtained from The National Bank of Stem Cells (ISCIII, Madrid). H1 and H9 hESC lines were purchased at Wicell.
	Information on cell line sources used in this study is also provided in the Methods section of the manuscript.
	Human kidney material:
	Primary human proximal tubular cells were obtained from collaborators at Hospital Clinic de Barcelona, Spain. The ethics committee of Hospital Clinic de Barcelona approved the procedure, and signed consent forms are available upon request (project number: 2009/5023). Isolation of primary renal proximal tubular epithelial cells was performed as previously described. Briefly, tubular cells were prepared from renal tissue after nephrectomy. Cortical renal tissue was digested in

Iscove's modified Dulbecco's medium with 1% collagenase IV (Invitrogen) for 1h under shaking. Cell suspension was placed on a pre-cooled Percoll density gradient solution (Amersham Biosciences) and centrifuged for 40 min at 4 °C at 16,000 rpm (gradient with densities between 1.019 and 1.139 g/ml was generated). The cell fraction between 1.05 and 1.076 g/ml was collected and cells were plated on plastic plates with DMEM (Invitrogen) supplemented with 10% fetal bovine serum (FBS; Invitrogen), Glutamax (1 mM), penicillin/streptomycin, and nonessential amino acids (100 µM).
Relevant reference:
Montserrat N, Ramírez-Bajo MJ, Xia Y, Sancho-Martinez I, Moya-Rull D, Miquel-Serra L, Yang S, Nivet E, Cortina C, González F, Izpisua Belmonte JC, Campistol JM. Generation of induced pluripotent stem cells from human renal proximal tubular cells with only two transcription factors, OCT4 and SOX2. J Biol Chem. 2012 Jul 13;287(29):24131-8.

Human fetal kidney samples included in this study were provided by the Fetal Tissue Bank of Vall d'Hebron University Hospital Biobank (PT13/0010/0021), integrated in the Spanish National Biobanks Network and they were processed following standard operating procedures with the appropriate approval of the Ethical and Scientific Committees (project number: 0336E/9934/2015). Human fetal kidney samples from 13, 16 and 22 weeks of gestation were supplied as whole tissues embedded in OCT (at -80 ºC) and as frozen tissue samples for RNA extraction.

Information on human kidney material used in this study is also provided in the Methods section of the manuscript.

Authentication	Human pluripotent stem cell lines: Human embryonic stem cells (ES4, H1 and H9 lines) and human induced pluripotent stem cells (CBiPSsv-4F-40 line) were authenticated in their lab of origin through the expression of pluripotency-associated markers. Human kidney material: Primary human proximal epithelial cells were authenticated in the lab of origin for the expression of specific proximal tubular cell markers, as previously reported. Relevant reference: Montserrat N, Ramírez-Bajo MJ, Xia Y, Sancho-Martinez I, Moya-Rull D, Miquel-Serra L, Yang S, Nivet E, Cortina C, González F, Izpisua Belmonte JC, Campistol JM. Generation of induced pluripotent stem cells from human renal proximal tubular cells with only two transcription factors, OCT4 and SOX2. J Biol Chem. 2012 Jul 13;287(29):24131-8. The gestational age of human fetal kidney samples was determined per guidelines specified by the American College of Obstetricians and Gynecologists using ultrasound heel-to-toe, and crown-to-rump measurements. Relevant reference: O'Rahilly R, Müller F: Developmental stages in human embryos: Revised and new measurements. Cells Tissues Organs 192: 73–84, 2010.
Mycoplasma contamination	All cell lines tested negative for mycoplasma contamination.
Commonly misidentified lines (See ICLAC register)	No commonly misidentified cell lines were used.

Animals and other organisms

Policy information about studies involving animals; ARRIVE guidelines recommended for reporting animal research

Laboratory animals	For mice experiments: Animal care and experiments were carried out according to protocols approved by the Ethics Committee on Animal Research of the University of Barcelona, Spain (protocol number: OB 391/18). Embryonic kidneys from 11.5-12.5 days post conception (d.p.c) were collected from time-mated pregnant C57BL/6J mice. For chicken experiments: According to animal care guidelines in Spain, no approval was necessary to perform the experiments described herein. Fertilized white Leghorn chicken eggs were provided by Granja Gibert, rambla Regueral, S/N, 43850 Cambrils, Spain.
Wild animals	The study does not involve wild animals.
Field-collected samples	The study does not involve samples collected from the field.

Flow Cytometry

Plots

Confirm that:

☒ The axis labels state the marker and fluorochrome used (e.g. CD4-FITC).

☒ The axis scales are clearly visible. Include numbers along axes only for bottom left plot of group (a 'group' is an analysis of identical markers).

☒ All plots are contour plots with outliers or pseudocolor plots.

☒ A numerical value for number of cells or percentage (with statistics) is provided.

Methodology

Sample preparation	Cells were dissociated using accumax (07921, Stem Cell Technologies) for 5 min at 37ºC and stained according to a standard

Sample preparation	methodology described in the Methods section of the manuscript. Kidney organoids were stained according to a standard methodology described in the Methods section of the manuscript. Kidney organoids were then dissociated to single cells using accumax (07921, Stem Cell Technologies) for 15 min followed by 0.25% (wt/vol) trypsin (25300-054, Life Technologies) for 15 min at 37ºC.
Instrument	Sony SA3800 spectral cell analyzer (SONY) was used to acquire flow cytometry samples (Supplementary Fig.1b and Supplementary Fig.2b), whereas FACSAria Fusion instrument (BD Biosciences) was used for cell sorting experiments (Supplementary Fig. 5b).
Software	SA3800 software version 2.0.4 (SONY) was used to acquire flow cytometry samples in the Sony SA3800 spectral cell analyzer (SONY), whereas FACSDiva software version 8.0.1 (BD Biosciencies) was used in the FACS Aria Fusion instrument (BD Biosciences) for cell sorting experiments. FlowJo software version 10 was used to analyze these data.
Cell population abundance	The abundance of the relevant cell populations was based on the expression of specific nuclear and surface markers that were analyzed by immunofluorescence and quantitative RT-PCR.
Gating strategy	Supplementary Fig. 1b: For assessment of OCT4 and T staining, cells were first gated on a SS-A versus FS-A plot, the polulation from which was then gated on the LIVE/DEAD negative population (LIVE/DEAD versus FS-A plot), the population from which was then analyzed on a plot of T-APC versus OCT4-A488. Supplementary Fig. 2b: For assessment of PAX2 staining, cells were first gated on a SSC-A versus FSC-A plot, the polulation from which was then gated on the LIVE/DEAD negative population (LIVE/DEAD versus FSC-A plot), the population from which was then analyzed on a plot of SSC-A versus PAX2-A488. Supplementary Fig. 5b: For fluorescence activated cell sorting of LTL-FITC positive and negative cell fractions, cells were first gated on a SSC-A versus FSC-A plot, the polulation from which was then gated on singlets (FSC-W versus FSC-A plot), the population from which was then gated on the LIVE/DEAD negative population (LIVE/DEAD versus FSC-A plot), the population from which was then analyzed on a plot of autofluorescence (AU) versus LTL-FITC.

☒ Tick this box to confirm that a figure exemplifying the gating strategy is provided in the Supplementary Information.

In the format provided by the authors and unedited.

Fine tuning the extracellular environment accelerates the derivation of kidney organoids from human pluripotent stem cells

Elena Garreta[1,11], Patricia Prado[1,11], Carolina Tarantino[1], Roger Oria [2,3], Lucia Fanlo[4], Elisa Martí[4], Dobryna Zalvidea[2], Xavier Trepat[2,3,5,6], Pere Roca-Cusachs[2,3], Aleix Gavaldà-Navarro[7], Luca Cozzuto[8], Josep M. Campistol[9], Juan Carlos Izpisúa Belmonte[10], Carmen Hurtado del Pozo[1] and Nuria Montserrat [1,5,6]*

[1]Pluripotency for Organ Regeneration, Institute for Bioengineering of Catalonia (IBEC), The Barcelona Institute of Technology (BIST), Barcelona, Spain. [2]Institute for Bioengineering of Catalonia (IBEC), The Barcelona Institute of Technology (BIST), Barcelona, Spain. [3]University of Barcelona, Barcelona, Spain. [4]Instituto de Biología Molecular de Barcelona (IBMB-CSIC), Parc Científic de Barcelona, Barcelona, Spain. [5]Centro de Investigación Biomédica en Red en Bioingeniería, Biomateriales y Nanomedicina, Madrid, Spain. [6]Catalan Institution for Research and Advanced Studies (ICREA), Barcelona, Spain. [7]Departament de Bioquímica i Biomedicina Molecular, Institut de Biomedicina (IBUB), Universitat de Barcelona and CIBER Fisiopatología de la Obesidad y Nutrición, Barcelona, Spain. [8]Centre for Genomic Regulation (CRG), The Barcelona Institute of Science and Technology, Barcelona, Spain. [9]Hospital Clinic, University of Barcelona, IDIBAPS, Barcelona, Spain. [10]Gene Expression Laboratory, Salk Institute for Biological Studies, La Jolla, CA, USA. [11]These authors contributed equally: Elena Garreta, Patricia Prado. *e-mail: nmontserrat@ibecbarcelona.eu

Supplementary information

This document contains:

- Supplementary Figures 1 to 17

- Legends for Supplementary Tables 1 to 5, and supplementary Table 7 (provided as separate excel files)

- Supplementary Table 6

- Legends for Supplementary Videos 1 to 3

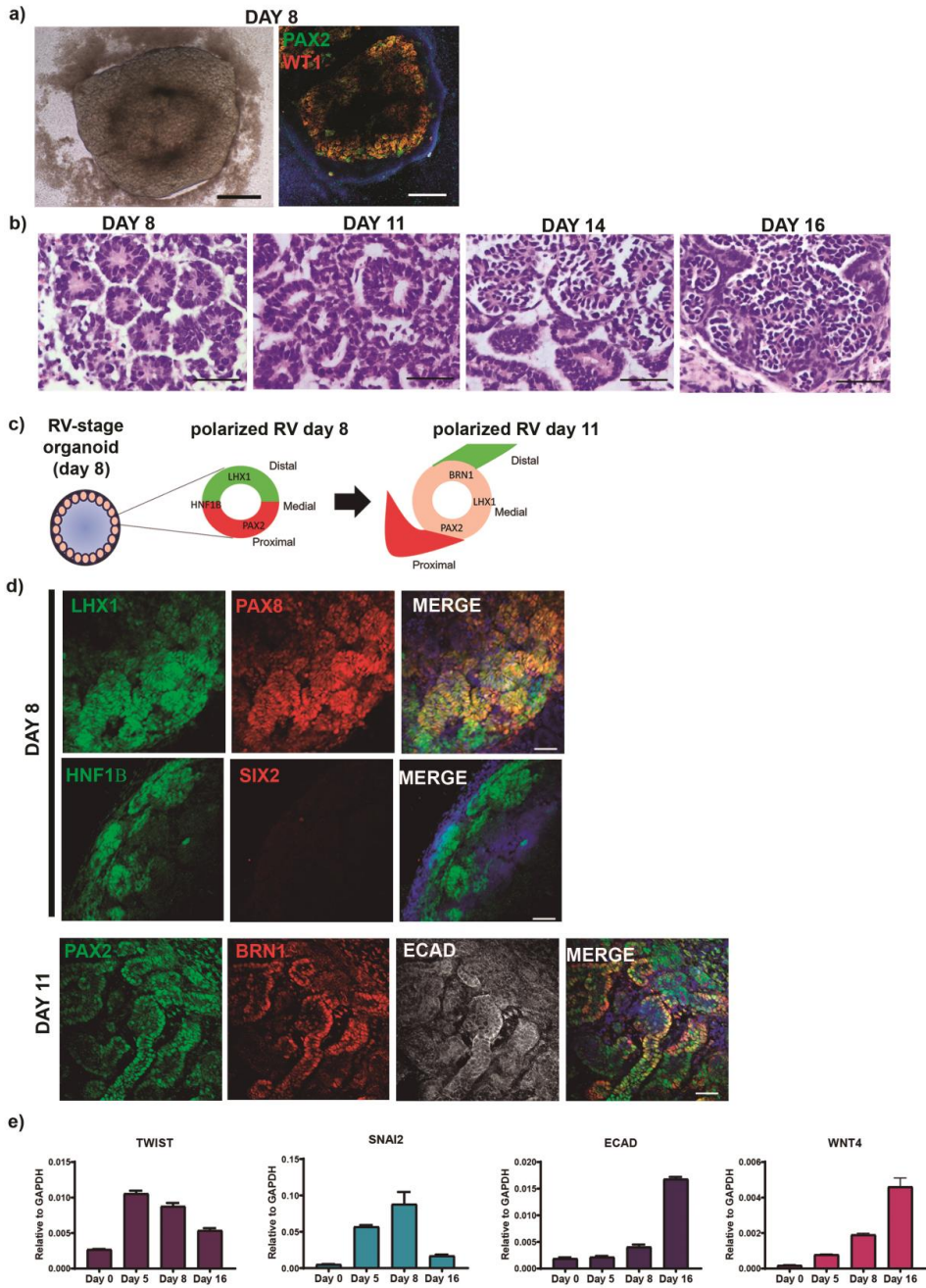# Supplementary Figure 1

a)

b)

c)

d)
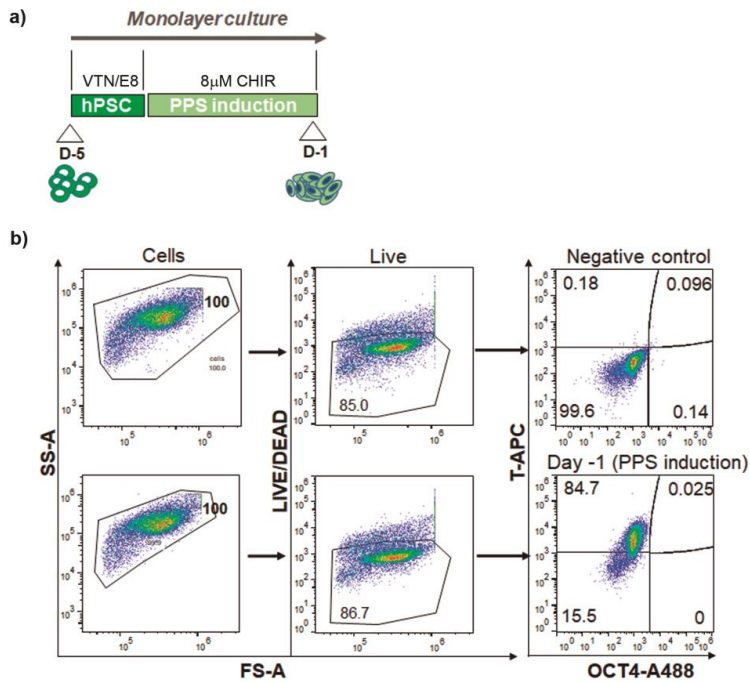
Supplementary Fig. 1 | Induction of PPS-committed cells from hPSC. a, Schematic of the timeline for the directed differentiation of hPSCs (*day -5*) into PPS-committed cells by 3-day exposure to 8 µM CHIR in 2D monolayer culture (*day -1*). **b,** Flow cytometry analysis for the intracellular staining of brachyury (referred as T) and OCT4 in PPS-committed cells (*day -1*). Numbers in quadrants indicate percent cells in each. Data are representative of three independent experiments. The mean percentage of T^+ $OCT4^-$ cells is 82.2 ± 2.6 % (mean ± SD, n = 3). **c,** Immunocytochemistry for T and OCT4 expression after PPS induction (*day -1*). Scale bars, 25 µm. Images are representative of four independent experiments. **d,** qPCR analysis for APS and PPS markers after PPS induction (*day -1*). Genes are indicated. Data are mean ± SD (technical replicates). The experiment was repeated independently two times with similar results.
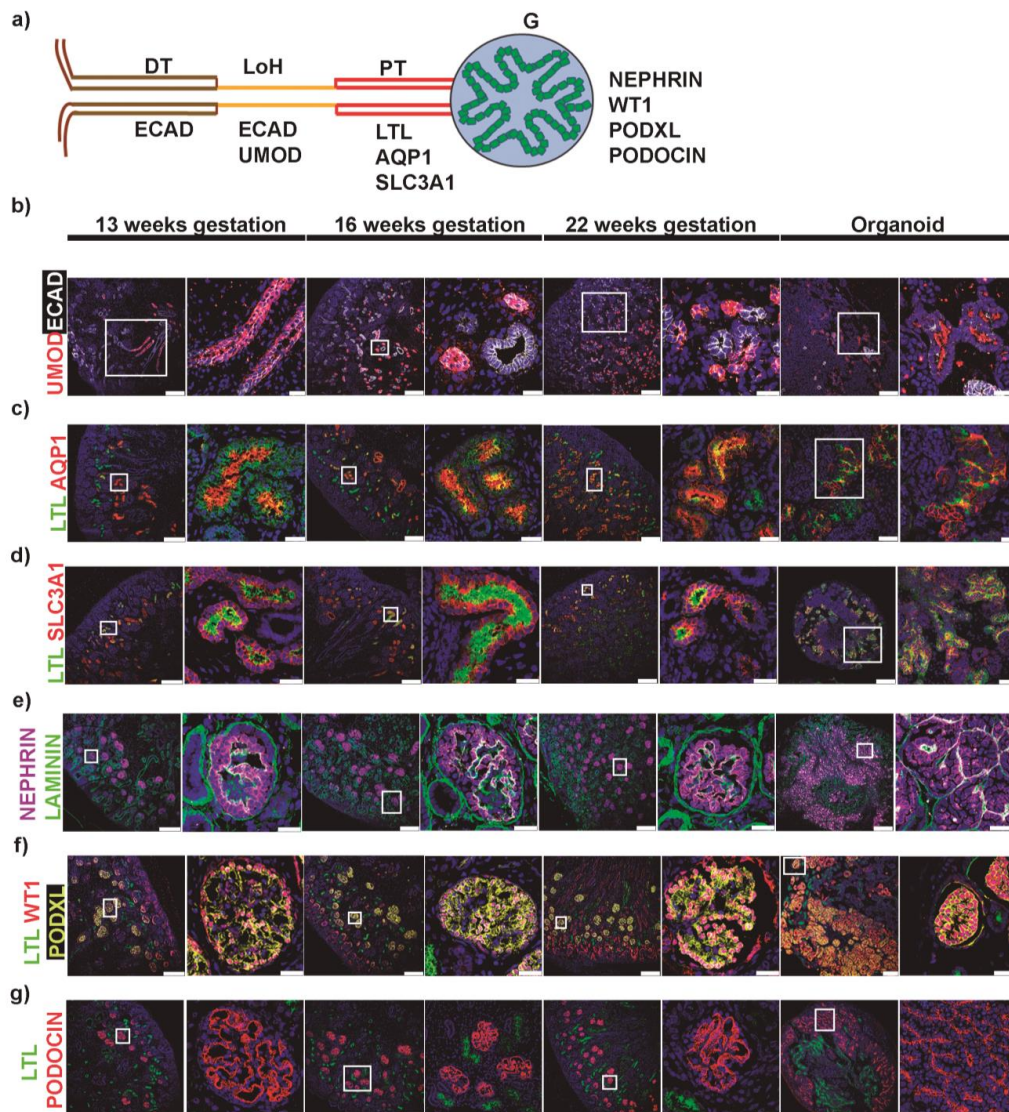
Supplementary Figure 2

a)

b)

c)

d)
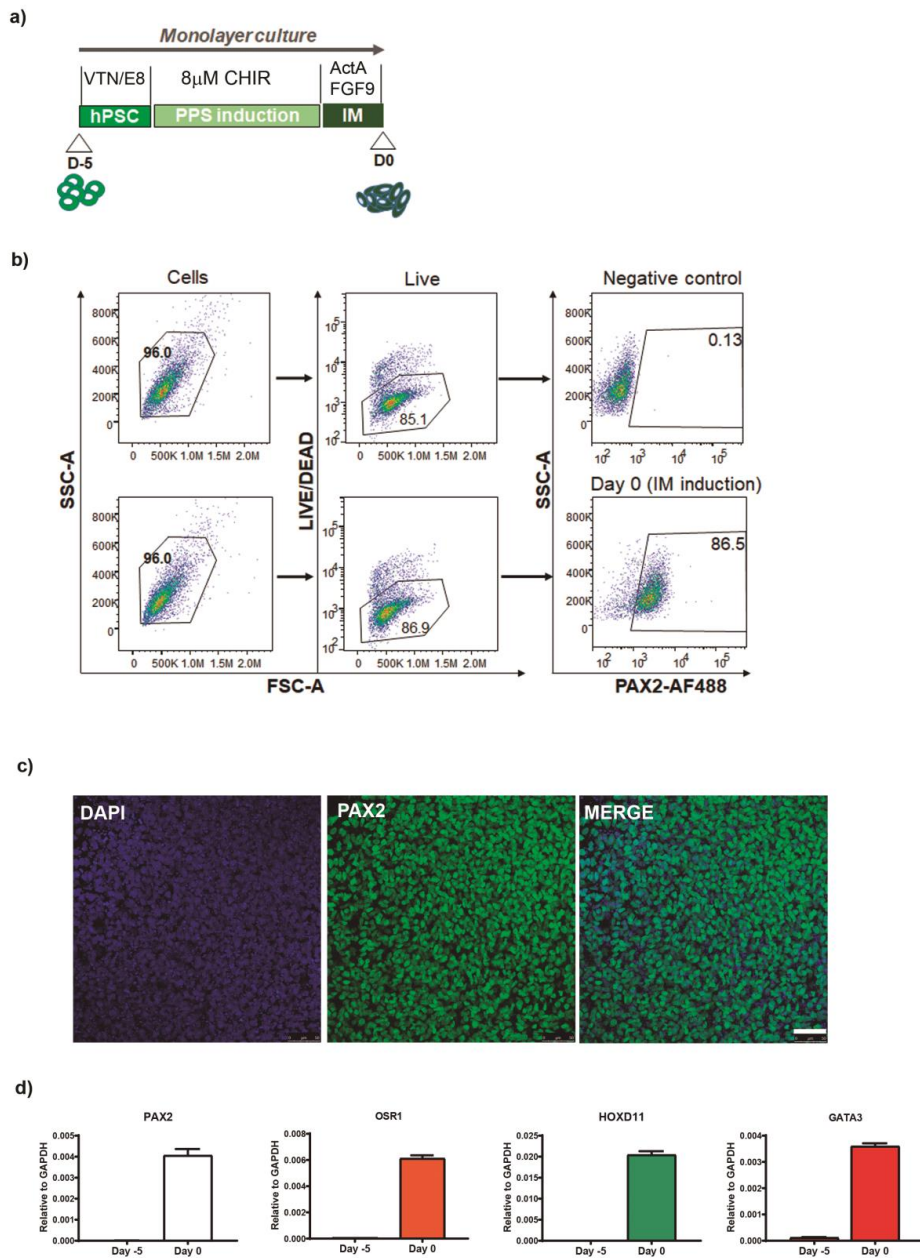
Supplementary Fig. 2 | Differentiation of hPSC-derived PPS cells into IM cells. a, Schematic of the timeline for the directed differentiation of hPSCs (*day -5*) into IM-committed cells (*day 0*). After PPS induction (*day -1*), treatment with FGF9 and Activin A for 1 day promotes the efficient generation of IM-committed cells (*day 0*). **b,** Flow cytometry analysis for the intracellular staining of PAX2 in IM-committed cells (*day 0*). Numbers in outlined areas indicate percent cells. Data are representative of three independent experiments. The mean percentage of PAX2$^+$ cells is 85.0 ± 1,4 % (mean ± SD, n = 3). **c,** Immunocytochemistry for PAX2 after IM induction (*day 0*). Scale bars, 50 μm. Images are representative of four independent experiments. **d,** qPCR analysis for the expression of IM markers before (*day -5*) and after IM induction (*day 0*). Genes are indicated. Data are mean ± SD (technical replicates). The experiment was repeated independently two times with similar results.
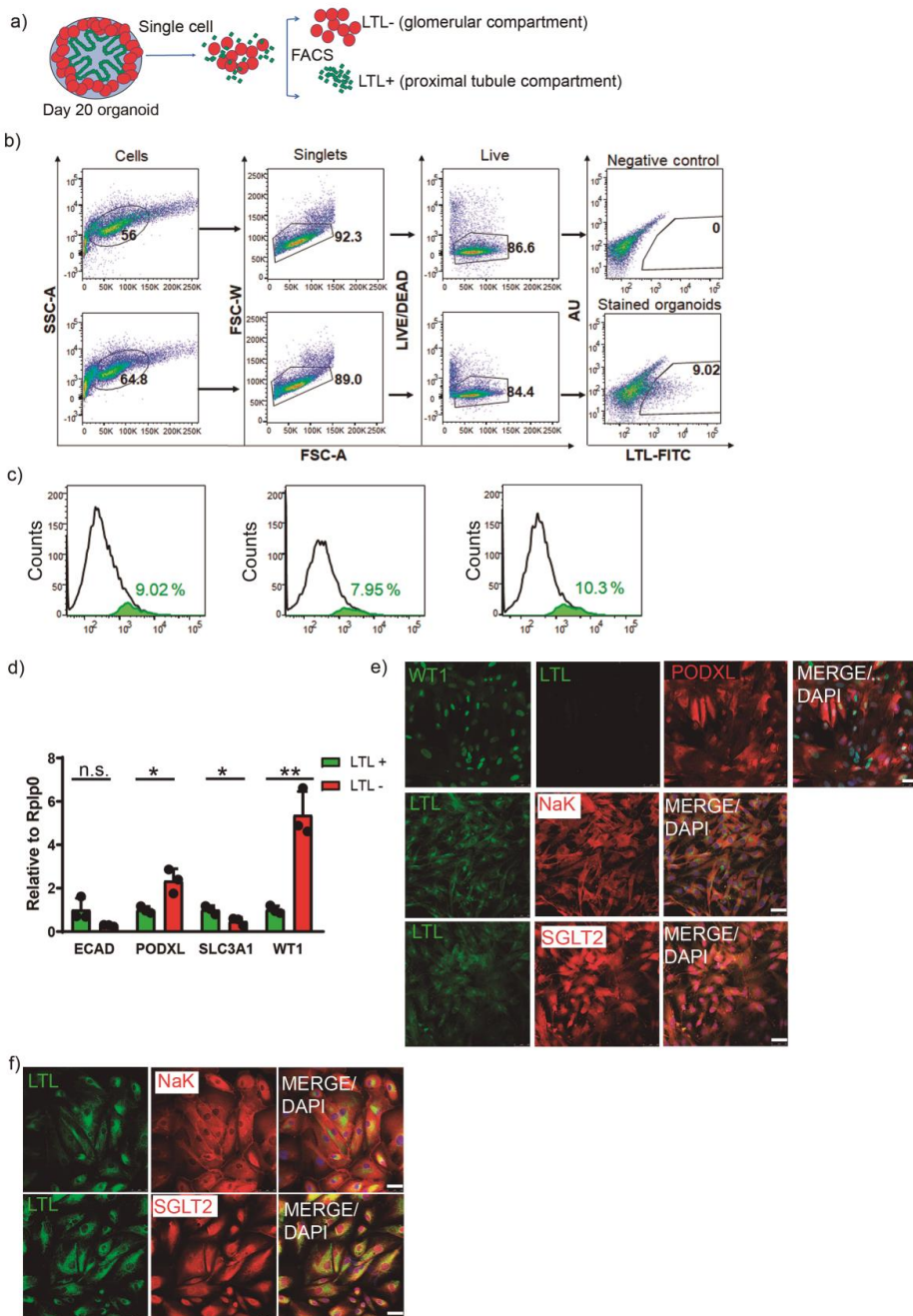
Supplementary Figure 3

a)

DAY 8

b)

DAY 8　　　　DAY 11　　　　DAY 14　　　　DAY 16

c)

RV-stage organoid (day 8)　　polarized RV day 8　　polarized RV day 11

d)

DAY 8

LHX1　　PAX8　　MERGE

HNF1B　　SIX2　　MERGE

DAY 11

PAX2　　BRN1　　ECAD　　MERGE

e)

TWIST　　SNAI2　　ECAD　　WNT4

Supplementary Fig. 3 | *Day 8* kidney organoids express characteristic markers of RVs.
a, Bright-field and tile scan confocal images of a whole kidney organoid showing the formation of RV structures that expressed PAX2 and WT1 on *day 8* of differentiation. Scale bars, 500 µm. **b,** Hematoxylin-eosin staining of kidney organoids at *day 8*, *11*, *14* and *16* of differentiation. **c,** Schematic of the acquisition of RV proximal-distal polarity by RV-stage organoids. Markers characteristic of distal, medial and proximal identities are indicated. **d,** Immunocytochemistry for RV markers LHX1, PAX8, HNF1β, PAX2, BRN1, ECAD and the MM marker SIX2 in *day 8* and *day 11* RV-stage organoids. Scale bars, 50 µm. Images are representative of three independent experiments (**a, b, d**). **e,** qPCR analysis for *TWIST*, *SNAI2*, *ECAD* and *WNT4* during kidney organoid differentiation (days are indicated). Data are mean ± SD (technical replicates). The experiment was repeated independently two times with similar results.

Supplementary Figure 4

Supplementary Fig. 4 | Immunohistochemistry of human fetal kidneys and kidney organoids. **a,** Schematic of a nephron illustrating the different nephron compartments, including: distal tubule (DT), Loop of Henle (LoH), proximal tubule (PT) and glomerulus (G). Characteristic late-stage nephron markers for each nephron segment are indicated. **b-g,**

Immunohistochemistry for the indicated late-stage nephron markers in human fetal kidney samples from first (13 and 16 weeks of gestation) and second trimester (22 weeks of gestation) of gestation, and *day 16* kidney organoids. Magnified views of boxed regions are shown for all the experimental conditions. Scale bars, 250 µm and 25 µm (magnified views). One human fetal kidney sample per gestational age was analysed. Images are representative of two independent experiments.

Supplementary Figure 5

Supplementary Fig. 5 | Sorting of renal cell populations from kidney organoids. a, Schematics of the separation of glomerular (LTL⁻) and tubular (LTL⁺) compartments in *day 16* kidney organoids by fluorescence-activated cell sorting. Kidney organoids were stained with LTL, dissociated to single cells and sorted. **b**, Gating strategy for cell sorting of LTL⁺ and LTL⁻ cell populations from *day 16* kidney organoids. Numbers in outlined areas indicate percent cells. AU, autofluorescence. **c**, Histograms representing the overlay of live cells and LTL⁺ cells from three independent cell sorting experiments. The mean percentage of LTL⁺ cells is 9.1 ± 1.2 % (mean ± SD, n = 3). Each experiment is a pool of eight organoids. **d,** Total RNA was extracted from LTL⁺ and LTL⁻cell populations and analysed by qPCR (genes are indicated). LTL⁻ cells expressed higher mRNA levels for PODXL and WT1 glomerular segment markers (in red) in comparison with LTL⁺ cells that expressed higher mRNA levels for ECAD and SLC3A1 proximal tubular markers (in green). Data are mean ± SD. n = 3 independent experiments. LTL⁻ *versus* LTL⁺: *ECAD*, $t(4) = 2.3135$, ns, not significant, $P = 0.0817$; *PODXL*, $t(4) = 4.0118$, *$P = 0.016$; *SLC3A1*, $t(4) = 3.4534$, *$P = 0.026$; *WT1*, $t(4) = 6.8786$, **$P = 0.0023$. Two-tailed student's *t*-test. **e**, Immunocytochemistry for glomerulus (WT1 and PODXL) and proximal tubule (NaK, SGLT2) markers in LTL⁻ and LTL⁺ cell fractions, respectively. Images are representative of three independent experiments. **f**, Immunocytochemistry for proximal tubule markers (NaK, SGLT2) in adult human kidney proximal tubular epithelial cells that were used as positive control. One adult human kidney proximal tubular epithelial cell sample was analysed. Scale bars, 50 μm (**e, f**).
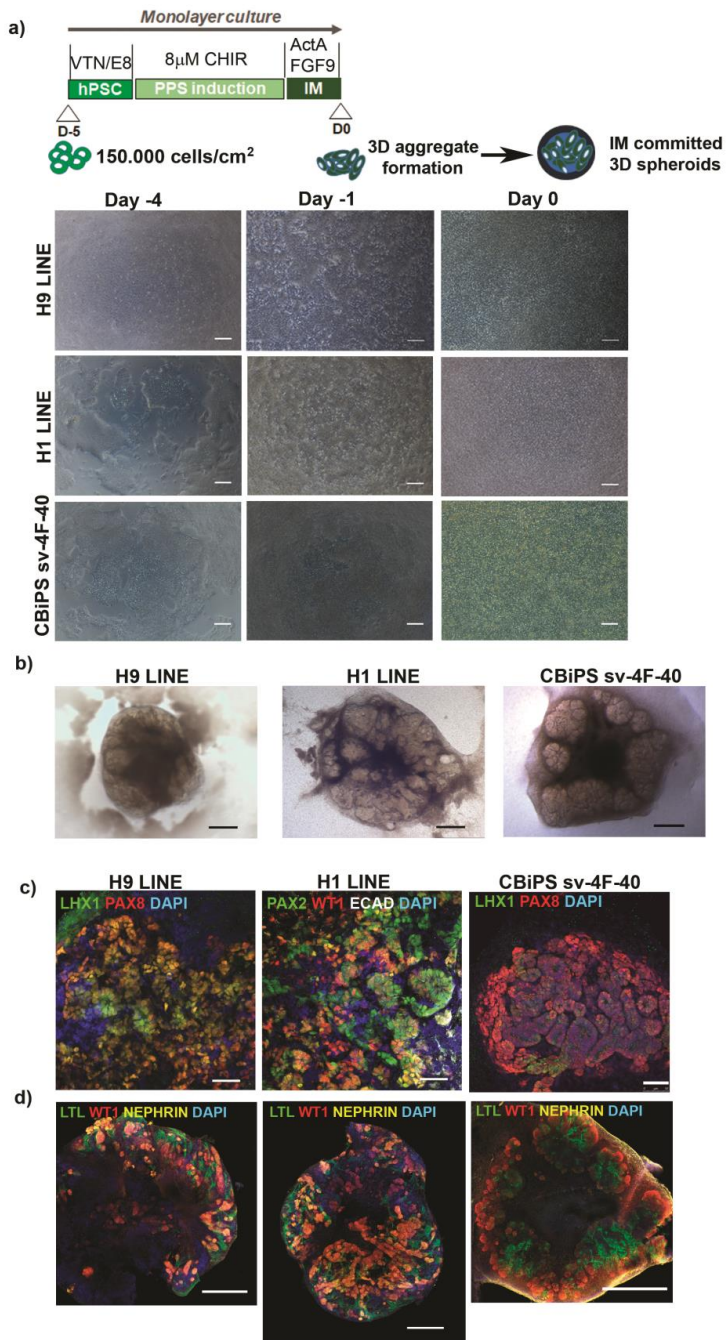
Supplementary Figure 6
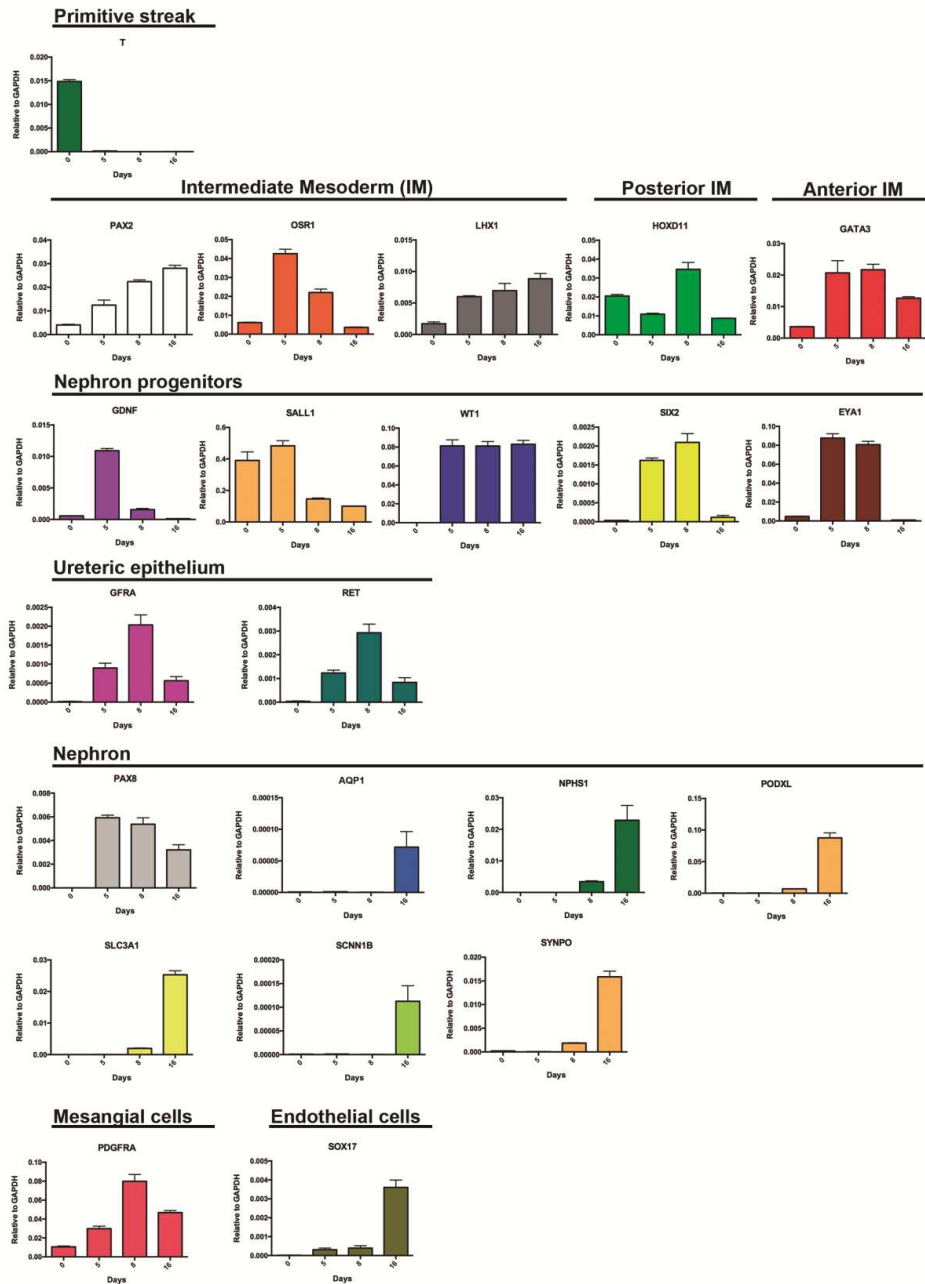
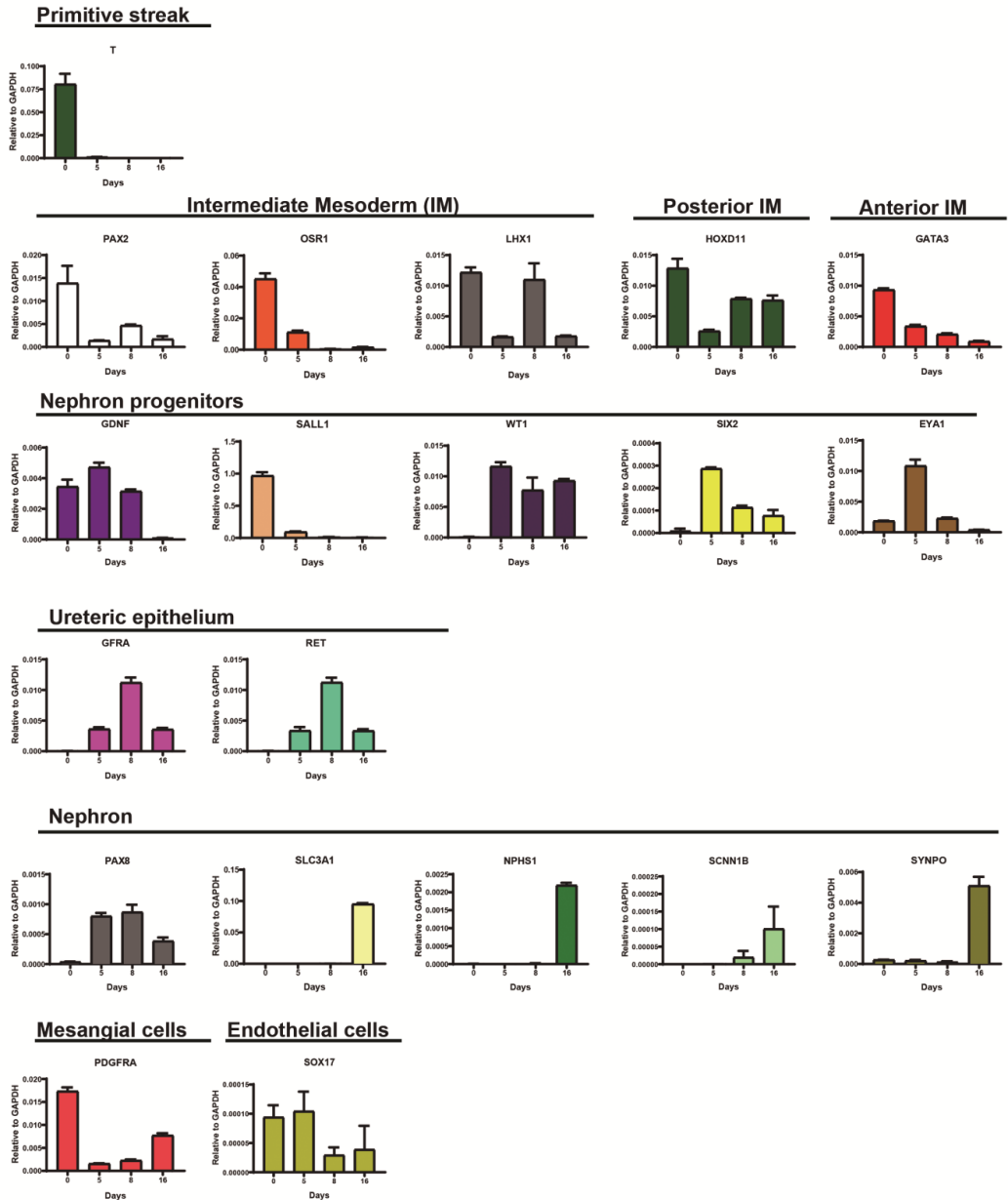**Supplementary Fig. 6 | qPCR analysis of kidney organoids from ES[4] hESC line.**
mRNA levels for differentiation markers were analysed by qPCR during the time course of kidney organoid differentiation at the indicated days. Markers included those for PS, IM, posterior and anterior IM, NPC, ureteric epithelium, nephron, mesangial, and endothelial cells (genes are indicated). Data are mean ± SD (technical replicates). Each sample is a pool of six organoids per time point. The experiment was repeated independently two times with similar results.

Supplementary Figure 7

a)

Day -4   Day -1   Day 0

H9 LINE

H1 LINE

CBiPS sv-4F-40

b)

H9 LINE   H1 LINE   CBiPS sv-4F-40

c)

H9 LINE   H1 LINE   CBiPS sv-4F-40
LHX1 PAX8 DAPI   PAX2 WT1 ECAD DAPI   LHX1 PAX8 DAPI

d)

LTL WT1 NEPHRIN DAPI   LTL WT1 NEPHRIN DAPI   LTL WT1 NEPHRIN DAPI

Supplementary Fig. 7 | Generation of kidney organoids from hESC and hiPSCs. a, Schematic of the timeline for the directed differentiation of hPSCs (*day -5*) into IM-committed cells (*day 0*). Culture conditions and growth factors / molecules are indicated. Bright-field images during the time course of IM induction from hESC lines (H9 and H1) and hiPSCs (CBiPSsv-4F-40) (days are indicated). Scale bars, 200 μm. **b,** Bright-field images of *day 16* whole kidney organoids derived from hESC lines (H9 and H1) and hiPSCs (CBiPSsv-4F-40). Scale bars, 500 μm. **c,** Immunocytochemistry for RV markers in RV-stage organoids (*day 8*) derived from the indicated hESC and hiPSC lines (markers are indicated). Scale bars, 50 μm. **d,** Immunocytochemistry for the podocyte markers NEPHRIN and WT1, and the proximal tubule marker LTL in *day 16* whole kidney organoids derived from the indicated hPSC lines. Scale bars, 500 μm. Experiments were repeated independently three times with similar results.

Supplementary Figure 8

Supplementary Fig. 8 | qPCR analysis of kidney organoids from H9 hESC line. mRNA levels for differentiation markers were analysed by qPCR during the time course of kidney organoid differentiation at the indicated days. Markers included those for PS, IM, posterior and anterior IM, NPC, ureteric epithelium, nephron, mesangial, and endothelial cells (genes are indicated). Data are mean ± SD (technical replicates). Each sample is a pool of six organoids per time point. The experiment was repeated independently two times with similar results.
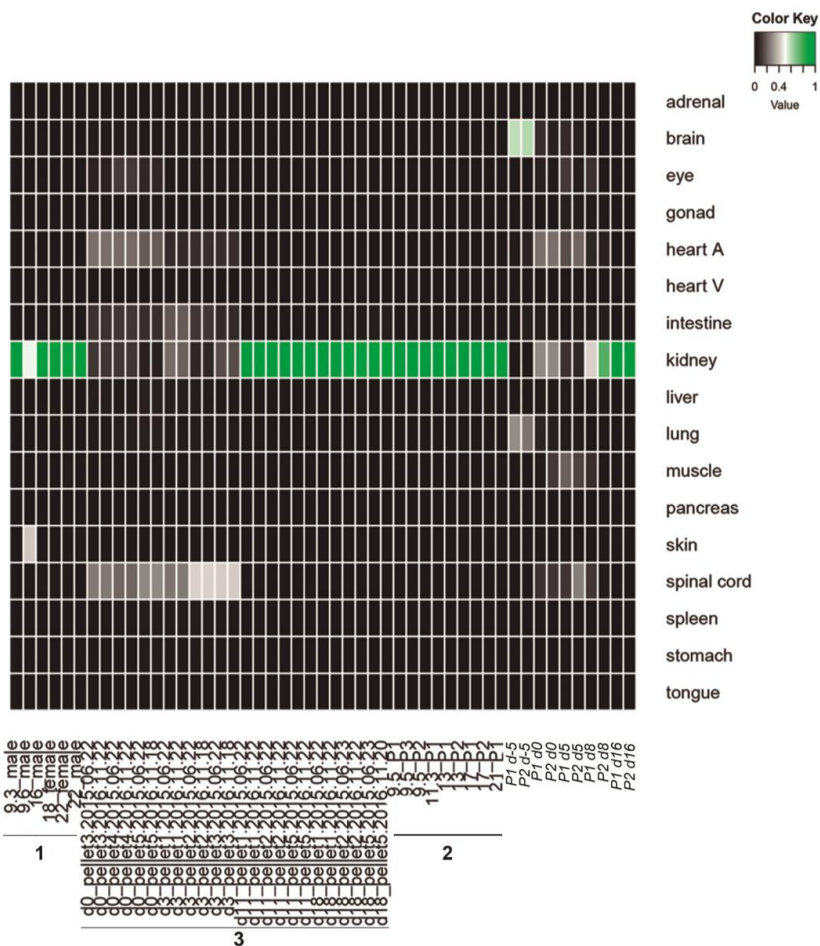
Supplementary Fig. 9 | Transcriptional resemblance of kidney organoids to human fetal tissues. Heat map showing the relative transcriptional identity of kidney organoids to 16 human fetal tissues. RNA-seq was performed on whole kidney organoids from 5 time points (*day -5, 0, 5, 8,* and *16*) during differentiation. Six pooled organoids per time point were analysed. Two independent experiments were included in the analysis. Data from Chuva de Sousa Lopes SM [SRP055513][18] (1), McMahon AP [SRP111183][19] (2) and Little MH [SRP059518][9] (3) are included in the analysis.

Supplementary Figure 10

a)

b)

c)
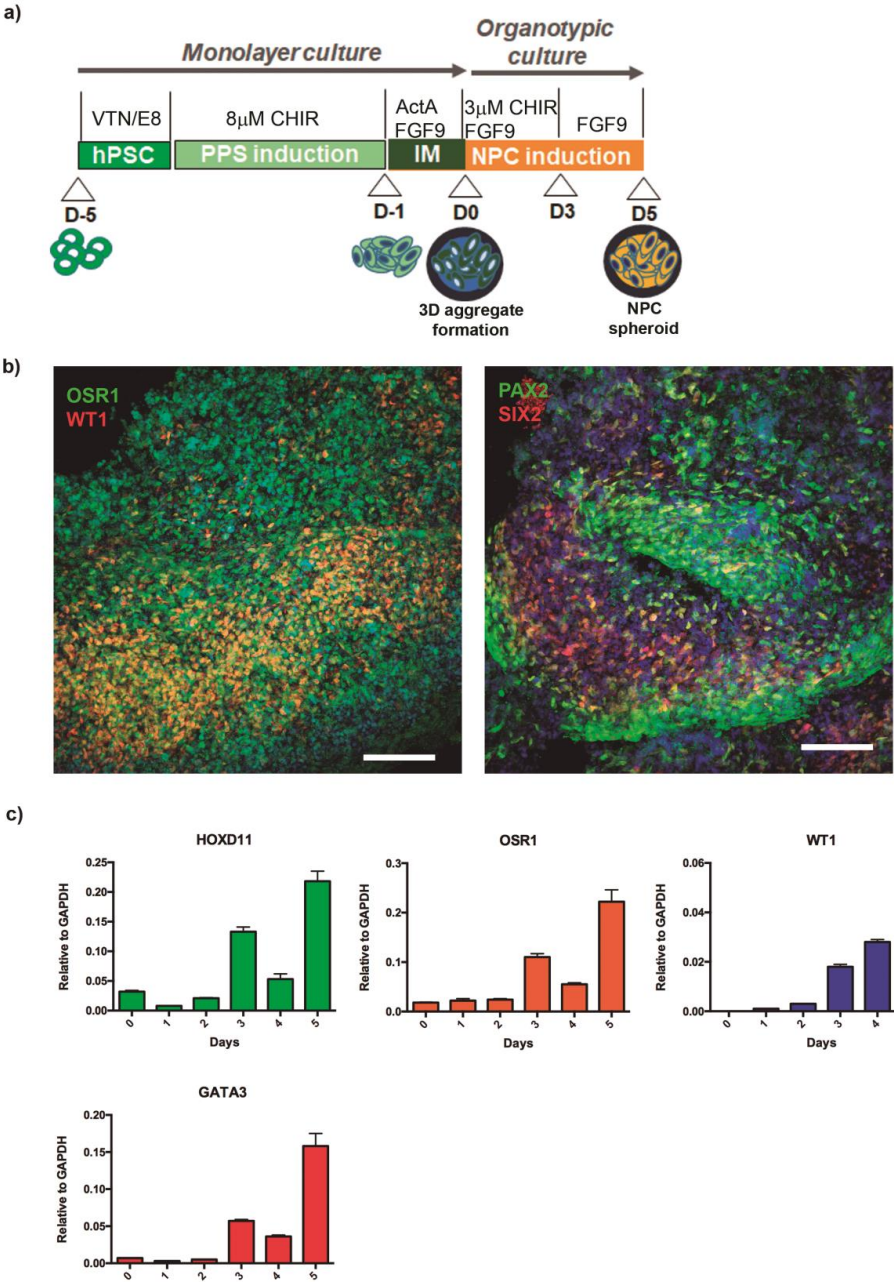
Supplementary Fig. 10 | *Day 5* differentiating organoids contain NPC-committed cells.
a, Schematic of the timeline for kidney organoid differentiation from the formation of IM-committed spheroids (*day 0*) to the generation of NPC-committed cells (*day 5*). Culture conditions and growth factors / molecules are indicated. **b,** Confocal images of *day 5* NPCs showing the expression of markers characteristic of the NPC signature, including OSR1, WT1, PAX2 and SIX2. Scale bars, 100 μm. **c,** qPCR analysis for *HOXD11, OSR1*, *WT1*, and *GATA3* during the time course of differentiation from IM to NPC-committed cells (days are indicated). Data are mean ± SD (technical replicates). Each sample is a pool of six organoids per time point. Experiments were repeated independently two times with similar results.
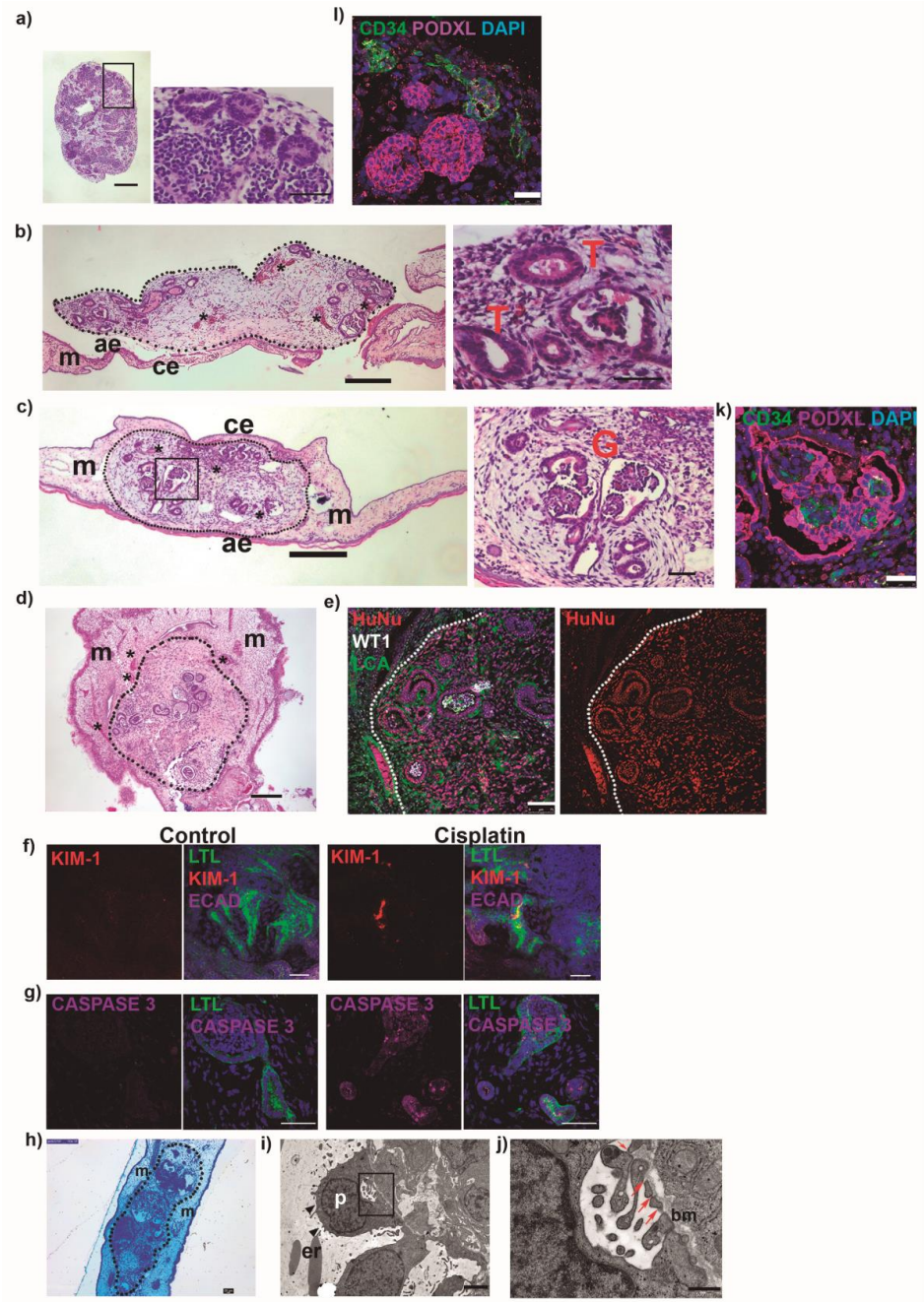
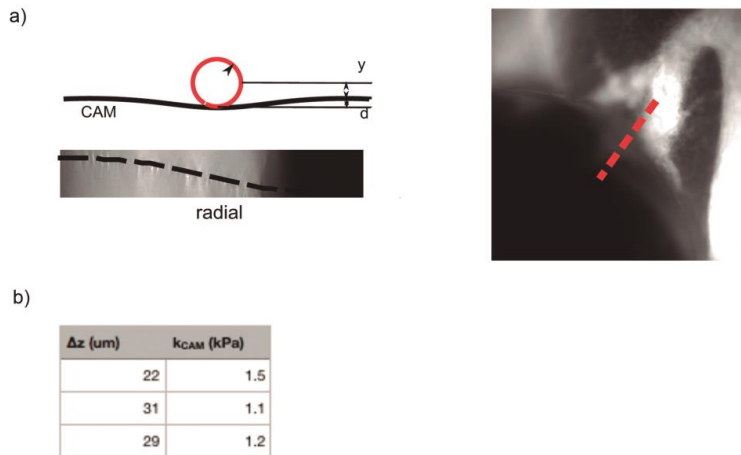**Supplementary Figure 11**

a)

b)

c)
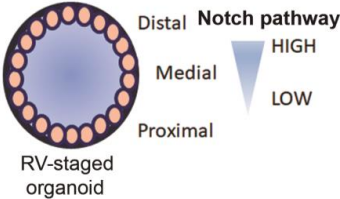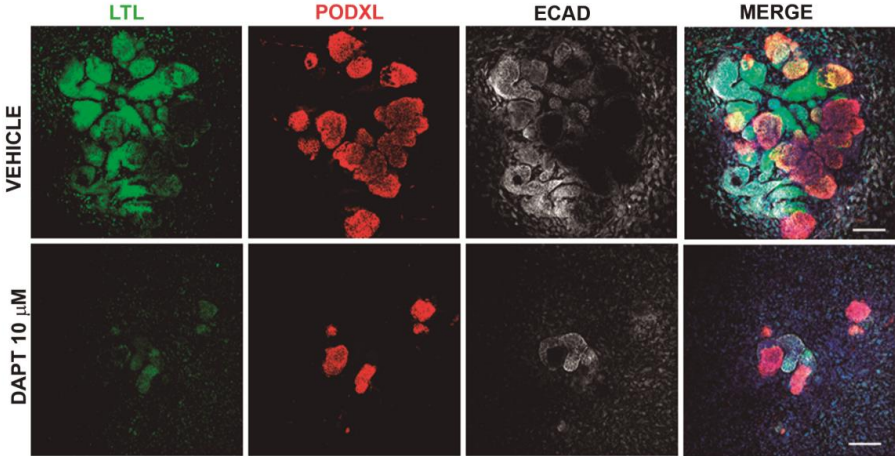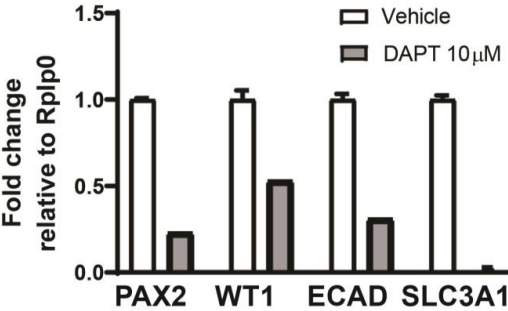
Supplementary Fig. 11 | Inhibition of Notch signaling in kidney organoids. a, Model of predicted alterations in nephron patterning when inhibiting Notch signaling with the γ-secretase inhibitor (DAPT) in kidney organoids from *day 8* to *day* 16 of differentiation. **b,** Immunocytochemistry for proximal tubule-like structures (LTL, ECAD) and podocyte-like cells (PODXL) in kidney organoids treated with vehicle, or DAPT (10 µM) for 8 days. Scale bars, 50 µm. **c,** qPCR analysis of *day 16* kidney organoids treated with vehicle, or DAPT (10 µM) for 8 days (genes are indicated). Data are mean ± SD (technical replicates). Each sample is a pool of four organoids per time point. Experiments were repeated independently three times with similar results.
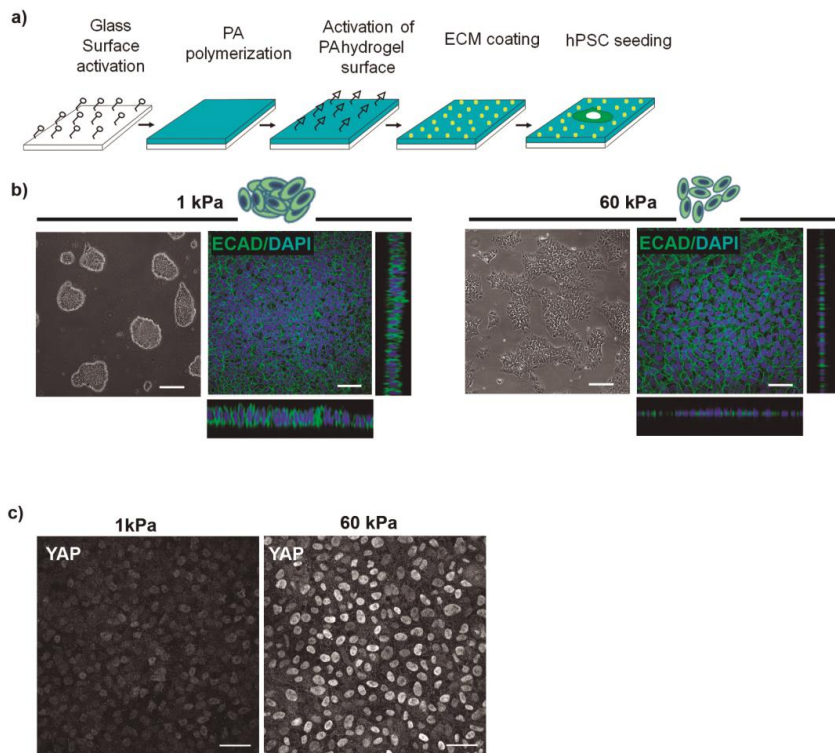
Supplementary Figure 12

Supplementary Fig. 12 | Implantation of kidney organoids into the chick CAM. a-d, Hematoxylin-eosin staining of *in vitro* maintained (**a**) and implanted kidney organoids (**b-d**). Chorionic epithelium (ce). Allantoic epithelium (ae). Mesenchyme (m). Blood vessels (asterisks). Tubule-like (T) and glomeruli-like (G) structures. The estimated organoid dimension (area of a middle organoid section) is 0.93 (**a**), 0.66 (**b**), 0.29 (**c**), 0.98 (**d**) mm^2. Scale bars, 250 μm and 50 μm (magnified views). Images are representative of n = 5 biologically independent *in vitro* maintained (**a**) and n = 8 biologically independent implanted organoids (**b-d**) from three independent experiments. **e,** Immunohistochemistry of **d** for LCA, HuNu and WT1. Scale bars, 75 μm. Images are representative of n = 2 biologically independent implanted organoids from two independent experiments. **f, g,** Immunohistochemistry for LTL, KIM-1, ECAD (**f**) and cleaved Caspase 3, LTL (**g**) in implanted kidney organoids (control: injected with saline) and 24 h after cisplatin injection. Scale bars, 50 μm. The experiment was performed independently two times with similar results. **h**, Semithin section of an implanted kidney organoid (dashed line). Scale bar, 200 μm. **i, j,** TEM of implanted kidney organoids. **i,** Podocyte-like cells (p) exhibiting apical microvilli (indicated with black triangles), and primary and secondary processes. Basement membrane (bm). Chicken erythrocytes (er). **j,** A magnified view of **i** showing primitive slit diaphragm–like structures (red arrows) between the cell processes. Scale bars, 2 μm (**i**) and 500 nm (**j**). Images (**h-j**) are representative of n = 2 biologically independent implanted organoids from two independent experiments. **k, l**, Immunohistochemistry for CD34 and PODXL in implanted (**k**) and *in vitro* maintained (**l**) kidney organoids. Scale bars, 25 μm. Images are representative of n = 2 biologically independent implanted organoids from two independent experiments (**k**), and n = 3 biologically independent *in vitro* maintained organoids from three independent experiments (**l**).
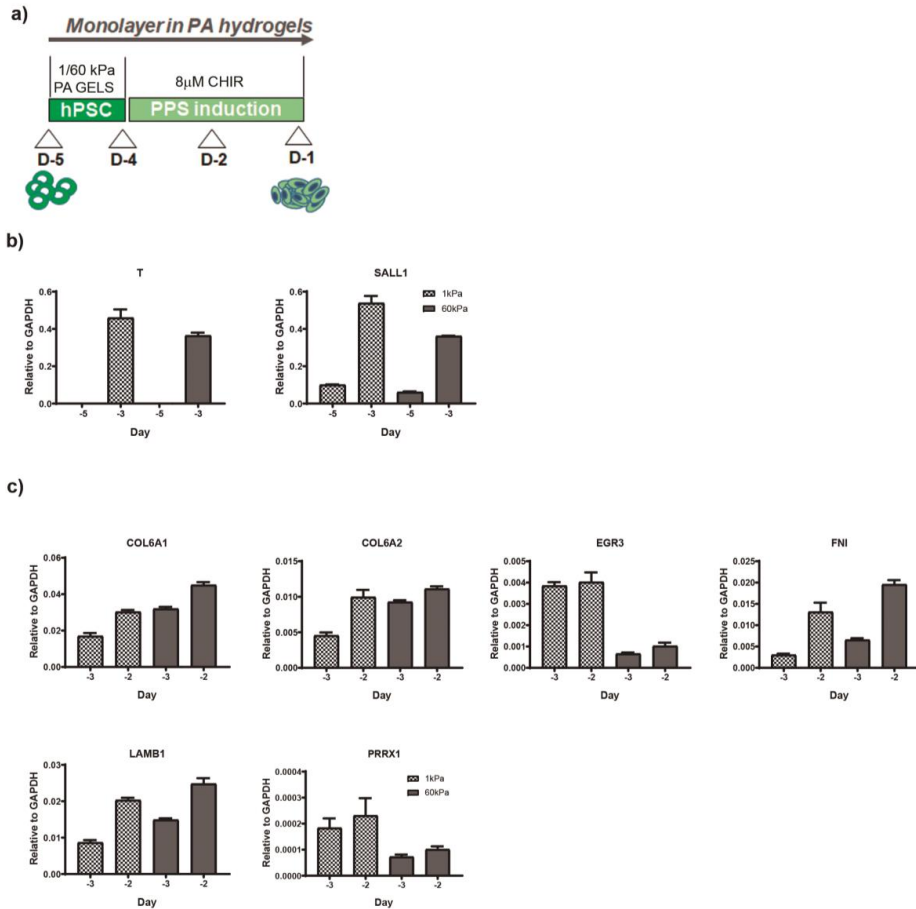
Supplementary Figure 13

a)

radial

b)

Δz (um)	k$_{CAM}$ (kPa)
22	1.5
31	1.1
29	1.2

Supplementary Fig. 13 | Measurement of the chick CAM stiffness. a, Schematic of the ball indentation method (left panel). Using a custom made Matlab code, the indentation depth (d) was determined based on the derivative of the fluorescence intensity profile of the FITC-labeled CAM along a line crossing the border of the ball (red dashed line in right panel). **b,** Young modulus values of the chick CAM measured using the ball indentation method from three separate experiments.

Supplementary Figure 14

Supplementary Fig. 14 | Fabrication of hydrogels with controlled stiffness. a, Schematic of the methodology for the fabrication of functionalized polyacrylamide (PA) hydrogels for the directed differentiation of hPSCs. Glass surface is activated prior polymerization of the PA hydrogel (light blue) on top of the activated glass. After surface activation NHS ester groups are available to bond to free amines of the ECM proteins (yellow dots) and then hPSCs (green) are allowed to adhere under undifferentiated culture conditions. **b,** Bright-field and confocal images for ECAD expression in hPSCs grown on soft (1 kPa) and rigid (60 kPa) PA hydrogels under undifferentiated culture conditions. Scale bars, 100 μm (bright field images) and 50 μm (confocal images). **c,** Confocal images for YAP immunofluorescence in hPSCs grown on soft (1 kPa) and rigid (60 kPa) PA hydrogels under undifferentiated culture conditions. Scale bars 50 μm. Experiments were repeated independently three times with similar results.
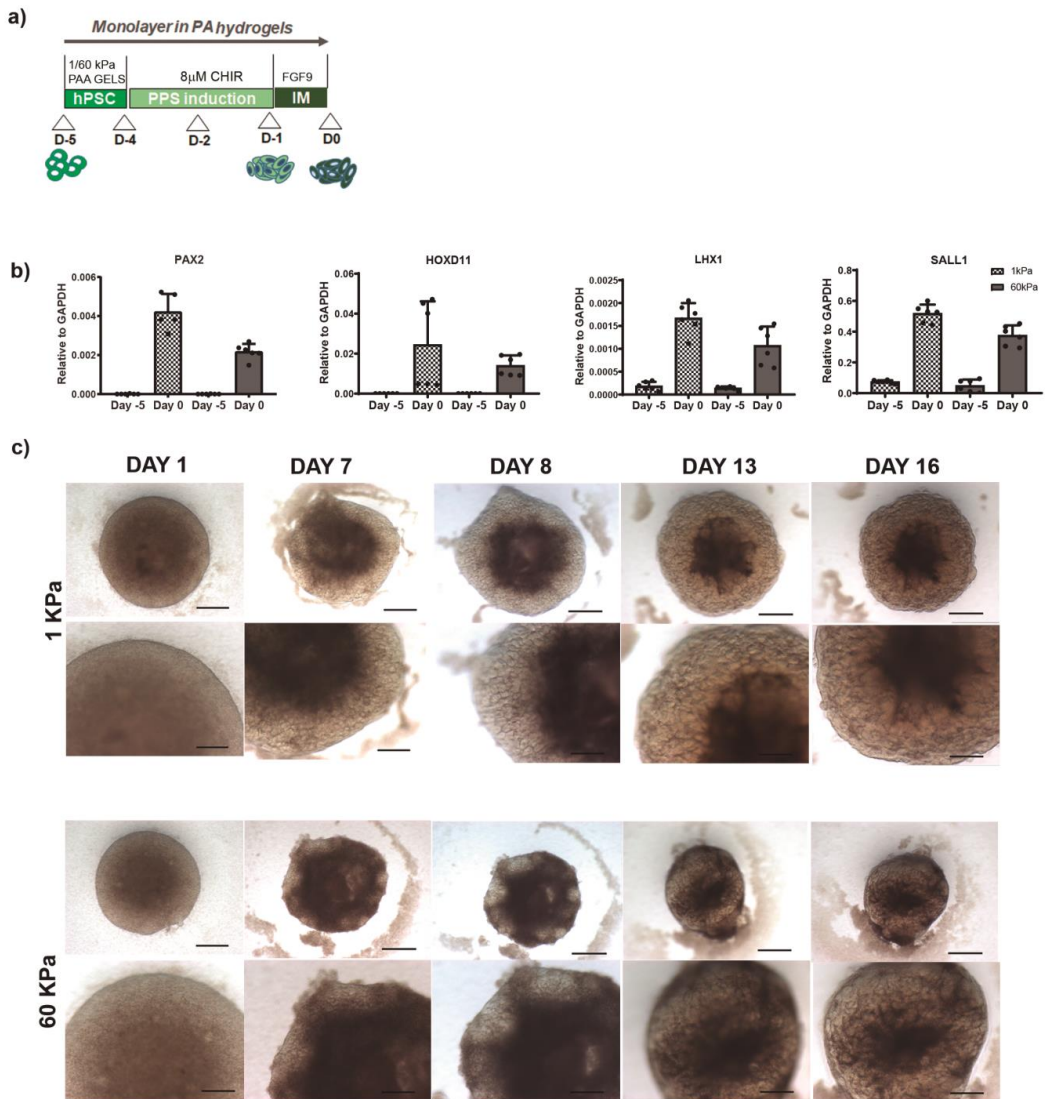
Supplementary Figure 15

Supplementary Fig. 15 | Induction of PPS-committed cells in soft and rigid substrates.
a, Schematic of the timeline for the directed differentiation of hPSCs (*day -5*) into PPS-committed cells (*day -1*) under 2D monolayer culture conditions. **b,** mRNA levels for the indicated genes analysed by qPCR at *day -5* and *day -3* of the PPS induction under soft (1 kPa) and rigid (60 kPa) conditions. **c,** mRNA levels for the indicated genes analysed by qPCR at *day -3* and *day -2* of PPS induction under soft (1 kPa) and rigid (60 kPa) conditions. Data are mean ± SD (technical replicates). Experiments were repeated independently two times with similar results.
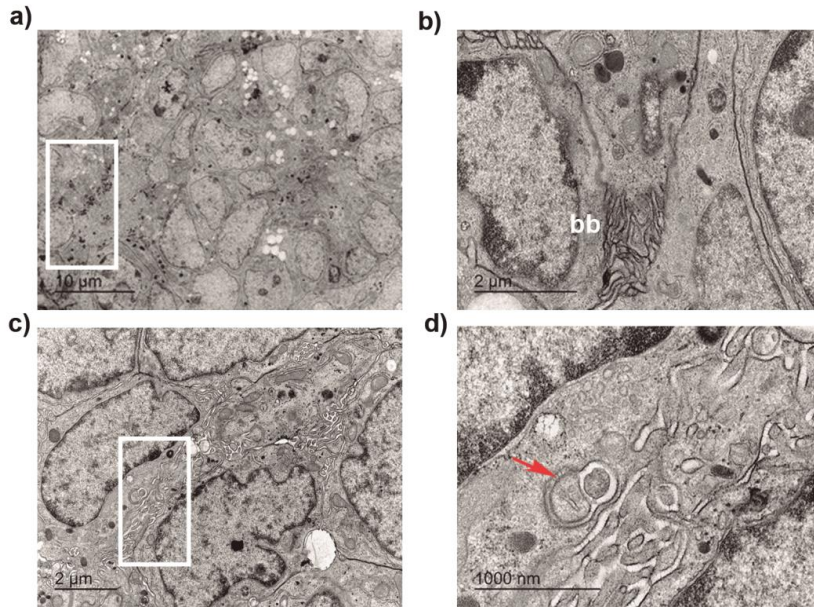
Supplementary Figure 16

a)

Monolayer in PA hydrogels

1/60 kPa PAA GELS — hPSC — 8µM CHIR — PPS induction — FGF9 — IM

D-5   D-4   D-2   D-1   D0

b)

PAX2 | HOXD11 | LHX1 | SALL1 (Relative to GAPDH; Day -5, Day 0; 1kPa, 60kPa)

c)

| | DAY 1 | DAY 7 | DAY 8 | DAY 13 | DAY 16 |

1 KPa

60 KPa

Supplementary Fig. 16 | Induction of IM-committed cells in soft and rigid substrates.
a, Schematic of the timeline for the directed differentiation of hPSCs (*day -5*) into IM-committed cells (*day 0*) in soft (1 kPa) and rigid (60 kPa) PA hydrogels. **b,** mRNA levels for the indicated genes analysed by qPCR at *day -5* and *day 0* of IM induction under soft (1 kPa) and rigid (60 kPa) conditions. Data are mean ± SD, n = 2 independent experiments. Three technical replicates are shown per sample. **c,** Bright field images of kidney organoids derived in soft (1 kPa) or rigid (60 kPa) conditions during differentiation (days are indicated). Scale bars, 500 µm and 250 µm (magnified views). Images are representative of n = 10 kidney organoids (1 kPa) and n = 10 kidney organoids (60 kPa) from three independent experiments.

Supplementary Figure 17

Supplementary Fig. 17 | TEM of kidney organoids from 60 kPa PA hydrogels. a-d, TEM of *day 16* kidney organoids generated using 60 kPa PA hydrogels. **a,** Tubular-like structures with epithelial cells that exhibit high mitochondrial content and brush borders. **b,** A magnified view of the boxed region in **a** showing a detail of brush borders (bb). **c,** Differentiated podocyte-like cells exhibiting cell processes. **d,** A magnified view of the boxed region in **c** showing immature slit diaphragm-like structures (indicated with a red arrow). Scale bars, 10 µm (**a**), 2 µm (**b**), 2 µm (**c**) and 1000 nm (**d**). Images are representative of two independent experiments.

Supplementary Tables

Supplementary Table 1. RNA-seq values across samples at the indicated time frames for Keygenes analysis.

Supplementary Table 2. Normalized RNA-seq values across samples at the indicated time frames for clustering analysis after correction for batches effect.

Supplementary Table 3. Genes found to be significantly down or up-regulated in hESCs grown for 24 h (*day -4*) on soft (1 kPa) compared to rigid (60 kPa) PA hydrogels. Difference in expression is reported as log fold change (see Methods). n = 4. Adjusted *P* value smaller than 0.05 (Wald Test).

Supplementary Table 4. Genes found to be significantly down or up-regulated in hESCs differentiated on soft (1 kPa) compared to rigid (60 kPa) PA hydrogels at *day -3* and *day -2* of the differentiation process. Difference in expression is reported as log fold change (see Methods). Genes are grouped according to their biological function. n = 4. Adjusted *P* value smaller than 0.05 (Wald test).

Supplementary Table 5. List of primary antibodies used in immunocytochemistry and immunohistochemistry.

Supplementary Table 6. List of primers used for RT-qPCR analysis.

Gene	Forward	Reverse
CDX1	CGTTACATCACAATCCGGCG	CCAGATCTTCACCTGCCGTT
CDX2	GAACCTGTGCGAGTGGATG	GGATGGTGATGTAGCGACTG
CER1	GTGCCCTTCAGCCAGACTA	CAGACCCGCATTTCCCAAA
CRIPTO	CGGAACTGTGAGCACGATGT	GGGCAGCCAGGTGTCATG
ECAD	CGAGAGCTACACGTTCACGG	GGGTGTCGAGGGAAAAATAGG
EOMES	TGCAGGGCAACAAAATGTATG	GTCTCATCCAGTGGGAACCAGTA
EVX1	GAAGAAATCGAGGGTCCGGC	CCGTTGCTCTTGGGGGTC
EYA1	ATCTAACCAGCCCGCATAGC	GTGCCATTGGGAGTCATGGA
ENDOGLIN	CCTACGTGTCCTGGCTCATC	GGTGTGTCTGGGAGCTTGAA
FGF4	GGTGAGCATCTTCGGCGT	CTCATCGGTGAAGAAGGGCG
FOXA2	GTGAAGATGGAAGGGCACG	CATGTTGCTCACGGAGGAGTAG
GAPDH	AGCAATGCCTCCTGCACCACCAAC	CCGGAGGGGCCATCCACAGTCT
GATA3	CGTCCTGTGCGAACTGTCA	GTCCCCATTGGCATTCCTCC
GDNF	CCAACCCAGAGAATTCCAGA	AGCCGCTGCAGTACCTAAAA
GFRα1	AAGCACAGCTACGGAATGCT	GTTGGGCTTCTCCCTCTCTT
GSC2	CCAGTATCCTGACGTGAGTACG	GGTTCTTGAACCAGACCTCCA
HOXD11	GCCAGTGTGCTGTCGTTCCC	CTTCCTACAGACCCCGCCGT
LHX1	CTTCTTCCGGTGTTTCGGTA	TCATGCAGGTGAAGCAGTTC
MIXL1	GGTACCCCGACATCCACTTG	ACCTGGAAGAGGGGAGAAAA
NANOG	CAAAGGCAAACAACCCACTT	TCTGCTGGAGGCTGAGGTAT
NODAL	TGTTGGGGAGGAGTTTCATC	GCACAACAAGTGGAAGGGAC
NPHS1	GGCTCCCAGCAGAAACTCTT	CACAGACCAGCAACTGCCTA
OCT4	AGTGAGAGGCAACCTGGAGA	ACACTCGGACCACATCCTTC
OSR1	CTGCCCAACCTGTATGGTTT	CGGCACTTTGGAGAAAGAAG
PAX2	CCCAAAGTGGTGGACAAGAT	GAAAGGCTGCTGAACTTTGG
PAX8	GGCTCCACCTCATCCATCAA	CTGCTGCTGCTCTGTGAGTC
PDGFRA	GAGCGCTGACAGTGGCTACAT	TCGTCCTCTCTCTTGATGAAGGT
PODXL	GATAAGTGCGGCATACGGCT	GCTCGTACACATCCTTGGCA
RET	CTCGACGACATTTGCAAGAA	AGCATTCCGTAGCTGTGCTT
RPLP0	CCATTCTATCATCACGGGTACAA	AGCAAGTGGGAAGGTGTAATCC
SALL1	TCATGTCCGAGCAGTTCAAG	TCCCCAGTGTGTGTCCTGTA
SCNN1B	CCTGGAACTGAATTCGGCCT	GGGTATGACCTCTGCTCGTG
SIX2	GGCCAAGGAAAGGGAGAACA	GAGCTGCCTAACACCGACTT
SLC3A1	CACCAATGCAGTGGGACAAT	CTGGGCTGAGTCTTTTGGAC
SMAD2	CCAGAAACGCCACCTCCTG	GCTGGAGAGCCTGTGTCCA
SNAI2	CGAACTGGACACACATACAGTG	CTGAGGATCTCTGGTTGTGGT
SOX17	AGCAGAATCCAGACCTGCAC	TTGTAGTTGGGGTGGTCCTG
SYNPO	GCTGAGGAGGTGAGATGCAG	CTCTGGAGAAGGTGCTGGTG
T	GCAAAAGCTTTCCTTGATGC	ATGAGGATTTGCAGGTGGAC
TBX6	CATCCACGAGAATTGTACCCG	AGCAATCCAGTTTAGGGGTGT
TWIST1	GTCCGCAGTCTTACGAGGAG	GCTTGAGGGTCTGAATCTTGCT
VEGFR	CACATTGGCCACCATCTGAAC	CCATCAGAGGCCCTCCTTG
WNT4	TCGTCTTCGCCGTCTTCTCAG	GGCCCTTGAGTTTCTCGCAC
WT1	GCGGAGCCCAATACAGAATA	GATGCCGACCGTACAAGAGT

Supplementary Table 7. Summary of statistics and reproducibility information.

Supplementary Video Files

Supplementary video 1. Evidence for the circulation of chick blood within an implanted kidney organoid at day 3 of the implantation period. Video recording was performed in n = 3 biologically independent implanted kidney organoids with similar results.

Supplementary video 2. Evidence for the circulation of chick blood within an implanted kidney organoid at day 5 of the implantation period. White arrow indicates a blood vessel going through the kidney organoid. Video recording was performed in n = 2 biologically independent implanted kidney organoids with similar results.

Supplementary video 3. Evidence for the circulation of chick blood within an implanted kidney organoid at day 5 of the implantation period after intravital injection of dextran-FITC into the CAM vasculature. Intravital injection of dextran-FITC was performed in n = 3 biologically independent implanted kidney organoids with similar results.

2. Paper II

Dhillon, P., Park, J., Hurtado del Pozo, C., Li, L., Doke, T., Huang, S., Zhao, J., Kang, H. M., Shrestra, R., Balzer, M. S., Chatterjee, S., **Prado, P.**, Han, S. Y., Liu, H., Sheng, X., Dierickx, P., Batmanov, K., Romero, J. P., Prósper, F., … Susztak, K.
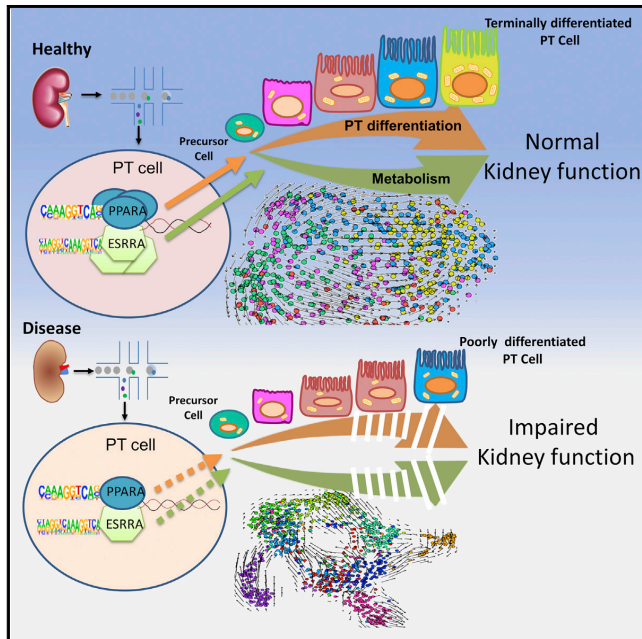
The Nuclear Receptor ESRRA Protects from Kidney Disease by Coupling Metabolism and Differentiation.

Cell Metabolism (2020)

The Nuclear Receptor ESRRA Protects from Kidney Disease by Coupling Metabolism and Differentiation

Graphical Abstract

Authors

Poonam Dhillon, Jihwan Park, Carmen Hurtado del Pozo, ..., Junhyong Kim, Nuria Montserrat, Katalin Susztak

Correspondence

jihwan.park@gist.ac.kr (J.P.),
nmontserrat@ibecbarcelona.eu (N.M.),
ksusztak@pennmedicine.upenn.edu (K.S.)

In Brief

Using single-cell RNA sequencing, Susztak and colleagues, show major changes in cell diversity in mouse models of kidney fibrosis. Proximal tubule (PT) cells are highly vulnerable to dysfunction in fibrosis and show altered differentiation. Nuclear receptors such as ESRRA maintain both PT cell metabolism and differentiation by directly regulating PT-cell-specific genes.

Highlights

- scRNA-seq analysis identified 30 cell types in mouse models of renal fibrosis

- PTs are highly vulnerable to dysfunction diseased kidneys

- PT cell differentiation is altered in renal fibrosis

- ESRRA protects from renal disease by coupling PT metabolism and differentiation

Cell Metabolism

CellPress

Article

The Nuclear Receptor ESRRA Protects from Kidney Disease by Coupling Metabolism and Differentiation

Poonam Dhillon,[1,2,14] Jihwan Park,[1,2,3,14,*] Carmen Hurtado del Pozo,[4] Lingzhi Li,[1,2] Tomohito Doke,[1,2] Shizheng Huang,[1,2] Juanjuan Zhao,[10] Hyun Mi Kang,[1,2,13] Rojesh Shrestra,[1,2] Michael S. Balzer,[1,2] Shatakshee Chatterjee,[1,2] Patricia Prado,[4] Seung Yub Han,[5] Hongbo Liu,[1,2] Xin Sheng,[1,2] Pieterjan Dierickx,[2] Kirill Batmanov,[1,2] Juan P. Romero,[6,7,8] Felipe Prósper,[6,7,8] Mingyao Li,[9] Liming Pei,[2,10] Junhyong Kim,[5] Nuria Montserrat,[4,11,12,*] and Katalin Susztak[1,2,15,*]

[1]Renal, Electrolyte, and Hypertension Division, Department of Medicine, University of Pennsylvania, Perelman School of Medicine, Philadelphia, PA 19104, USA
[2]Institute for Diabetes, Obesity, and Metabolism, University of Pennsylvania, Perelman School of Medicine, Philadelphia, PA 19104, USA
[3]School of Life Sciences, Gwangju Institute of Science and Technology (GIST), 123 Cheomdangwagi-ro, Buk-gu, Gwangju, Republic of Korea
[4]Pluripotency for Organ Regeneration, Institute for Bioengineering of Catalonia (IBEC), The Barcelona Institute of Technology (BIST), Barcelona, Spain
[5]Department of Biology, University of Pennsylvania, Philadelphia, PA 19104, USA
[6]Cell Therapy Program, Center for Applied Medical Research (CIMA), University of Navarra, Pamplona, Spain
[7]Oncohematology Program, Center for Applied Medical Research (CIMA), University of Navarra, Pamplona, Spain
[8]Hematology and Area of Cell Therapy, Clínica Universidad de Navarra, University of Navarra, Pamplona, Spain
[9]Department of Epidemiology and Biostatistics, University of Pennsylvania, Perelman School of Medicine, Philadelphia, PA 19104, USA
[10]Center for Mitochondrial and Epigenomic Medicine, Department of Pathology and Laboratory Medicine, Children's Hospital of Philadelphia, Perelman School of Medicine, University of Pennsylvania, Philadelphia, PA 19104, USA
[11]Catalan Institution for Research and Advanced Studies (ICREA), Barcelona, Spain
[12]Centro de Investigación Biomédica en Red en Bioingeniería, Biomateriales y Nanomedicina, Madrid, Spain
[13]Laboratory of Disease Modeling and Therapeutics, Korea Research Institute of Bioscience and Biotechnology, Daejeon, Republic of Korea
[14]These authors contributed equally
[15]Lead Contact
*Correspondence: jihwan.park@gist.ac.kr (J.P.), nmontserrat@ibecbarcelona.eu (N.M.), ksusztak@pennmedicine.upenn.edu (K.S.)
https://doi.org/10.1016/j.cmet.2020.11.011

SUMMARY

Kidney disease is poorly understood because of the organ's cellular diversity. We used single-cell RNA sequencing not only in resolving differences in injured kidney tissue cellular composition but also in cell-type-specific gene expression in mouse models of kidney disease. This analysis highlighted major changes in cellular diversity in kidney disease, which markedly impacted whole-kidney transcriptomics outputs. Cell-type-specific differential expression analysis identified proximal tubule (PT) cells as the key vulnerable cell type. Through unbiased cell trajectory analyses, we show that PT cell differentiation is altered in kidney disease. Metabolism (fatty acid oxidation and oxidative phosphorylation) in PT cells showed the strongest and most reproducible association with PT cell differentiation and disease. Coupling of cell differentiation and the metabolism was established by nuclear receptors (estrogen-related receptor alpha [ESRRA] and peroxisomal proliferation-activated receptor alpha [PPARA]) that directly control metabolic and PT-cell-specific gene expression in mice and patient samples while protecting from kidney disease in the mouse model.

INTRODUCTION

Kidney disease is becoming a major health issue in modern society. Chronic kidney disease (CKD) is the tenth leading cause of death worldwide with a steadily increasing incidence affecting eight hundred million people globally (Levin et al., 2017). The increase in the number of people affected by CKD is of concern because it is associated with an increased risk of death and progression to end-stage renal disease (ESRD). In addition, kidney disease is a massive personal and societal economic burden (Breyer and Susztak, 2016; Kovesdy et al., 2013).

Genetic studies examining the heritability of kidney function, such as integration of genome-wide association studies (GWAS) (Wuttke et al., 2019) and functional genomic studies, highlighted the role of proximal tubule (PT)-specific genes in kidney function (Hellwege et al., 2019; Park et al., 2018; Qiu et al., 2018). PT cells are highly susceptible to toxic and hypoxic injury, representing the primary cause of acute kidney injury (AKI) (Qiu et al., 2018). PT-cell-specific injury observed in AKI probably has the most rapid effect on kidney function. CKD is characterized by PT cell atrophy almost independent of disease etiology. PT cell atrophy strongly correlates with kidney function in CKD (Chang-Panesso and Humphreys,
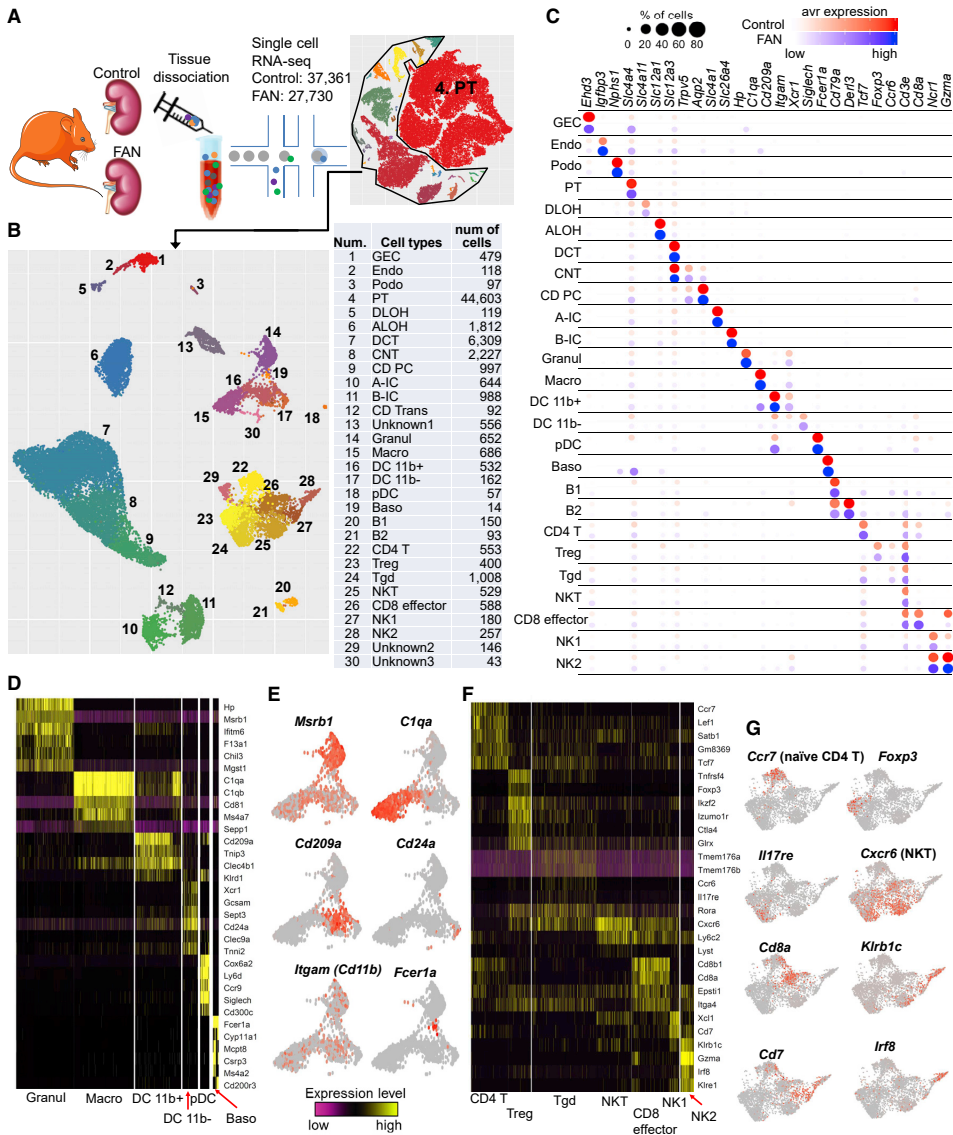
Figure 1. The Cellular Diversity of Diseased Kidney Samples

(A) A schematic diagram illustrating the experimental procedure involving the digestion of whole-kidney tissue from 6 control and 2 FAN mice followed by sequencing using a 10X Genomics protocol and transcriptomic analysis of 65,091 individual cells.

(B) Left, the UMAP of 29 distinct cell types identified by unsupervised clustering after excluding PT cells. Right, the tSNE (t-distributed stochastic neighbor embedding) plot for the entire dataset including PT cells. Assigned cell types are summarized in the right panel. GEC, glomerular endothelial cells; Endo, endothelial; Podo, podocyte; PT, proximal tubule; DLOH, descending loop of Henle; ALOH, ascending loop of Henle; DCT, distal convoluted tubule; CNT, connecting tubule; CD-PC, collecting duct principal cell; A-IC, alpha intercalated cell; B-IC, beta intercalated cell; CD-trans. collecting duct transitional cell; Granul, granulocyte; Macro, macrophage; DC 11b+, CD11b+ dendritic cell; pDC, plasmacytoid DC; Baso, basophile B, B lymphocyte; Treg, regulatory T cell; Tgd, gamma Delta T cell, and; NK, natural killer cell.

(C) Bubble plots of cell cluster marker genes identified in control and FAN samples (size of the dot indicates the % positive cells, color indicates relative expression).

(D) Heatmap showing expression pattern of myeloid lineage markers.

(legend continued on next page)

Cell Metabolism
Article

CellPress

2017; Reidy et al., 2014) (Liu et al., 2014) (Kang et al., 2015; Li et al., 2012).

Comprehensive genome-wide kidney tissue transcriptomics analysis has been used to define the molecular hallmarks of CKD, both in patient samples and mouse models (Beckerman et al., 2017; Qiu et al., 2018; Woroniecka et al., 2011). These studies highlighted a correlation between a large number of transcripts and kidney fibrosis. Cellular metabolism such as genes involved in lipid metabolism, fatty acid oxidation (FAO), and oxidative phosphorylation (OXPHOS) showed a strong correlation with disease state, both in patients and mouse CKD models (Chung et al., 2019; Kang et al., 2015). Pharmacological or genetic approaches that enhance FAO and mitochondrial biogenesis improved kidney function; however, the exact mechanism is not fully understood (Gomez et al., 2015; Tran et al., 2011; Tran et al., 2016; Zheng et al., 2019). Mitochondrial defects can also lead to the leakage of the mitochondrial DNA into the cytoplasm, resulting in the activation of the cyclic GMP–AMP synthase (cGAS) and stimulator of interferon genes(STING) innate immune system pathways, cytokine release, and influx of immune cells and downstream fibrosis development (Chung et al., 2019; Maekawa et al., 2019).

Single-cell RNA sequencing (scRNA-seq) analysis is transforming our understanding of complex diseases. In our previous study, we identified 21 distinct cell types, including three novel cell types in the kidney (Park et al., 2018). At the same time, we defined cell identity genes that can stably and reproducibly classify key kidney cell types in mice and humans (Menon et al., 2020; Young et al., 2018).

Here, we analyzed the transcriptome of different CKD mouse models, human kidney samples, and human organoids. Prior studies mostly relied on single nuclear sequencing and did not properly capture immune cell diversity (Lake et al., 2019; Wu et al., 2019). We identify several PT cell subgroups, and using cell trajectory analyses, we show an alteration in the differentiation state of PT cells in diseased kidneys. Single-cell epigenetics and transcriptomics indicate the critical role of HNF4A and HNF1B (hepatocyte nuclear factor 4A and 1B), PPARA (peroxisome proliferation-activated receptor alpha), and ESRRA (estrogen-related receptor alpha) in defining PT cell identity. Using mouse knock out and human kidney transcriptomics data, we demonstrate the protective role of ESRRA, which links energy metabolism, PT differentiation, and kidney function by directly binding to PT-cell-specific genes regulating their expression.

RESULTS

The Single-Cell Landscape Shows Increased Cellular Heterogeneity in Fibrotic Kidneys

To unravel cellular changes associated with kidney fibrosis, we first analyzed the transcriptome of 65,091 individual cells from 6 mouse control kidneys and 2 folic acid (FA)-induced fibrotic kidneys (folic acid nephropathy [FAN]) (Figure 1A). This is a well-established kidney disease model that presents both with structural damage (fibrosis) and kidney function decline indicated by serum blood urea nitrogen (BUN) level (Figures S1A–S1C). We observed that PT cells represented the majority of cell types in the dataset. To accurately cluster smaller cell populations, we first focused on non-PT cells (Figure 1B). Our unbiased clustering identified 30 cell populations, including kidney epithelial, immune, and endothelial cells based on marker gene expression (Figures 1C and S1D; Table S1). The proportion of cells were relatively stable in biological replicates but were substantially different between control and FAN samples (Figure S1E). Gene sets previously used to define cell types (cell identity genes) showed conserved expression in the disease state (Figure S1F). Immune cell diversity was markedly increased in the FAN mice (Figures S1D and S1E). We identified 14 immune cell clusters in our FAN model, whereas our previous study characterized 5 immune clusters (Park et al., 2018). Among the newly identified, we observed granulocytes, macrophages, dendritic cells (DCs), and basophils. DCs were further sub-clustered into DC 11b+ (Cd209a and Cd11b), DC 11b- (Cd24a and Clec9a), and plasmacytoid DC clusters (Siglech and Cd300c) (Figures 1D and 1E). A large number of lymphoid cells were also identified, including B cells, T cells, and natural killer (NK) cells (Figures 1B and 1C). T lymphocytes were sub-clustered into CD4⁺ T, Treg, gamma delta T, NKT, and CD8⁺ effector cells (Figures 1F and 1G). We made this dataset publicly available on our interactive website (http://susztaklab.com/VisCello/).

Bulk RNA Sequencing Strongly Influenced by Cell Fraction Changes

We next performed RNA-seq of whole-kidney (i.e., bulk tissue) samples, as single-cell sequencing may experience uneven cell drop-out. Differential expression analysis of bulk RNA-seq data indicated changes in expression of more than 4,000 genes (2,776 with higher and 1,361 with lower expression, using false discovery rate [FDR] of 0.05 and 2-fold change) (Figure 2A). Gene ontology analysis highlighted that the expression of genes associated with the immune system and inflammation was higher in the FAN model (Figure 2A). Analysis of genes showing the highest increased expression in the bulk dataset indicated that most of these genes were exclusively expressed by immune cells (Figure 2B). Genes whose levels were lower in the FAN model were enriched for metabolic processes such as lipid metabolism, FAO, and OXPHOS (Figure 2A). Genes with lower expression in the FAN model showed enrichment for PT cell expression (Figure 2B), suggesting a strong role for PT cells and immune cells driving transcriptional changes in bulk RNA-seq data. In addition, we observed that highly expressed and top differentially expressed genes, including *Lyz2*, *Cd52*, and

(E) Gene expression feature plots of myeloid lineage cells projected onto the UMAP. Msrb1 (methionine sulfoxide reductase B1), Granul; C1qa (Complement C1q A Chain), Macro; CD209a (CD209 antigen-like protein A), DC 11b+; CD24a (CD24a antigen), DC 11b-; Itgam (integrin Subunit alpha M), DC 11b+; and Fcer1a (Fc Fragment of IgE Receptor Ia), Baso.

(F) Heatmap showing the expression pattern of lymphoid lineage markers.

(G) Gene expression feature plots of lymphoid lineage cells projected onto the UMAP. Ccr7 (chemokine C-C motif receptor 7), CD4 T; *Foxp3* (Forkhead Box P3), Treg; *Il-17re* (interleukin-17 receptor E), Tgd; *Cxcr6* (chemokine C–X–C motif receptor 6), NKT; *CD8a* (CD8 antigen, alpha chain), CD8 effector; *Klrb1c* (Killer cell lectin-like receptor subfamily B member 1C), NK1-2; *CD7* (CD7 antigen), NK1, and; *Irf-8* (interferon regulatory factor-8), NK2
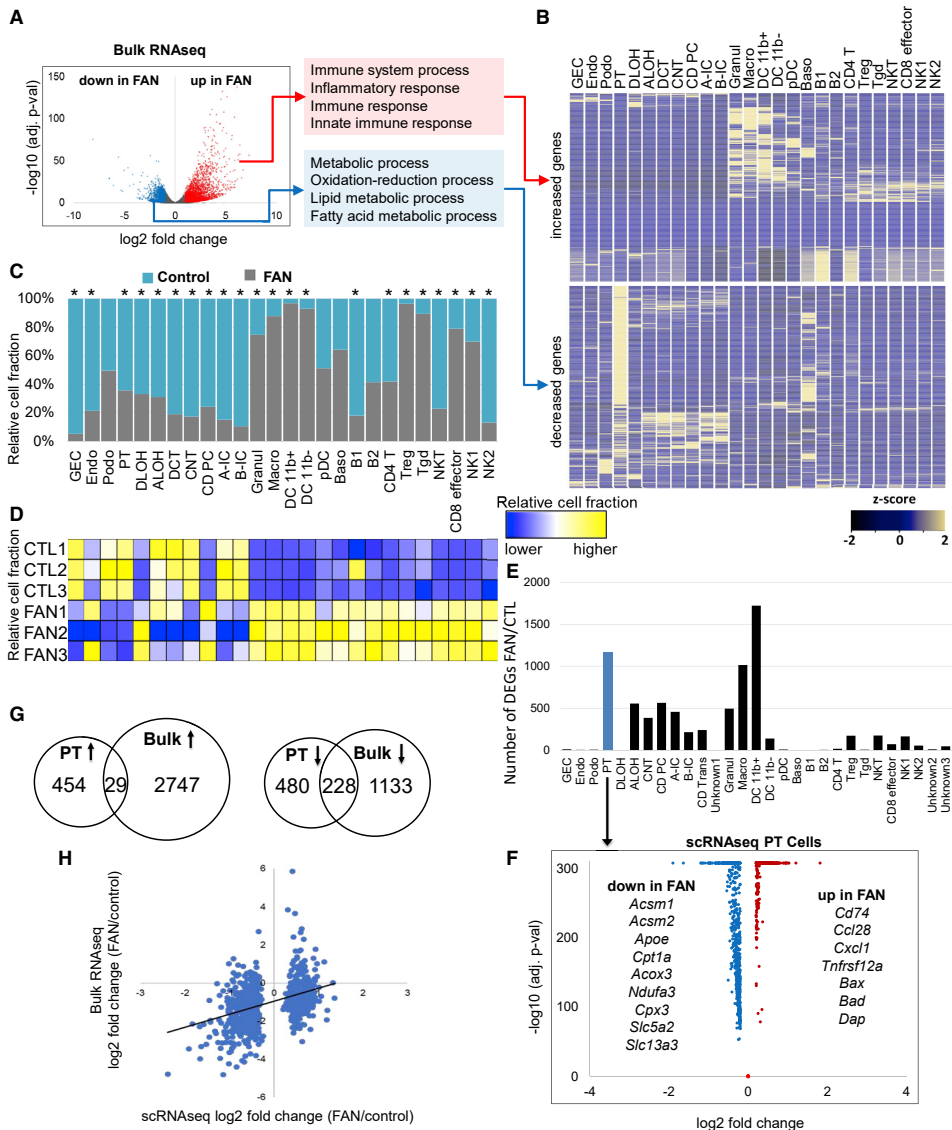
Figure 2. Cell Composition and Cell-Type-Specific Changes in Kidney Fibrosis

(A) DEGs in whole kidneys of control and FAN mice. Volcano plot: the x axis indicates log_2-fold change and y axis indicates statistical significance adjusted p = –log10. Gene ontology analysis of genes showing higher (red) and lower (blue) in FAN kidneys.

(B) Cell-type-specific expression of top DEGs identified in bulk RNA-seq analysis in the single-cell dataset. Mean expression values of the genes were calculated in each cluster. The color scheme is based on Z score distribution.

(C) Cell proportion changes in control and FAN kidneys revealed by scRNA-seq. * indicates significant changes by proportion test.

(D) Cell proportion changes revealed by in silico deconvolution of bulk RNA-seq data.

(E) The numbers of cell-type-specific differentially expressed genes identified in control FAN kidneys in the 30 cell clusters.

(F) Volcano plot for DEGs between control and FAN PTs identified in the single-cell data. The x axis is log_2-fold change and y axis is statistical significance adjusted p = –log10.

(legend continued on next page)

Cell Metabolism
Article

CellPress

Tyrobp, in the bulk RNA-seq data showed similar expression patterns in control and FAN samples at a single-cell level (Figure S2A). This suggests that the majority of genes showing higher expression in disease were related to immune cell proportion changes rather than cell-specific changes.

Next, we determined cell proportion changes using single-cell and bulk RNA-seq data. We found marked differences in cell proportion, such as a distinct increase in the proportion of myeloid and lymphoid cells (e.g., macrophages [7.2-fold], granulocytes [2.9-fold], Tregs [27-fold], and CD8 effector cells [3.8-fold]) but a decrease in the proportion of tubule epithelial cells (e.g., PT [0.55-fold] and distal convoluted tubule [0.23-fold]) in the single-cell data of the FAN model (Figure 2C). In contrast, consistent with prior observations, the proportion of podocytes did not show clear changes in the FAN model (Figure 2C). We also performed *in silico* deconvolution of bulk RNA-seq data implemented in the CellCODE package. This analysis yielded results broadly consistent with the single-cell RNA-seq data (Figure 2D), such as higher immune cell fractions and lower epithelial cell fractions. Finally, cell proportion changes in epithelial and immune cells were confirmed by histological analysis (Figure S1A).

To further understand the contribution of cell-type-specific and cell fraction changes in bulk RNA-seq results, we directly compared the single-cell with the bulk data. After adjusting the data to the observed cell fraction changes, the number of genes showing differential expression was markedly reduced. Among the 4,137 differentially expressed genes in the bulk data, only 14, 2, 902, and 753 genes remained significant after adjustment to the proximal convoluted tubule (PCT), proximal straight tubule (PST), and myeloid or lymphoid cell fractions, respectively (Figure S2B).

To unravel cell-type-specific gene expression changes in the FAN model, we performed differential expression analysis in all identified cell types. Keeping in mind the limitation of this analysis, such as the complete confounding of the disease-state and possible batch effect, we found that myeloid cells such as macrophages showed a large number of differentially expressed genes (Figure 2E). We found that among the epithelial cells, PT cells showed the largest number of differentially expressed genes (Figure 2E; Table S2). Genes that showed lower expression levels in diseased PT cells were solute carriers (cell-differentiation-related genes), such as *Slc5a2* and *Slc13a3*, as well as genes involved in FAO and OXPHOS (e.g., *Acsm1*, *Acsm2*, *Cpt1a*, *Acox3*) (Figure 2F).

Even though PT cells represented a large portion of the bulk dataset, only a fraction of differentially expressed genes observed in PT cells were shared in the bulk RNA-seq data (Figure 2G), and the correlation between the PT-cell-specific differentially expressed genes in the single-cell and bulk data was weak (Figure 2H).

Altered Differentiation Drives Proximal Tubule Response during Fibrosis
To better understand cell state changes in PT cells, we performed sub-clustering and cell trajectory analysis of healthy

and diseased samples from CKD mouse models. In healthy controls, we identified several PT cell subtypes, including PST cells expressing *Slc22a30*, and several subgroups of PCT expressing *Slc5a2* and *Slc5a12* (Figure 3A; Table S3). RNA velocity analysis is a new way of studying cellular differentiation (La Manno et al., 2018) by predicting the future state of individual cells. Our analysis indicated that in control kidneys, PT cells differentiated into two major cell types: PCT and PST segments (Figures 3B and 3C). Interestingly, the analysis highlighted that PT cells originated from a common precursor-like cell, expressing higher levels of *Med28* and *Cycs* (Figure 3D). Importantly, our analysis also suggested that PT cell differentiation did not necessitate cell proliferation, as we did not observe changes in the expression of proliferation markers (Figure 3D).

PT cells from FAN samples sub-clustered into nine groups. Using anchor genes to identify key cell types such as PCT and PST segments, we were able to recognize more heterogeneous cell populations, including proliferating cells, immune marker (*Cd74*)-expressing cells, transitional cells, and precursor cells expressing higher *Igfbp7* (Figure 3E; Table S3). In diseased samples, we also identified a prominent proliferating (i.e., *Ki67*-positive) cell population, and it appeared that cells entered and exited this *Ki67*-positive state. These data are consistent with a facultative progenitor model in kidney tubule cells (Angelotti et al., 2012; Kang et al., 2016) (Figure 3F). Notably, we identified a cell population expressing *Notch2* and *Lgr4*, which were previously identified as progenitor and transit-amplifying cells in the kidney and other organs (de Lau et al., 2011; Zhang et al., 2019). We observed that PCT cells co-expressed PST markers, suggesting that under disease conditions, PCT cells may endure transcriptomic changes impacting their phenotypic signature. Similar to our observation in the control samples (Figure 3B), FAN samples showed a differentiation trajectory toward PCT and PST segments (Figures 3G and 3H) but followed a less organized differentiation path than healthy PT cells (Figure 3G). In contrast, we failed to observe a clear reversal of the differentiation of cells already expressing terminal differentiation markers such as *Slc5a2* or *Slc22a30*, indicating that a failure of differentiation rather than dedifferentiation is the reason for the identified cell-state changes.

Differentiation Defects in Fibrotic Proximal Tubules Track with Changes in Lipid Metabolism
Next, we opted to take advantage of the continuous cell trajectory analysis using the Monocle package by combining all samples under healthy and disease states (Trapnell et al., 2014). Initial exploration showed a clear branching of PT cells into PCT and PST segments (Figures 4A, 4B, and S3A), which was mostly consistent with the RNA velocity analysis. To identify genes whose expression changed along the trajectory, we first performed a trajectory analysis for the PST segment, as this segment is highly susceptible to injury (Figures 4C, 4D, and S3B). Cells from control and diseased kidneys seemed to follow a similar linear trajectory toward PST segment differentiation

---

(G) Venn diagrams showing the overlaps between the identified differentially expressed genes in PT cells by scRNA-seq data and bulk RNA-seq data in control versus FAN kidneys (Up arrow: upregulated genes and down arrow: downregulated genes).

(H) Scatter plot showing the correlation of DEGs identified in PT cells and bulk data. The x axis shows the fold change expression in PT cells in the single-cell data, y axis shows the fold change expression in the whole kidney (bulk) samples.
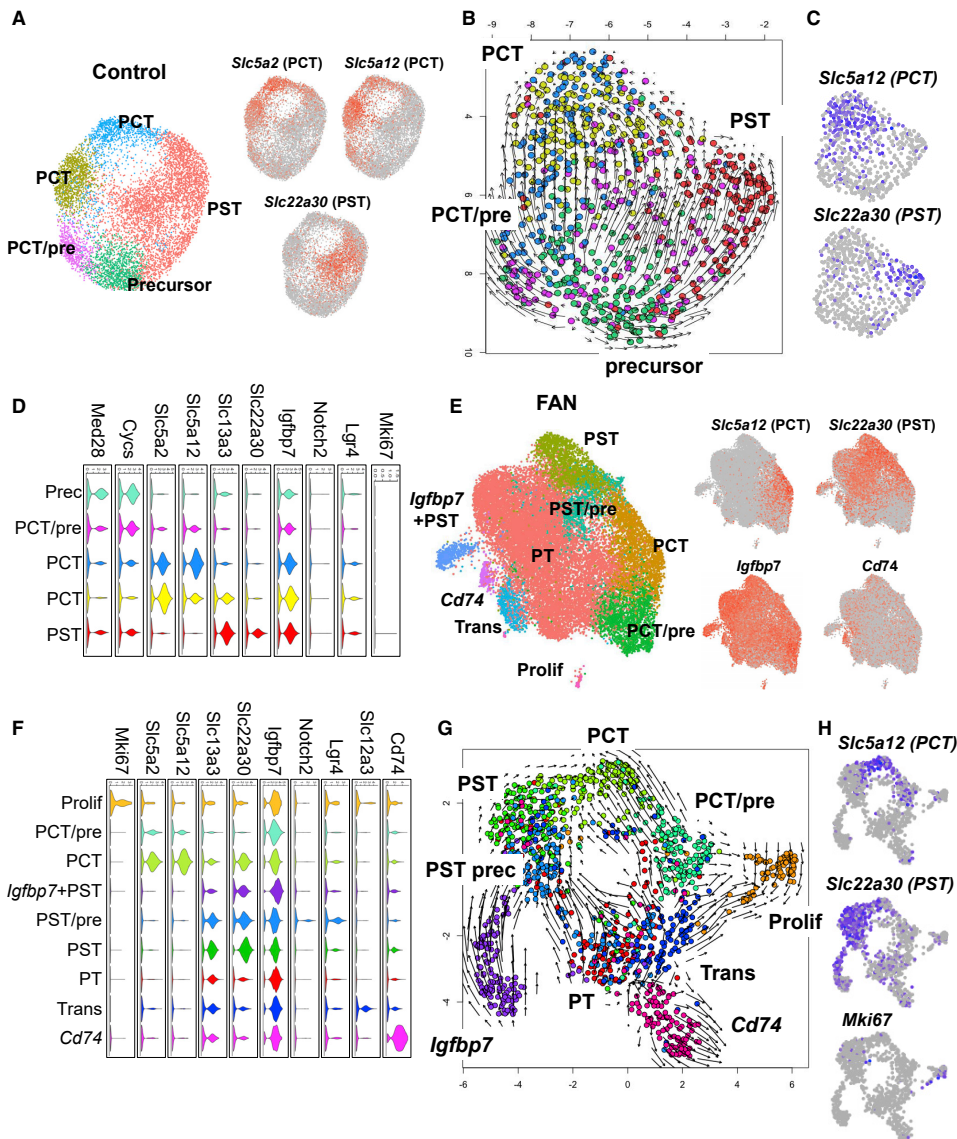
Figure 3. Heterogeneous PT Cell Populations in Fibrotic Kidneys

(A) Sub-clustering of PT cells into five subpopulations in control kidneys. Feature plots showing the expression of key PCT (*Slc5a2* and *Slc5a12*) and PST (*Slc22a30*) segment markers.

(B) RNA velocity analysis of the control of PT cells. Each dot is one cell, and each arrow represents the time derivative of the gene expression state.

(C) Feature plots showing the expression of key PCT (*Slc5a12*) and PST (*Slc22a30*) segment markers in control.

(D) Violin plots showing the expression patterns of markers across PT cell sub-clusters in control. The y axis shows the log-scale normalized read count.

(E) Sub-clustering of PT cells into nine sub-populations in FAN kidneys. Feature plots showing the expression of key PCT (*Slc5a12*) and PST (*Slc22a30*), *Igfbp7* (precursor), and *CD74* (immune) PT cell state markers.

(F) Violin plots showing the expression patterns of markers across PT cell sub-clusters in FAN. The y axis shows the log-scale normalized read count.

(G) RNA velocity analysis of FAN PT cells. Each dot is one cell, and each arrow represents the time derivative of the gene expression state.

(H) Feature plots showing the expression of key PCT (*Slc5a12*) and PST (*Slc22a30*) and proliferating (*MKi67*) PT cell markers.
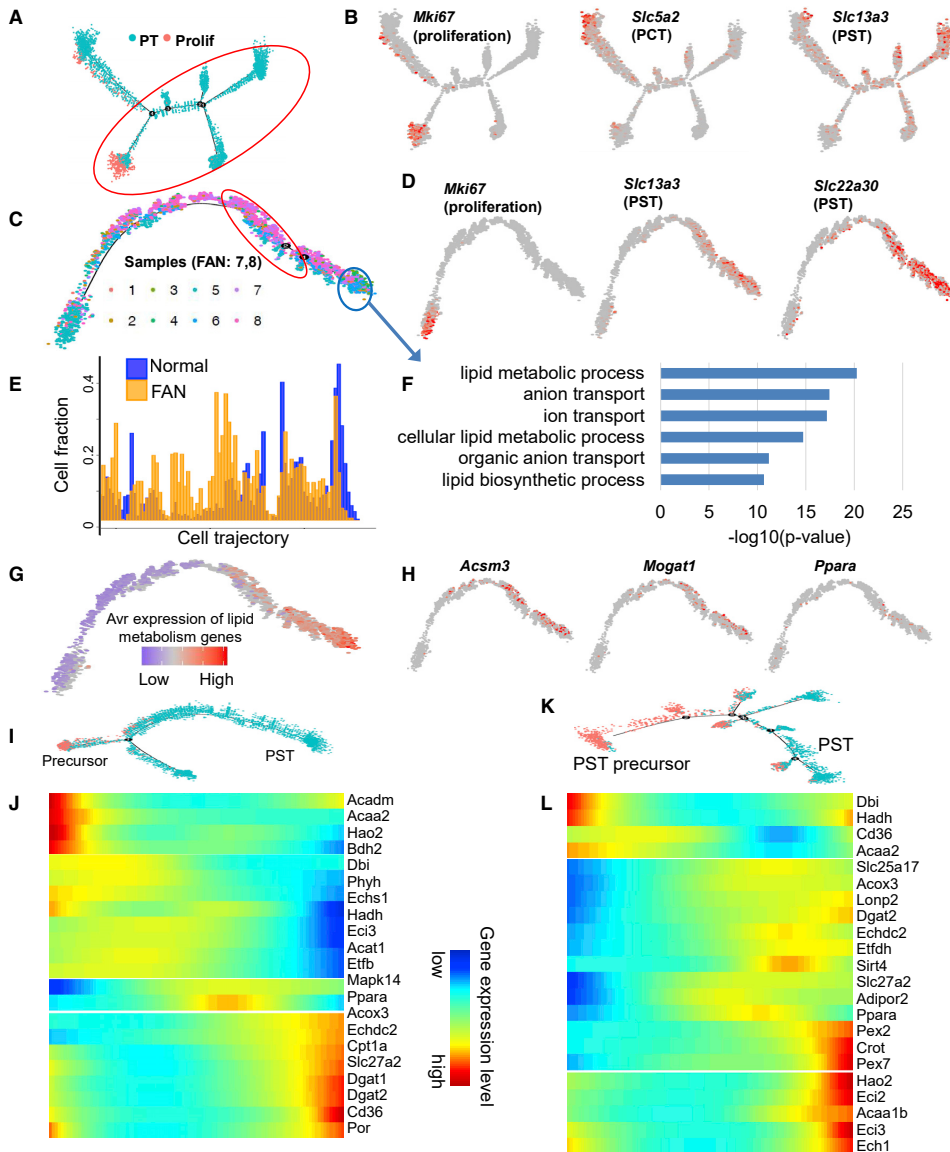
Cell Metabolism
Article

CellPress

Figure 4. Cell Trajectory Analysis Identifies Differentiation Defect in PT in Fibrosis

(A) trajectory analysis of PT cells (including proliferating cells) using Monocle, including all control and FAN samples.

(B) Feature plots showing the expression levels of key cell state markers (*Mki67*: proliferating cell, *Slc5a2*:PCT, *Slc13a3*:PST) on the cell trajectory.

(C) Cell trajectory analysis focused on the PST cluster (cells under red circle in A). Batches 1–6 represent healthy kidneys, whereas batches 7–8 were obtained from FAN samples.

(D) Feature plots showing the expression levels of key cell state markers (*Mki67*: proliferating cell, *Slc22a30*:PST, *Slc13a3*:PST) on the cell trajectory.

(E) Distributions of cells along the pseudotime trajectory. Note the shift of Normal (blue) and FAN samples (yellow).

(F) Functional annotation (gene ontology) analysis of genes showing changes along the trajectory (cells highlighted by red and blue circles on C).

(G) Average expression levels of the highly variable genes that are involved in lipid metabolism along the cell trajectory.

(H) Feature plots showing the expression levels of the lipid metabolism genes (*Acsm3, Mogat1,* and *Ppara*) along the cell trajectory.

(legend continued on next page)

(i.e., no major branching), but FAN samples were significantly depleted from the terminally differentiated PT cells (two-sample proportion test between cells in the red and blue area, p value < $2.2e^{-16}$) (Figures 4C and 4E). Trajectory analysis of PCT segment cells showed a similar pattern (Figures S3C and S3D). These data are consistent with prior observations, indicating lower levels of terminally differentiated markers in FAN samples (Figure 3G).

When we interrogated genes and pathways that underlie the PT cell differentiation state, we found that the expression of genes associated with terminal differentiation, such as those with ion transport function (i.e., SLCs, solute carriers), increased along the differentiation trajectory (Figure 4F). In addition to ion transport, lipid metabolism showed a positive correlation with cellular differentiation (Figures 4F–4H and S3E). Moreover, we observed changes in FAO genes along the differentiation path from precursor to PT cells in both healthy controls and FAN samples (Figures 4I–4L).

We also generated scRNA-seq data from the unilateral ureteral obstruction (UUO) model of kidney fibrosis and compared cell trajectories in the UUO and the FAN models. Continuous cell trajectory analysis showed a selective lack of terminally differentiated PT cells in UUO kidneys, recapitulating the results obtained from the FAN model (Figures S3F–S3H). In addition, when examining pathways associated with the differentiation of PT cells along the cell trajectory, we found enrichment for FAO, OXPHOS, and ion transport (Figures S3I and S3J). There was a strong (>50%) overlap of gene expression changes along the respective differentiation trajectories in the UUO and FAN models (Figure S3K).

Partial epithelial-mesenchymal transition (EMT) has been used to describe the aberrantly differentiated PT cells (Grande et al., 2015; Lovisa et al., 2015; Zeisberg and Duffield, 2010). We found that EMT markers tended to be lower upon PT cell differentiation (Figure S3L). However, we failed to observe significant expression of Zeb, Twist, and Snai in the different PT cell sub-clusters in fibrotic samples (Table S4). We also failed to observe cells exhibiting classic senescence markers (senescence-associated secretory phenotype [SASP]) (Table S4).

Proximal Tubule Differentiation in Kidney Organoids Correlates with Metabolic Changes

To distinguish whether lipid metabolism and OXPHOS only correlate with PT-cell-specific gene expression or are true drivers of PT cell maturation, we tested the role of FAO and OX-PHOS in tubule cell differentiation of developing kidney organoids. Previously, we showed three-dimensional (3D) culture systems that recapitulate architectural and functional features of the human developing kidney, the so-called kidney organoids (Garreta et al., 2019). We generated human pluripotent stem cell (hPSC)s-kidney organoids in free-floating conditions by assembling nephron progenitor cells (NPCs) derived from hPSCs (Figure 5A). Bulk gene expression analysis of differentiating organoids indicated an increase in the expression of PPARGC1A

on days 16 and 21. The increase in the expression of PPARGC1A in organoids correlated with the expression of PT cell markers, such as SLC27A2, SLC3A1, and SLC5A12 (Figure 5B). As bulk RNA expression data cannot provide a faithful read-out for PT differentiation, we performed unbiased scRNA-seq analysis (Figure 5C). Clustering analysis based on cell-type-specific marker gene expression indicated that in addition to mesenchymal clusters, we could also identify a variety of kidney cell types resembling those of collecting duct, actively cycling cells, endothelial cells, podocytes, loop of Henle, and PT cells (Figures 5C and 5D). Next, we specifically examined the differentiation trajectory of organoid PT cells. Cells differentiated from a SIX1 positive progenitor and gained PT cell marker SLC3A1 expression (Figure 5E). Next, we analyzed genes whose expression changed along this trajectory and found that the expression of differentiation markers such as solute carriers increased along the trajectory and their expression strongly correlated with genes in FAO, including PPARA (Figure 5F). Finally, to confirm that FAO is a driver of cellular differentiation, we cultured kidney organoids in the glycolytic-promoting media (EGM, endothelial cell growth medium) or the OXPHOS-promoting media (REGM, renal epithelial cell growth medium). We found higher expression of PPARGC1A mRNA and lipid metabolic genes such as ACOX2, ACOT12, and CPT1A, when organoids were cultured in the REGM media for 4 days versus the EGM media (Figure 5G). We further assessed the protein levels of mitochondrial OXPHOS proteins in organoids exposed to both the REGM and EGM culture media (Figures 5H, S4A, and S4B). Concomitantly to these metabolic changes, we observed that the REGM media led to an increase in the expression of PT cell markers such as SLC34A1, SLC27A2, SLC5A12, SLC6A19, and SLC3A1 compared with the EGM media (Figure 5G). These results run in parallel with our in vitro observations of cultured PT cells from mice (Figures S4C and S4D). In addition, organoids exhibited a visibly higher number of PTs as observed by immunofluorescence (IF) analysis for Lotus Tetragonolobus Lectin (LTL) labeling (Figures 5I and 5J).

ESRRA Drives Proximal Tubule Differentiation in Mouse Models and Couples Metabolism with Differentiation

In order to define the key transcriptional regulatory organization of PT cells, we analyzed mouse kidney single-cell open chromatin data (scATACseq) (Cao et al., 2018). Using a computation motif search algorithm, we found that the most enriched open binding motifs were HNF4A, HNF1B, PPARA, and ESRRA in PCT and PST cells (Figure 6A). Our single-cell gene expression analysis confirmed transcript enrichment for these 4 transcription factors in PT cells (Figure S5A). Next, we defined putative PPARA and ESRRA target genes by intersecting PCT- or PST-specific open chromatin region at promoters (transcription start site ±5kb) or gene body regions chromatin regions that contained PPARA- or ESRRA-binding motifs. Gene set enrichment analysis showed enrichment for PPARA- and ESRRA-target genes (Table S5) in differentiated PST and PCT cells (Figures

---

(I) Cell trajectory analysis for PST and precursor clusters identified in control kidneys (Figure 3A).

(J) Heatmap showing the expression changes of highly variable FAO genes along the cell trajectory in control kidneys.

(K) Cell trajectory analysis for PST and precursor clusters identified in FAN samples (Figure 3E).

(L) Heatmap showing the expression changes of highly variable FAO genes along the cell trajectory in FAN samples.
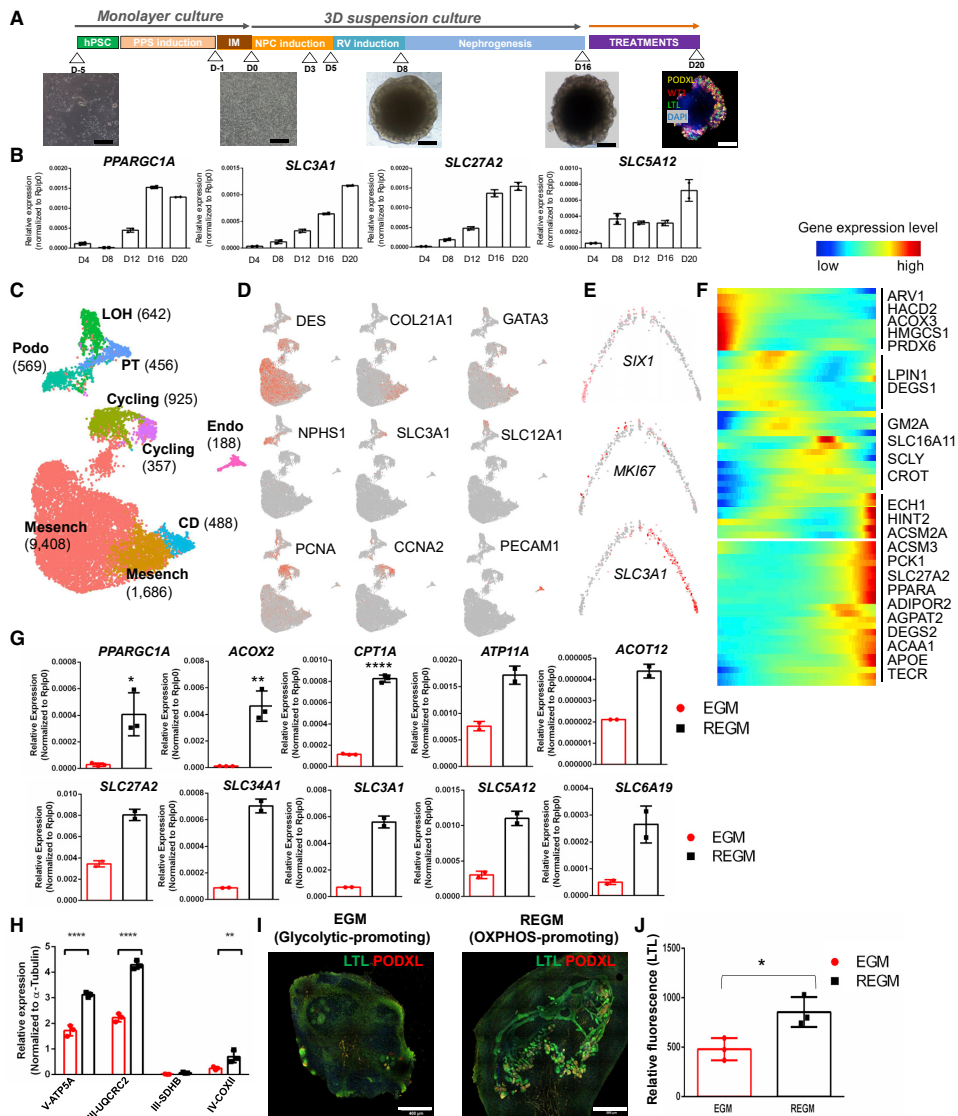
Cell Metabolism
Article

CellPress

Figure 5. FAO and OXPHOS Drive PT Differentiation in Human Kidney Organoid

(A) Experimental scheme for the generation of human kidney organoid. Briefly, hPSCs were first differentiated into posterior primitive streak (PPS) fate and then into intermediate mesoderm (IM). Cells were aggregated (day 0, D0) and further differentiated in a 3D culture into renal vesicle (RV) and nephron stage. At D20 of differentiated kidney, organoids were stained for podocalyxin (PODXL: podocyte marker, yellow), Wilm's tumor 1 (WT1, red), and Lotus Tetragonolobus Lectin (LTL: PT marker, green). Scale bar, 200 μM.

(B) Transcript expression levels (in bulk organoids) of *PPARGC1A*, *SLC3A1*, *SLC5A12*, and *SLC27A2* on days 4, 8, 12, 16, and 20 of organoid differentiation. Data are represented as mean ±SEM. n = 2 independent experimental replicates analyzed from a pool of 12 organoids/group.

(C) scRNA-seq analysis of human kidney organoid. UMAP showing nine distinct cell types identified by unsupervised clustering. Mesench, mesenchymal cells; CD, collecting duct; Endo, endothelial cells; cycling, cell cycling cells; Podo, podocytes; LOH, loop of Henle; and PT, proximal tubule.

(D) Feature plots of key cell type markers (*DES, COL21A1, Gata3*; mesenchyme, *NPHS1*; podocytes, *SLC3A1*; PT cell, *SLC12A1*; LOH, PCNA, *CCNA2*; proliferating cells, *PECAM11*; endothelial cells).

(E) Expression of *SIX1* (nephron progenitor marker), *MKI67* (proliferation maker), and *SLC3A1* (PT cell marker) along the differentiation trajectory.

(legend continued on next page)

6B and S5B). PT-specific PPARA and ESRRA target genes were enriched for kidney development, lipid metabolism, and epithelial transport functions (Figures 6C and S5C).

To functionally confirm the role of ESRRA in cellular differentiation, we treated LTL+ PT cells with *Esrra* siRNA or XCT790, a pharmacological inhibitor (inverse agonist) of ESRRA. We observed that reduced *Esrra* activity led to compromised mitochondrial function, as assessed by oxygen consumption rate (OCR) and OXPHOS protein levels as well as decreased mitochondrial DNA content. In addition, reduced *Esrra* led to a lower expression of PT differentiation genes (Figures 6D–6G and S6A–S6D). We next transfected LTL+ PT cells with ESRRA, PPARA, or all four TFs (ESRRA, PPARA, HNF4A, and HNF1B) plasmids. ESRRA overexpression in PT cells not only improved mitochondrial function and mtDNA copy number but also led to an increase in the expression of SLC genes (Figures 6D–6G and S6D–S6F). We found that the overexpression of PPARA, HNF1B, and HNF4A had a synergistic effect as evidenced by the strong additive effect on cellular differentiation, such as the expression of SLCs (Figures S6E and S6F). To establish the role of ESRRA in human PT cell differentiation, we treated human primary renal PT epithelial cells (HPTCs) and kidney organoids cultured in the REGM media with XCT790 for 48 h. Kidney organoids and HPTCs treated with XCT790 showed impaired FAO (Figures S6G and S6I) and reduced expression of SLC genes such as *SLC3A1, SLC27A2, SLC34A1, SLC6A19*, and *ATP11A* (Figures S6G and S6I). Overall, we found that ESRRA inhibition negatively affected PT differentiation as shown by the decreased LTL fluorescence intensity (Figure S6H).

Finally, to distinguish whether ESRRA directly (via binding of the promoter) or indirectly (via improving metabolism) regulated PT cell differentiation, we performed chromatin immunoprecipitation (ChIP) coupled with detection by quantitative real-time PCR (ChIP-qPCR) to study the ESRRA transcription factor binding to DNA in PT cells. We found enrichment for multiple PT-specific genes such as *Slc5a11, Slc6a13, Slc6a19, Slc13a3, Slc7a13, Slc22a6*, and *Slc22a28* and metabolic genes such as *Adipor2* and *Acadm* (Figure 6H).

To define the role of *Esrra* in kidney disease, we challenged *Esrra* knockout (KO) mice with FA (Figure 6I). We found that the expression of *Esrra* was lower in FAN and UUO models of fibrosis when compared with controls (Figures 6I and S6J). We observed that *Esrra* KO mice showed increased susceptibility to FA-induced kidney injury compared with wild-type littermates as detected by histological analysis (Figure S6K). Levels of pro-fibrotic markers such as *Col1a1* and *Col3a1* were higher in FA-treated *Esrra* KO mice (Figure S6L) compared with wild-type

counterparts. Animals showed increased collagen accumulation on Sirius red stain (Figure S6M) and increased cell proliferation by Ki67 staining (Figure S6N). We further confirmed the decrease in SLC proteins (SLC6A13 and SLC34A1) and increase in pro-fibrotic proteins (SMA and FN) in *Esrra* KO mice upon FAN injury (Figures 6J and S6O). Further, we found that the genetic deletion of ESRRA in PT cells was associated with impaired mitochondrial function despite the compensatory increase in other nuclear receptors, such as *Esrrg* and *Ppara* (Figures S6P–S6Q), that improved by the re-expression of ESRRA. Similar to prior results, we found that PPARA also regulated PT metabolism and cellular differentiation both *in vitro* and *in vivo* by using fenofibrate: a pharmacologic activator of PPARA (Figures S4C and S5D) (Kang et al., 2015), indicating a likely complex interaction between the different nuclear receptors in PT cells.

ESRRA Driven Metabolic Changes Correlates with Kidney Disease Severity in Patient Samples

Finally, we wanted to ascertain whether ESRRA-driven metabolism and PT cell differentiation that appears to drive disease development in mouse kidney disease models can also be recapitulated in patients with CKD. We analyzed 91 microdissected human kidney tubule samples obtained from healthy subjects and patients with diabetic and hypertensive kidney disease (Table S7). First, we examined the expression of genes involved in FAO and found a group of genes, which strongly correlated with kidney fibrosis (Figure 7A). These genes included *ADIPOR2, PPARA, ACSM2A, ACSM3, and APOE*, for which we had previously demonstrated an increase along the PT differentiation trajectory (Figure 4J). Correlation analysis revealed that the expression of lipid metabolism genes showed a positive correlation with the expression of PT cell differentiation and negative correlation with fibrosis (Figure 7B). *In silico* deconvolution of bulk transcriptome data from 91 human samples showed that the proportion of PCT and PST cells decreased in fibrotic tissues (Figure 7C). Next, we assessed the effect of cell proportion changes on gene expression changes observed in bulk gene profiling data (Figure 7C). Expression of a total of 1,980 genes significantly correlated with fibrosis scores in 91 human kidney samples analyzed by linear regression using age, gender, race, and diabetes and hypertension status as covariates (FDR < 0.05). Next, we performed *in silico* deconvolution analysis of the data using CellCODE. Adjusting the model to the 4 cell lineages (PCT, PST, myeloid, and lymphoid cells) reduced the number of differentially expressed genes (DEGs) from 1,980 to 22 genes, indicating the key role of cell heterogeneity in driving bulk gene expression changes (Figure S7A).

(F) Heatmap showing the expression changes of highly variable genes involved in FAO identified (Figures 4J and 4L) along the organoid cell differentiation trajectory.

(G) Expression level of genes associated with FAO (*PPARGC1A, ACOX2*, and *CPT1A*), and PT cell markers (*ATP11A, ACOX12, SLC27A2, SLC34A1, SLC3A1, SLC5A2*, and *SLC6A19*) in kidney organoids cultured in the EGM and REGM media. The data are represented as mean ±SEM. n ≥ 2 independent experimental replicates from a pool of 12 organoids/group; *p < 0.05, **p < 0.01, ***p < 0.001, and ****p < 0.0001 paired Student's t test.

(H) Quantification of changes in the protein expression of OXPHOS proteins in organoids cultured in the EGM or REGM media. Tubulin is used as loading control. The data are represented as mean ±SEM. n = 3 independent experimental replicates from a pool of 16 organoids/group; *p < 0.05, **p < 0.01, ***p < 0.001, and ****p < 0.0001 two-way ANOVA, followed by the Bonferroni post-test.

(I) Representative immunofluorescence staining of LTL (green) and PODXL (red) in kidney organoids cultured in the EGM and REGM media. Scale bar represents 400 μM (EGM) and 500 μM (REGM).

(J) Quantification of LTL positive cells in kidney organoids cultured in the EGM or REGM media. The y axis represents relative fluorescence. The data are presented as mean ±SEM. n = 3 organoids/group.

Cell Metabolism
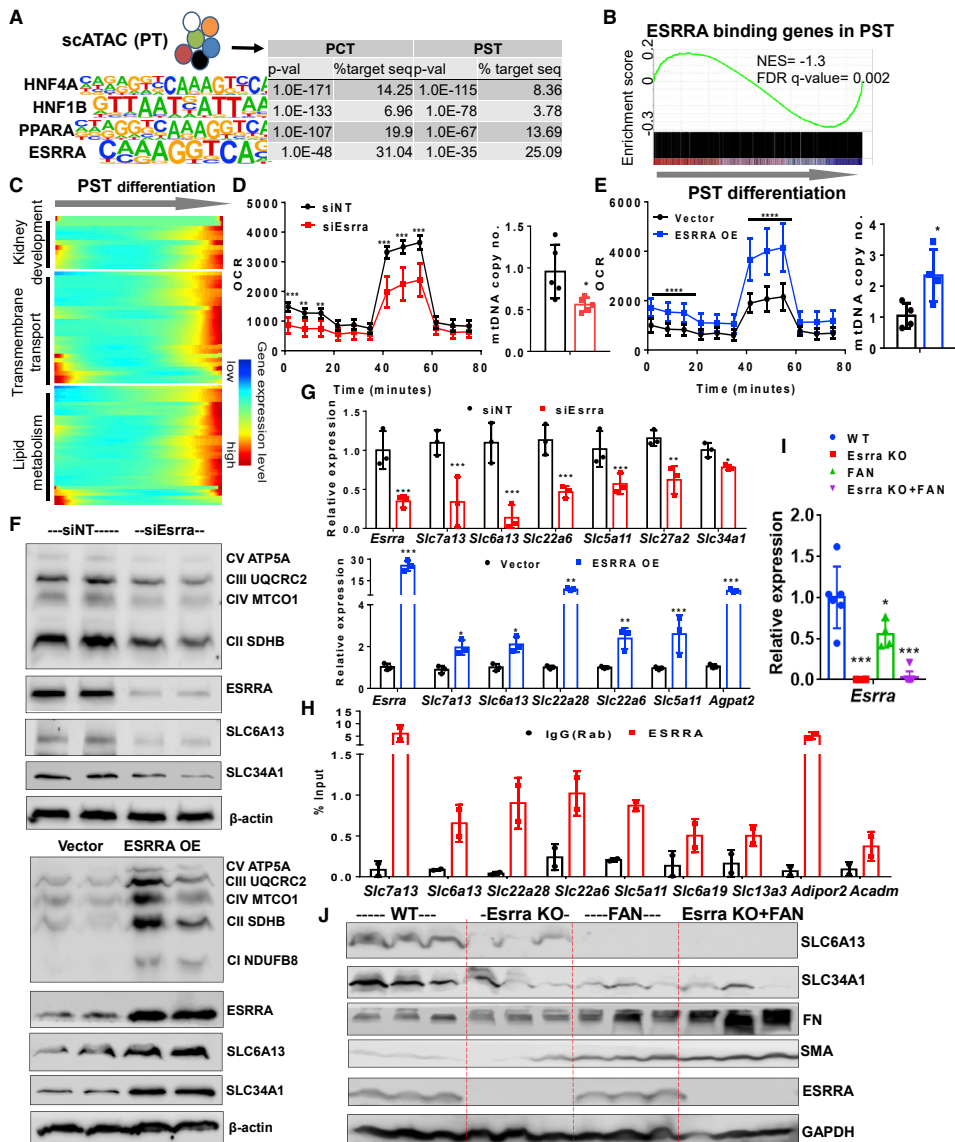## Article

CellPress

Figure 6. ESRRA Drives PT Differentiation State and Protects from Kidney Disease

(A) Top transcription factor-binding motifs significantly enriched in PT-cell-specific open chromatin regions that are identified from mouse single-cell ATAC-sequencing. p values and percentages of target sequences among all open chromatin regions are shown in the table on right.

(B) Gene set enrichment analysis (GSEA) enrichment plot of ESRRA target genes along with PST cell differentiation.

(C) Heatmap showing the expression changes of ESRRA target genes along the PST differentiation trajectory (ordered from Figure 4C) grouped by functional annotation (kidney development, transmembrane transport, and lipid metabolism).

(D) OCR (pmol/min/μg of protein) and mtDNA copy number (ratio of mtDNA to nuclear DNA) in LTL$^+$ PT cells transfected with non-target siRNA (siNT: black) and ESRRA siRNA (si$Esrra$: red) for 2 days. *$p < 0.05$, **$p < 0.01$, ***$p < 0.001$ versus siNT.

(E) OCR and mtDNA copy no. in LTL$^+$ PT cells transfected with vector alone (black) and ESRRA expressing vector (ESSRA OE: Blue) for 48 h. *$p < 0.05$, **$p < 0.01$, ***$p < 0.001$ versus vector.

(F) Protein levels of OXPHOS, ESRRA, SLC6A13, and SLC34A1 in LTL$^+$ PT cells transfected with si$Esrra$ (upper panel) or ESRRA OE (lower panel) shown by Western blot. β-actin was used as a loading control.

(legend continued on next page)

Finally, we examined the expression of *ESRRA* and its target genes in 431 microdissected human kidneys (Table S7). The expression of *ESRRA* was lower in disease samples and strongly correlated with both eGFR and kidney fibrosis (Figure S7B). Protein expression of ESRRA was mostly localized to the nuclei of PTs, and it was markedly lower in human CKD samples (Figure S7C). The expression of *ESRRA* in human kidney tubule samples correlated with lipid metabolism and PT markers as well as with membrane transporter genes that are ESRRA targets (Figure 7D). These results confirm the relationship between the PT (differentiation) state and metabolism via ESRRA and PPARA.

DISCUSSION

Here, we present a comprehensive analysis using mouse scRNA and epigenome analysis, cultured cells, mouse models, patient samples, and kidney organoids to demonstrate that PT cells exist in different differentiation states in health and disease conditions. Our results highlight PT cellular metabolism as one of the main drivers of PT cell differentiation, identifying ESRRA as a central player in coupling metabolism and differentiation by directly binding and regulating the expression of PT genes. Furthermore, our observations describe how ESRRA together with HNF1B, HNF4A, and PPARA likely forms a complex network regulating PT metabolism and differentiation. ESRRA-driven PT metabolism and differentiation plays a critical role in protecting the kidney from injury and correlates with kidney disease severity in patient samples.

We show that the gene expression changes observed in bulk RNA-seq analysis mostly reflected cell heterogeneity of diseased mouse and human kidney samples. For example, PT-specific genes had lower expression levels in bulk RNA-seq analysis; however, many of these genes showed no clear change at a single-cell level. Genes that showed higher expression in disease samples were mostly genes exclusively expressed in immune cells; however, they did not show marked changes in the single-cell data when control and disease samples were compared. There was a marked increase in cell diversity of healthy and diseased samples, which mostly related to the increase in the diversity of immune cells.

We provide a high-resolution comprehensive analysis of cell-type-specific changes in two different mouse kidney fibrosis models. We identified different PT cell subtypes in healthy and disease states. In addition to the known PCT and PST segments, we also identified precursor-like cells. Cell heterogeneity was significantly higher in diseased PT cells as we identified proliferating cells, immune marker expressing cells and transitional cells (such as PCT and PST intermediate cells), and PT-LOH intermediate cells. Future studies will determine the role of these cells in disease development. It is important to note that these cell populations represented a continuum between the established PCT and PST cells rather than true discrete groups. Using trajectory and clustering methods, we identified cell state differences among PT cells. We identified precursor cells that expressed high levels of *Igfbp7* but lower levels of differentiated PT cell markers. IGFBP7 is one of the best-known biomarkers of AKI (Meersch et al., 2014; Vijayan et al., 2016). Further studies shall examine the connection between the kidney and urinary IGFBP7 expression, renal injury, and outcome.

We found that in diseased kidneys, fewer PT cells were in the terminal differentiation state. Increased death of differentiated cells could have contributed to this finding; however, only minimal changes in cell death were observed at the stages examined (Bielesz et al., 2010). Consistent with prior reports, Wingless-related integration site (Wnt) gene expression correlated with cell differentiation in one but not in the second kidney fibrosis model (Edeling et al., 2016; He et al., 2009; Kato et al., 2011; Rinkevich et al., 2014). Changes in lipid metabolism, FAO, and OX-PHOS were consistent in both models. This might be consistent with earlier reports that such developmental pathways regulate metabolic changes in diseased kidneys (Huang et al., 2018). Overall, our results indicate that kidney PT cells exist in different states where higher expression of cell function genes (e.g., SLCs) strongly correlates with higher expression of FAO and OX-PHOS genes.

Biologically, the coupling of metabolism and cell state makes perfect sense, as it harmoniously couples energy production and utilization with cellular function. Coupling of cell state and metabolism have been best demonstrated in the field of immunometabolism. For example, effector T cells exhibit high glycolysis, whereas regulatory cells have higher FAO and mTORC1 activation, which in turn drives effector differentiation while suppressing regulatory generation (Angelin et al., 2017; Delgoffe et al., 2009; Michalek et al., 2011). Dysregulated metabolism contributes to disease development, as T cells from systemic lupus erythematosus patients exhibit increased glycolysis and OXPHOS, whereas increased fatty acid biosynthesis and reduced ROS levels are associated with rheumatoid arthritis (Kornberg et al., 2018; Shen et al., 2017; Yang et al., 2013; Yin et al., 2015). Recently, sodium-glucose cotransporter 2 inhibitors have shown remarkable success in reducing the decline the kidney function (Barnett et al., 2014), therefore it is possible that reducing the PT cellular energy requirement is part of their mechanism of action.

Our results, for the first time, define the key role of several nuclear receptors such as PPARA and ESRRA in driving PT cell differentiation. ESRRA is a critical transcription factor that regulates mitochondrial biogenesis and FAO (Singh et al., 2018; Soriano et al., 2006). ESRRA remains an underappreciated nuclear receptor and metabolic target owing to its diverse role in multiple

(G) Relative mRNA levels of *Esrra* and variety of SLC markers (*Slc7a13, Slc6a13, Slc22a6, Slc5a11, Slc27a2,* and *Slc34a1*) in LTL+ PT cells transfected with siNT, *siEsrra* (red), and ESRRA OE plasmid (blue). *$p < 0.05$, **$p < 0.01$, ***$p < 0.001$ versus siNT/vector.

(H) ChIP-qPCR of ESRRA showed enrichment in genes including SLC markers (*Slc7a13, Slc6a13, Slc22a28, Slc5a11, Slc6a19,* and *Slc13a3*) and metabolic genes (*Adipor2* and *Acadm*) in LTL+ PT cells compared with IgG control. The data are represented as mean ± SEM.

(I) Relative gene expression of *Esrra* measured by qRT-PCR in kidneys of wild-type (n = 4), Esrra KO mice (n = 6), and FA-treated wild-type mice (n = 4) or FA-treated Esrra KO mice (n = 8). *$p < 0.05$, **$p < 0.01$, and ***$p < 0.001$ versus wild-type.

(J) Protein levels of SLC6A13, SLC34A1, FN, SMA, and ESRRA in kidneys of wild-type, Esrra KO mice, and FA-injected or FA-treated Esrra KO mice were analyzed by western blot. GAPDH was used as a loading control.
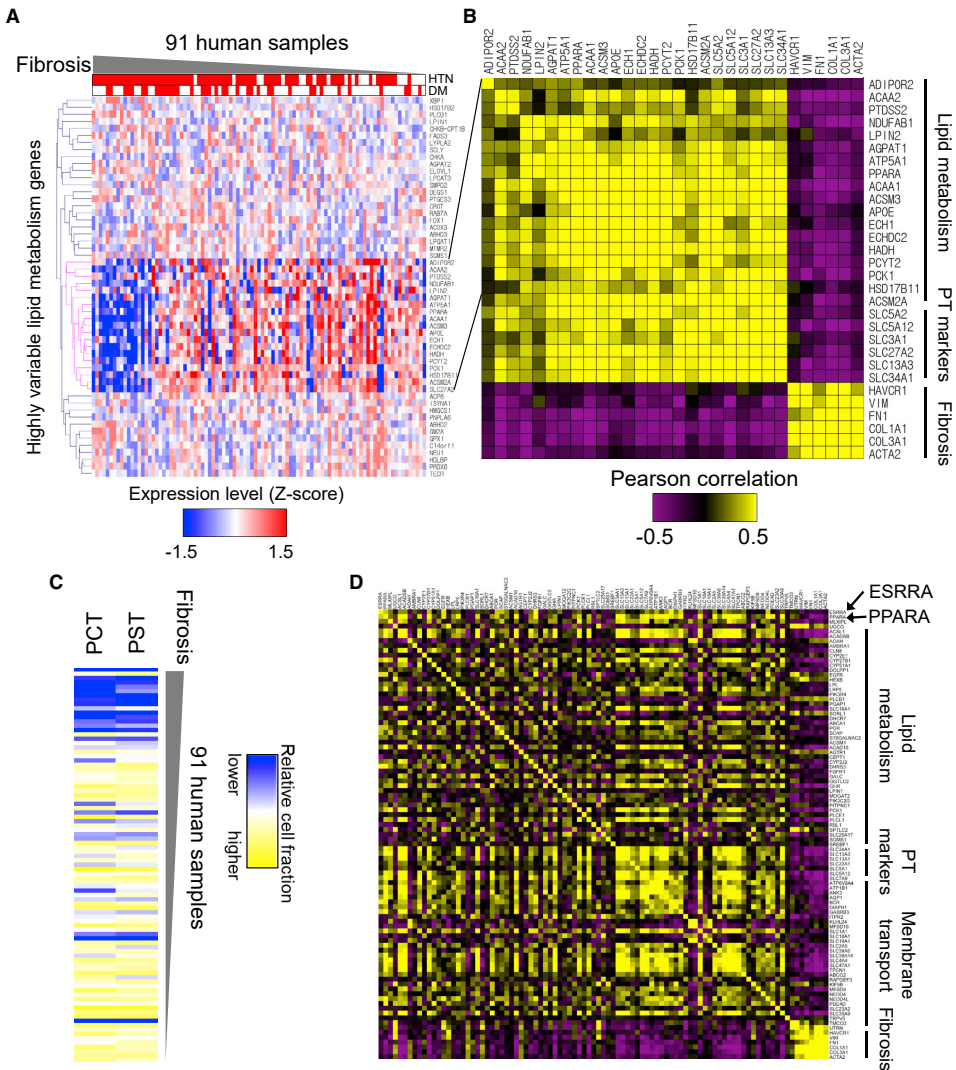
Cell Metabolism
Article

CellPress

Figure 7. ESRRA-Driven Metabolic Changes Correlate with Kidney Disease Severity in Patient Samples

(A) relative expression levels of the highly variable lipid metabolism genes that were identified along the mouse PT cell differentiation trajectory (Figure 4) in 91 microdissected human tubules. The human kidney samples were ordered based on the degree of fibrosis.

(B) Heatmap showing Pearson's correlation coefficient between lipid metabolism genes, PT cell markers, and fibrosis markers in the human samples (yellow positive correlation, purple negative correlation, and intensity indicates the strength of correlation).

(C) Heatmap showing the relative cell fraction changes, calculated by in silico deconvolution (CellCODE) of the 91 human kidney RNA profiling data. The human kidney samples were ordered based on their fibrosis scores.

(D) Heatmap showing correlation coefficients between lipid metabolism genes, PT cell markers, and transmembrane transport genes that contain ESRRA binding motifs in their promoter or gene body and fibrosis markers in the human samples (yellow positive correlation, purple negative correlation, and intensity indicates the strength of correlation).

cellular signaling pathways and its function as a co-regulator of metabolism. Here, we show that ESRRA not only transcriptionally regulates mitochondrial and metabolic genes but also

directly binds to genes associated with PT differentiation, such as a variety of SLCs. ESRRA target gene expression shows consistent changes in PT cell differentiation in vivo in mice and

CellPress

Cell Metabolism
Article

in patients, thus supporting the key role of ESRRA in driving cell state. ESRRA overexpression improved not only metabolism and mitochondrial function but also PT differentiation, and its inhibition resulted in impaired FAO and OXPHOS with altered differentiation state. We found that other transcription factors such as ESRRG and PPARA levels increased in the absence of ESRRA, which might be responsible for the lack of phenotypic changes at baseline; however, this compensation was insufficient to protect *Esrra* KO mice during kidney injury (Zhao et al., 2018; Marable et al., 2020). Previous studies have also showed the role of *Esrrg* in kidney tubules (Zhao et al., 2018).

It has been difficult to induce PT cell differentiation in cultured organoids (Combes et al., 2019; Wu et al., 2018). Using human kidney organoids, we show that FAO and OXPHOS directly drive the differentiation of PT cells. Our data indicate that increasing the activity of *Esrra* (and *Ppara*) could be beneficial for PT cell differentiation not only in mouse model in vivo but also in cultured organoids in vitro.

In summary, we show the continuum of PT cell states in health and disease and the key role of metabolism in driving PT cell state. ESRRA couples cell differentiation state and metabolism by regulating not only the expression of cellular metabolism but also the expression of key cell-type-specific genes. The work provides new opportunities to manipulate cell fate, PT cell differentiation, and metabolism based on their reliance on nuclear receptors such as ESRRA.

Limitations of the Study
There are several limitations of our study, and future studies shall carefully examine changes observed in non-PT cells in the context of kidney fibrosis and in patients with kidney disease. Follow-up studies should examine the large number of genes and cell type changes identified by single-cell analysis. Future studies are needed to study the detailed ESRRA regulatory network in the kidney and its interaction with other key PT transcription factors such as PPARA, HNF1B, and HNF4A.

STAR★METHODS

Detailed methods are provided in the online version of this paper and include the following:

- KEY RESOURCES TABLE
- RESOURCE AVAILABILITY
  - Lead contact
  - Materials Availability
  - Data and Code Availability
- EXPERIMENTAL MODEL AND SUBJECT DETAILS
  - Mouse Models
  - Isolation and Culture of *LTL*+ PT Cells
  - Kidney Organoids Differentiation
- METHOD DETAILS
  - Preparation of Single-Cell Suspension
  - Single-cell RNA Sequencing
  - Alignment and Generation of Data Matrix
  - Data Quality Control, Preprocessing and Dimension Reduction
  - Removal of Doublet-like Cells
  - Cell Clustering Analysis

- Mouse Bulk RNA-sequencing Analysis
- Estimation of Cell Proportions
- Identification of Marker Genes and Differentially Expressed Genes
- Cell Trajectory Analysis
- Monocle2
- Single Cell ATAC Sequencing Analysis
- Human Bulk Gene Profiling Data Analysis
- Single Cell Suspension from Kidney organoid
- Mitotracker Green FM Flow Cytometric Analysis
- Protein Extraction and Western Blot Analysis in Kidney Organoids
- Immunofluorescence
- Mitochondrial DNA Analysis
- PT Cell Transfection
- Oxygen Consumption Rate (OCR)
- Chromatin Immunoprecipitation qPCR
- Fenofibrate Treatment
- XCT790 Treatment
- qRT-PCR
- Western Blot
- Histological Analysis
- QUANTIFICATION AND STATISTICAL ANALYSIS
  - Data Representation and Statistical Analysis

SUPPLEMENTAL INFORMATION

Supplemental Information can be found online at https://doi.org/10.1016/j.cmet.2020.11.011.

AUTHOR CONTRIBUTIONS

K.S., J.P., P.D., and N.M. conceived and led this study. J.P. performed all the single-cell data analysis. P.D., S.H., and R.S. performed animal studies. P.D. performed all cell culture experiments. P.D. and S.H. performed histological analysis. C.H.d.P. and P.P. performed organoid studies. T.D. and R.S.

Cell Metabolism
Article

CellPress

performed kidney functional assay. S.Y.H., J.P.R., and F.P. contributed to organoid data analysis. J.P. performed computation analysis and helped by S.C., M.B., H.L., and X.S. P.J.D., H.M.K., K.B., M.L., L.P., and J.K. helped with data analysis. J.P., P.D., N.M., and K.S. wrote the paper.

REFERENCES

Angelin, A., Gil-de-Gómez, L., Dahiya, S., Jiao, J., Guo, L., Levine, M.H., Wang, Z., Quinn, W.J., 3rd, Kopinski, P.K., Wang, L., et al. (2017). Foxp3 reprograms T cell metabolism to function in low-glucose, high-lactate environments. Cell Metab. 25, 1282–1293.e7.

Angelotti, M.L., Ronconi, E., Ballerini, L., Peired, A., Mazzinghi, B., Sagrinati, C., Parente, E., Gacci, M., Carini, M., Rotondi, M., et al. (2012). Characterization of renal progenitors committed toward tubular lineage and their regenerative potential in renal tubular injury. Stem Cells 30, 1714–1725.

Barnett, A.H., Mithal, A., Manassie, J., Jones, R., Rattunde, H., Woerle, H.J., Broedl, U.C., and EMPA-REG RENAL trial investigators. (2014). Efficacy and safety of empagliflozin added to existing antidiabetes treatment in patients with type 2 diabetes and chronic kidney disease: a randomised, double-blind, placebo-controlled trial. Lancet Diabetes Endocrinol. 2, 369–384.

Beckerman, P., Qiu, C., Park, J., Ledo, N., Ko, Y.A., Park, A.D., Han, S.Y., Choi, P., Palmer, M., and Susztak, K. (2017). Human kidney tubule-specific gene expression based dissection of chronic kidney disease traits. EBioMedicine 24, 267–276.

Bielesz, B., Sirin, Y., Si, H., Niranjan, T., Gruenwald, A., Ahn, S., Kato, H., Pullman, J., Gessler, M., Haase, V.H., and Susztak, K. (2010). Epithelial Notch signaling regulates interstitial fibrosis development in the kidneys of mice and humans. J. Clin. Invest. 120, 4040–4054.

Breyer, M.D., and Susztak, K. (2016). The next generation of therapeutics for chronic kidney disease. Nat. Rev. Drug Discov. 15, 568–588.

Cao, J., Cusanovich, D.A., Ramani, V., Aghamirzaie, D., Pliner, H.A., Hill, A.J., Daza, R.M., McFaline-Figueroa, J.L., Packer, J.S., Christiansen, L., et al. (2018). Joint profiling of chromatin accessibility and gene expression in thousands of single cells. Science 361, 1380–1385.

Chang-Panesso, M., and Humphreys, B.D. (2017). Cellular plasticity in kidney injury and repair. Nat. Rev. Nephrol. 13, 39–46.

Chikina, M., Zaslavsky, E., and Sealfon, S.C. (2015). CellCODE: a robust latent variable approach to differential expression analysis for heterogeneous cell populations. Bioinformatics 31, 1584–1591.

Chung, K.W., Dhillon, P., Huang, S., Sheng, X., Shrestha, R., Qiu, C., Kaufman, B.A., Park, J., Pei, L., Baur, J., et al. (2019). Mitochondrial damage and activation of the STING pathway lead to renal inflammation and fibrosis. Cell Metab. 30, 784–799.e5.

Combes, A.N., Zappia, L., Er, P.X., Oshlack, A., and Little, M.H. (2019). Single-cell analysis reveals congruence between kidney organoids and human fetal kidney. Genome Med 11, 3.

de Lau, W., Barker, N., Low, T.Y., Koo, B.K., Li, V.S., Teunissen, H., Kujala, P., Haegebarth, A., Peters, P.J., van de Wetering, M., et al. (2011). Lgr5 homologues associate with Wnt receptors and mediate R-spondin signalling. Nature 476, 293–297.

Delgoffe, G.M., Kole, T.P., Zheng, Y., Zarek, P.E., Matthews, K.L., Xiao, B., Worley, P.F., Kozma, S.C., and Powell, J.D. (2009). The mTOR kinase differentially regulates effector and regulatory T cell lineage commitment. Immunity 30, 832–844.

Edeling, M., Ragi, G., Huang, S., Pavenstädt, H., and Susztak, K. (2016). Developmental signalling pathways in renal fibrosis: the roles of Notch, Wnt and Hedgehog. Nat. Rev. Nephrol. 12, 426–439.

Garreta, E., Prado, P., Tarantino, C., Oria, R., Fanlo, L., Martí, E., Zalvidea, D., Trepat, X., Roca-Cusachs, P., Gavaldà-Navarro, A., et al. (2019). Fine tuning the extracellular environment accelerates the derivation of kidney organoids from human pluripotent stem cells. Nat. Mater. 18, 397–405.

Gomez, I.G., MacKenna, D.A., Johnson, B.G., Kaimal, V., Roach, A.M., Ren, S., Nakagawa, N., Xin, C., Newitt, R., Pandya, S., et al. (2015). Anti-microRNA-21 oligonucleotides prevent Alport nephropathy progression by stimulating metabolic pathways. J. Clin. Invest. 125, 141–156.

Grande, M.T., Sánchez-Laorden, B., López-Blau, C., De Frutos, C.A., Boutet, A., Arévalo, M., Rowe, R.G., Weiss, S.J., López-Novoa, J.M., and Nieto, M.A. (2015). Snail1-induced partial epithelial-to-mesenchymal transition drives renal fibrosis in mice and can be targeted to reverse established disease. Nat. Med. 21, 989–997.

He, W., Dai, C., Li, Y., Zeng, G., Monga, S.P., and Liu, Y. (2009). Wnt/beta-catenin signaling promotes renal interstitial fibrosis. J. Am. Soc. Nephrol. 20, 765–776.

Hellwege, J.N., Velez Edwards, D.R., Giri, A., Qiu, C., Park, J., Torstenson, E.S., Keaton, J.M., Wilson, O.D., Robinson-Cohen, C., Chung, C.P., et al. (2019). Mapping eGFR loci to the renal transcriptome and phenome in the VA Million Veteran program. Nat. Commun. 10, 3842.

Huang, S., Park, J., Qiu, C., Chung, K.W., Li, S.Y., Sirin, Y., Han, S.H., Taylor, V., Zimber-Strobl, U., and Susztak, K. (2018). Jagged1/Notch2 controls kidney fibrosis via Tfam-mediated metabolic reprogramming. PLoS Biol. 16, e2005233.

Kang, H.M., Ahn, S.H., Choi, P., Ko, Y.A., Han, S.H., Chinga, F., Park, A.S., Tao, J., Sharma, K., Pullman, J., et al. (2015). Defective fatty acid oxidation in renal tubular epithelial cells has a key role in kidney fibrosis development. Nat. Med. 21, 37–46.

Kang, H.M., Huang, S., Reidy, K., Han, S.H., Chinga, F., and Susztak, K. (2016). Sox9-positive progenitor cells play a key role in renal tubule epithelial regeneration in mice. Cell Rep. 14, 861–871.

Kato, H., Gruenwald, A., Suh, J.H., Miner, J.H., Barisoni-Thomas, L., Taketo, M.M., Faul, C., Millar, S.E., Holzman, L.B., and Susztak, K. (2011). Wnt/beta-catenin pathway in podocytes integrates cell adhesion, differentiation, and survival. J. Biol. Chem. 286, 26003–26015.

Kornberg, M.D., Bhargava, P., Kim, P.M., Putluri, V., Snowman, A.M., Putluri, N., Calabresi, P.A., and Snyder, S.H. (2018). Dimethyl fumarate targets GAPDH and aerobic glycolysis to modulate immunity. Science 360, 449–453.

Kovesdy, C.P., Bleyer, A.J., Molnar, M.Z., Ma, J.Z., Sim, J.J., Cushman, W.C., Quarles, L.D., and Kalantar-Zadeh, K. (2013). Blood pressure and mortality in U.S. veterans with chronic kidney disease: a cohort study. Ann. Intern. Med. 159, 233–242.

La Manno, G., Soldatov, R., Zeisel, A., Braun, E., Hochgerner, H., Petukhov, V., Lidschreiber, K., Kastriti, M.E., Lönnerberg, P., Furlan, A., et al. (2018). RNA velocity of single cells. Nature 560, 494–498.

Lake, B.B., Chen, S., Hoshi, M., Plongthongkum, N., Salamon, D., Knoten, A., Vijayan, A., Venkatesh, R., Kim, E.H., Gao, D., et al. (2019). A single-nucleus RNA-sequencing pipeline to decipher the molecular anatomy and pathophysiology of human kidneys. Nat. Commun. 10, 2832.

Levin, A., Tonelli, M., Bonventre, J., Coresh, J., Donner, J.A., Fogo, A.B., Fox, C.S., Gansevoort, R.T., Heerspink, H.J.L., Jardine, M., et al. (2017). Global kidney health 2017 and beyond: a roadmap for closing gaps in care, research, and policy. Lancet 390, 1888–1917.

Li, Y., Wen, X., and Liu, Y. (2012). Tubular cell dedifferentiation and peritubular inflammation are coupled by the transcription regulator Id1 in renal fibrogenesis. Kidney Int. 81, 880–891.

Liu, J., Krautzberger, A.M., Sui, S.H., Hofmann, O.M., Chen, Y., Baetscher, M., Grgic, I., Kumar, S., Humphreys, B.D., Hide, W.A., and McMahon, A.P. (2014). Cell-specific translational profiling in acute kidney injury. J. Clin. Invest. 124, 1242–1254.

Lovisa, S., LeBleu, V.S., Tampe, B., Sugimoto, H., Vadnagara, K., Carstens, J.L., Wu, C.C., Hagos, Y., Burckhardt, B.C., Pentcheva-Hoang, T., et al. (2015). Epithelial-to-mesenchymal transition induces cell cycle arrest and parenchymal damage in renal fibrosis. Nat. Med. 21, 998–1009.

Maekawa, H., Inoue, T., Ouchi, H., Jao, T.M., Inoue, R., Nishi, H., Fujii, R., Ishidate, F., Tanaka, T., Tanaka, Y., et al. (2019). Mitochondrial damage causes inflammation via cGAS-STING signaling in acute kidney injury. Cell Rep. 29, 1261–1273.e6.

Marable, S.S., Chung, E., and Park, J. (2020). Hnf4a is required for the development of Cdh6-expressing progenitors into proximal tubules in the mouse kidney. bioRxiv. https://doi.org/10.1101/2020.02.16.951731.

McGinnis, C.S., Murrow, L.M., and Gartner, Z.J. (2019). DoubletFinder: doublet detection in single-cell RNA sequencing data using artificial nearest neighbors. Cell Syst. 8, 329–337.e4.

Meersch, M., Schmidt, C., Van Aken, H., Martens, S., Rossaint, J., Singbartl, K., Görlich, D., Kellum, J.A., and Zarbock, A. (2014). Urinary TIMP-2 and IGFBP7 as early biomarkers of acute kidney injury and renal recovery following cardiac surgery. PLoS One 9, e93460.

Menon, R., Otto, E.A., Hoover, P., Eddy, S., Mariani, L., Godfrey, B., Berthier, C.C., Eichinger, F., Subramanian, L., Harder, J., et al. (2020). Single cell transcriptomics identifies focal segmental glomerulosclerosis remission endothelial biomarker. JCI Insight 5, e133267.

Michalek, R.D., Gerriets, V.A., Jacobs, S.R., Macintyre, A.N., MacIver, N.J., Mason, E.F., Sullivan, S.A., Nichols, A.G., and Rathmell, J.C. (2011). Cutting edge: distinct glycolytic and lipid oxidative metabolic programs are essential for effector and regulatory CD4+ T cell subsets. J. Immunol. 186, 3299–3303.

Park, J., Shrestha, R., Qiu, C., Kondo, A., Huang, S., Werth, M., Li, M., Barasch, J., and Susztak, K. (2018). Single-cell transcriptomics of the mouse kidney reveals potential cellular targets of kidney disease. Science 360, 758–763.

Qiu, C., Huang, S., Park, J., Park, Y., Ko, Y.-A., Seasock, M.J., Bryer, J.S., Xu, X.X., Song, W.C., Palmer, M., et al. (2018). Renal compartment-specific genetic variation analyses identify new pathways in chronic kidney disease. Nat. Med. 24, 1721–1731.

Quiros, P.M., Goyal, A., Jha, P., and Auwerx, J. (2017). Analysis of mtDNA/nDNA ratio in mice. Curr. Protoc. Mouse Biol. 7, 47–54.

Reidy, K., Kang, H.M., Hostetter, T., and Susztak, K. (2014). Molecular mechanisms of diabetic kidney disease. J. Clin. Invest. 124, 2333–2340.

Rinkevich, Y., Montoro, D.T., Contreras-Trujillo, H., Harari-Steinberg, O., Newman, A.M., Tsai, J.M., Lim, X., Van-Amerongen, R., Bowman, A., Januszyk, M., et al. (2014). In vivo clonal analysis reveals lineage-restricted progenitor characteristics in mammalian kidney development, maintenance, and regeneration. Cell Rep. 7, 1270–1283.

Shen, Y., Wen, Z., Li, Y., Matteson, E.L., Hong, J., Goronzy, J.J., and Weyand, C.M. (2017). Metabolic control of the scaffold protein TKS5 in tissue-invasive, proinflammatory T cells. Nat. Immunol. 18, 1025–1034.

Singh, B.K., Sinha, R.A., Tripathi, M., Mendoza, A., Ohba, K., Sy, J.A.C., Xie, S.Y., Zhou, J., Ho, J.P., Chang, C.-Y., et al. (2018). Thyroid hormone receptor and ERRα coordinately regulate mitochondrial fission, mitophagy, biogenesis, and function. Sci. Signal. 11, eaam5855.

Smillie, C.S., Biton, M., Ordovas-Montanes, J., Sullivan, K.M., Burgin, G., Graham, D.B., Herbst, R.H., Rogel, N., Slyper, M., Waldman, J., et al. (2019). Intra- and inter-cellular rewiring of the human colon during ulcerative colitis. Cell 178, 714–730.e22.

Soriano, F.X., Liesa, M., Bach, D., Chan, D.C., Palacín, M., and Zorzano, A. (2006). Evidence for a mitochondrial regulatory pathway defined by peroxisome proliferator-activated receptor-gamma coactivator-1 alpha, estrogen-related receptor-alpha, and mitofusin 2. Diabetes 55, 1783–1791.

Tran, M., Tam, D., Bardia, A., Bhasin, M., Rowe, G.C., Kher, A., Zsengeller, Z.K., Akhavan-Sharif, M.R., Khankin, E.V., Saintgeniez, M., et al. (2011). PGC-1alpha promotes recovery after acute kidney injury during systemic inflammation in mice. J. Clin. Invest. 121, 4003–4014.

Tran, M.T., Zsengeller, Z.K., Berg, A.H., Khankin, E.V., Bhasin, M.K., Kim, W., Clish, C.B., Stillman, I.E., Karumanchi, S.A., Rhee, E.P., and Parikh, S.M. (2016). PGC1α drives NAD biosynthesis linking oxidative metabolism to renal protection. Nature 531, 528–532.

Trapnell, C., Cacchiarelli, D., Grimsby, J., Pokharel, P., Li, S., Morse, M., Lennon, N.J., Livak, K.J., Mikkelsen, T.S., and Rinn, J.L. (2014). The dynamics and regulators of cell fate decisions are revealed by pseudotemporal ordering of single cells. Nat. Biotechnol. 32, 381–386.

Vijayan, A., Faubel, S., Askenazi, D.J., Cerda, J., Fissell, W.H., Heung, M., Humphreys, B.D., Koyner, J.L., Liu, K.D., Mour, G., et al. (2016). Clinical use of the urine biomarker [TIMP-2] × [IGFBP7] for acute kidney injury risk assessment. Am. J. Kidney Dis. 68, 19–28.

Woroniecka, K.I., Park, A.S., Mohtat, D., Thomas, D.B., Pullman, J.M., and Susztak, K. (2011). Transcriptome analysis of human diabetic kidney disease. Diabetes 60, 2354–2369.

Wu, H., Kirita, Y., Donnelly, E.L., and Humphreys, B.D. (2019). Advantages of single-nucleus over single-cell RNA sequencing of adult kidney: rare cell types and novel cell states revealed in fibrosis. J. Am. Soc. Nephrol. 30, 23–32.

Wu, H., Uchimura, K., Donnelly, E.L., Kirita, Y., Morris, S.A., and Humphreys, B.D. (2018). Comparative analysis and refinement of human PSC-derived kidney organoid differentiation with single-cell transcriptomics. Cell Stem Cell 23, 869–881.e8.

Wuttke, M., Li, Y., Li, M., Sieber, K.B., Feitosa, M.F., Gorski, M., Tin, A., Wang, L., Chu, A.Y., Hoppmann, A., et al. (2019). A catalog of genetic loci associated with kidney function from analyses of a million individuals. Nat. Genet. 51, 957–972.

Yang, Z., Fujii, H., Mohan, S.V., Goronzy, J.J., and Weyand, C.M. (2013). Phosphofructokinase deficiency impairs ATP generation, autophagy, and redox balance in rheumatoid arthritis T cells. J. Exp. Med. 210, 2119–2134.

Yin, Y., Choi, S.C., Xu, Z., Perry, D.J., Seay, H., Croker, B.P., Sobel, E.S., Brusko, T.M., and Morel, L. (2015). Normalization of CD4+ T cell metabolism reverses lupus. Sci. Transl. Med. 7, 274ra18.

Young, M.D., Mitchell, T.J., Vieira Braga, F.A., Tran, M.G.B., Stewart, B.J., Ferdinand, J.R., Collord, G., Botting, R.A., Popescu, D.M., Loudon, K.W., et al. (2018). Single-cell transcriptomes from human kidneys reveal the cellular identity of renal tumors. Science 361, 594–599.

Zeisberg, M., and Duffield, J.S. (2010). Resolved: EMT produces fibroblasts in the kidney. J. Am. Soc. Nephrol. 21, 1247–1253.

Zhang, R., Boareto, M., Engler, A., Louvi, A., Giachino, C., Iber, D., and Taylor, V. (2019). Id4 downstream of Notch2 maintains neural stem cell quiescence in the adult hippocampus. Cell Rep. 28, 1485–1498.e6.

Zhao, J., Lupino, K., Wilkins, B.J., Qiu, C., Liu, J., Omura, Y., Allred, A.L., McDonald, C., Susztak, K., Barish, G.D., and Pei, L. (2018). Genomic integration of ERRgamma-HNF1beta regulates renal bioenergetics and prevents chronic kidney disease. Proc. Natl. Acad. Sci. USA 115, E4910–E4919.

Zheng, M., Cai, J., Liu, Z., Shu, S., Wang, Y., Tang, C., and Dong, Z. (2019). Nicotinamide reduces renal interstitial fibrosis by suppressing tubular injury and inflammation. J. Cell. Mol. Med. 23, 3995–4004.

Cell Metabolism
Article

 CellPress

STAR★METHODS

KEY RESOURCES TABLE

REAGENT or RESOURCE	SOURCE	IDENTIFIER
Antibodies		
Primary antibodies for Immunoblots		
Anti-COX IV antibody	Abcam	Cat# ab16056; RRID: AB_443304
Total OXPHOS Rodent WB Antibody Cocktail	Abcam	Cat# ab110413; RRID: AB_2629281
GAPDH	CST(14C10)	Cat# 2118; RRID: AB_561053
PGC1a	Calbiochem	Cat#KP9803
SLC6A13	Invitrogen	Cat# PA5-68331; RRID: AB_2691971
α-Tubulin	Sigma	Cat# T9026; RRID: AB_477593
SMA	Sigma	Cat# A5228; RRID: AB_262054
FN	Abcam	Cat# ab2413; RRID: AB_2262874
ESRRA	CST	Cat# 13826; RRID: AB_2750873
β-actin	Millipore	Cat# A3854; RRID: AB_262011
Secondary antibodies for Immunoblots		
Anti-mouse IgG, HRP-linked Antibody	CST	Cat# 7076; RRID: AB_330924
Anti-rabbit IgG, HRP-linked Antibody	CST	Cat# 7074; RRID: AB_2099233
Antibodies for Immunohistochemistry (IHC)		
ESRRA	CST	Cat# 13826; RRID: AB_2750873
SLC34A1	Novus Biologicals	Cat# NBP2-42216; RRID: AB_2801654
SLC7A13	Creative Diagnostics	Cat# CPBT-45312RH; RRID: AB_2378853
SLC6A13	Invitrogen	Cat# PA5-68331; RRID: AB_2691971
Antibodies for Immunofluorescence (IF)		
LTL	Vector laboratories	Cat# FL-1321; RRID: AB_2336559
PODXL	Thermofischer	Cat# 39-3800; RRID: AB_2533411
IRDye®680RD	LI-COR	Cat# 926-68070; RRID: AB_10956588
Ki67	CST	Cat# 12202; RRID: AB_2620142
A555	Life technology	Cat# A-31572; RRID: AB_162543
Antibodies for FACS		
LTL	Vector laboratories	Cat# B-1325; RRID: AB_2336558
Biological Samples		
Human kidney samples	Chung et al., 2019	N/A
Chemicals, Peptides, and Recombinant Proteins		
MitoTracker Green	Life Technology	Cat#M7514
Collagenase IV	Life Technologies	Cat#17104019
Trypan blue solution	Sigma	Cat#T8154
Protease inhibitor cocktail	Roche	Cat#11836153001
EDTA solution	Life Technologies	Cat#15575-038
Accumax	Stem Cell Technologies	Cat#07921
Phosphate buffered saline (PBS) pH 7.4 (1x)	Life Technologies	Cat#1001–015
Essential 8 medium	Life Technologies	Cat#A1517001
Vitronectin	Life Technologies	Cat#A14700
Fenofibrate	Sigma	CAS#49562-28-9
RPMI 1640	Gibco	Cat#21875-034
EGM media	Lonza	Cat#CC-3162
REGM media	Lonza	Cat#CC-4127
RIPA buffer	Cell signaling	Cat#9806

(Continued on next page)

Continued

REAGENT or RESOURCE	SOURCE	IDENTIFIER
SYBR Green PCR Master Mix	Applied Biosystem	Cat#KK4605
Fluoromount-G	Southern Biotech	Cat# 0100-01
XCT790	Tocris	Cat#3928
Folic Acid	Fisher Scientific	Cat#AC216630500
Lipofectamine 3000	ThermoFisher	Cat#11668027
CHIR99021	Merck	Cat#SML1046; CAS: 252917-06-9
Recombinant human FGF9	PeproTech	Cat#100-23
Heparin	Merck	Cat#H3149; CAS: 9041-08-1
Activin A	Vitro	Cat#338-AC-050
Dimethyl Sulfoxide (DMSO)	Merck	Cat#D2650; CAS: 67-68-5
Cell culture grade distilled water	Life Technologies	Cat#15230-089
Paraformaldehyde solution 4% in PBS	Santa Cruz	Cat#sc-281692
Hoechst	Molecular probes	Cat# H-1399
Critical Commercial Assays		
BCA Protein Assay Kit	Thermo Scientific	Cat#23225
Multi Tissue dissociation kit	Miltenyi	Cat#130-110-201
Anti-Biotin microbeads	Miltenyi	Cat#130-090-485
cDNA Reverse Transcription Kit	Applied Biosystems	Cat#4368813
Rneasy Mini Kit	Qiagen	Cat#74106
MAGnify™ ChIP Kit	Thermo Scientific	Cat# 492024
DNeasy Blood & Tissue Kits	Qiagen	Cat#69506
Seahorse XF Cell Mito Stress Test kit	Agilent Technologies	Cat#103708-100
Seahorse XFe96 FluxPak mini	Agilent Technologies	Cat#102601-100
VECTASTAIN® Elite ABC-HRP Kit	Vector laboratories	Cat# PK-6100
Streptavidin/Biotin blocking kit	Vector laboratories	Cat#SP-2002
Deposited Data		
scATAC seq data	(Cao et al., 2018)	GSE117089
scRNA-seq of FAN kidneys of mice	GEO	GSE156686
scRNA seq data kidney organoids	GEO	GSE152765
Experimental Models: Organisms/Strains		
ESRRA Knock-out	Dr. Vincent Giguère Research Lab	McGill University
Oligonucleotides		
Primers for qPCR, mtDNA copy no., and ChIP-qPCR, see Table S6	This paper	N/A
Recombinant DNA		
pAd-track-Esrra	Dr. Liming Pei lab	University of Pennsylvania
pcDNA3.1-Ppara	Dr. Liming Pei lab	University of Pennsylvania
pc-DNA3.1-HNF1B	Dr. Liming Pei lab	University of Pennsylvania
pAd-track-HNF4A	Dr. Liming Pei lab	University of Pennsylvania
Experimental Models: Cell Lines		
ES[4] Human Embryonic Stem Cell line	The National Bank of Stem Cells (ISCIII,Madrid)	https://www.isciii.es/
Software and Algorithms		
ImageJ	NIH	https://imagej.nih.gov/ij
Prism 5	Graphpad Software	https://www.graphpad.com/scientific-software/prism
Image Studio Lite Version 5.2 software	LICOR	https://www.licor.com/bio/image-studio-lite/d5
FlowJo Software	FlowJo	N/A

(Continued on next page)

Cell Metabolism
Article

CellPress

REAGENT or RESOURCE	SOURCE	IDENTIFIER
Cell Ranger 2.0	10x Genomics	https://support.10xgenomics.com/single-cell-gene-expression/software/downloads/latest
Seurat R package 2.3.4	open source	https://satijalab.org/seurat/
DoubletFinder	open source	https://github.com/chris-mcginnis-ucsf/DoubletFinder
STAR-2.4.1d	open source	https://github.com/alexdobin/STAR
HTSeq-0.6.1	open source	https://htseq.readthedocs.io/en/release_0.11.1/history.html#version-0-6-1
DESeq2 1.10.1	open source	https://bioconductor.org/packages/release/bioc/html/DESeq2.html
CellCODE	open source	https://github.com/mchikina/CellCODE/
Velocyto	open source	https://github.com/velocyto-team/velocyto.R
Monocle2 2.4.0	open source	http://cole-trapnell-lab.github.io/monocle-release/

RESOURCE AVAILABILITY

Lead contact
Further information and requests for resources and reagents should be directed to and will be fulfilled by the lead contact: Katalin Susztak. Email: ksusztak@pennmedicine.upenn.edu

Materials Availability
This study did not generate new unique reagents.

Data and Code Availability
The accession number for the scRNA-seq data reported in this paper are NCBI GEO: GSE156686 and GSE152765. All other data are available upon reasonable request for corresponding author. Furthermore, the data is available via an interactive web browser at http://susztaklab.com/VisCello/.

EXPERIMENTAL MODEL AND SUBJECT DETAILS

Mouse Models
Animal studies were approved by the Institutional Animal Care and Use Committee (IACUC) of the University of Pennsylvania. Mice were housed in the Institute pathogen free animal house (12 h dark/light cycle) in a temperature- and humidity-controlled environment ($23 \pm 1°C$) and fed with standard mouse diet and water ad libitum. 5- to 8-week-old male C57BL/6 wild type mice were used in the study. *Esrra* KO mice were kindly provided by Dr. Liming Pei (University of Pennsylvania) and littermates were used from in-house matings. All animals were pathogen free and healthy prior to the beginning of experiments. For all the mice experiments, mice were randomly assigned to experimental groups, unless stated otherwise.

For fenofibrate experiment, the PPARA agonist fenofibrate (50 mg/kg for 3 days and 100 mg/kg for 5 days) was administered by oral gavage starting one day before the folic acid (FA) injection. Mice were injected with FA (250 mg/kg once, dissolved in 300 mM $NaHCO_3$) intraperitoneally and sacrificed on day 7. For the unilateral ureteral obstruction (UUO) model, mice underwent ligation of the left ureter and were sacrificed on day 7.

Isolation and Culture of LTL+ PT Cells
Primary mouse proximal tubule epithelial cells were isolated from kidneys of 4 weeks old wild type mice and LTL+ cells fractions were purified from single cell suspension of PT cells by using biotinylated lotus tetragonolobus lectin antibody (LTL) (L-132; Vector Laboratories) and anti-biotin microbeads (MACS Miltenyi Biotec). LTL+ cells were grown in primary cell culture media (RPMI 1640 supplemented with 10% FBS, 20 ng ml^{-1} EGF, 20 ng ml^{-1} bFGF and 1% penicillin-streptomycin).

Kidney Organoids Differentiation
ES[4] human embryonic stem cells were grown on vitronectin coated plates (1001-015, Life Technologies). Cells were incubated in 0.5mM EDTA (Merck) at 37°C for 3 minutes for disaggregation. To avoid the separation of the stem cell clusters, cells were then carefully collected into 12 ml supplemented Essential 8 Basal medium. For cell counting, 1 mL cell suspension was centrifuged for 4 minutes at 400 g and the pellet was resuspended in 200 µl of AccumaxTM (StemCell Technologies) to obtain single cells. Cells were incubated in AccumaxTM at 37°C for 3 minutes and next, 800 µL of FBS were added to stop the disaggregation. After cell counting (Countess ® Automated Cell Counter), 100,000 cells/well were plated on a 24 multi-well plate coated with 5µl/ml vitronectin. Cells

were incubated in supplemented Essential 8 Basal medium at 37°C overnight. The next day (day 0), the differentiation was initiated by treating the cells with 8 μM CHIR (Merck) in Advanced RPMI 1640 basal medium (ThermoFisher) supplemented with 1% Penicillin-Streptomycin and 1% of GlutaMAXTM (ThermoFisher) for 3 days and changing the medium every day. On day 3, CHIR treatment was removed and cells were cultured in 200 ng·ml^{-1} FGF9 (Peprotech), 1 μg·ml^{-1} heparin (Merck) and 10 ng·ml-1 activin A (Act A) (Vitro) in supplemented Advanced RPMI for 1 day. On day 4, spheroid organoids were generated. Cells were rinsed twice with PBS, collected using supplemented Advanced RPMI and plated at 100,000 cells/well on a V-shape 96 multi-well plate. They were treated with 5 μM CHIR, 200ng·ml-1 FGF9 and 1 μg·ml-1 Heparin in supplemented Advanced RPMI. Organoids were incubated for 1 hour at 37°C, CHIR induction was removed and they were incubated in 200 ng·ml-1 FGF9 and 1 μg·ml-1 Heparin in supplemented Advanced RPMI for 7 days with medium change every other day. From day 11, factors were eliminated, and cells were incubated only in supplemented Advanced RPMI for 5 days, medium was changed every other day.

METHOD DETAILS

Preparation of Single-Cell Suspension
Euthanized mice were perfused with chilled 1x PBS via the left ventricle. Kidneys were harvested, minced into approximately 1 mm^3 cubes and digested using Multi Tissue dissociation kit (Miltenyi, 130-110-201). The tissue was homogenized using 21G and 26 1/2G syringes. Up to 0.25 g of the tissue was digested with 50ul of Enzyme D, 25 ul of Enzyme R and 6.75 μl of Enzyme A in 1 ml of RPMI and incubated for 30mins at 37°C. Reaction was deactivated by 10% FBS. The solution was then passed through a 40 μm cell strainer. After centrifugation at 400 g for 5 mins, cell pellet was incubated with 1ml of RBC lysis buffer on ice for 3 mins. Cell number and viability were analyzed using Countess AutoCounter (Invitrogen, C10227). This method generated single cell suspension with greater than 80% viability.

Single-cell RNA Sequencing
Single cell RNA sequencing was performed as described in our previous study (Park et al., 2018). Briefly, the single cell suspension was loaded onto a well of a 10x Chromium Single Cell instrument (10x Genomics). Barcoding and cDNA synthesis were performed according to the manufacturer's instructions. Qualitative analysis was performed using the Agilent Bioanalyzer High Sensitivity assay. The cDNA libraries were constructed using the 10x Chromium^{TM} Single cell 3' Library Kit according to the manufacturer's original protocol. Libraries were sequenced on an Illumina HiSeq or NextSeq 2x150 paired-end kits using the following read length: 26bp Read1 for cell barcode and UMI, 8bp I7 index for sample index and 98bp Read2 for transcript.

Alignment and Generation of Data Matrix
Cell Ranger 2.0 (http://10xgenomics.com) was used to process Chromium single cell 3' RNA-seq output. First, "cellranger count" aligned the Read2 to the mouse reference genome (mm10) and exons of protein coding genes (Ensembl GTFs GRCm38.p4). Sequencing reads that were marked by multiple mapping were removed by adjusting the cellranger to unique mapping (marked MM:i:1 in the bam files). Third, the fastq files extracted from bam files of the first run were used again for "cellranger count" to generate data matrix. Finally, the output files for 6 normal and 2 FAN samples were aggregated into one gene-cell matrix using "cellranger aggr" with read depth normalization by total number of mapped reads.

Data Quality Control, Preprocessing and Dimension Reduction
Seurat R package (version 2.3.4) was used for data QC, preprocessing and dimension reduction analysis. Once the gene-cell data matrix was generated, poor quality cells were excluded, such as cells with < 200 or > 3,000 expressed genes. Genes that were expressed in less than 10 cells, mitochondrial genes, ribosomal protein genes and HLA genes, that were reported to induce unwanted batch effects, were removed for further analysis (Smillie et al., 2019). Cells were also discarded if their mitochondrial gene percentages were over 50%. The data were natural log transformed and normalized for scaling the sequencing depth to a total of 10,000 molecules per cell, followed by regressing-out the number of UMI and genes. Batch effect was corrected by using removeBatchEffect function of edgeR. The expression values after batch correction were only used for PCA, t-Distributed Stochastic Neighbor Embedding (tSNE) visualization and clustering, and the original expression values before batch correction were used for all downstream analyses such as identification of marker genes and differentially expressed genes. For the dimension reduction, highly variable genes across the single cells were identified using 0.0125 low cutoff and 0.3 high cutoff. PCA was performed using the variable genes as input and top 20 PCs were used for initial tSNE projection.

Removal of Doublet-like Cells
Doublet-like cells were identified using DoubletFinder which is a computational doublet detection tool with following parameters: proportion.artificial = 0.25 and proportion.NN = 0.01(McGinnis et al., 2019). Then, the number of expected doublets were calculated for each sample based on expected rates of doublets, which are provided by 10x Genomics. After removing the doublet-like cells, all steps including normalization, regressing out variables, batch effect removal, and dimension reduction were performed again.

Cell Metabolism
Article

CellPress

Cell Clustering Analysis

Density-based spatial clustering algorithm, DBSCAN, was used to identify cell clusters on the tSNE plot with the eps value 0.4. Clusters were removed if their number of cells was less than 20. Proximal tubule clusters expressing a proximal tubule marker, *Slc27a2*, were separated from the rest of cell clusters in order to identify subgroups. PCA and UMAP (Uniform Manifold Approximation and Projection) were performed only for the remaining cells. DBSCAN was used to identify cell clusters on the UMAP plot with initial setting for the eps value 0.5. Each of the resulting clusters was subjected to sub-clustering by a shared nearest neighbor (SNN) modularity optimization-based clustering algorithm, which is implemented in Seurat package. Resolution 0.5 was used for sub-clustering of the clusters except T lymphocytes which required higher resolution (0.7) to identify T lymphocyte subgroups. Post-hoc differential expression analysis was performed for every pair of sub-clusters. Sub-clusters were merged when they had 15 or less than 15 (10 differential genes for T lymphocytes) differentially expressed genes (average expression difference > 1 natural log with an FDR corrected p<0.01). This clustering analysis resulted in 30 cell clusters. PT cell clusters were also subjected to sub-clustering. With same procedure used for other clusters, PT cells from control and FAN samples were subclustered into 5 and 9 sub-cell types, respectively.

Mouse Bulk RNA-sequencing Analysis

Total RNAs were isolated using the RNeasy mini kit (Qiagen). Sequencing libraries were constructed using the Illumina TruSeq RNA Preparation Kit. High-throughput sequencing was performed using Illumina HiSeq4000 with 100bp single-end according to the manufacturer's instruction. Adaptor and lower-quality bases were trimmed with Trim-galore. Reads were aligned to the Gencode mouse genome (GRCm38) using STAR-2.4.1d. The aligned reads were mapped to the genes (GRCm38, version 7 Ensembl 82) using HTSeq-0.6.1. Differentially expressed genes between control and disease groups were identified using DESeq2 version 1.10.1. To examine the enrichment of the differentially expressed genes in single cell clusters, a z-score of normalized expression value was first obtained for every single cell. Then, we calculated the mean z-scores for individual cells in the same cluster, resulting in 30 values for each gene. The z-scores were visualized by heatmap showing the enrichment patterns of the genes across the cell types.

Estimation of Cell Proportions

From single cell datasets, the numbers of cells in each cluster were enumerated and normalized by total number of cells for each condition (6 control and 2 diseased samples). Since a number of PT cells in FAN samples showed higher expression of apoptosis markers, we removed the cells that express *Bax, Bad* or *Dap* from all samples only for the cell proportion test. Deconvolution of bulk RNA sequencing data was performed to validate the cell proportion changes that were detected in single cell data. CellCODE package was used for deconvolution using 30 cell type-specific marker genes (Chikina et al., 2015).

Identification of Marker Genes and Differentially Expressed Genes

Conserved marker genes between control and UUO samples were identified using FindConservedMakers function of Seurat with default options. Average expression difference > 0.5 natural log and FDR corrected p value < 0.01 were applied. Cell type-specific differentially expressed genes were identified using MAST, which is implemented in Seurat package with log fold change threshold = 0.2, minimum percent of cells expressing the genes=0.05 and adjusted p value < 0.05.

Cell Trajectory Analysis
RNA Velocity

To calculate RNA velocity, Velocyto.R package was used as instructed (La Manno et al., 2018). We used Velocyto to impute the single-cell trajectory/directionality using the spliced and the unspliced reads. Resulting loom files were merged and loaded into R following the instructions. Furthermore, RNA velocity was estimated using gene-relative model with k-nearest neighbor cell pooling (k = 25). To visualize RNA velocity, we performed Principle Component Analysis and used the top 20 principle components to calculate UMAP embedding. The parameter n was set at 200, when visualizing RNA velocity on the UMAP embedding.

Monocle2

To construct single cell pseudotime trajectory and to identify genes that change as the cells undergo transition, Monocle2 (version 2.4.0) algorithm was applied to the cells from proximal tubules and proliferating proximal tubules (Trapnell et al., 2014). To show the cell trajectory from the small cell population (proliferating proximal tubules) to predominant cell type (proximal tubules), 6,000 randomly selected PT cells and proliferating proximal tubules were used for Monocle analysis. Genes for cell ordering were selected if they were expressed in ≥ 10 cells, their mean expression value was ≥ 0.05 and dispersion empirical value was ≥ 2. Highly variable genes along the pseudotime were identified using differential GeneTest function of Monocle2 with q-value < 0.01. The trajectory analysis was also performed for precursors and PST cells from the control and FAN samples separately. DAVID GO term analysis was performed for the highly variable genes along the control and FAN trajectory, and then genes in the lipid metabolism GO term were visualized by heatmap.

Single Cell ATAC Sequencing Analysis

Data matrix for PCT and PST cells-specific open chromatin regions was downloaded (Cao et al., 2018). HOMER package was used to identify known transcription factor binding motifs that are highly enriched in the PCT and PST-specific open chromatin regions. GSEA package was used to determine the enrichment patterns of ESRRA binding genes in differentiated PT cells and to identify core enrichment genes.

Human Bulk Gene Profiling Data Analysis

Kidney samples were collected from nephrectomies. Samples were permanently deidentified and clinical information was collected by an honest broker, therefore the study was deemed exempt by the institutional review board (IRB) of the University of Pennsylvania. Two datasets were used, one dataset included 91 human kidney samples and gene expression analysis was performed using Affymetrix U133A arrays (E-MTAB-2502) (Table S7) Raw expression levels of microarray data sets were normalized using the RMA algorithm and log transformed. The identified marker genes were used as an input for CellCODE deconvolution analysis to estimate the cell proportion changes in human patient kidney samples. To assess the effect of cell proportions changes on the correlation between gene expression and fibrosis score, we implemented linear regression models using age, gender, race and diabetes and hypertension status as covariates with and without cell proportions of PCT, PST, myeloid and lymphoid cells. The second dataset included 431 samples and gene expression was analyzed using RNAseq (Table S7).

Single Cell Suspension from Kidney organoid

Day 20 mature kidney organoids were washed twice with PBS and incubated first with AccumaxTM for 10 min at 37°C, followed by Trypsin-EDTA 0.25% incubation in order to dissociate into single cells. Cells were spun down at 400 g for 5 min resuspended in ADV RPMI and checked for viability using Countess Automated Cell Counter.

Mitotracker Green FM Flow Cytometric Analysis

Developing kidney organoids on day 14 of differentiation were cultured in EGM or REGM media for 4 additional days. In order to assess mitochondrial mass, organoids were stained with MitoTracker Green FM (100 nM), a mitochondrial specific fluorescent dye at 37°C for 30 min. After incubation, kidney organoids were washed twice with PBS and disaggregated into single cell suspension using AccumaxTM for 10 minutes followed by Trypsin-EDTA 0.25% (ThermoFisher) incubation for at least 10 minutes at 37°C. Once cells dissociated, FACS buffer (PBS supplemented with 5% of FBS) was added to cease the trypsin activity and samples were centrifuged for 5 minutes at 1800 rpm. After removing the supernatant, the pellet was resuspended in 300 μl of FACS buffer and the suspension was filtered into FACS tubes. Nuclei were stained with DAPI (ThermoFisher). Cells were counted using FACS Aria Fusion Instrument (BD Biosciences). FlowJo software version 10 was used for data analysis.

Protein Extraction and Western Blot Analysis in Kidney Organoids

Protein was extracted from kidney organoids cultured in EGM or REGM media for 4 days using RIPA buffer (Thermofisher) supplemented with complete protease inhibitor cocktail (Thermofisher), and centrifuged at 13,000 g for 15 mins at 4°C. The supernatant was collected, and protein concentration was measured using a bicinchoninic acid (BCA) protein quantification kit (Thermo Scientific). For western blot analyses, 25 ug of protein were separated in 10% sodium dodecyl sulphate-polyacrylamide gel (SDS-PAGE) and blotted onto nitrocellulose membranes. Membranes were blocked at room temperature for 1 hour with TBS 1X- 5% BSA. Membranes were then incubated in primary antibody (dilution 1:1000) Total OXPHOS cocktail (Abcam) overnight at 4°C. The membranes were then washed with PBST (PBS1X + 0.05% Tween20; Merck) for 5 minutes three times and incubated with anti-mouse secondary antibody (dilution 1:10,000) (IRDye®680RD Goat anti-Mouse; LI-COR). After washing with PBST for 5 minutes twice and with PBS for 5 minutes once, membrane-bound antibodies were detected by fluorescence with the Odyssey ® Fc Imaging System. Alpha-tubulin (1:5000; Sigma) was used as a loading control for normalization and quantification. Images were analyzed with Image Studio Lite Version 5.2 software.

Immunofluorescence

Kidney organoids were cultured in EGM or REGM media were transferred to 96 well plates. Fixation was performed with paraformaldehide 4% (Thermo Fisher) for 20 minutes followed by 10 minutes washing in three changes PBS. Kidney organoids were incubated in Streptavidin/Biotin Blocking Kit (Vector Laboratories) and TBS – 1% triton + 6% donkey serum for 2 h at room temperature. Podocalyxin (PODXL, Dilution 1:250) and LTL (Dilution 1:200) antibodies were diluted in TBS-0.5% Triton + 1% BSA. Kidney organoids were then treated overnight at 4°C with primary antibodies. The next day, organoids were washed with TBS-0.5% triton + 1% BSA for 5 minutes three times and incubated with secondary antibody (Dilution 1:500) in TBS-0.5% Triton + 1% BSA at room temperature for 2 hours. Subsequently, organoids were washed with TBS twice for 5 minutes and nuclei were stained with DAPI (Dilution 1:5000) for 10 minutes. Organoids were collected with special wide-end tips, and placed on slides and mounted with Fluoromount-G (Southern Biotech). Confocal images were acquired using Leica SP5 microscope and LTL positive cells were analyzed using ImageJ.

Mitochondrial DNA Analysis

MtDNA copy number is represented by the ratio of mitochondrial DNA to nuclear DNA (mtDNA/nDNA). Total DNA was isolated from LTL$^+$ PT cells 48 hours after transfection using DNeasy Blood & Tissue Kit. The mtDNA/nDNA ratio was determined by quantifying two

Cell Metabolism
Article

CellPress

mitochondrial genes (16S rRNA and ND1) and two nuclear genes (HK2 or 18S rRNA) using qPCR (Quiros et al., 2017). The primer sequences are listed in Table S6.

PT Cell Transfection

PT cells were transfected with Non-targeted (NT) siRNA or si*Esrra* (purchased from Dharmacon) and pcDNA3.0 (vector) or pAd-Track-Esrra/pcDNA3.1-Ppara/pcDNA3.1-HNF1A/pAd-track-HNF4A (overexpression constructs) (kind gift from Dr. Liming Pei, University of Pennsylvania). siRNA and plasmid transfections were performed using Lipofectamine 3000. For transfection, cells were seeded in 6-well plates, grown for overnight until 60–70% confluent, and then transfected with 100nM (final concentration) si*RNA*/si*Esrra* and 5μg of vector/ESRRA/PPARA/HNF1B/HNF4A overexpression plasmids. Transfection efficiency was determined under fluorescence microscope by the presence of Cy3 transfection control (data not shown). Cells were harvested and scraped off 48 h post transfection under different condition.

Oxygen Consumption Rate (OCR)

The measurement of OCR in PT cells transfected with si*Esrra* or ESRRA plasmid were performed using XFe96 extracellular flux analyzer (Seahorse Bioscience) as previously described (Kang et al., 2015). Briefly, PT cells were plated at density of 10,000 cells/well in a Sea-horse cell culture microplate and transfected with si*Esrra*/ESRRA OE. Cellular OCR was measured 48 h post-transfection and normalized to protein quantity in each well. The final concentration for oligomycin, FCCP, rotenone and antimycin used was 2 μM, 1 μM, 1 μM and 1 μM, respectively.

Chromatin Immunoprecipitation qPCR

ChIP was performed to evaluate enrichment of ESRRA binding regions in targets SLCs genes in PT cells following the manufacturer's instructions (492024, Invitrogen). Briefly, 10^7 PT cells were cross-linked with 1% formaldehyde for 10 min at room temperature. Then the reaction was stopped by adding glycine (final concentration, 0.125M). The cells were sonicated in lysis buffer to achieve a chromatin size of 100–500 bp. The sonicated chromatin was diluted by using dilution buffer. 5 μg ESRRA/IgG antibody was coupled with Dynabead protein A and G (1:1 mixed), the mixture was incubated with chromatin lysates overnight at 4 °C with rotation. Immune complexes were washed with IP buffers. Antibody-bound chromatin was reverse-cross-linked, and the ChIP DNA samples were purified for PCR reaction. Primers used for ChIP-qPCR are shown in Table S6.

Fenofibrate Treatment

LTL⁺ PT cells isolated from mouse kidneys were cultured in either presence of 1μM fenofibrate (PPARA agonist) to activate PPARA or DMSO in primary culture media from Day 0. Cells were harvested for RNA and protein isolation for Western Blot on Day 7.

XCT790 Treatment

Kidney organoids cultured in REGM media for 7 days were treated with 10μM of XCT790 for 48 hours followed by immunostaining or RNA isolation. Human proximal tubule cells (HPTC) and LTL⁺ mouse PT cells were cultured in REGM media and treated with 10 μM of XCT790 or DMSO for 48 hours and 24 hours respectively.

qRT-PCR

RNA was isolated from cells, kidney organoids and kidneys tissue using Trizol (Invitrogen). 2 μg RNA was reverse transcribed using the cDNA archival kit (Life Technologies), and qRT-PCR was run in the ViiA 7 System (Life Technologies) machine using SYBRGreen Master Mix (Applied Biosystem) and gene-specific primers. The data were normalized and analyzed using the ΔΔCt method. The primers sequences used are shown in Table S6.

Western Blot

Cells were lysed in radioimmunoprecipitation assay buffer (RIPA; Cell Signaling Technology) and protein was quantified by BCA method (Thermo Fisher Scientific). Protein samples (10 to 30 μg) were separated by SDS-PAGE and then transferred to PVDF membranes. After blocking, for 30 min with 5% milk in TBST and three times washing, membranes were incubated overnight with primary antibody (COX IV 1:1000, OXPHOS 1:250, GAPDH 1:2000, PGC1a 1:500, SLC6A13 1:1000, SMA 1:1000, FN 1:1000, ESRRA 1:2000, β-actin 1:20,000) in TBST (see KRT). After three washes for 5 min, membranes were incubated for 45 min at RT to 1 hour with secondary HRP-conjugated antibody (1:20,000) in TBST. The signal was developed with Immobilon forte western HRP substrate (Milipore) and measured using Odyssey®Fc Imaging System (*LICOR*) equipment and software. The following antibodies were used in this study are listed in Key Resources Table.

Histological Analysis

Kidneys samples were fixed in 10% neutral formalin and paraffin-embedded sections were stained Periodic acid–Schiff (PAS) and hematoxylin and eosin (H&E) to analyze the histology of samples. Sirius-red staining (Boekel Scientific, #147122) was performed to determine the degree of fibrosis. We performed immunocyto- and -histochemistry on paraformaldehyde fixed cells and formalin-fixed, paraffin-embedded kidney sections. We used the following primary antibodies: ESRRA (1:200), SLC6A13 (1:100), SLC34A1 (1:100), and SLC7A13 (1:100). Staining was visualized using peroxidase-conjugated antibodies to mouse immunoglobulin using

the Vectastain Elite kit and 3,3-diaminobenzidine (DAB) (Vector Labs). For cell proliferation, we used Ki67 (1:150) primary antibody and Alexa Fluor 555 as secondary antibody, and nuclei was stained by Hoechst dye.

QUANTIFICATION AND STATISTICAL ANALYSIS

Data Representation and Statistical Analysis

Student's t-test was used to analyze differences between two groups, and One-way or Two-way ANOVA was used to analyze inter-group differences (tukey's multiple comparisons test). *P*-values less than 0.05 were considered statistically significant. The analysis was performed using GraphPad Prism 5 (GraphPad software). Densitometry results of Western Blots were quantified using ImageJ software. All data are presented as mean ± SEM and other details such as the number of replicates and the level of significance is mentioned in figure legends and supplementary tables. For mice experiments, animals were randomly allocated to different groups prior the experiments. No samples or animals were excluded from analysis. Sample size estimation was not performed, and sample size was determined based on the number of available age and gender matched animals in the colony. For single-cell data analysis, statistical details are provided in designated method section. All samples were processed in blinded fashion.

Supplemental Information

The Nuclear Receptor ESRRA Protects from Kidney

Disease by Coupling Metabolism and Differentiation

Poonam Dhillon, Jihwan Park, Carmen Hurtado del Pozo, Lingzhi Li, Tomohito Doke, Shizheng Huang, Juanjuan Zhao, Hyun Mi Kang, Rojesh Shrestra, Michael S. Balzer, Shatakshee Chatterjee, Patricia Prado, Seung Yub Han, Hongbo Liu, Xin Sheng, Pieterjan Dierickx, Kirill Batmanov, Juan P. Romero, Felipe Prósper, Mingyao Li, Liming Pei, Junhyong Kim, Nuria Montserrat, and Katalin Susztak

Figure S1 (Related to Figure 1)
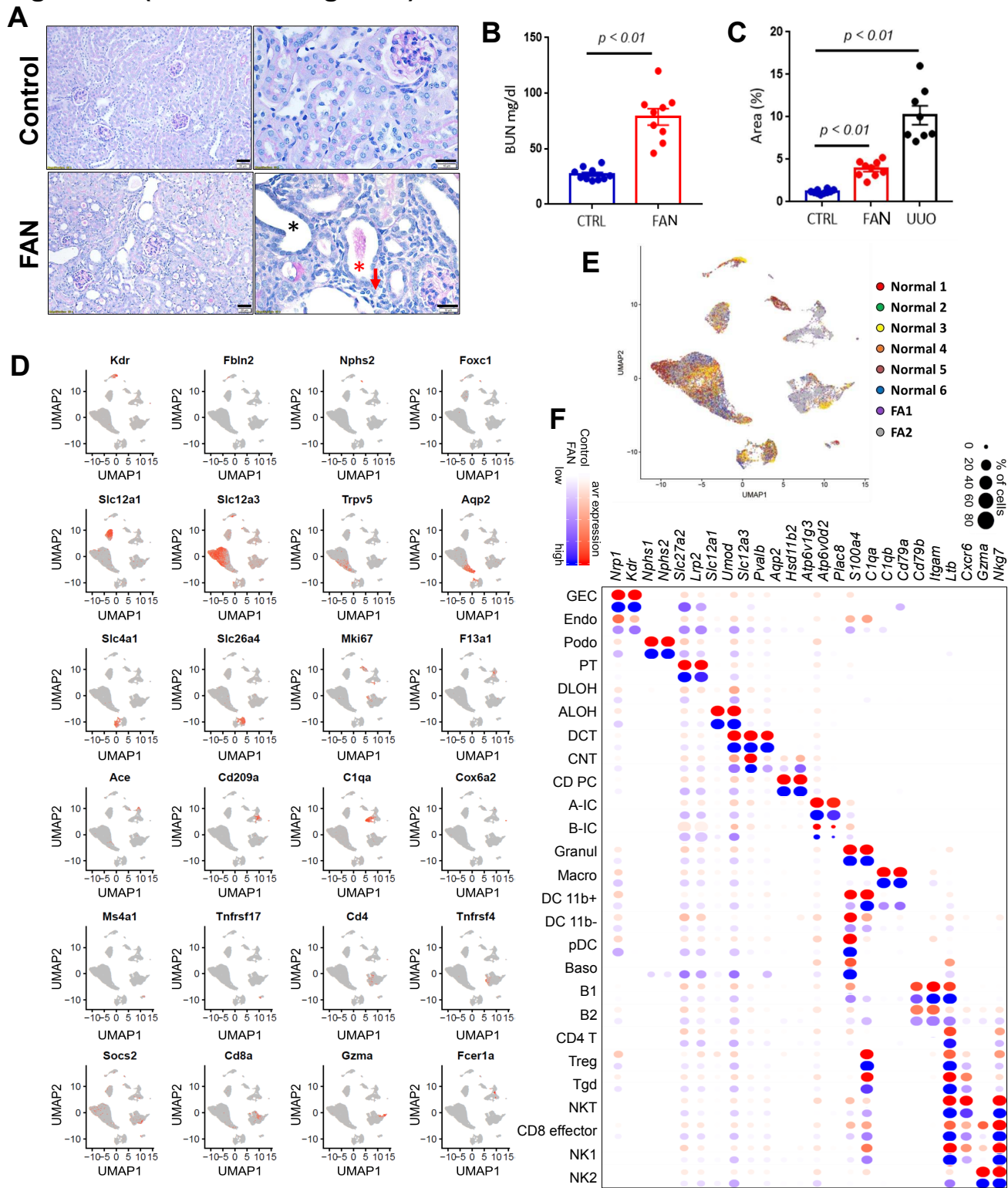
Figure S1 (Related to Figure 1). The cellular diversity of diseased kidney samples.

(A) Representative images of Periodic Schiff stained (PAS) kidney sections from control and FAN mice. Red star highlights casts and black star represent tubular dilation with loss of brush border. Red arrow indicates infiltrating immune cells. Scale bar=10µm.

(B) Blood urea nitrogen (BUN) levels in control (CTRL) and FAN mice.

(C) Quantification of Sirius red stained area in kidney sections of control (CTRL), FAN and unilateral ureteral obstruction (UUO).

(D) Feature plots show expression of cell type markers identified by differential expression analysis.

(E) UMAP plot showing the distribution of cells from six different control and two different FAN kidneys.

(F) Expression of cell type markers identified in control samples (Park et al. 2018) in control (red) and FAN kidneys (blue). Color intensity indicates expression level, circle size correlates with % of positive cells.

Figure S2 (Related to Figure 2)
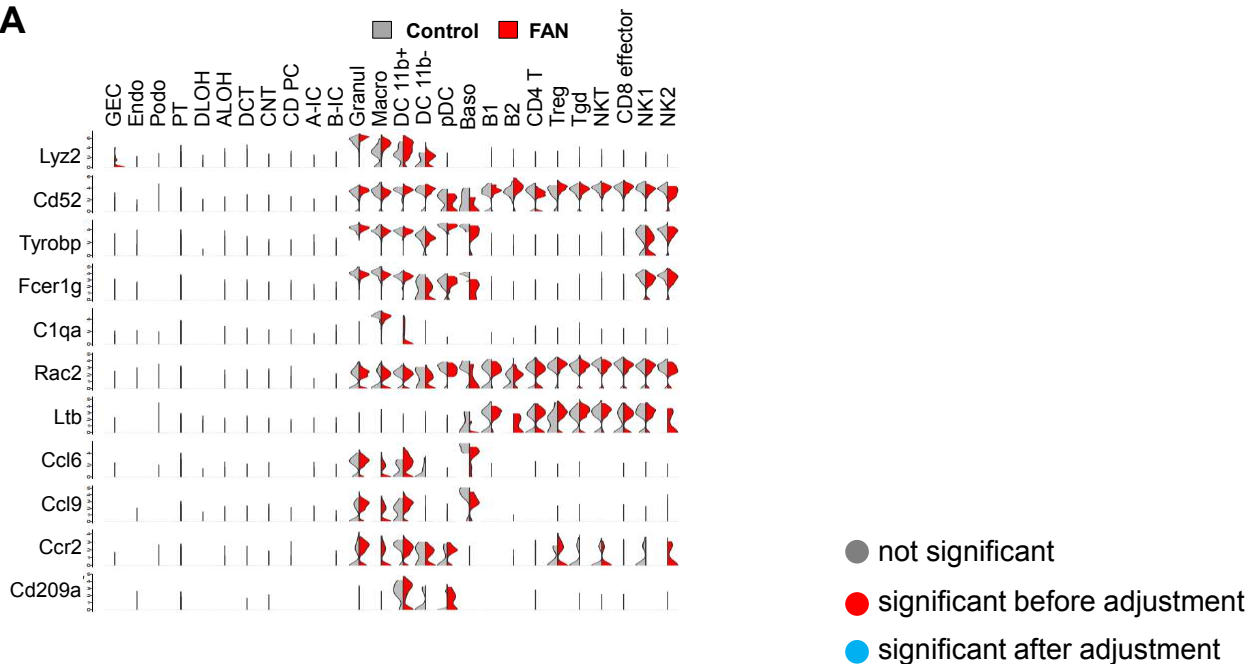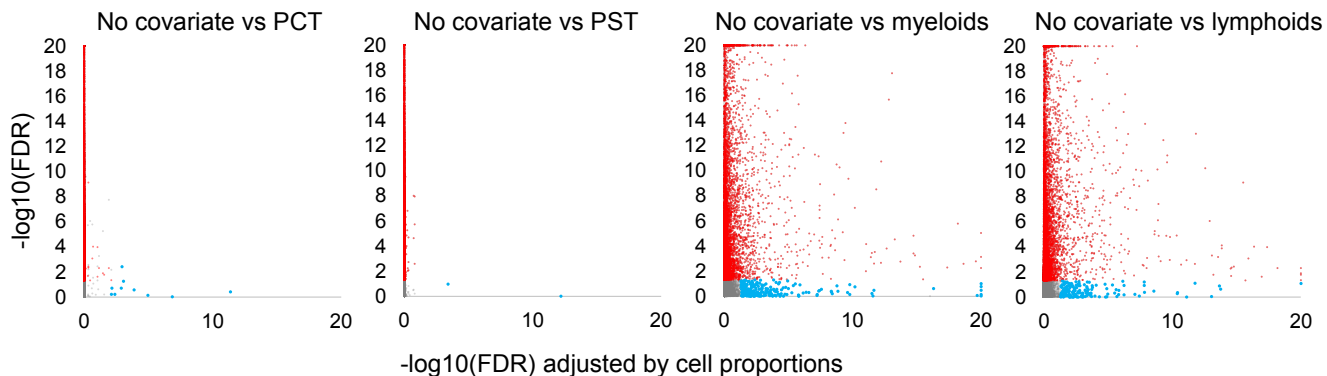
Figure S2 (Related to Figure 2). Cell composition and cell type specific changes in kidney fibrosis

(A) Half violin plots (control: gray and FAN: red) showing the expression the top differentially expressed genes in bulk RNAseq across the single cell clusters. The y axis shows the log-scale normalized read count.

(B) X-axis denoted -log(10)FDR adjusted by cell proportions (PCT, PST, myeloid or lymphoid cells), y-axis -log(10) FDR in unadjusted bulk RNAseq data. Gray shows genes without significant change in expression, red shows significant differences before, blue after cell proportion adjustment.

Figure S3 (Related to Figure 4)
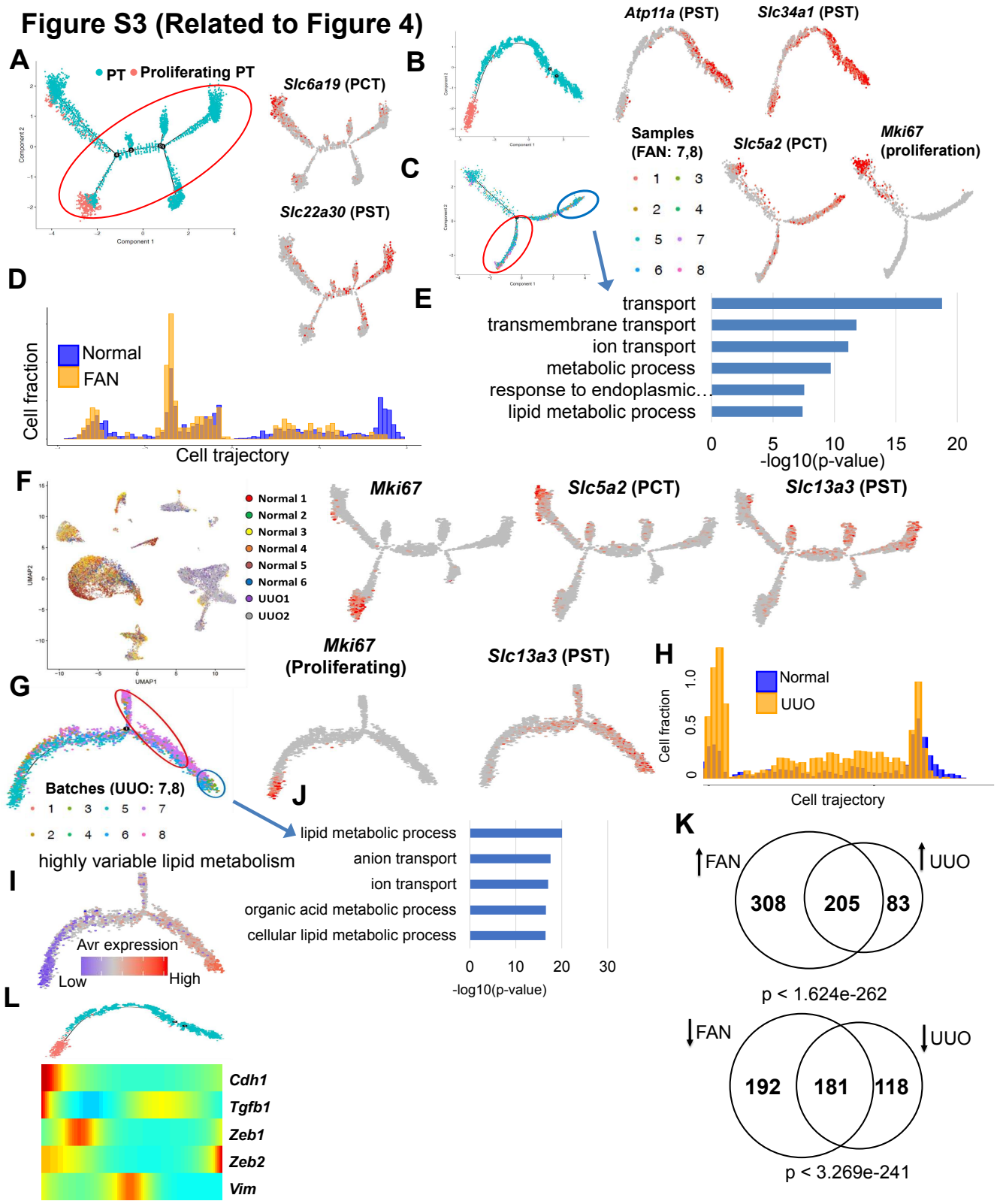
Figure S3 (Related to Figure 4). Cell trajectory analysis of fibrotic proximal tubules.

(A) Cell trajectory analysis for PT cells (including proliferating PT cells) in control and FAN samples. On the right, feature plots showing the expression of the indicated markers along the cell trajectory (*Slc6a19:* PCT marker and *Slc22a30*: PST marker).

(B) Cell trajectory analysis of PST cells (cells circled in red Figure S3A) in control and FAN samples. On the right, expression of *PST markers such as Atp11a* and *Slc34a1* along the cell trajectory.

(C) Monocle-based cell trajectory (all control and FAN samples included) along PCT differentiation trajectory. Batches 1-6 are healthy and 7 and 8 are from FAN kidneys. On the right, feature plots of proliferating (*Mki67*) and PCT segment markers (*Slc5a2*) along the cell trajectory.

(D) Distributions of cells along the PCT pseudo-time trajectory. Note the difference between healthy (Blue) and FAN samples (Yellow).

(E) Functional annotation analysis of genes showing differential expression along the differentiation trajectory (cells under red and blue circles in **Figure S3C**).

(F) UMAP plot showing the distribution of cells from six different control and two different UUO kidneys. On the right, feature plots showing the expression of the indicated markers projected onto the monocle cell trajectory.

(G) Cell trajectory analysis of PT cell including proliferating PT cell in control and UUO samples. Batches 7 and 8 correspond to UUO samples. On the right, feature plots showing the expression of the indicated markers on the cell trajectory.

(H) Distributions of cells along the PST pseudo-time trajectory. Healthy samples are colored blue while UUO samples are colored yellow. Note the differences of the cell distribution.

(I) Average expression levels of the highly variable genes that are involved in lipid metabolism on the cell trajectory.

(J) Functional annotation analysis of genes showing differential expression along the PT differentiation trajectory (red circle and blue circle in **Figure S3G compared**).

(K) Venn diagrams showing overlaps of the differentially expressed along the PT differentiation trajectory in the FAN and UUO models. Up arrow: upregulated genes and down arrow: downregulated genes.

(L) Heatmap showing the expression changes of EMT genes along the cell trajectory (**Figure 4C**).
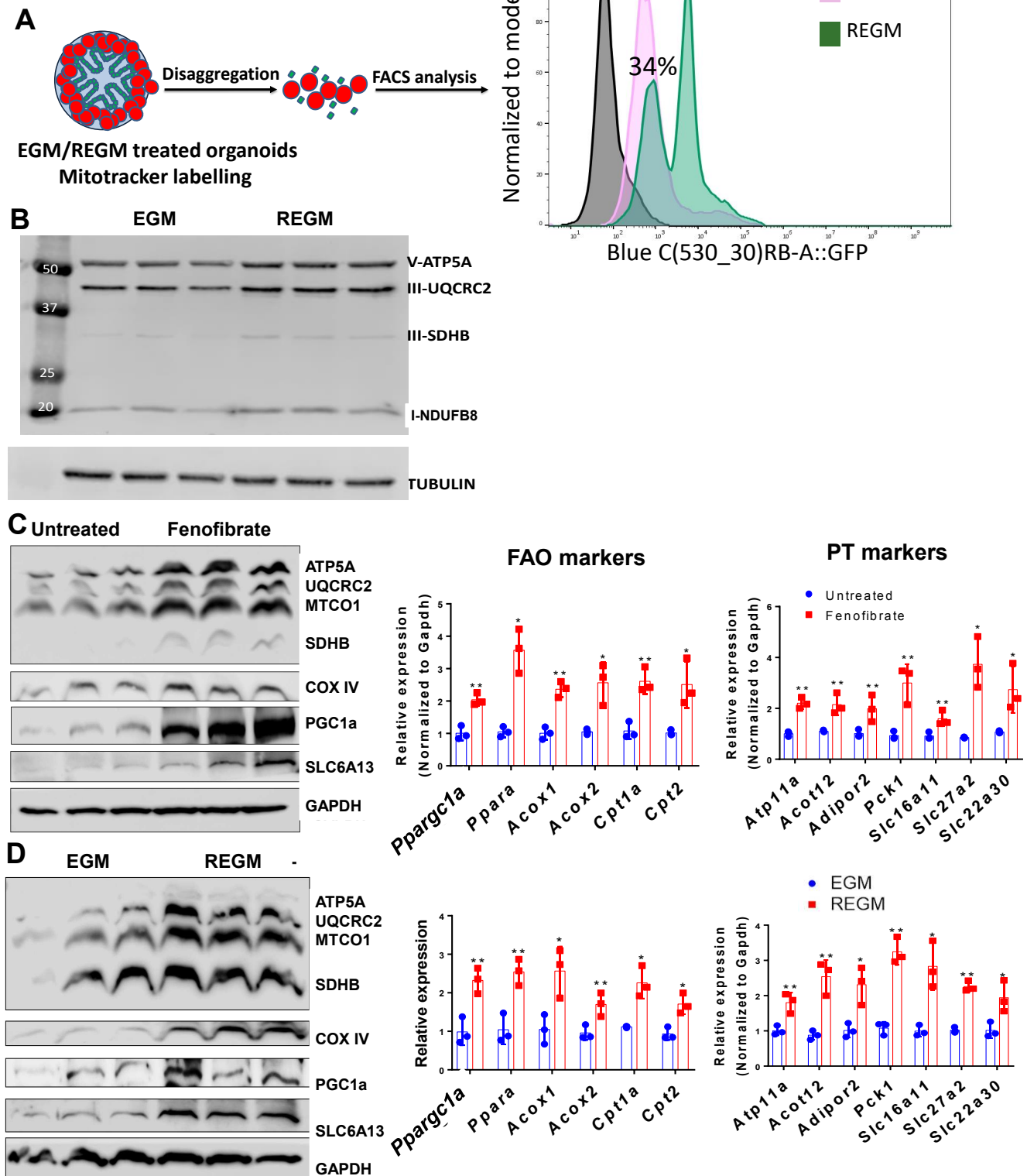
Figure S4 (Related to Figure 5)

Figure S4 (Related to Figure 5). Fatty acid oxidation and OXPHOS correlates with proximal tubule differentiation in human kidney organoids and LTL+ PT cells

(A) On the left, schematics of kidney organoids cultured in EGM or REGM. Disaggregated cells were stained with Mitotracker green and analyzed by flow cytometry. X-axis indicates Mitotracker green fluorescence (Blue laser 530/30) while y-axis shows the cell number.

(B) Representative Western blot of mitochondrial OXPHOS proteins and beta tubulin as loading control of kidney organoids cultured in EGM or REGM for 4 days.

(C) LTL$^+$ PT cells cultured in presence or absence of fenofibrate (1μM) for 7 days. Western Blot showing expression of mitochondrial OXPHOS complexes, COX IV, PGC1a, and SLC6A13 proteins. GAPDH was used as a loading control. Relative mRNA level of genes associated the FAO (*Ppargc1a, Ppara, Acox1, Acox2, Cpt1*, and *Cpt2*) and PT cell markers (*Atp11a, Acot12, Adipor2, Pck1, Slc16a11, Slc27a2,* and *Slc22a30*) (*from left to right*). * $P < 0.05$, ** $P < 0.01$, *** $P < 0.001$ vs. untreated.

(D) Representative Western Blot of mitochondrial OXPHOS, COX IV, PGC1a, SLC6A13, and GAPDH in isolated LTL$^+$ PT cells cultured in EGM or REGM media for 7 days. GAPDH was used as loading control. Relative mRNA level of genes associated with FAO (*Ppargc1a, Ppara, Acox1, Acox2, Cpt1,* and *Cpt2*) and PT cell markers (*Atp11a, Acot12, Adipor2, Pck1, Slc16a11, Slc27a2,* and *Slc22a30*) in isolated PT cells cultured in EGM and REGM. * $P < 0.05$, ** $P < 0.01$, *** $P < 0.001$ vs. EGM (*from left to right*).
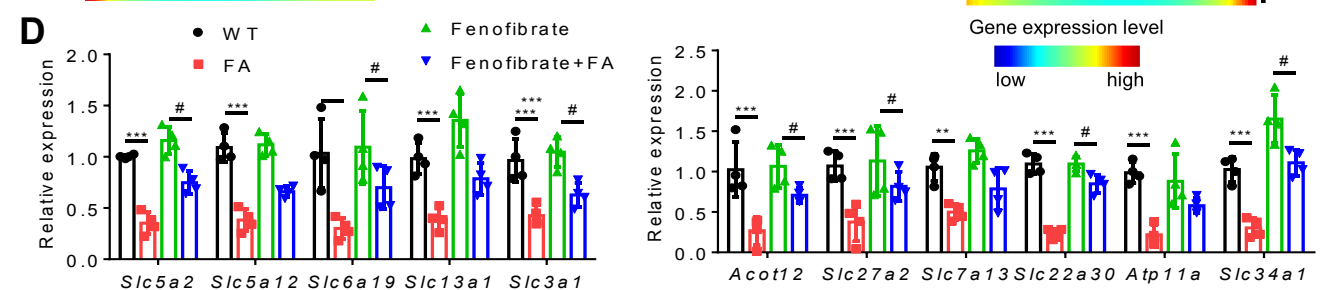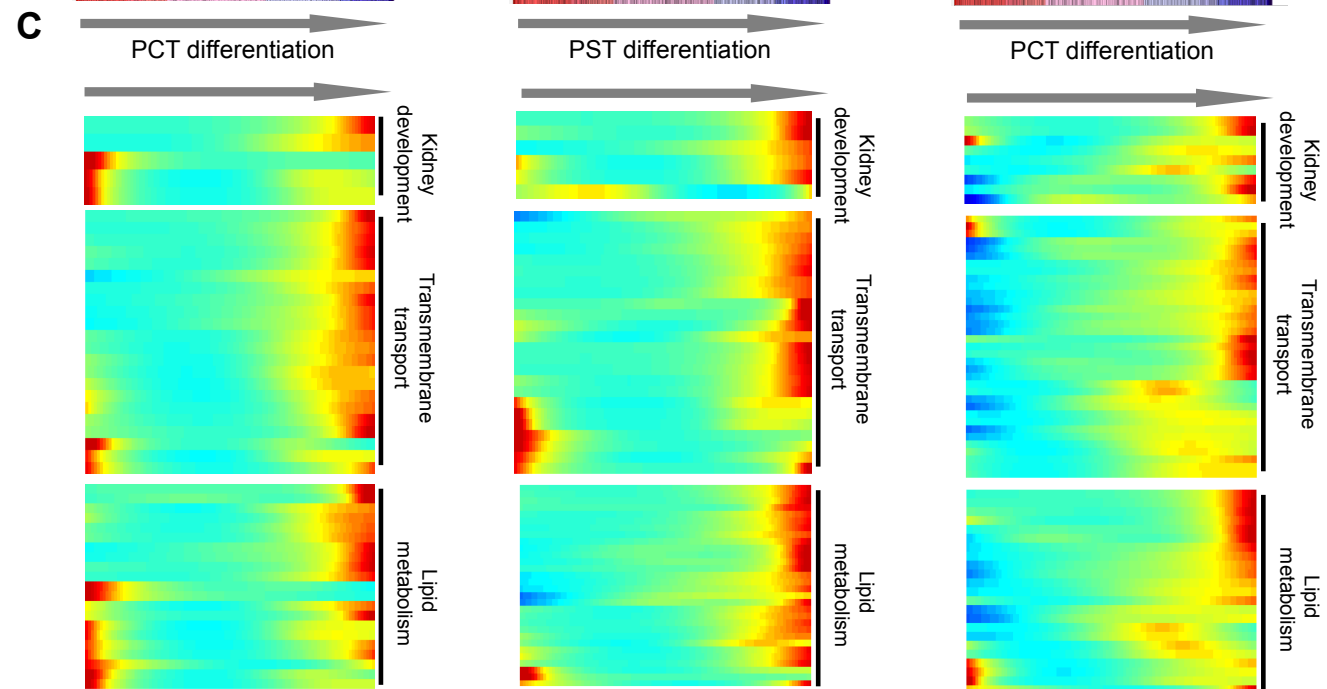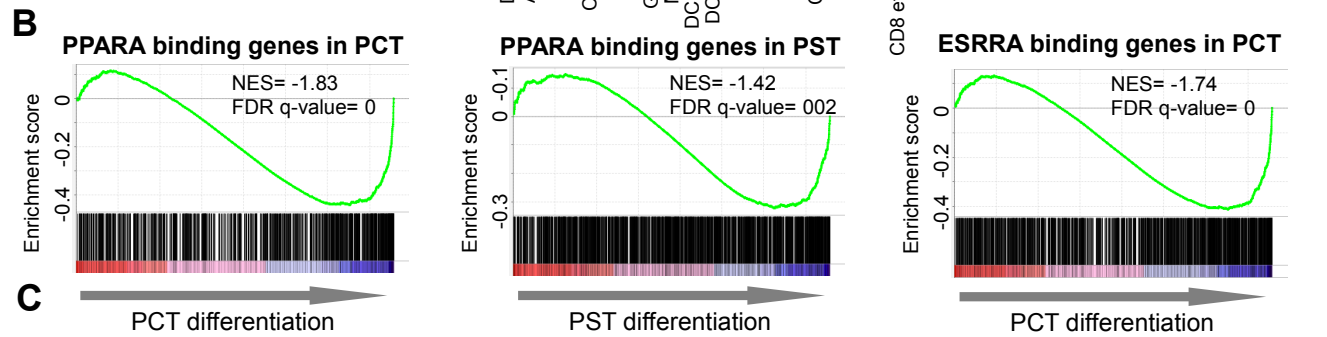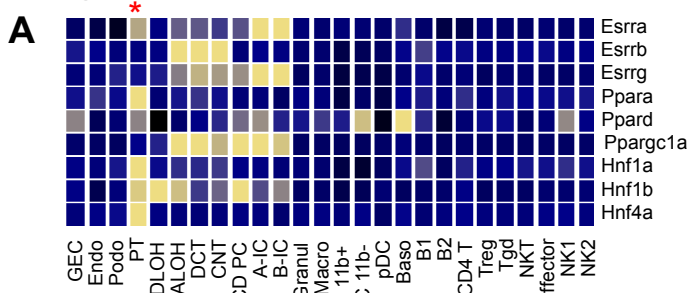
Figure S5 (Related to Figure 6)

Figure S5 (Related to Figure 6). ESRRA and PPARA binding dynamics along PT cell differentiation.

(A) Expression of selected transcription factors in mouse kidney single cell dataset. Mean expression values of genes were calculated in each cluster. The color scheme is based on z-score distribution. * represents PT cell cluster.

(B) Gene Set Enrichment Analysis (GSEA) enrichment plot of PPARA target genes along PCT cell differentiation, PST cell differentiation. GSEA enrichment plot of ESRRA target genes along PCT cell differentiation (*from left to right*).

(C) Heatmap showing the expression changes of PPARA target genes along the PCT cell trajectory, PST cell trajectory. Genes were grouped by functional clusters such as kidney development, transmembrane transport, and lipid metabolism genes.

(D) Relative expression of PST marker genes (*Atp11a, Acot12, Slc27a2, Slc22a30, Slc34a1,* and *Slc7a13*) and PCT marker genes (*Slc5a2, Slc5a12, Slc6a19, Slc13a1*, and *Slc3a1*) in kidneys of control (WT), FAN, fenofibrate treated sham, and fenofibrate treated FA-injected mice. (*n=4* in each group). * $P < 0.05$, ** $P < 0.01$, *** $P < 0.001$ *vs.* WT. # $P < 0.01$ vs. FAN mice.
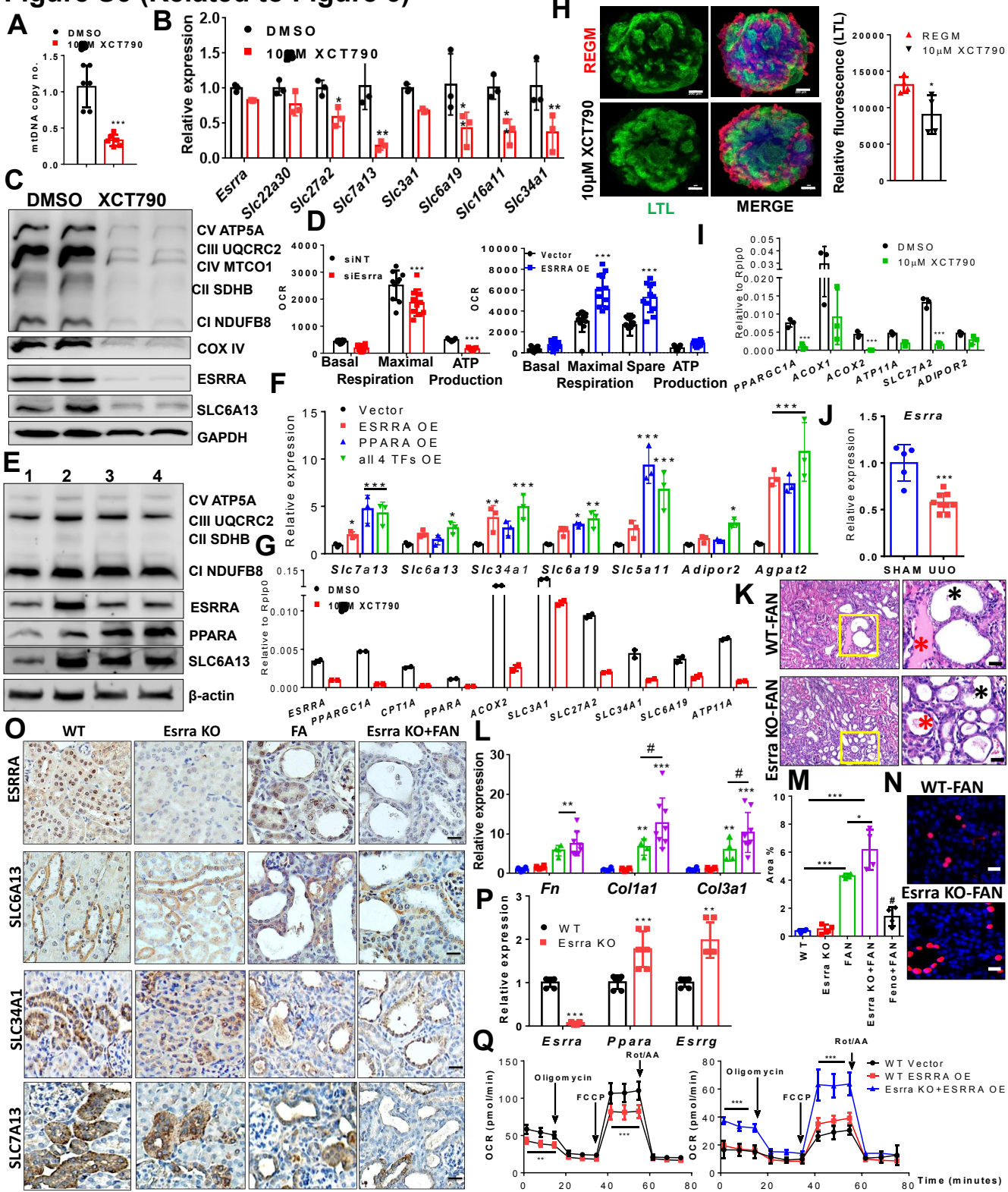
Figure S6 (Related to Figure 6)

Figure S6 (Related to Figure 6). Reduced ESRRA expression leads to impaired mitochondrial function and PT differentiation defect.

(A) Decrease in mtDNA content represented as mtDNA copy number in LTL⁺ PT cells (cultured in REGM media) treated with 10μM of ESRRA inhibitor XCT790 for 24 hours. *** *P< 0.001 vs.* DMSO.

(B) Relative transcript level of *Esrra* and PT marker genes (*Slc22a30, Slc27a2, Slc7a13, Slc3a1, Slc6a19, Slc16a11,* and *Slc34a1*) in LTL⁺ PT cells treated with 10μM XCT790 or DMSO for 24 hours. * *P < 0.05*, ** *P < 0.01*, *** *P< 0.001 vs.* DMSO.

(C) Representative Western Blot of OXPHOS, COX IV, ESRRA, and SLC6A13 expression in LTL⁺ PT cells cultured with 10μM of XCT790 for 24 hours. GAPDH is used as loading control.

(D) Basal respiration, maximal respiration capacity and ATP production in LTL+ PT cells transfected with non-target siRNA (siNT: black), ESRRA siRNA (siEsrra: Red) or control vector (vector: black) and ESRRA expressing vector (ESSRA OE: Blue). * *P < 0.05, ** P < 0.01, *** P< 0.001* vs. siNT/vector.

(E) Representative Western Blot of mitochondrial OXPHOS proteins, ESRRA, PPARA and SLC6A13 in LTL+ PT cells transfected with (**1**) Vector alone, (**2**) ESRRA OE plasmid, (**3**) PPARA OE plasmid, and (**4**) co-transfected all 4 TFs OE plasmids (ESRRA, PPARA, HNF1B, and HNF4A). β-actin was used as loading control.

(F) Relative mRNA levels of PT markers (*Slc7a13, Slc6a13, Slc34a1, Slc6a19, Slc5a11, Adipor2*, and *Agpat2*) in LTL⁺ PT cells transfected with vector (black), ESRRA OE (red), PPARA (Blue), and all 4 TFs (green) for 2 days. * *P < 0.05*, ** *P < 0.01*, *** *P< 0.001 vs.* vector.

(G) Relative transcript level of genes associated with FAO (*ESRRA, PPARGC1A, CPT1A, PPARA,* and *ACOX2*) and PT marker genes (*SLC3A1, SLC27A2, SLC34A1, SLC6A19* and *ATP11A*) in kidney organoids post 48 hours treatment of 10μM of XCT790 or DMSO. Data are represented as mean ± SEM. n= 2 independent experimental replicates from a pool of 12 organoids/group.

(H) Representative immunofluorescence staining of LTL (green) and PODXL (red) in human kidney organoids cultured in REGM media and treated with 10μM ESRRA inhibitor (XCT790) or DMSO for 48 hours. Quantification of LTL positive cells in kidney organoids shown on right. Data are represented as mean ± SEM. n= 3 independent experimental replicates from a pool of 3 organoids/group. * *P* < 0.05 *vs* REGM control (t-test paired). Scale bar=200μm.

(I) Relative transcript level of genes associated with FAO (*PPARGC1A, ACOX1,* and *ACOX2*) and PT marker genes (*ATP11A, SLC27A2,* and *Adipor2*) human PT cells treated with 10μM XCT790 or DMSO for 48 hours. Data are represented as mean ± SEM. *n*= 2 independent experimental replicates.

(J) Relative transcript level of *Esrra* in sham or UUO mouse kidneys. *** *P< 0.001 vs*. sham (*n=5, 9*).

(K) Representative images of hematoxylin and eosin (H&E) stained kidneys sections from FA-injected wild type (WT) and Esrra knock-out (KO) mice. The black star represents tubule dilation with loss of brush border and red star represent cast formation surrounded by inflammatory cells in diseased tissue. Scale bar=20μm.

(L) Relative transcript level of fibrosis associated genes (*Fn, Col1a1,* and *Col3a1*) in wild type, Esrra KO mice, sham or FAN treated kidneys (n= 4, 4, 6 and 8 respectively). * *P < 0.05*, ** *P < 0.01*, *** *P< 0.001* vs. WT. # *P < 0.05* vs FAN.

(M) Fibrosis levels scored from picrosirius red stained kidney sections from WT, Esrra knock-out (KO), FAN, FA treated Esrra KO and fenofibrate treated FA-injected mice and quantified using Image J. * *P < 0.05, ** P < 0.01, *** P< 0.001 vs*. WT. # *P < 0.01* vs. FAN mice.
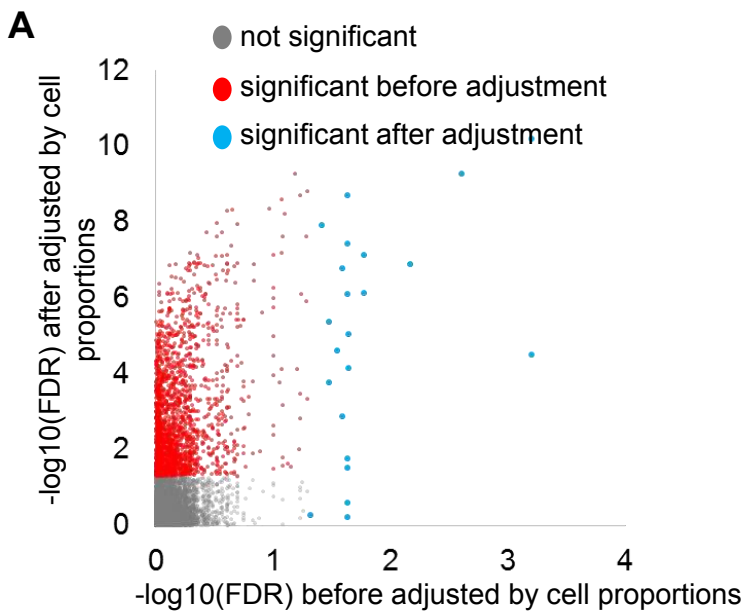
(N) Representative immunofluorescence images showing Ki67 staining in kidneys section from WT+FAN and Esrra KO+FAN mice. Scale bar=20µm.

(O) Immunohistochemical stain for ESRRA, SLC6A13, SLC34A1, and SLC7A13 of kidney sections of WT, Esrra KO, FAN and FA treated Esrra KO mice. Scale bar=20 µm.
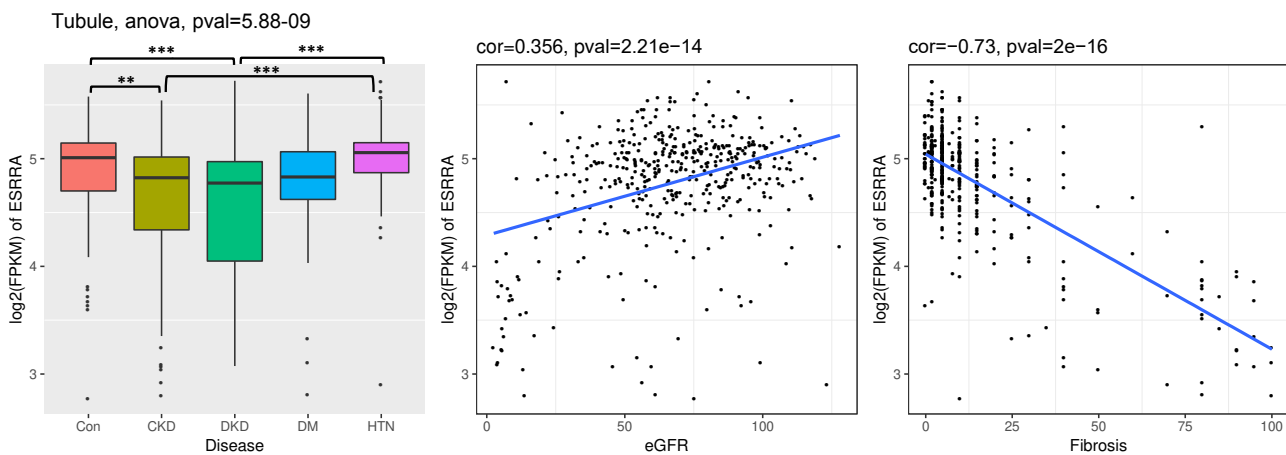
(P) Relative mRNA of *Esrra, Ppara*, and *Esrrg* in LTL$^+$ WT PT cells and Esrra KO PT cells. *$P < 0.05$, ** $P < 0.01$, *** $P < 0.001$ vs. WT.

(Q) Oxygen consumption rate (OCR) (pmol/min) in LTL$^+$ WT PT cells and Esrra KO PT cells (*on left*), and ESRRA transfected WT and Esrra KO PT cells (*on right*) for 2 days. *$P < 0.05$, ** $P < 0.01$, *** $P < 0.001$ vs. WT.

Figure S7 (Related to Figure 7)

A

- ● not significant
- ● significant before adjustment
- ● significant after adjustment

x-axis: -log10(FDR) before adjusted by cell proportions

y-axis: -log10(FDR) after adjusted by cell proportions

B

Tubule, anova, pval=5.88-09

y-axis: log2(FPKM) of ESRRA

x-axis: Disease (Con, CKD, DKD, DM, HTN)

cor=0.356, pval=2.21e−14

x-axis: eGFR

cor=−0.73, pval=2e−16

x-axis: Fibrosis

C

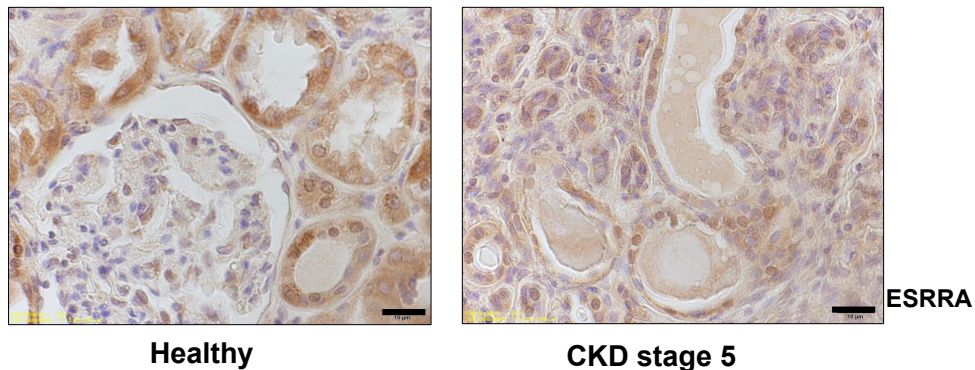Healthy   CKD stage 5   ESRRA

Figure S7 (Related to Figure 7). Changes in ESRRA expression in kidneys of patients with kidney fibrosis

(A) The number of DEGs that were correlated with fibrosis scores in 91 human samples significantly reduced after adjusting for cell fraction changes. X-axis represents significance of the correlation before adjusting to cell proportions. Y-axis represents significance of the correlation after the adjustment by cell proportions.

(B) ESRRA expression in 431 microdissected human kidney tissue samples CTL (control), HTN (hypertension), DM (diabetes), DKD (diabetic kidney disease) and CKD (chronic kidney disease). ESRRA transcript levels were compared between groups by ANOVA and post hoc comparison, $* P < 0.05$, $** P < 0.01$, $*** P < 0.001$). On the right, correlation between ESRRA transcript level and eGFR or fibrosis in microdissected human kidney tissue samples (Clinical information is available in **Table S7**).

(C) Representative immunostaining for ESRRA in healthy and CKD stage 5 human kidney samples. Scale bar= 10µm.

3. Paper III

Monteil, V., Kwon, H., **<u>Prado, P</u>**., Hagelkrüys, A., Wimmer, R. A., Stahl, M., Leopoldi, A., Garreta, E., Hurtado Del Pozo, C., Prosper, F., Romero, J. P., Wirnsberger, G., Zhang, H., Slutsky, A. S., Conder, R., Montserrat, N., Mirazimi, A., & Penninger, J. M.

Inhibition of SARS-CoV-2 Infections in Engineered Human Tissues Using Clinical-Grade Soluble Human ACE2.

Cell (2020), *181*(4), 905-913.e7.

Cell

Inhibition of SARS-CoV-2 Infections in Engineered Human Tissues Using Clinical-Grade Soluble Human ACE2

Graphical Abstract
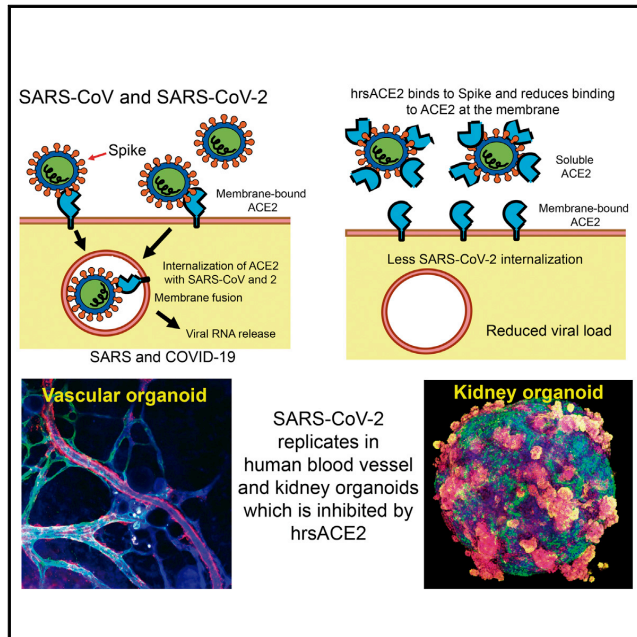
Authors

Vanessa Monteil, Hyesoo Kwon, Patricia Prado, ..., Nuria Montserrat, Ali Mirazimi, Josef M. Penninger

Correspondence

ali.mirazimi@sva.se (A.M.),
josef.penninger@ubc.ca (J.M.P.),
nmontserrat@ibecbarcelona.eu (N.M.)

In Brief

Clinical-grade recombinant human ACE2 can reduce SARS-CoV-2 infection in cells and in multiple human organoid models.

Highlights

- Soluble human ACE2 can inhibit SARS-CoV-2 infections

- SARS-CoV-2 can directly infect human blood vessel and kidney organoids

- Human organoids as model systems to study SARS-CoV-2 infections/COVID-19

CellPress

Cell

Article

Inhibition of SARS-CoV-2 Infections in Engineered Human Tissues Using Clinical-Grade Soluble Human ACE2

Vanessa Monteil,[1] Hyesoo Kwon,[2] Patricia Prado,[3] Astrid Hagelkrüys,[4] Reiner A. Wimmer,[4] Martin Stahl,[5] Alexandra Leopoldi,[4] Elena Garreta,[3] Carmen Hurtado del Pozo,[3] Felipe Prosper,[6] Juan Pablo Romero,[6] Gerald Wirnsberger,[7] Haibo Zhang,[8] Arthur S. Slutsky,[8] Ryan Conder,[5] Nuria Montserrat,[3,9,10,*] Ali Mirazimi,[1,2,*] and Josef M. Penninger[4,11,12,*]

[1]Karolinska Institute and Karolinska University Hospital, Department of Laboratory Medicine, Unit of Clinical Microbiology, 17177 Stockholm, Sweden
[2]National Veterinary Institute, 751 89 Uppsala, Sweden
[3]Pluripotency for Organ Regeneration, Institute for Bioengineería of Catalonia (IBEC), The Barcelona Institute of Technology (BIST), 08028 Barcelona, Spain
[4]Institute of Molecular Biotechnology of the Austrian Academy of Sciences, Dr. Bohr-Gasse 3, 1030 Vienna, Austria
[5]STEMCELL Technologies, Vancouver, BC V6A 1B6, Canada
[6]Cell Therapy Program, Center for Applied Medical Research (CIMA), University of Navarra, 31008 Pamplona, Spain
[7]Apeiron Biologics, Campus Vienna Biocenter 5, 1030 Vienna, Austria
[8]Keenan Research Centre for Biomedical Science at Li Ka Shing Knowledge Institute of St. Michael Hospital, University of Toronto, Toronto, ON M5B 1W8, Canada
[9]Catalan Institution for Research and Advanced Studies (ICREA), 08010 Barcelona, Spain
[10]Centro de Investigación Biomédica en Red en Bioingeniería, Biomateriales y Nanomedicina, 28029 Madrid, Spain
[11]Department of Medical Genetics, Life Science Institute, University of British Columbia, Vancouver, BC V6T 1Z3, Canada
[12]Lead Contact
*Correspondence: nmontserrat@ibecbarcelona.eu (N.M.), ali.mirazimi@sva.se (A.M.), josef.penninger@ubc.ca (J.M.P.)
https://doi.org/10.1016/j.cell.2020.04.004

SUMMARY

We have previously provided the first genetic evidence that angiotensin converting enzyme 2 (ACE2) is the critical receptor for severe acute respiratory syndrome coronavirus (SARS-CoV), and ACE2 protects the lung from injury, providing a molecular explanation for the severe lung failure and death due to SARS-CoV infections. ACE2 has now also been identified as a key receptor for SARS-CoV-2 infections, and it has been proposed that inhibiting this interaction might be used in treating patients with COVID-19. However, it is not known whether human recombinant soluble ACE2 (hrsACE2) blocks growth of SARS-CoV-2. Here, we show that clinical grade hrsACE2 reduced SARS-CoV-2 recovery from Vero cells by a factor of 1,000–5,000. An equivalent mouse rsACE2 had no effect. We also show that SARS-CoV-2 can directly infect engineered human blood vessel organoids and human kidney organoids, which can be inhibited by hrsACE2. These data demonstrate that hrsACE2 can significantly block early stages of SARS-CoV-2 infections.

INTRODUCTION

Outbreaks of emerging infectious diseases continue to challenge human health. The reported incidence of emerging and re-emerging zoonotic disease is increasing in many parts of the world. The severe acute respiratory syndrome coronavirus (SARS-CoV) first emerged 17 years ago (Drosten et al., 2003). In December 2019, a novel coronavirus (SARS-CoV-2) crossed species barriers to infect humans (Gorbalenya et al., 2020) and was effectively transmitted from person to person, leading to a pneumonia outbreak first reported in Wuhan, China (Guan et al., 2020; Jiang et al., 2020; Zhou et al., 2020b). This virus causes coronavirus disease-19 (COVID-19) with influenza-like symptoms ranging from mild disease to severe lung injury and multi-organ failure, eventually leading to death, especially in older patients with other co-morbidities. The WHO has declared that COVID-19 is a public health emergency of pandemic proportions (https://www.who.int/). The SARS-CoV-2 pandemic is not only an enormous burden to public health but has already markedly affected civil societies and the global economy.

SARS-CoV-2 shares multiple similarities with SARS-CoV (Andersen et al., 2020; Lu et al., 2020; Zhu et al., 2020). Phylogenetic analysis of SARS-CoV-2 demonstrated that this virus belongs to lineage B of the betacoronavirus genus (Chan et al., 2020; Letko et al., 2020). The receptor binding domain (RBD) of SARS-CoV-2 is similar to the SARS-CoV RBD, suggesting a possible common host cell receptor. ACE2 was identified as the functional SARS-CoV receptor *in vitro* and, by our group, *in vivo* (Imai et al., 2005; Kuba et al., 2005). Overexpression of human ACE2 enhanced disease severity in mice infected with
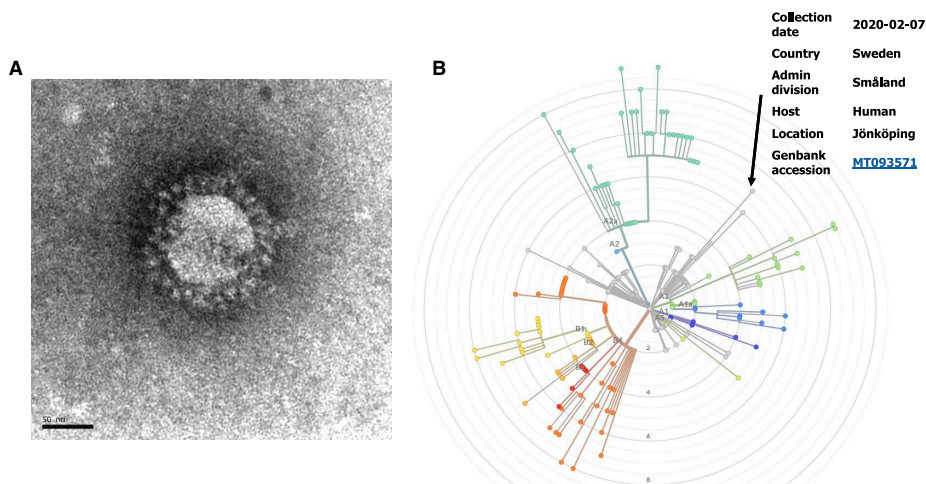
Collection date	2020-02-07
Country	Sweden
Admin division	Småland
Host	Human
Location	Jönköping
Genbank accession	MT093571

Figure 1. SARS-CoV-2 Sweden Virus Analyses
(A) Electron microscopy image of a viral particle of the Swedish SARS-CoV-2 isolate.
(B) Phylogenetic tree mapping the Swedish SARS-CoV-2 to clade A3.

SARS-CoV, demonstrating that ACE2-dependent viral entry into cells is a critical step (Yang et al., 2007). We reported that injecting SARS-CoV spike into mice decreased ACE2 expression levels, thereby worsening lung injury (Imai et al., 2005; Kuba et al., 2005). Thus, ACE2 serves both as the entry receptor of SARS-CoV and to protect the lung from injury (Zhang et al., 2020b).

Three recent cryoelectron microscopy (cryo-EM) studies demonstrated that SARS-CoV-2 spike protein directly binds to ACE2, and the SARS-CoV-2 spike protein recognizes human ACE2 with even higher binding affinity than Spike from SARS-CoV (Walls et al., 2020; Wan et al., 2020; Wrapp et al., 2020). Recently, it has been demonstrated in cell culture that soluble ACE2 fused to Ig (Wrapp et al., 2020) or a nonspecific protease inhibitor called camostat mesylate (Hoffmann et al., 2020), can inhibit infections with a pseudovirus bearing the S protein of SARS-CoV-2. High doses (100 μg/mL) of camostat mesylate were also shown to partially reduce SARS-CoV-2 growth, as expected from previous studies with other viruses (Hoffmann et al., 2020).

In a normal adult human lung, ACE2 is expressed primarily in alveolar epithelial type II cells, which can serve as a viral reservoir (Zhao et al., 2020). These cells produce surfactant that reduces surface tension, thus preventing alveoli from collapsing, and hence are critical to the gas exchange function of the lung (Dobbs, 1989). Injury to these cells could explain the severe lung injury observed in COVID-19 patients. We and others have also shown that ACE2 is expressed in multiple extrapulmonary tissues including heart, kidneys, blood vessels, and intestine (Crackower et al., 2002; Danilczyk and Penninger, 2006; Ding et al., 2004; Gu et al., 2005; Hamming et al., 2004; Zhang et al., 2020b). The ACE2 tissue distribution in these organs may explain the multi-organ dysfunction observed in patients

(Guan et al., 2020; Huang et al., 2020). Here, we report that clinical-grade human recombinant soluble ACE2 (hrsACE2), which has already been tested in phase 1 and phase 2 clinical trials (Haschke et al., 2013; Khan et al., 2017), can reduce viral growth in Vero E6 cells by a factor of 1,000–5,000. Moreover, we show that human blood vessel organoids and kidney organoids can be readily infected, which can be significantly inhibited by hrsACE2 at the early stage of infection.

RESULTS

Isolation of a SARS-CoV-2
To study potential therapeutic interventions for COVID-19, in early February 2020 we isolated the SARS-CoV-2 from a nasopharyngeal sample of a patient in Sweden with confirmed COVID-19. After successful culture on Vero E6 cells, the isolated virus was sequenced by next-generation sequencing (GenBank: MT093571). Electron microscopy showed the prototypic coronal shape of viral particles of our SARS-CoV-2 isolate (Figure 1A). Phylogenetic analysis showed the virus belongs to the clad A3 (Figure 1B).

hrsACE-2 Can Inhibit SARS-CoV-2 Infection in a Dose-Dependent Manner
hrsACE2 has already undergone clinical phase 1 and phase 2 testing (Khan et al., 2017) and is being considered for treatment of COVID-19 (Zhang et al., 2020b). Because ACE2 is the SARS-CoV-2 receptor, we wanted to provide direct evidence that clinical-grade hrsACE2 can indeed interfere with SARS-CoV-2 infections. To this end, we infected Vero-E6 cells (cells used for SARS-CoV-2 isolation) with different numbers of SARS-CoV-2: 10^3 plaque-forming units (PFUs; MOI 0.02), 10^5 PFUs (MOI 2), and 10^6
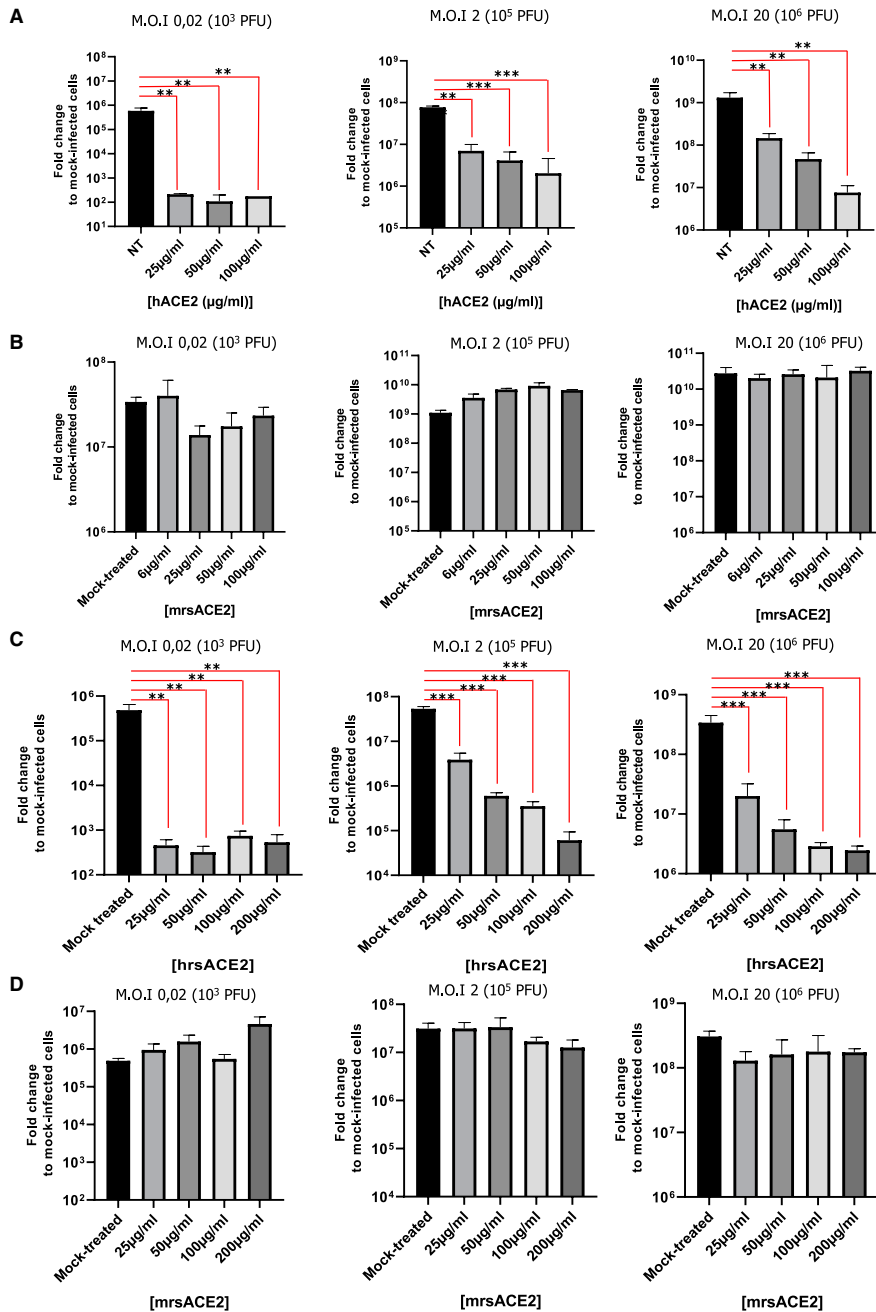
(legend on next page)

PFUs (MOI 20). Viral RNA as a marker for replication was purified from cells and assayed by qRT-PCR (Figure 2A). Infection of cells in the presence of hrsACE2 during 1 h, followed by washing and incubation without hrsACE2 significantly inhibited SARS-CoV-2 infections of Vero-E6 15 h post-infection (Figure 2A).

These data demonstrate that hrsACE2 inhibits the attachment of the virus to the cells. Importantly, as expected from a neutralizing agent, this inhibition was dependent on the initial quantity of the virus in the inoculum and the dose of hrsACE2 (Figure 2A), establishing dose-dependency. In contrast to hsrACE-2, the equivalent mouse recombinant soluble ACE2 (mrsACE2), produced in the same way as hrsACE2, did not inhibit the infection (Figure 2B). Finally, we performed experiments where cells were infected with SARS-CoV-2 in the presence of hrsACE2 or mrsACE2 for 15 h, to capture any newly produced virus particles during the 15 h that could infect neighboring cells. Again, we observed significantly reduced virus infections in the presence of hrsACE2 (Figure 2C), but not mrsACE2 (Figure 2D). Of note, addition of human or mouse rsACE2 was not toxic to the Vero-E6 cells, monitored for 15 h (data not shown). These data show that hrsACE2 significantly reduces SARS-CoV-2 infections *in vitro*.

hrsACE-2 Inhibits SARS-CoV-2 Infections of Human Capillary Organoids

A primary site of SARS-CoV-2 infection appears to be the lung, which may be a source for viral spread to other tissues such as the kidney and intestine, where virus has been found (stool [Wang et al., 2020; Young et al., 2020] and urine [Ling et al., 2020]).. Moreover, viremia is established during the course of the disease, although viral RNA in blood is only infrequently observed (Wang et al., 2020). However, the virus has a size of 80–100 nm indicating that viremic SARS-CoV-2 must first infect blood vessels prior to local tissue infections. To test this hypothesis, we established human capillary organoids from induced pluripotent stem cells (iPSCs) (Figure 3A) and infected them with our SARS-CoV-2 isolate. Of note, these organoids closely resemble human capillaries with a lumen, CD31^{+} endothelial lining, PDGFR^{+} pericyte coverage, as well as formation of a basal membrane (Wimmer et al., 2019). The capillary organoids were analyzed by qRT-PCR for the presence of viral RNA at day 3 and 6 after primary SARS-CoV-2 exposure. Importantly, following infection, we could detect viral RNA in the blood vessel organoids with viral RNA increasing from day 3 to day 6 post-infection (Figure 3B), indicating active replication of SARS-CoV-2.

Supernatant of infected organoids collected at day 6 post-infection could efficiently infect Vero E6 cells (Figure 3C), showing that the infected capillary organoids produced progeny virus. Importantly, addition of hrsACE2 markedly reduced SARS-CoV-2 infections of the engineered human blood vessels (Figure 3D). Of note, addition of human or mouse rsACE2 was not toxic to human blood vessels, monitored for 3 days (data not shown). These data show that human capillary organoids can be infected with SARS-CoV-2, and this infection can be significantly inhibited by hrsACE2.

hrsACE-2 Can Inhibit SARS-CoV-2 Infections of Human Kidney Organoids

We and others have previously shown that ACE2 is strongly expressed in kidney tubules (Danilczyk and Penninger, 2006). Moreover, it has been reported that SARS-CoV-2 can be found in the urine (Ling et al., 2020). To test whether SARS-CoV-2 can directly infect human tubular kidney cells, we generated kidney organoids from human embryonic stem cells into 3D suspension culture, adapting our own protocol (Garreta et al., 2019). Importantly, kidney differentiation organoids demonstrated prominent tubular-like structures as detected by Lotus tetraglobus lectin (LTL) as a marker of proximal tubular epithelial cells (Figure 4A). Tubular-like cells also expressed the solute carrier SCL3A1 (Figure S1A) together with SCL27A2 and SCL5A12. Furthermore, LTL-positive (LTL[+]) cell fractions from organoids expressed markers of proximal tubular identity (Figures S1B and S1C). Single-cell profiling of kidney organoids showed the presence of cells expressing ACE2 in the proximal tubule and podocyte II cell clusters that express key marker genes of proximal tubular cells (SLC3A1 and SLC27A2) and podocytes (PODXL, NPHS1, and NPHS2), respectively (Figure S2). Thus, kidney organoids contain cell clusters that express ACE2 in a similar fashion to that observed in the native tissue (Lin et al., 2020).

Infections of kidney organoids were monitored 6 days after SARS-CoV-2 infection and assayed for the presence of viral RNA using qRT-PCR. Progeny virus was determined as above using re-infections of Vero E6 cells. As expected from cells and tissues that express ACE2, SARS-CoV-2 replicated in kidney organoids (Figure 4B). Supernatant of infected kidney organoids collected at day 6 post-infection could efficiently infect Vero E6 cells (Figure 4C), showing that the engineered kidney organoids produced infectious progeny virus. Importantly, addition of hrsACE2 significantly reduced SARS-CoV-2

Figure 2. Human Recombinant Soluble ACE2 (hrsACE2) Blocks SARS-CoV-2 Infections

(A) Different concentrations of human recombinant ACE2 (hrsACE2) were mixed with SARS-CoV-2 for 30 min and then added to the culture medium of Vero-E6 cells. Cells were washed after 1 h post-infection (hpi) and incubated with fresh medium. Cell were recovered 15 hpi, and viral RNA was assayed by qRT-PCR. Data are represented as mean ± SD. (Student's t test:**p < 0.01; ***p < 0.001).

(B) Murine recombinant soluble ACE2 (mrsACE2) did not significantly affect SARS-CoV-2 infections of Vero-E6 cells, highlighting the specificity of hrsACE2 in blocking SARS-CoV-2 entry. mrsACE2 was mixed with SARS-CoV-2 for 30 min and then added to the culture medium of Vero E6 cells. Cells were washed after 1 hpi and incubated with fresh medium. Cells were recovered 15 hpi, and viral RNA was assayed by qRT-PCR. Data are represented as mean ± SD.

(C) Effect of hrsACE2 treatment on progeny virus. Vero E6 cells were infected with the indicated MOI of SARS-CoV-2, (the inoculum was not removed). Cells were recovered 15 hpi and viral RNA was assayed by qRT-PCR. Inhibition of the progeny virus by hsrACE2 resulted in significantly reduced virus infections. Data are represented as mean ± SD (Student's t test: *p < 0.05; **p < 0.01).

(D) Murine recombinant soluble ACE2 (mrsACE2) did not significantly affect SARS-CoV-2 infections of Vero-E6 cells, highlighting the specificity of hsrACE2 in blocking SARS-CoV-2 entry. Vero-E6 cells were infected with the indicated MOI of SARS-CoV-2 treated with murine recombinant soluble ACE2. Cells were harvested at 15 hpi, and viral RNA was assayed by qRT-PCR.
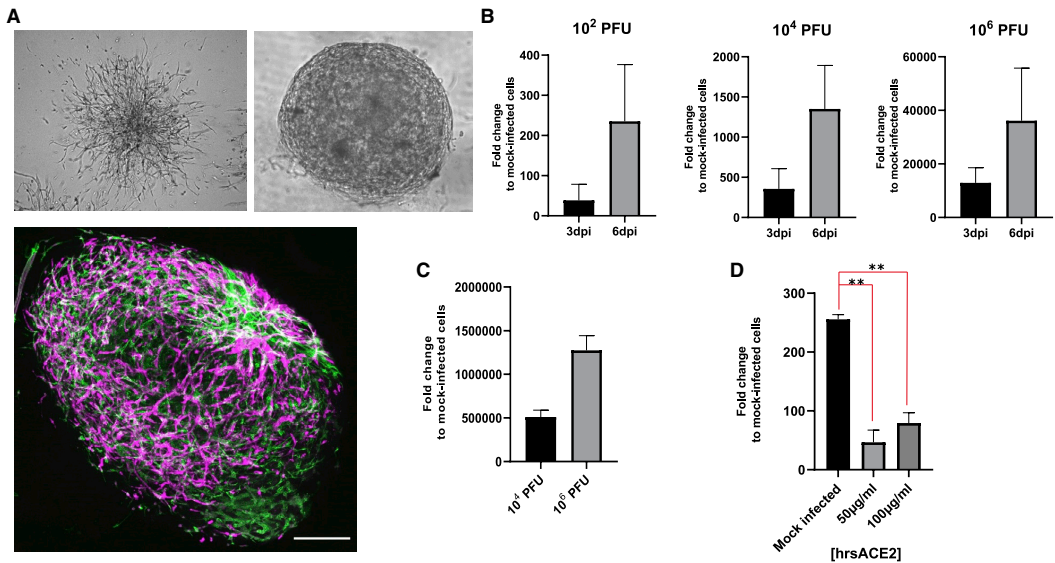
Figure 3. SARS-CoV-2 Infections of Blood Vessels Organoids

(A) Representative images of vascular capillary organoids using light microscopy (magnifications ×10) (upper panels) and immunostaining of blood vessel organoids using anti-CD31 to detect endothelial cells and anti-PDGFRβ to detect pericytes. DAPI (blue) was used to visualize nuclei. Scale bars, 500 μm and 50 μm (inset).

(B) Recovery of viral RNA from blood vessel organoids at day 3 and 6 post-infection (dpi) with SARS-CoV-2, demonstrating that the virus can infect the vascular organoids. Data are represented as mean ± SD.

(C) Determination of progeny virus. Supernatants of SARS-CoV-2 infected blood vessel organoids were collected 6 dpi and then used to infect Vero E6 cells. After 48 h, Vero E6 cells were washed and viral RNA assessed by qRT-PCR. The data show that infected blood vessel organoids can produce progeny SARS-CoV-2 viruses, depending on the initial level of infection. Data are represented as mean ± SD.

(D) Effect of hrsACE2 on SARS-CoV-2 infections of blood vessel organoids. Organoids were infected with a mix of 10^6 infectious viral particles and hrsACE2 for 1 h. 3 dpi, levels of viral RNA were assessed by qRT-PCR. hrsACE2 significantly decreased the level of SARS-CoV-2 infections in the vascular organoids. Data are represented as mean ± SD (Student's t test: **p < 0.01).

infections of the human kidney organoids in a dose-dependent manner (Figure 4D). Of note, addition of human or mouse rsACE2 was not toxic to the kidney, monitored for 3 days (data not shown). These data indicate that besides blood vessels, engineered human kidney organoids can also be infected with SARS-CoV-2, and this infection can be inhibited by hrsACE2.

DISCUSSION

ACE2 took center stage in the COVID-19 outbreak as the key receptor for the spike glycoprotein of SARS-CoV-2, as demonstrated in multiple structural and biochemical interaction studies (Wrapp et al., 2020; Zhou et al., 2020b). Moreover, multiple drug development projects, including development of vaccines are focusing on the ACE2-SARS-CoV-2 Spike interactions. We initially identified mammalian ACE2 when we realized that flies carry two orthologs of ACE (angiotensin-converting enzyme). Our first ace2 mutant mice then demonstrated that ACE2 is a negative regulator of the renin-angiotensin system (RAS) and genetically controls cardiovascular function and damage of multiple organs such as the lung, liver, and kidney

(Clarke and Turner, 2012; Crackower et al., 2002). ACE2 catalytically removes the last amino acid of angiotensin II, thereby counterbalancing ACE and Ang II actions and generating "beneficial" downstream peptides such as Ang1-7. ACE2 also catalytically acts on other peptides such as in the Apelin/APJ system (Clarke and Turner, 2012).

Importantly, we reported that ACE2 protects from lung injury, based on its catalytic domain, and ACE2 is the critical *in vivo* SARS-CoV spike glycoprotein receptor (Imai et al., 2005; Kuba et al., 2005). Initially two receptors had been identified for SARS-CoV in cell lines, namely ACE2 (Li et al., 2003) and the lectin L-SIGN (Jeffers et al., 2004). The severity of SARS could be partially explained by SARS-CoV Spike protein binding to ACE2 at a molecular interaction site that does not interfere with its catalytic activity (Li et al., 2005), which then leads to endocytosis of the virus and loss of ACE2 (Kuba et al., 2005), establishing a vicious circle of viral infection and local loss of lung injury protection. This led to the initiation of a drug development program—the development of soluble recombinant human ACE2, a drug that has undergone phase 1 testing in healthy volunteers and phase 2 testing in some patients with acute respiratory distress syndrome (ARDS) (Haschke et al., 2013; Khan et al.,
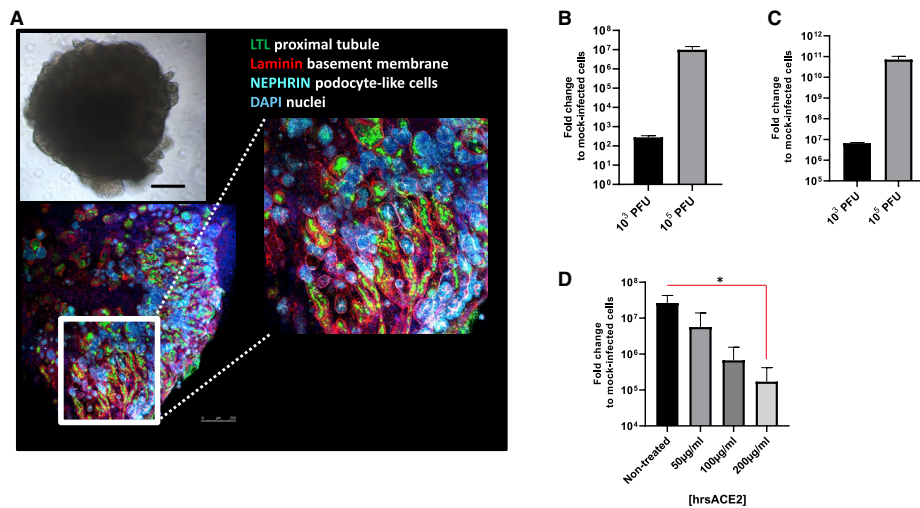
Figure 4. SARS-CoV-2 Infections of Human Kidney Organoids

(A) Representative images of a kidney organoid at day 20 of differentiation visualized using light microscopy (top left inset; scale bar, 100 μm) and confocal microscopy. Confocal microscopy images show tubular-like structures labeled with Lotus tetraglobus lectin (LTL, in green) and podocyte-like cells showing positive staining for nephrin (in turquoise). Laminin (in red) was used as a basement membrane marker. DAPI labels nuclei. A magnified view of the boxed region shows a detail of tubular structures. Scale bars, 250 and 100 μm, respectively.

(B) Recovery of viral RNA in the kidney organoids at day 6 dpi with SARS-CoV-2. Data are represented as mean ± SD.

(C) Determination of progeny virus. Supernatants of SARS-CoV-2 infected kidney organoids were collected 6 dpi and then used to infect Vero E6 cells. After 48 h, Vero E6 cells were washed and viral RNA assessed by qRT-PCR. The data show that infected kidney organoids can produce progeny SARS-CoV-2 viruses, depending on the initial level of infection. Data are represented as mean ± SD.

(D) Effect of hrsACE2 on SARS-CoV-2 infections kidney organoids. Organoids were infected with a mix of 10^6 infectious viral particles and hrsACE2 for 1 h. 3 dpi, levels of viral RNA were assessed by qRT-PCR. hrsACE2 significantly decreased the level of SARS-CoV-2 infections in the kidney organoids. Data are represented as mean ± SD (Student's t test: *$p < 0.05$).

2017; Treml et al., 2010). Our data now show that this clinical-grade human ACE2 molecule—but not mouse soluble ACE2—can significantly inhibit SARS-CoV-2 infections and reduce viral load by a factor of 1,000–5,000. However, as observed in antibody neutralizing experiments of many viruses, the inhibition is not complete, although clearly dose-dependent. This may be due to the fact that there might be other co-receptors/auxiliary proteins or even other mechanisms by which viruses can enter cells, as had been initially proposed for SARS (Jeffers et al., 2004; Qi et al., 2020). Such a second receptor has been also suggested based on clinical data: SARS transmissibility was very low possibly due to the low level expression of ACE2 in the upper respiratory tract (Bertram et al., 2012; Hamming et al., 2004). Transmissibility of SARS-CoV-2 is much greater than that of SARS-CoV, suggesting that SARS-CoV-2 might use a co-receptor and/or other factors that allow infection of ACE2-expressing cells in the upper respiratory tract (Lukassen et al., 2020). Most importantly, our results demonstrate that hrsACE2 significantly blocks SARS-CoV-2 infections, providing a rationale that soluble ACE2 might not only protect from lung injury but also block the SARS-CoV-2 from entering target cells.

Pathology due to SARS, MERS, and now COVID-19 is not limited to the lung; damage can occur in multiple organs (Gu et al., 2005; Wu and McGoogan, 2020; Yeung et al., 2016).

ACE2 is expressed in various tissues including the heart, kidney tubules, the luminal surface of the small intestine, and blood vessels (Crackower et al., 2002; Danilczyk and Penninger, 2006; Ding et al., 2004; Gu et al., 2005; Hamming et al., 2004; Zhang et al., 2020b), suggesting that SARS-CoV-2 could also infect these tissues. We now show that blood vessels as well as kidney organoids can be readily infected by SARS-CoV-2. SARS-CoV-2 must enter the blood stream to infect other tissues. However, the size of the infectious viral particles is ~80–100 nm (Wrapp et al., 2020). Thus, unless there is already tissue damage, the virus must enter vascular endothelial cells to migrate into the organs. Our data in engineered human capillary organoids now suggest that SARS-CoV-2 could directly infect blood vessel cells. Infected blood vessel organoids also shed progeny viruses. Importantly, hrsACE2 markedly inhibited SARS-CoV-2 infections of the vascular organoids.

ACE2 is strongly expressed in kidney tubules, controlling a local RAS circuit (Clarke and Turner, 2012; Hashimoto et al., 2012). As an infection model, we therefore engineered human kidneys organoids from stem cells differentiated to contain tubular networks (Garreta et al., 2019). We now show that SARS-CoV-2 can infect such human kidney organoids, resulting in infectious viral progeny, inhibited by hrsACE2. Clinically,

SARS-CoV-2 has been found in the urine (Ling et al., 2020), and many patients with COVID-19 present with cardiovascular and renal dysfunctions (Huang et al., 2020; Yang et al., 2020; Zhang et al., 2020a; Zhou et al., 2020a). Whether direct viral infection of the vasculature and kidneys directly contributes to the observed multi-organ damage in COVID-19 patients needs to be established. Given the fact that cardiac cells express high levels of ACE2, and heart alterations were the first phenotype observed in our *ace2* mutant mice (Crackower et al., 2002), it will be important to expand on our studies to heart and in particular lung organoids to better understand the multi-organ dysfunction in patients with COVID-19.

Our Study Has Limitations

The design of our studies focused on the early stages of infection, demonstrating that hrsACE2 can block early entry of SARS-CoV-2 infections in host cells. As such, we cannot make any predictions with respect to the effect of hrsACE2 in later stages of the disease process. Second, we did not study lung organoids, and the lung is the major target organ for COVID-19. Finally, the RAS system represents a complex network of pathways that are influenced by external processes that are not simulated in our model systems. To address these issues, further studies are needed to illuminate the effect of hrsACE2 at later stages of infection *in vitro* and *in vivo*.

STAR★METHODS

Detailed methods are provided in the online version of this paper and include the following:

- KEY RESOURCES TABLE
- RESOURCE AVAILABILITY
  - Lead Contact
  - Materials Availability
  - Data and Code Availability
- EXPERIMENTAL MODEL AND SUBJECT DETAILS
  - Virus
  - Cells and human capillary organoids
- METHOD DETAILS
  - Preparation of soluble recombinant human and murine ACE2
  - Kidney organoid differentiation
  - Phylogenetic analysis
  - Treatments of Vero E6 cells with human rsACE2 and murine rsACE2
  - SARS-CoV-2 infections of kidney and blood vessel organoids
  - Treatment of organoids with hrsACE2
  - Cytotoxicity assay
  - qRT-PCR
  - Single cell sequencing of kidney organoids
  - Histological analysis
  - Flow cytometry
- QUANTIFICATION AND STATISTICAL ANALYSIS
  - Kidney Organoid scRNA-seq Data Analysis
  - Statistics

REFERENCES

Andersen, K.G., Rambaut, A., Lipkin, W.I., Holmes, E.C., and Garry, R.F. (2020). The proximal origin of SARS-CoV-2. Nat. Med. Published online March 17, 2020. https://doi.org/10.1038/s41591-020-0820-9.

Becker, M.M., Graham, R.L., Donaldson, E.F., Rockx, B., Sims, A.C., Sheahan, T., Pickles, R.J., Corti, D., Johnson, R.E., Baric, R.S., Denison, M.R., et al. (2008). Synthetic recombinant bat SARS-like coronavirus is infectious in cultured cells and in mice. Proc. Natl. Acad. Sci. U S A *105*, 19944–19949.

Bertram, S., Heurich, A., Lavender, H., Gierer, S., Danisch, S., Perin, P., Lucas, J.M., Nelson, P.S., Pöhlman, S., and Soilleux, E.J. (2012). Influenza and SARS-coronavirus activating proteases TMPRSS2 and HAT are expressed at multiple sites in human respiratory and gastrointestinal tracts. PLoS ONE *7*, e35876.

Chan, J.F., Kok, K.H., Zhu, Z., Chu, H., To, K.K., Yuan, S., and Yuen, K.Y. (2020). Genomic characterization of the 2019 novel human-pathogenic coronavirus isolated from a patient with atypical pneumonia after visiting Wuhan. Emerg. Microbes Infect. 9, 221–236.

Clarke, N.E., and Turner, A.J. (2012). Angiotensin-converting enzyme 2: the first decade. Int. J. Hypertens. 2012, 307315.

Crackower, M.A., Sarao, R., Oudit, G.Y., Yagil, C., Kozieradzki, I., Scanga, S.E., Oliveira-dos-Santos, A.J., da Costa, J., Zhang, L., Pei, Y., et al. (2002). Angiotensin-converting enzyme 2 is an essential regulator of heart function. Nature 417, 822–828.

Danilczyk, U., and Penninger, J.M. (2006). Angiotensin-converting enzyme II in the heart and the kidney. Circ. Res. 98, 463–471.

Ding, Y., He, L., Zhang, Q., Huang, Z., Che, X., Hou, J., Wang, H., Shen, H., Qiu, L., Li, Z., et al. (2004). Organ distribution of severe acute respiratory syndrome (SARS) associated coronavirus (SARS-CoV) in SARS patients: implications for pathogenesis and virus transmission pathways. J. Pathol. 203, 622–630.

Dobbs, L.G. (1989). Pulmonary surfactant. Annu. Rev. Med. 40, 431–446.

Drosten, C., Günther, S., Preiser, W., van der Werf, S., Brodt, H.R., Becker, S., Rabenau, H., Panning, M., Kolesnikova, L., Fouchier, R.A., et al. (2003). Identification of a novel coronavirus in patients with severe acute respiratory syndrome. N. Engl. J. Med. 348, 1967–1976.

Elbe, S., and Buckland-Merret, G. (2017). Data, disease and diplomacy: GISAID's innovative contribution to global health. Glob Chall 1, 33–46.

Garreta, E., Prado, P., Tarantino, C., Oria, R., Fanlo, L., Martí, E., Zalvidea, D., Trepat, X., Roca-Cusachs, P., Gavaldà-Navarro, A., et al. (2019). Fine tuning the extracellular environment accelerates the derivation of kidney organoids from human pluripotent stem cells. Nat. Mater. 18, 397–405.

Gorbalenya, A.E., Baker, S.C., Baric, R.S., de Groot, R.J., Drosten, C., Gulyaeva, A.A., Haagmans, B.L., Lauber, C., Leontovich, A.M., Neuman, B.W., et al.; Coronaviridae Study Group of the International Committee on Taxonomy of Viruses (2020). The species Severe acute respiratory syndrome-related coronavirus: classifying 2019-nCoV and naming it SARS-CoV-2. Nat. Microbiol. 5, 536–544.

Gu, J., Gong, E., Zhang, B., Zheng, J., Gao, Z., Zhong, Y., Zou, W., Zhan, J., Wang, S., Xie, Z., et al. (2005). Multiple organ infection and the pathogenesis of SARS. J. Exp. Med. 202, 415–424.

Guan, W.J., Ni, Z.Y., Hu, Y., Liang, W.H., Ou, C.Q., He, J.X., Liu, L., Shan, H., Lei, C.L., Hui, D.S.C., et al.; China Medical Treatment Expert Group for Covid-19 (2020). Clinical Characteristics of Coronavirus Disease 2019 in China. N. Engl. J. Med. Published online February 28, 2020. https://doi.org/10.1056/NEJMoa2002032.

Hadfield, James, Megill, Colin, Bell, Sidney M., Huddleston, John, Potter, Barney, Callender, Charlton, Sagulenko, Pavel, Bedford, Trevor, and Neher, Richard A. (2018). Nextstrain: real-time tracking of pathogen evolution. Bioinformatics 34, 4121–4123.

Hamming, I., Timens, W., Bulthuis, M.L., Lely, A.T., Navis, G., and van Goor, H. (2004). Tissue distribution of ACE2 protein, the functional receptor for SARS coronavirus. A first step in understanding SARS pathogenesis. J. Pathol. 203, 631–637.

Haschke, M., Schuster, M., Poglitsch, M., Loibner, H., Salzberg, M., Bruggisser, M., Penninger, J., and Krähenbühl, S. (2013). Pharmacokinetics and pharmacodynamics of recombinant human angiotensin-converting enzyme 2 in healthy human subjects. Clin. Pharmacokinet. 52, 783–792.

Hashimoto, T., Perlot, T., Rehman, A., Trichereau, J., Ishiguro, H., Paolino, M., Sigl, V., Hanada, T., Hanada, R., Lipinski, S., et al. (2012). ACE2 links amino acid malnutrition to microbial ecology and intestinal inflammation. Nature 487, 477–481.

Hoffmann, M., Kleine-Weber, H., Schroeder, S., Krüger, N., Herrler, T., Erichsen, S., Schiergens, T.S., Herrler, G., Wu, N.H., Nitsche, A., et al. (2020). SARS-CoV-2 Cell Entry Depends on ACE2 and TMPRSS2 and Is Blocked by a Clinically Proven Protease Inhibitor. Cell. Published online March 4, 2020. https://doi.org/10.1016/j.cell.2020.02.052.

Huang, C., Wang, Y., Li, X., Ren, L., Zhao, J., Hu, Y., Zhang, L., Fan, G., Xu, J., Gu, X., et al. (2020). Clinical features of patients infected with 2019 novel coronavirus in Wuhan, China. Lancet 395, 497–506.

Imai, Y., Kuba, K., Rao, S., Huan, Y., Guo, F., Guan, B., Yang, P., Sarao, R., Wada, T., Leong-Poi, H., et al. (2005). Angiotensin-converting enzyme 2 protects from severe acute lung failure. Nature 436, 112–116.

Jeffers, S.A., Tusell, S.M., Gillim-Ross, L., Hemmila, E.M., Achenbach, J.E., Babcock, G.J., Thomas, W.D., Jr., Thackray, L.B., Young, M.D., Mason, R.J., et al. (2004). CD209L (L-SIGN) is a receptor for severe acute respiratory syndrome coronavirus. Proc. Natl. Acad. Sci. USA 101, 15748–15753.

Jiang, S., Du, L., and Shi, Z. (2020). An emerging coronavirus causing pneumonia outbreak in Wuhan, China: calling for developing therapeutic and prophylactic strategies. Emerg. Microbes Infect. 9, 275–277.

Khan, A., Benthin, C., Zeno, B., Albertson, T.E., Boyd, J., Christie, J.D., Hall, R., Poirier, G., Ronco, J.J., Tidswell, M., et al. (2017). A pilot clinical trial of recombinant human angiotensin-converting enzyme 2 in acute respiratory distress syndrome. Crit. Care 21, 234.

Kuba, K., Imai, Y., Rao, S., Gao, H., Guo, F., Guan, B., Huan, Y., Yang, P., Zhang, Y., Deng, W., et al. (2005). A crucial role of angiotensin converting enzyme 2 (ACE2) in SARS coronavirus-induced lung injury. Nat. Med. 11, 875–879.

Letko, M., Marzi, A., and Munster, V. (2020). Functional assessment of cell entry and receptor usage for SARS-CoV-2 and other lineage B betacoronaviruses. Nat. Microbiol. 5, 562–569.

Li, W., Moore, M.J., Vasilieva, N., Sui, J., Wong, S.K., Berne, M.A., Somasundaran, M., Sullivan, J.L., Luzuriaga, K., Greenough, T.C., et al. (2003). Angiotensin-converting enzyme 2 is a functional receptor for the SARS coronavirus. Nature 426, 450–454.

Li, F., Li, W., Farzan, M., and Harrison, S.C. (2005). Structure of SARS coronavirus spike receptor-binding domain complexed with receptor. Science 309, 1864–1868.

Lin, W., Hu, L., Zhang, Y., Ooi, J.D., Meng, T., Jin, P., Ding, X., Peng, L., Song, L., Xiao, Z., Ao, X., Xiao, X., Zhou, Q., Xiao, P., Fan, J., Zhong, Y., et al., 2020. Single-cell Analysis of ACE2 Expression in Human Kidneys and Bladders Reveals a Potential Route of 2019-nCoV Infection. bioRxiv. https://doi.org/10.1101/2020.02.08.939892. https://www.biorxiv.org/content/biorxiv/early/2020/02/18/2020.02.08.939892.full.pdf 2020. (Accessed 18 February 2020).

Ling, Y., Xu, S.B., Lin, Y.X., Tian, D., Zhu, Z.Q., Dai, F.H., Wu, F., Song, Z.G., Huang, W., Chen, J., et al. (2020). Persistence and clearance of viral RNA in 2019 novel coronavirus disease rehabilitation patients. Chin. Med. J. (Engl). Published online February 28, 2020. https://doi.org/10.1097/CM9.0000000000000774.

Lu, R., Zhao, X., Li, J., Niu, P., Yang, B., Wu, H., Wang, W., Song, H., Huang, B., Zhu, N., et al. (2020). Genomic characterisation and epidemiology of 2019 novel coronavirus: implications for virus origins and receptor binding. Lancet 395, 565–574.

Lukassen, S., Chua, R.L., Trefzer, T., Kahn, N.C., Schneider, M.A., Muley, T., Winter, H., Meister, M., Veith, C., Boots, A.W., et al. (2020). SARS-CoV-2 receptor ACE2 and TMPRSS2 are predominantly expressed in a transient secretory cell type in subsegmental bronchial branches. bioRxiv. https://doi.org/10.1101/2020.03.13.991455.

Motulsky, H.J., and Brown, R.E. (2006). Detecting outliers when fitting data with nonlinear regression - a new method based on robust nonlinear regression and the false discovery rate. BMC Bioinformatics 7, 123.

Qi, F., Qian, S., Zhang, S., and Zhang, Z. (2020). Single cell RNA sequencing of 13 human tissues identify cell types and receptors of human coronaviruses. Biochem. Biophys. Res. Commun. Published online March 18, 2020. https://doi.org/10.1016/j.bbrc.2020.03.044.

Schneider, C.A., Rasband, W.S., and Eliceiri, K.W. (2012). NIH Image to ImageJ: 25 years of image analysis. Nat. Methods 9, 671–675.

Stuart, T., Butler, A., Hoffman, P., Hafemeister, C., Papalexi, E., Mauck, W.M., 3rd, Hao, Y., Stoeckius, M., Smibert, P., and Satija, R. (2019). Comprehensive Integration of Single-Cell Data. Cell *177*, 1888–1902.

Treml, B., Neu, N., Kleinsasser, A., Gritsch, C., Finsterwalder, T., Geiger, R., Schuster, M., Janzek, E., Loibner, H., Penninger, J., and Loeckinger, A. (2010). Recombinant angiotensin-converting enzyme 2 improves pulmonary blood flow and oxygenation in lipopolysaccharide-induced lung injury in piglets. Crit. Care Med. *38*, 596–601.

Walls, A.C., Park, Y.-J., Tortorici, M.A., Wall, A., McGuire, A.T., and Veesler, D. (2020). Structure, Function, and Antigenicity of the SARS-CoV-2 Spike Glycoprotein. Cell. Published online March 6, 2020. https://doi.org/10.1016/j.cell.2020.02.058.

Wan, Y., Shang, J., Graham, R., Baric, R.S., and Li, F. (2020). Receptor recognition by novel coronavirus from Wuhan: An analysis based on decade-long structural studies of SARS. J. Virol. *94*, e00127-20.

Wang, W., Xu, Y., Gao, R., Lu, R., Han, K., Wu, G., and Tan, W. (2020). Detection of SARS-CoV-2 in Different Types of Clinical Specimens. JAMA. Published online March, 11, 2020. https://doi.org/10.1001/jama.2020.3786.

Wimmer, R.A., Leopoldi, A., Aichinger, M., Wick, N., Hantusch, B., Novatchkova, M., Taubenschmid, J., Hämmerle, M., Esk, C., Bagley, J.A., et al. (2019). Human blood vessel organoids as a model of diabetic vasculopathy. Nature *565*, 505–510.

Wrapp, D., Wang, N., Corbett, K.S., Goldsmith, J.A., Hsieh, C.L., Abiona, O., Graham, B.S., and McLellan, J.S. (2020). Cryo-EM structure of the 2019-nCoV spike in the prefusion conformation. Science *367*, 1260–1263.

Wu, Z., and McGoogan, J.M. (2020). Characteristics of and Important Lessons From the Coronavirus Disease 2019 (COVID-19) Outbreak in China: Summary of a Report of 72314 Cases From the Chinese Center for Disease Control and Prevention. JAMA. Published online February 24, 2020. https://doi.org/10.1001/jama.2020.2648.

Wu, H., Malone, A.F., Donnelly, E.L., Kirita, Y., Uchimura, K., Ramakrishnan, S.M., Gaut, J.P., and Humphreys, B.D. (2018a). Single-Cell Transcriptomics of a Human Kidney Allograft Biopsy Specimen Defines a Diverse Inflammatory Response. J. Am. Soc. Nephrol. *29*, 2069–2080.

Wu, H., Uchimura, K., Donnelly, E.L., Kirita, Y., Morris, S.A., and Humphreys, B.D. (2018b). Comparative Analysis and Refinement of Human PSC-Derived Kidney Organoid Differentiation with Single-Cell Transcriptomics. Cell Stem Cell *23*, 869–881.

Yang, X.H., Deng, W., Tong, Z., Liu, Y.X., Zhang, L.F., Zhu, H., Gao, H., Huang, L., Liu, Y.L., Ma, C.M., et al. (2007). Mice transgenic for human angiotensin-converting enzyme 2 provide a model for SARS coronavirus infection. Comp. Med. *57*, 450–459.

Yang, X., Yu, Y., Xu, J., Shu, H., Xia, J., Liu, H., Wu, Y., Zhang, L., Yu, Z., Fang, M., et al. (2020). Clinical course and outcomes of critically ill patients with SARS-CoV-2 pneumonia in Wuhan, China: a single-centered, retrospective, observational study. Lancet Respir. Med. Published online February 24, 2020. https://doi.org/10.1016/S2213-2600(20)30079-5.

Yeung, M.L., Yao, Y., Jia, L., Chan, J.F., Chan, K.H., Cheung, K.F., Chen, H., Poon, V.K., Tsang, A.K., To, K.K., et al. (2016). MERS coronavirus induces apoptosis in kidney and lung by upregulating Smad7 and FGF2. Nat. Microbiol. *1*, 16004.

Young, B.E., Ong, S.W.X., Kalimuddin, S., Low, J.G., Tan, S.Y., Loh, J., Ng, O.-T., Marimuthu, K., Ang, L.W., Mak, T.M., et al.; Singapore 2019 Novel Coronavirus Outbreak Research Team (2020). Epidemiologic Features and Clinical Course of Patients Infected With SARS-CoV-2 in Singapore. JAMA. Published online March 3, 2020. https://doi.org/10.1001/jama.2020.3204.

Zhang, F., Yang, D., Li, J., Gao, P., Chen, T., Cheng, Z., Cheng, K., Fang, Q., Pan, W., Yi, C., et al. (2020a). Myocardial injury is associated with in-hospital mortality of confirmed or suspected COVID-19 in Wuhan, China: A single center retrospective cohort study. medRxiv. https://doi.org/10.1101/2020.03.21.20040121.

Zhang, H., Penninger, J.M., Li, Y., Zhong, N., and Slutsky, A.S. (2020b). Angiotensin-converting enzyme 2 (ACE2) as a SARS-CoV-2 receptor: molecular mechanisms and potential therapeutic target. Intensive Care Med. *46*, 586–590.

Zhao, Y., Zhao, Z., Wang, Y., Zhou, Y., Ma, Y., and Zuo, W. (2020). Single-cell RNA expression profiling of ACE2, the putative receptor of Wuhan 2019-nCov. bioRxiv. https://doi.org/10.1101/2020.01.26.91998.

Zhou, F., Yu, T., Du, R., Fan, G., Liu, Y., Liu, Z., Xiang, J., Wang, Y., Song, B., Gu, X., et al. (2020a). Clinical course and risk factors for mortality of adult inpatients with COVID-19 in Wuhan, China: a retrospective cohort study. Lancet *395*, 1054–1062.

Zhou, P., Yang, X.L., Wang, X.G., Hu, B., Zhang, L., Zhang, W., Si, H.R., Zhu, Y., Li, B., Huang, C.L., et al. (2020b). A pneumonia outbreak associated with a new coronavirus of probable bat origin. Nature *579*, 270–273.

Zhu, N., Zhang, D., Wang, W., Li, X., Yang, B., Song, J., Zhao, X., Huang, B., Shi, W., Lu, R., et al.; China Novel Coronavirus Investigating and Research Team (2020). A Novel Coronavirus from Patients with Pneumonia in China, 2019. N. Engl. J. Med. *382*, 727–733.

STAR★METHODS

KEY RESOURCES TABLE

REAGENT or RESOURCE	SOURCE	IDENTIFIER
Antibodies		
Fluorescein labeled Lotus Tetragonolobus (LTL)	Vector Labs	Cat#FL-1321; RRID:AB_2336559
Anti-SLC3A1 polyclonal antibody	Merck	Cat#HPA038360-100U; RRID:AB_2675975
Anti-SGLT2	Abcam	Cat#ab37296; RRID:AB_777895
Anti-LAMININ	Merck	Cat#L9393; RRID:AB_477163
Human Nephrin Affinity Purified Polyclonal Ab antibody	R&D Systems	Cat#AF4269; RRID:AB_2154851
Recombinant Anti-Sodium Potassium ATPase antibody	Abcam	Cat#ab209299; RRID:AB_1968790
Bacterial and Virus Strains		
SARS-CoV-2, GENBANK: MT093571	Isolated from patient	N/A
Chemicals, Peptides, and Recombinant Proteins		
CHIR99021	Merck	Cat#SML1046; CAS: 252917-06-9
Recombinant human FGF9	PeproTech	Cat#100-23
Heparin	Merck	Cat#H3149; CAS: 9041-08-1
Activin A	Vitro	Cat#338-AC-050
Paraformaldehyde solution 4% in PBS	Santa Cruz	Cat#sc-281692
1% Triton X-100	Merck	Cat#T8787
Glutaraldehyde	Sigma-Aldrich	Cat#G7776
srhACE2	Apeiron	N/A
Trizol	ThermoFisher	Cat#15596018
Recombinant Human VEGF165	Peprotech	Cat#100-20
Human FGF-2	Miltenyi Biotech	Cat#130-093-841
Critical Commercial Assays		
streptavidin/biotin blocking kit	Vector Labs	Cat#SP-2002
CellTiter-Glo® Luminescent cell viability assay	Promega	Cat#G7570
Direct-zol RNA MiniPrep kit	Zymo Reasearch	Cat#R2051
Chromium Single Cell 3′ Library & Gel Bead Kit V**3**	10X Genomics (USA)	Cat#PN-1000075
NSQ 500/550 Hi Output KT v2.5 (75 CYS)	Illumina (San Diego, CA 92122 USA)	Cat#20024906
Sytox® blue dead cell stain	Thermofisher (Eugene, Oregon,USA)	Cat#S34857
Deposited Data		
Kidney Organoid scRNA-seq	This paper	GEO: GSE 147863
Experimental Models: Cell Lines		
ES[4] Human Embryonic Stem Cell line	The National Bank of Stem Cells (ISCIII, Madrid)	https://www.isciii.es/QueHacemos/Servicios/BIOBANCOS/BNLC/Lists/Lneas%20embrionarias/Attachments/6/Caracteristicas%20-%20Documento_Deposito_Lineas_v32_ES4_def.pdf
Vero E6 cells	ATCC	CRL-1586
Oligonucleotides		
Primer: RPLP0 Forward: CCATTCTATCATCAACGGGTACAA Reverse: AGCAAGTGGGAAGGTGTAATCC	N/A	N/A
Primer: SLC3A1 Forward: CACCAATGCAGTGGGACAAT Reverse: CTGGGCTGAGTCTTTTGGAC	N/A	N/A

Continued

REAGENT or RESOURCE	SOURCE	IDENTIFIER
Primer: SLC27A2	N/A	N/A
Forward: TACTCTTGCCTTGCGGACTAA		
Reverse: CCGAAGCAGTTCACCGATATAC		
Primer: SLC5A12	N/A	N/A
Forward: ACACGGTACAGACCTTCGTCA		
Reverse: GCTGCTCCCAGGTATTTGTC		
Primer: SARS-CoV-2 E gene	N/A	N/A
Forward: ACAGGTACGTTAATAGTTAATAGCGT		
Reverse: ATATTGCAGCAGTACGCACACA		
Primer: Human RNase P	N/A	N/A
Forward: AGATTTGGACCTGCGAGCG		
Reverse: GAGCGGCTGTCTCCACAAGT		
Recombinant DNA		
Human RNase P probe: FAM-TTCTGACCTGAAGGCTCT GCGCG-MGB	N/A	N/A
SARS-CoV-2 E gene probe: FAM-ACACTAGCCATCCTT ACTGCGCTTCG-QSY	N/A	N/A
Software and Algorithms		
GraphPad Prism 8 (GraphPad)	Motulsky and Brown, 2006	https://www.graphpad.com
ImageJ	Schneider et al., 2012	https://imagej.net/ImageJ
FACSDiva software version 8.0.1 (BD Biosciences)	Becton, Dickinson and Company	https://www.bdbiosciences.com/en-us/ instruments/research-instruments/research- software/flow-cytometry-acquisition/facsdiva- software
FlowJo software version 10	Becton, Dickinson and Company	https://www.flowjo.com/
Cell Ranger v3.0.1	10X Genomics	https://support.10xgenomics.com/single-cell- gene-expression/software/overview/welcome
R v3.5.1	R Core	https://cran.r-project.org/
Seurat v3.0.2	Stuart et al., 2019	https://satijalab.org/seurat/
Kidney Interactive Transcriptomics (KIT)	Wu et al., 2018a	http://humphreyslab.com/SingleCell/

RESOURCE AVAILABILITY

Lead Contact
Further information and requests for resources and reagents should be directed to and will be fulfilled by the Lead Contact, Joseph Penninger (josef.penninger@ubc.ca).

Materials Availability
All unique organoids generated in this study are available from the Lead Contact with a completed Materials Transfer Agreement.

Data and Code Availability
Raw sequencing data for the single cell kidney organoid reported in this paper were deposited in Gene Gene Expression Omnibus. (GEO) under the accession number GEO: GSE147863, GSM4447249.

Scripts reproducing the single cell kidney analysis are deposited in: https://github.com/jpromeror/SC_KidneyOrganoid_ACE2

EXPERIMENTAL MODEL AND SUBJECT DETAILS

Virus
SARS-CoV-2 was isolated on Vero-E6 cells, from a nasopharyngeal sample of a patient in Sweden. Virus was titered using a plaque assay as previously described (Becker et al., 2008) with fixation of cells 72 hours post infection. The SARS-CoV-2 isolate was

sequenced by Next-Generation Sequencing (GenBank accession number MT093571). For electron microscopy, viral stocks were inactivated using 35% Glutaraldehyde.

Cells and human capillary organoids

Vero-E6 cells (ATCC) were grown in Dulbecco's Modified Eagle's Medium (DMEM, Thermofisher) supplemented with 1% Non-Essential Amino-Acid (Thermofisher), 10mM HEPES (Thermofisher) and 10% FBS at 37°C, 5% CO2. Blood vessels organoids were engineered from human iPS cells and immunostained as previously described (Wimmer et al., 2019).

METHOD DETAILS

Preparation of soluble recombinant human and murine ACE2

Clinical-grade soluble recombinant human ACE2 (amino acids 1-740) was produced by Polymun Scientific (contract manufacturer) from CHO cells according to Good Manufacturing Practice guidelines and formulated as a physiologic aqueous solution. The equivalent domain of murine ACE2 was similarly overexpressed in CHO cells under serum free conditions and purified by sequentially performing a capture step on DEAE-Sepharose, ammonium sulfate precipitation, purification via a HIC-Phenyl Sepharose column, followed by purification via a Superdex 200 gel filtration column. The purity of the murine protein was determined via HPLC, concentrations were determined with 280nm photometric measurements.

Kidney organoid differentiation

Human embryonic stem cells were grown on vitronectin coated plates (1001-015, Life Technologies) and incubated with 0.5mM EDTA (Merck) at 37°C for 3 minutes for disaggregation. 100,000 cells/well were plated on a 24 multi-well plate coated with 5 μl/ml vitronectin and further incubated with supplemented Essential 8 Basal medium at 37°C overnight. The day after (day 0), cells were treated for 3 subsequent days in Advanced RPMI 1640 basal medium (ThermoFisher) supplemented with 8 μM CHIR (Merck) and 1% Penicillin-Streptomycin and 1% of GlutaMAX TM (ThermoFisher). The medium was changed every day. From day 3 to 4, media were changed to Advanced RPMI supplemented with 200ng/ml FGF9 (Peprotech), 1 μg/ml heparin (Merck) and 10ng/ml activin A (Vitro). On day 4, cultures were rinsed twice with PBS, and resuspended in Advanced RPMI supplemented with 5 μM CHIR, 200ng/ml FGF9 and 1 μg/ml Heparin. Cellular suspensions were seeded in V-shape 96 multi-well plate at a final concentration of 100,000 cells/well and centrifuged at 2000 rpm for 3 minutes. The resulting spheroids were incubated during 1h at 37°C. Culture media was replaced by Advanced RPMI supplemented with 200ng/ml FGF9 and 1 μg/ml Heparin for 7 additional days, the media was changed every second day. From day 11 to 16, developing organoids were incubated only in the presence of Advanced RPMI, the media was every second day.

Phylogenetic analysis

To generate a phylogenetic tree, we created a genomic epidemiology map of different SARS-CoV-2 isolates using NextStrain tools (https://nextstrain.org/) (Hadfield et al., 2018). The sequences of the different isolates were obtained from GISAID (https://www.gisaid.org/) (Elbe and Buckland-Merret, 2017). Screenshots is used under a CC-BY-4.0 license.

Treatments of Vero E6 cells with human rsACE2 and murine rsACE2

Vero E6 cells were seeded in 48-well plates (5.10^4 cells per well) (Sarstedt) in DMEM containing 10% FBS. 24 hours post-seeding, hrsACE2 or mrsACE2 were mixed with different concentration of virus (1:1) in a final volume of 100μl per well in DMEM (0% FBS) at 37°C. After 30 minutes, Vero-E6 were infected either with mixes containing hrsACE2/SARS-CoV-2 and mrsACE2/SARS-CoV-2 for 1 hour followed by washing or for 15 hours without washing, cells were washed 3 times with PBS and 500μl of new complete medium supplemented with hrsACE2 or mrsACE2 were added. 15 hours post-infection, supernatants were removed, cells were washed 3 times with PBS and then lysed using Trizol (Thermofisher) before analysis by qRT-PCR for viral RNA detection.

SARS-CoV-2 infections of kidney and blood vessel organoids

Kidney organoids were infected with 10^3 or 10^5 SARS-CoV-2 infectious particles in advanced RPMI medium (Thermofisher). Blood vessels organoids were infected with 10^2, 10^4, or 10^6 SARS-CoV-2 infectious particles in StemPro complete media containing 15% FBS (GIBCO cat.10500064), 100ng/ml of VEGF-A (Peprotech cat. no. 100-20) and 100ng/ml of FGF-2 (Milteny Biotech cat. no. 130-093-841) as previously described (Wimmer et al., 2019) in a volume of 50μl per well of a 96-well ultra-low attachment plate for 1 hour. One hour post-infection, organoids were washed 3 times with PBS and kept in 100μl of corresponding medium for 3 to 6 days. On day 3 post-infection, organoids were washed 3 times with PBS before being lysed with Trizol (Thermofisher). At day 6 post-infection, supernatants were recovered and organoids washed 3 times with PBS before to lysis with Trizol (Thermofisher). Samples were then analyzed for the presence of viral RNA by qRT-PCR. 100μl of each supernatant were used to infect Vero E6 in 48-well plate plates. Cells were recovered 48 hours post-infection, pooled (5 blood vessels organoids/ condition, 3 kidney organoids/condition), and the level of infection was determined by viral RNA detection using qRT-PCR.

Treatment of organoids with hrsACE2

Different concentrations of hrsACE2 were mixed with 10^6 particles of SARS-CoV-2 for 30min at 37°C in a final volume of 50μl per well in STemPro 34 complete medium (blood vessels) or advanced RPMI medium (Kidneys) as described above. Organoids were then infected with the mixes for 1 hour at 37°C, washed 3 times with PBS and 100μl per well of new medium was added. To detect intracellular viral RNA, organoids were washed 3 times with PBS, pooled (5 organoids/condition for blood vessels; 3 organoids/condition for kidneys) and lysed using Trizol (Thermofisher) before analysis by qRT-PCR for viral RNA detection.

Cytotoxicity assay

To determine whether human or mouse rsACE2 are toxic to cells, 10^4 Vero E6 cells per well were seeded in a 96-well plate. 24h post-seeding, 25μl of different concentrations (25 – 200 μg/ml of rsACE2 were added in triplicate and incubated for 15h. 15h post-treatment, cytotoxicity was determined using the CellTiter-Glo® Luminescent cell viability assay (Promega) following the following the manufacturer's protocol using 50μl of CellTiter-Glo® Reagent per well.

qRT-PCR

Samples were extracted using Direct-zol RNA MiniPrep kit (Zymo Research). qRT-PCR was performed using E-gene SARS-CoV-2 primers/probe following guidelines by the World Health Organization (https://www.who.int/docs/default-source/coronaviruse/wuhan-virus-assay-v1991527e5122341d99287a1b17c111902.pdf)

Forward primer: 5'-ACAGGTACGTTAATAGTTAATAGCGT-3'
Reverse primer: 5'-ATATTGCAGCAGTACGCACACA-3'
Probe: FAM-ACACTAGCCATCCTTACTGCGCTTCG-QSY
RNase P was used as an endogenous gene control to normalize the levels of intracellular viral RNA.
Forward primer: AGATTTGGACCTGCGAGCG
Reverse primer GAGCGGCTGTCTCCACAAGT
probe: FAM-TTCTGACCTGAAGGCTCTGCGCG-MGB

Primers used for tubular markers in kidney organoids are listed in the Key Resources Table.

Single cell sequencing of kidney organoids

Kidney organoids were homogenized using 21G and 26 1/2G syringes and further dissociated using Accumax (07921, Stem Cell Technologies9 for 15 min at 37°C followed by Trypsin-EDTA 0,25% (wt/vol) trypsin (25300-054, Life Technologies) for additional 15 min at 37°C. The reaction was deactivated by adding 10% FBS. The solution was then passed through a 40 μm cell strainer and frozen in Advanced RPMI 1640 basal medium (ThermoFisher) in the presence of DMSO 10%. Cells were thawed and centrifuged at 1,500 RPM for 5 minutes, stained with sytox blue (Thermofisher) and sorted by FACS to remove the nonviable cells, generating a single cell suspension with greater than 90% viability analyzed using the cellometer K2 (Nexcelom Biocience). Libraries were prepared using the Chromium Single Cell 3' GEM, v3, (PN-1000075, 10X genomics) following the manufacturer's instructions and sequenced with a NEXTseq500 (R1:28, R2: 55, i7:8) up to 30.000 reads per cell.

Histological analysis

Kidneys organoid and LTL+ cells were washed with PBS. Next samples were fixed with 4% paraformaldehyde (153799, Aname) for 20 min at room temperature. Specimens were washed twice with PBS and further blocked using Tris-buffered saline (TBS) with 6% donkey serum (S30, Millipore) and 1% Triton X-100 (T8787, Sigma) for 1h at room temperature. After three rinses with antibody dilution buffer, samples were treated for 4h at room temperature with fluorescent conjugated secondary antibodies (Alexa Fluor (A) Cy3- or A647-; 1:200). A previous blocking step with a streptavidin/biotin blocking kit (SP-2002, Vector Labs) was performed for biotinylated LTL (B-1325, Vector Labs) and Alexa Fluor 488-conjugated streptavidin (SA5488, VectorLabs) to detect LTL+ cells. Antibodies to NEPHRIN (R&D SYSTEMS 4269; 1:100) and LAMININ (Sigma L9393; 1:50), SGLT2 (Abcam AB37296; 1:100), NaKAT-Pase (Abcam; AB209299; 1:200) and SLC3A1 (Sigma HPA038360; 1:50) were used overnight at 4°C diluted in antibody dilution buffer consisting of TBS with 6% donkey serum and 0.5% Triton X-100. Nuclei were detected using 4,6-diamidino-2-phenylindole (DAPI; 1:5000, D1306, Life Technologies) for 30min. For mounting, samples were immersed in Fluoromount-G (0100-01, Southern Biotech). Sample confocal images were acquired with an SP5 Leica microscope and LTL + were analyzed using ImageJ.

Flow cytometry

For the isolation of LTL+ cells kidney organoids were stained with fluorescein-conjugated LTL (FL-1321, Vector Laboratories). Then specimens were dissociated to single cells using Accumax (07921, Stem Cell Technologies) for 15min followed by 0.25% (wt/vol) trypsin (25300–054, Life Technologies) for 15min at 37 °C. For LTL+ cells isolation FACSDiva software version 8.0.1 (BD Biosciences) was used in the FACS Aria Fusion instrument (BD Biosciences).

QUANTIFICATION AND STATISTICAL ANALYSIS

Kidney Organoid scRNA-seq Data Analysis

Libraries were pre-processed using Cell Ranger (3.0.1) from 10X Genomics. The computational analysis was performed using Seurat (3.0.2) (Stuart et al., 2019). Initial quality control parameters were defined based on the distributions of the number of detected genes per cell, the number of UMIs per cell and the % of UMIs assigned to mitochondrial genes. The selected thresholds were: 668 < UMIs per cell < 23101, 489 < Genes per cell < 5651 and % UMIs assigned to mitochondrial genes < 50. The dataset was subjected to normalization, identification of highly variable features and scaling using the SCTransform function of the Seurat package. Principal component analysis was performed, and 20 components were kept for further analysis. Clustering was performed by setting the resolution parameter to 0.4. Dimensional reduction was done using the RunUMAP function of the Seurat R package. Cell markers were identified by using a Wilcoxon test. Genes with adjusted p.value < 0.5 were retained. Clusters were labeled by comparing the expression of the identified markers with publicly available databases (Wu et al., 2018b) located in KIT (Kidney Interactive Transcriptomics webpage (http://humphreyslab.com/SingleCell/).

Statistics

Statistical analyses were conducted using GraphPad Prism 8 (GraphPad) and significance was determined by Student's t test.
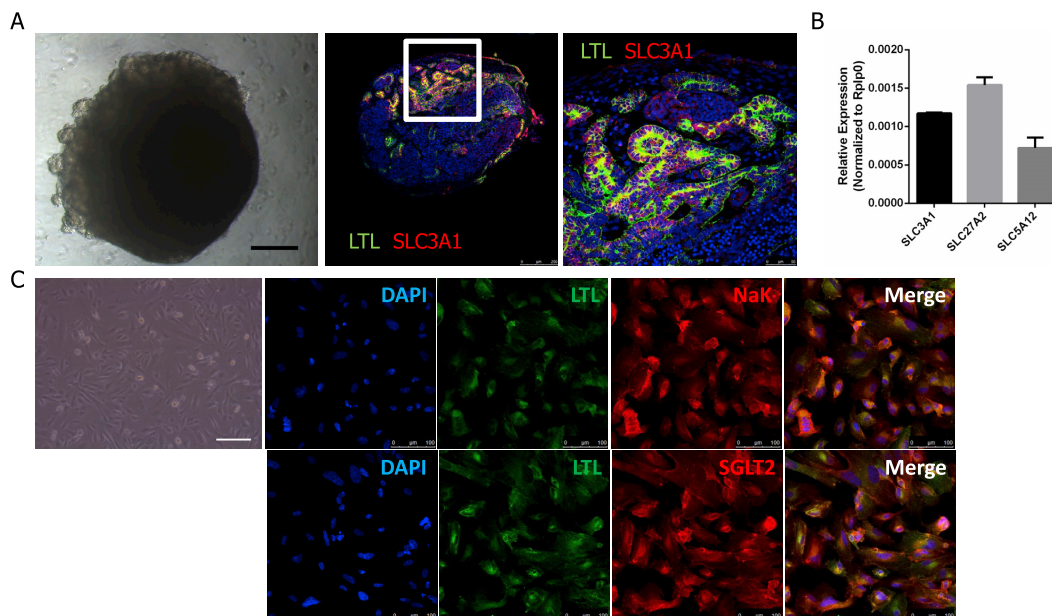
Supplemental Figures

Figure S1. Human Kidney Organoids as a Surrogate of Human Proximal Tubule Cell Culture Model, Related to Figure 4

(A) Left image corresponds to a kidney organoid at day 20 of differentiation visualized using light microscopy. Scale bar 100 μm. Confocal microscopy images of tubular-like structures labeled with Lotus Tetraglobus Lectin (LTL, in green) and the proximal tubular cell marker SCL3A1 (in red). DAPI labels nuclei. A magnified view of the boxed region shows a detail of the tubular structures. Scale bars 250 and 50 μm, respectively. (B) Expression changes of SLC3A1, SLC5A12 and SLC27A2 of bulk samples at day 20 of organoid differentiation. (C) Left image corresponds to LTL+ cells visualized using light microscopy. Scale bar 100 μm. Confocal microscopy images of LTL+ cells labeled with Lotus Tetraglobus Lectin (LTL, in green) and the proximal tubular cell markers NaK ATPase (NaK, in red) and the solute carrier SGLT2 (in red). DAPI was used to visualize nuclei. Scale bars 100 μm.
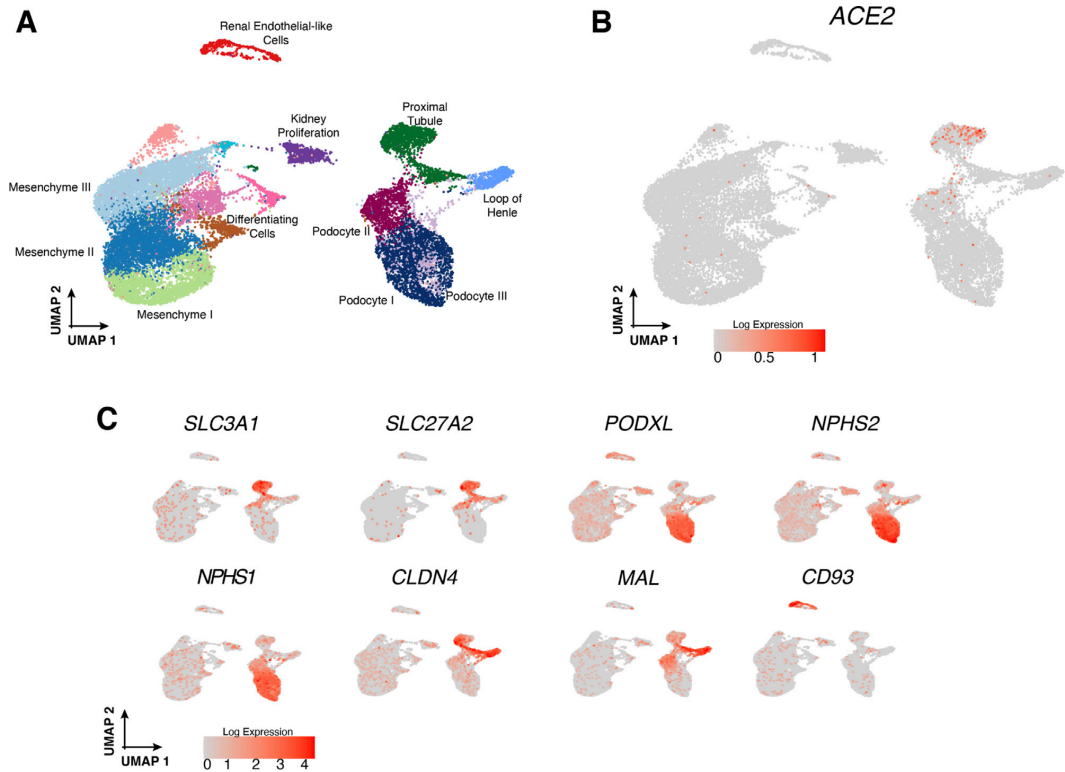
Figure S2. Single-Cell RNA-Seq Analysis of Kidney Organoids Reveals ACE2 Expression in Proximal Tubule Cells, Related to Figure 4
(A) UMAP plot displaying the results after unbiased clustering. Subpopulations of renal endothelial-like, mesenchymal, proliferating, podocyte and tubule cells were identified. (B) Expression of ACE2 projected in the UMAP reduction. (C) Expression of different cellular markers: SLC3A1, SLC27A2 (Proximal Tubule); PODXL, NPHS1, NPHS2 (Podocyte); CLDN4, MAL (Loop of Henle) and CD93 (Renal Endothelial-like cells).

IV.   DISCUSSION

IV. DISCUSSION

During these last years, several groups, including our laboratory, have shown the ability of hPSCs to differentiate into kidney organoids providing a new model system to study early steps of human kidney development and disease.

The development of different protocols for the derivation of hPSCs-kidney organoids (kidney organoids) has been possible based in our increased understanding of cell processes and signals driving kidney development, based on studies performed in the last century using different model organisms, including amphibians, avians, and mice. Those seminal works started to reveal the major morphogens and genes specifying the renal lineage in providing important hints on the major steps leading to kidney formation. In parallel, the field of stem cell biology started to define culture conditions promoting pluripotent stem cells culture and differentiation in mice and human cell sources with the seminal discovery of Professor Shinya Yamanaka (Takahashi et al. 2007) showing on the possibility to reprogram somatic cells into pluripotent stem cells-like cells, the so called iPSCs. Thus, as early as during 20123 many laboratories already showed on the possibility to generate iPSCs from patients affected by renal diseases (Thatava et al. 2011), but the lack of procedures sufficing for their differentiation into renal-like cells represented a major drawback to advance the field of renal disease modeling using iPSCs. In this regard, several groups reported on the possibility to generate renal-like cells from hPSCS, including hESCs and hiPSCs (Freedman et al. 2013; Mae et al. 2013; Narayanan et al. 2013; Song et al. 2012; Xia et al. 2013). Furthermore, a

seminal work from members of our laboratory did also shown on the ability of those renal derivates to further engraft and form chimeric kidney organoids composed of hPSCs derived UB and mice embryonic kidney cells (Xia et al. 2013). From that moment, many laboratories started to work in the definition of procedures for the generation of kidney organoids from hPSCs in the absence of cells from other animal species. It was then shown, that by exposing undifferentiated monolayers of hPSCs into specific morphogens mirroring those signaling molecules which promote early steps of renal commitment in mammals (that is Wnt signalling pathway and RA signaling), it was possible to nephron progenitor-like cells (NPCs) with different extent of differentiation potential which were further assembled as spheroids to promote 3D differentiation. Collectively, all those works started to show that even requiring different time scales, in general day 7 to 10 hPSCs-NPCs further exposed to 3D culture conditions (i.e., including transwell system or free floating conditions), could led to the generation of kidney organoids in 25 to 30 days. Collectively, all those works showed that kidney organoids exhibited the presence of nephron-like structures expressing markers of the glomerular and the tubular compartment (Morizane et al. 2015; Takasato et al. 2015). Indeed, the group of Melissa Little did show on the detection of Gata3+ cells in day 27 kidney organoids further claiming on the possibility to generate UB-like structures interconnected with nascent nephrons (Takasato et al. 2015).

In the context of the present thesis, we wanted to further investigate on the possibility to generate kidney organoids through the emulation of biophysical cues similar to those found in the native tissue. Following this logic, our main approach was to force cell-to-cell and cell-to-ECM interaction during the time course of kidney organoids generation in

order to better recapitulate the biophysical conditions that renal cells encounter *in vivo*. Towards this aim we first design a new approach to generate posterior IM (PIM)-like cells from hPSCs to define a robust progenitor state from where to derive kidney organoids. For this, we did generate posterior primitive streak (PS)-like cells using a high dose CHIR during three consecutive days to further promote Wnt-signaling mediated expression of posterior PS markers. After confirming the posterior PS identity of the generated cells, we further used Fgf9 and Activin A for one additional day in order to commit posterior-PS cells into cells PIM fate to be further assembled and cultured in 3D conditions and thus maximize the time exposure of renal-committed cells in culture conditions mirroring the *in vivo* situation. In this manner, and in contrast to other works which promoted a first phase of hPSCs-NPCs generation in 2D monolayer for 7 to 10 days, we assembled our day 4 PIM-like cells as 3D spheroids and culture them in presence of renal inductive signals during 4 more additional days generating kidney organoids upon 4 more days in culture. In total, our approach only required 16 days in 3D culture conditions in front of previous findings needing 25 to 30 days. We did take advantage of bulk RNA seq for transcriptomically profile the extent of kidney organoid differentiation under our culture conditions in comparison with human embryonic tissues (Lindström, McMahon, et al. 2018; Roost et al. 2015) and transcriptomic data from kidney organoids generated by Melissa Little's group (Garreta et al. 2019). Our results indicated that our approach sufficed for the generation of kidney organoids transcriptomically resembling the second trimester gestational kidney, an improvement over previous findings, in which kidney organoids resembled the first trimester gestational kidney requiring 25 to 30 days for their generation (Takasato et al. 2015). Overall, our

methodology reduced the time needed to generate kidney organoids by about 30%, and more importantly, demonstrated on the utility of forcing cell-to-cell and cell-to-ECM contact as a new approach to enhance organoid differentiation extent (Garreta et al. 2019).

But besides these advances, the kidney organoid field still faces important challenges with regards to the generation of 3D culture systems similar to the human embryonic kidney in terms of cellular composition and function. In this regard, the advancement in scRNA seq and transcriptomics technologies as single cell ATAC seq have increased the characterization of the cell types, gene expression and lineage relationships in both embryonic and adult human tissues (Combes, Phipson, et al. 2019; Park et al. 2018; Subramanian et al. 2019; Wu et al. 2018). Moreover, the application of scRNA seq in kidney organoids has started to shed light on differences between human and mouse kidneys (Combes, Phipson, et al. 2019; Lindström, Tran, et al. 2018; Little and Combes 2019). These analyses have been crucial to assess the maturation and transcriptomics status of the cells within kidney organoids of different laboratories (Wu et al. 2018) and even comparing intra-kidney organoid variability (Phipson et al. 2019). All in all, these works have established quantitative comparisons between protocols, batches, and pluripotent cell lines providing important information on how to improve protocol's reproducibility and quality (Phipson et al. 2019; Subramanian et al. 2019; Wu et al. 2018)

The consensus to date is being that the utility of human kidney organoids would be determined by how well they can model the complexity of *in vivo* renal tissues. In this regard, several works have revealed on the reconstruction of lineage trajectories to enhance maturation of specific

kidney cells types or inhibit differentiation of undesired off-target population (Combes, Zappia, et al. 2019; Wu et al. 2018). For example, Wu and colleagues demonstrated that the specific inhibition of the signaling between brain-derived neurotrophic factor and its receptor, neurotrophic kinase receptor, type 2, reduced the differentiation of neural cells in the kidney organoids by 90%, and resulting in a more efficient renal induction (Wu et al. 2018). In the next years it is expected that the convergence of scRNA seq and kidney organoid technology will provide crucial information on how to externally guide kidney differentiation in a predictable manner and further exploit these cell culture platforms to model renal disease and perform drug screening.

Kidney organoids own the potential to recreate the patterning and segmentation events leading to nephron formation, presenting an appropriate morphology and segment-specific protein expression. However, despite the important advances archived in the last years, current protocols provide immature kidney organoids that are still models of the developing human kidney with several challenges to face. One of the biggest limitations that need to be addressed to enhance maturation and functionality of the organoids, is the lack of functional vasculature. Kidneys are highly vascularized organs receiving around the 25% of the cardiac output and during kidney development the interaction between endothelia cells, podocytes and mesangial cells is key for the development, maturation, and maintenance of functional glomeruli (Dressler 2006). Several works have reported the presence of endothelial cells within the generated organoids (van den Berg et al. 2018; Freedman et al. 2015; Garreta et al. 2019; Takasato et al. 2015), but none of them have shown their organization into proper blood vessels and their invasion into the glomerulus. In this regard, there have been reported two

strategies aiming to enhance kidney vascularization. In one hand, either hPSCs-NPCs (Sharmin et al. 2016) or kidney organoids have been transplanted into the renal subcapsule of SCID mice to further provide a vascular component into the different hPSCs-renal derivatives (Bantounas et al. 2018; van den Berg et al. 2018; Sharmin et al. 2016) Collectively, those different works have shown on the utility of this strategy promoting host vascularization into developing renal derivatives *in vivo* after 1 week (Sharmin et al. 2016) or 4 weeks (van den Berg et al. 2018). On the other hand, we took advantage of the chick CAM to further promote kidney organoid growth as well as the organization of endogenous kidney endothelial cells making use of this animal model system as an *in ovo* bioreactor. Our work did show, for the first time, that the fluid flow of the chick CAM blood vessels sufficed for the organization of kidney organoid Cd34+ cells in a similar fashion as observed in the developing human glomeruli. Furthermore, our approach sufficed for the growth of the glomerular structures compared to non-implanted specimens (Garreta et al. 2019). Following a similar logic, Homan and colleagues have relayed on the use of microfluidics to further address on the relevance of the vascular flow during the vascularization of kidney organoids (Homan et al. 2019). In this manner, the authors showed a significant expansion of the organoid-derived endothelial network and its invasion within some of the glomerular-like structures together with an improved maturation of nephron epithelial, including podocytes and tubules, when compared with kidney organoids cultured under conventional static conditions (Homan et al. 2019). In general, the microfluidic technology has represented a powerful approach for creating complex biomolecule gradients for the generation of hPSCs derivatives. Importantly, in a recent study a microfluidic device was used

to generate orthogonal gradients of retinoic acid and smoothened agonist [a small molecule activator of the sonic hedgehog (SHH) pathway], either simultaneously or sequentially, to further allow for the derivation of motor neurons from mouse ESC-derived EBs by emulating *in vivo* neural tube patterning (Uzel et al. 2016). More recently, another work has shown on the fabrication of a microfluidic device to expose hPSC colonies to spatiotemporally controlled morphogen gradients generated from artificial signaling centers to promote the generation of different axially arranged differentiation domains in 2D hPSC (Manfrin et al. 2019). We expect that these approaches could be further applied to control size and geometry of 3D cultures and their exposure to controlled morphogen gradients, which represents an additional layer of complexity yet to be overcome in the organoid field.

Other technical drawbacks to overcome, are the lack of a urinary exit route within the human kidney organoids as well the lack of ongoing nephrogenesis. These two characteristics represent crucial aspects for the use of kidney organoids in future therapeutic applications, including transplantation. Of note, the work from the laboratory of Ryuichi Nishinakamura has demonstrated on the possibility to separately generate different renal stem cell progenitors from mouse and human PSCs in order to build kidney organoids through the manual assembly of transient MM- and UB-like cells together with kidney stromal cells from embryonic mice (Taguchi and Nishinakamura 2017). In this regard, it is expected that within the next years microfluidic platforms will allow for the proper delivery of renal-like physiological stimuli (i.e., shear stress, fluid flow, among others) for the proper assembly of hPSCs renal derivatives during the time course of kidney organoid generation (i.e., mesangial cells, renal fibroblasts, among others). Alternatively, the

modulation of biochemical signaling in space and time could be achieved using dynamic hydrogel systems which change their chemical and mechanical properties over time due to light-triggered reactions. Soluble biomolecules could be locally tethered in a target area within the hydrogel network in a reversible manner, permitting the fabrication of very precise 3D patterns and gradients of biochemical cues that are dynamically controlled upon light exposure (DeForest and Anseth 2012). These types of hydrogels could be useful to locally guide organoid self-organization (i.e., by locally softening or stiffening of the matrix (Guvendiren and Burdick 2012), and even to create stiffness gradients (Vincent et al. 2013). However, further research is needed to fulfill the potential of this approaches in the organoid field. Interestingly, our recently published work has also shown that the emulation of embryonic renal stiffness trough the fabrication of polyacrylamide hydrogels exhibiting soft mechanical properties (similar to embryonic kidney environment) represents a new approach to generate kidney organoids with increased differentiation features than those generated using hydrogels with stiffer values. Importantly, work from other laboratories has started to show on the possibility to control not only stiffness, but also viscoelasticity properties of the biomaterials (Bauer et al. 2017; Chaudhuri et al. 2016) to better emulate the physical characteristics of tissues. Thus, further work in these issues will positively impact on the definition of novel materials with close characteristics to those found in the native kidney, providing new tools to better program and promote hPSCs-kidney differentiation.

In general, accumulated data shows that kidney organoids yet do not fully mirror important treats of the native embryonic or perinatal tissue (i.e., filtration). Besides these caveats we have further hypothesized that

promoting metabolic activities during the generation of kidney organoids may represent a new approach to further force cell differentiation. It is well known that the human kidney is a highly metabolic organ and that renal epithelial tubular cells (PTCs), which account for the 90% of the renal mass, do possess the highest density of mitochondria after cardiomyocyte cells in our body. PTCs due to their high energy requirements uses fatty acid oxidation (FAO) and oxidative phosphorylation (OXPHOS) to obtain energy. To further ascertain on the impact of FAO in the generation of kidney organoids we have explored different media formulations promoting either a glycolytic or an OXPHOS-promoting profile during the time course of organoid generation. Our data shows that the exposure of renal vesicle stage (RV) organoids into an OXPHOS promoting media enhances the generation of PTC-like cells within kidney organoids, and that such changes work in concert with increases in oxygen consumption rate, as well as with increases in the expression of PTC differentiation markers (Dhillon et al. 2020; Garreta et al. 2019). To date there is no knowledge of mechanisms regulating stem cell niche metabolism during quiescence, proliferation and differentiation. Thus, advancing in these fundamental questions is a current limitation to the progression of basic cell biology, tissue engineering and regenerative medicine. Specifically, in the field of kidney organoid generation understanding such energy production mechanisms could establish a tangible link between stem cell proliferative capacity in relation to differentiation as a new mean to instruct lineage commitment. To further explore these questions, we profiled day 16 kidney organoids using scRNA seq with the aim to explore the direct crosstalk between metabolism and kidney organoids differentiation. Using differentiation trajectory analysis in PTC-like cells

195

our data indicated that increases in tubular differentiation markers (i.e., solute carriers, among others) strongly correlated with increases in the expression of genes of the FAO pathway (i.e., Pgc1α, Pparγ, Cpt1a, Cpt1b, among others). Then, we further proceed to challenge RV kidney organoids in front of OXPHOS or glycolytic promoting media to further interrogate on the impact of these cell culture regimes in the expression of FAO components. Our results showed that the OXPHOS promoting regime resulted in the induction of Pgc1α mRNA expression. Interestingly we also explored for changes in the expression of several Pgc1αfamily of transcription co-factors including Essra, Pparγ or Hnf4a, as all these transcription factors are well known to regulate the expression of most genes involved in cellular energy production as well as in the process of mitochondrial biogenesis. As alterations of mitochondrial metabolism have been linked with renal disease, including AKI, CKD or renal fibrosis (He et al. 2017) (He L., et al., 2017) we proceed to further explore on the putative role of Essrα on CKD. Importantly, Essrα represented a yet unexplored transcription factor in the context of renal differentiation or renal disease. Thanks to our international collaboration with experts in the field of kidney disease and metabolism we could identify, for the first time, on the role of Essrα protecting from CKD using two different *in vivo* models taking advantage of the mice model system. Furthermore, our results were confirmed in a cohort of 90 CKD patient samples (Dillon et al., 2020). All in all, this study demonstrates on the use of kidney organoids as model systems to identify new signaling pathways which may be compromised during human kidney disease. We are convinced that our recent work will open new venues to further reveal other metabolic pathways dysregulated during both renal differentiation and renal

disease. To date, several approaches have been proposed to explore molecular pathways that are responsible for kidney fibrosis initiation and progression. Comprehensive genome-wide kidney tissue transcriptomics analysis has been used to define the molecular hallmarks of this complex process both in patient samples and mouse models (Beckerman et al. 2017; Qiu et al. 2018; Woroniecka et al. 2011). These studies highlighted the role of a large number of transcripts that correlate with kidney fibrosis development. Cellular metabolism, such as genes in FAO and OXPHOS showed strong correlation with disease state both in human and mouse CKD models (Chung et al. 2019; Kang et al. 2015). Pharmacological or genetic approaches that enhance FAO and mitochondrial biogenesis improved kidney function, however, the exact mechanism remains to be solved. Now, our study establishes a causative role of CKD and FAO dysregulation via Essrα further showing that the modulation this pathway *in vitro* and *in vivo* restores kidney cellular function highlighting on the central role of kidney PTCs for further metabolic-related interventions.

Importantly, at the present time, and from December 2019, a novel coronavirus (SARS-CoV-2) crossed species barriers to infect humans (Gorbalenya et al., 2020) and was effectively transmitted from person to person, leading to a pneumonia outbreak first reported in Wuhan, China (Guan et al., 2020; Jiang et al., 2020; Zhou et al., 2020b). This virus causes coronavirus disease-19 (COVID-19) with influenza like symptoms ranging from mild disease to severe lung injury and multi-organ failure, eventually leading to death, especially in older patients with other co-morbidities. COVID-19 has spread worldwide with nearly 68,000,000 confirmed cases and already more than 1,500,000 fatalities. The WHO has declared that COVID-19 is a public health emergency of

pandemic proportions (https://www.who.int/). The primary symptoms of COVID19 patients are fever and cough (Chen et al. 2020) and this can be explained by angiotensin-converting enzyme 2 (ACE2), the key receptor for the spike glycoprotein of SARS-CoV-2, in alveolar epithelial type II (Zhao et al. 2020) cells, which are key for lung gas exchange (Dobbs 1989). The injury of these cells during SARS-CoV-2 infection explains the severe lung injury associated with this disease, however it has been observed a multi-organ dysfunction in COVID-19 patients (Guan et al. 2020; Huang et al. 2020). Indeed, ACE2, is also strongly expressed in kidney tubules, controlling a local renin-angiotensin-aldosterone system (RAAs) circuit (Clarke and Turner, 2012; Hashimoto et al., 2012). The various roles of ACE2 include the regulation of vasoconstriction, renal sodium reabsorption and potassium secretion, aldosterone synthesis, blood pressure elevation, and induction of inflammatory and pro-fibrotic pathways (Ferrario, Trask, and Jessup 2005; Tikellis and Thomas 2012). The wide distribution of ACE2 across the human body explains the multi-organ damage and dysfunction associated with SARS-CoV-2, which includes myocardial dysfunction (Bonow et al. 2020), gastrointestinal and liver (Fan et al. 2020) disorders, and AKI (Li et al. 2020). Since ACE2 exists both in membrane-bound and soluble circulating forms, one proposed therapy for COVID19 disease would be administering the soluble form of ACE2 (sACE2). In this manner sACE2 would act as a decoy to interfere with the binding of SARS-CoV-2 to the full-length ACE2 that is membrane bound.

In the context of the present thesis, we have developed a model system to study SARS-CoV-2 infection establishing a new procedure to generate kidney organoids from hESCs. To further assess on the utility of this novel procedure we first profiled kidney organoids cellular composition

taking advantage of scRNA seq. Then, we interrogated for the distribution of ACE2 expressing cells in our data set and further confirm on ACE2 expression in the proximal tubule and podocyte II cell clusters which also express key marker genes of proximal tubular cells (Slc3a1, Slc27a2) and podocytes (Podxl, Nphs1, Nphs2), respectively. Importantly, it was the first time that it was shown that the generation of kidney organoids suffices for the generation of cell clusters that express ACE2 in a similar fashion to that observed in the kidney native tissue (Lin et al. 2020). To further exploit kidney organoids for further applications in COVID19 research we set up experimental conditions showing how SARS-CoV-2 can infect human kidney organoids (Monteil et al. 2020). More importantly, we further proceed to assay on the putative effect of a human recombinant soluble ACE2 as a new approach to block SARS-CoV-2 infection, resulting in the inhibition of infectious viral progeny. Our study has limitations as our efforts are focused on the early stages of infection, demonstrating that hrsACE2 can block early entry of SARS-CoV-2 infections in host cells. As such, we cannot make any predictions with respect to the effect of hrsACE2 in later stages of the disease process. Secondly, we did not study lung organoids, and the lung is the major target organ for COVID-19. Of equal importance, the RAS system represents a complex network of pathways which are influenced by external processes which are not simulated in our kidney organoids. To address these complex issues, we are convinced that microfluidic platforms will allow us for a better modeling of systemic-related conditions in the time course of SARS-CoV-2 infection. In this regard, our current work is further investigating on the cross talk of the glucose metabolism in SARS-CoV-2 infection. Furthermore, at the present time we are also applying CRISPR/Cas9 mediated genome

editing for the generation of ACE2 knockout in hPSCs which are further differentiated into kidney and gastric organoids. We are convinced that this approach will allow us to better ascertain on ACE2-tissue dependent responses in front of SARS-CoV-2 infection providing further information on the effect of human soluble recombinant ACE2 in different model systems.

V.   CONCLUSIONS

V. CONCLUSIONS

I.   We have established a procedure that suffices for the generation of posterior intermediate mesoderm (PIM) committed hPSCs which upon further assembly and culture in 3D conditions (transwell system or free floating suspension) leads to the generation of kidney organoids transcriptomically matching the human kidney of the second trimester gestation upon 16 days in culture.

II. We have established a procedure for the implantation of day 16 hPSCs-kidney organoids into the chick developing chorioallantoic membrane (CAM) that sustains for the endogenous organization of human endothelial cells and the growth of developing glomeruli.

III. We have identified different cell culture media promoting metabolic activities in developing hPSCs-kidney organoids that further correlated with changes in the expression of metabolic regulators and the generation of tubular-like cells on demand.

IV. We have identified metabolic regulators of the lipid metabolism (Estrogen-related receptor alpha, namely Esrrα) involved in the differentiation of tubular-like cells in developing hPSCs-derived kidney organoids and further assessed on the impact of this factor in damage protection on these cells.

V. We have established a procedure for the study of the first steps
of SARS-CoV-2 infection taking advantage of hPSCs-kidney
organoids upon their characterization for the endogenous
expression of Angiotensin Converting Enzyme 2 (ACE2) using
single cell RNA seq and an exhaustive profiling for the
expression of tubular markers in hPSCs-kidney organoids.

VI.   REFERENCES

VI.REFERENCES

1. Andersen, K. G., Rambaut, A., Lipkin, W. I., Holmes, E. C., & Garry, R. F. (2020). The proximal origin of SARS-CoV-2. In *Nature Medicine*.

2. Auerbach, R., & Grobstein, C. (1958). Inductive interaction of embryonic tissues after dissociation and reaggregation. *Experimental Cell Research*, *15*(2), 384–397.

3. Bagherie-Lachidan, M., Reginensi, A., Pan, Q., Zaveri, H. P., Scott, D. A., Blencowe, B. J., Helmbacher, F., & McNeill, H. (2015). Stromal Fat4 acts non-autonomously with Dchs1/2 to restrict the nephron progenitor pool. *Development (Cambridge)*, *142*(15), 2564–2573.

4. Bantounas, I., Ranjzad, P., Tengku, F., Silajdžić, E., Forster, D., Asselin, M. C., Lewis, P., Lennon, R., Plagge, A., Wang, Q., Woolf, A. S., & Kimber, S. J. (2018). Generation of Functioning Nephrons by Implanting Human Pluripotent Stem Cell-Derived Kidney Progenitors. *Stem Cell Reports*, *10*(3), 766–779.

5. Bao, L., Deng, W., Huang, B., Gao, H., Liu, J., Ren, L., Wei, Q., Yu, P., Xu, Y., Qi, F., Qu, Y., Li, F., Lv, Q., Wang, W., Xue, J., Gong, S., Liu, M., Wang, G., Wang, S., … Qin, C. (2020). The pathogenicity of SARS-CoV-2 in hACE2 transgenic mice. *Nature*.

6. Barak, H., Rosenfelder, L., Schultheiss, T. M., & Reshef, R. (2005). Cell fate specification along the anterior-posterior axis of the intermediate mesoderm. *Developmental Dynamics : An Official Publication of the American Association of Anatomists*,

232(4), 901–914.

7. Bard, J. B., Gordon, A., Sharp, L., & Sellers, W. I. (2001). Early nephron formation in the developing mouse kidney. *Journal of Anatomy*, *199*(Pt 4), 385–392.

8. Barletta, G.-M., Kovari, I. A., Verma, R. K., Kerjaschki, D., & Holzman, L. B. (2003). Nephrin and Neph1 co-localize at the podocyte foot process intercellular junction and form cis hetero-oligomers. *The Journal of Biological Chemistry*, *278*(21), 19266–19271.

9. Bertram, J. F., Douglas-Denton, R. N., Diouf, B., Hughson, M. D., & Hoy, W. E. (2011). Human nephron number: implications for health and disease. *Pediatric Nephrology (Berlin, Germany)*, *26*(9), 1529–1533.

10. Bolin, G., & Burggren, W. W. (2013). Metanephric kidney development in the chicken embryo: Glomerular numbers, characteristics and perfusion. *Comparative Biochemistry and Physiology. Part A, Molecular & Integrative Physiology*, *166*(2), 343–350.

11. Bonow, R. O., Fonarow, G. C., O'Gara, P. T., & Yancy, C. W. (2020). Association of Coronavirus Disease 2019 (COVID-19) with Myocardial Injury and Mortality. In *JAMA Cardiology*.

12. Bouchard, M., Souabni, A., Mandler, M., Neubüser, A., & Busslinger, M. (2002). Nephric lineage specification by Pax2 and Pax8. *Genes & Development*, *16*(22), 2958–2970.

13. Bourgonje, A. R., Abdulle, A. E., Timens, W., Hillebrands, J. L., Navis, G. J., Gordijn, S. J., Bolling, M. C., Dijkstra, G., Voors, A. A., Osterhaus, A. D. M. E., van der Voort, P. H. J., Mulder, D. J., & van Goor, H. (2020). Angiotensin-converting enzyme 2

(ACE2), SARS-CoV-2 and the pathophysiology of coronavirus disease 2019 (COVID-19). In *Journal of Pathology*.

14. Boute, N., Gribouval, O., Roselli, S., Benessy, F., Lee, H., Fuchshuber, A., Dahan, K., Gubler, M. C., Niaudet, P., & Antignac, C. (2000). NPHS2, encoding the glomerular protein podocin, is mutated in autosomal recessive steroid-resistant nephrotic syndrome. *Nature Genetics*, *24*(4), 349–354.

15. Boyle, S., Misfeldt, A., Chandler, K. J., Deal, K. K., Southard-Smith, E. M., Mortlock, D. P., Baldwin, H. S., & de Caestecker, M. (2008). Fate mapping using Cited1-CreERT2 mice demonstrates that the cap mesenchyme contains self-renewing progenitor cells and gives rise exclusively to nephronic epithelia. *Developmental Biology*, *313*(1), 234–245.

16. Brändli, A. W. (1999). Towards a molecular anatomy of the Xenopus pronephric kidney. *The International Journal of Developmental Biology*, *43*(5), 381–395.

17. Brennan, H. C., Nijjar, S., & Jones, E. A. (1998). The specification of the pronephric tubules and duct in Xenopus laevis. *Mechanisms of Development*, *75*(1–2), 127–137.

18. Brophy, P. D., Ostrom, L., Lang, K. M., & Dressler, G. R. (2001). Regulation of ureteric bud outgrowth by Pax2-dependent activation of the glial derived neurotrophic factor gene. *Development (Cambridge, England)*, *128*(23), 4747–4756.

19. Cain, J. E., & Bertram, J. F. (2006). Ureteric branching morphogenesis in BMP4 heterozygous mutant mice. *Journal of Anatomy*.

20. Calvet, J. P., & Grantham, J. J. (2001). The genetics and physiology of polycystic kidney disease. *Seminars in*

Nephrology, *21*(2), 107–123.

21.   Carroll, T. J., Park, J.-S., Hayashi, S., Majumdar, A., & McMahon, A. P. (2005). Wnt9b plays a central role in the regulation of mesenchymal to epithelial transitions underlying organogenesis of the mammalian urogenital system. *Developmental Cell*, *9*(2), 283–292.

22.   Cebrián, C., Borodo, K., Charles, N., & Herzlinger, D. A. (2004). Morphometric index of the developing murine kidney. *Developmental Dynamics : An Official Publication of the American Association of Anatomists*, *231*(3), 601–608.

23.   Chan, J. F. W., Zhang, A. J., Yuan, S., Poon, V. K. M., Chan, C. C. S., Lee, A. C. Y., Chan, W. M., Fan, Z., Tsoi, H. W., Wen, L., Liang, R., Cao, J., Chen, Y., Tang, K., Luo, C., Cai, J. P., Kok, K. H., Chu, H., Chan, K. H., … Yuen, K. Y. (2020). Simulation of the clinical and pathological manifestations of Coronavirus Disease 2019 (COVID-19) in golden Syrian hamster model: implications for disease pathogenesis and transmissibility. *Clinical Infectious Diseases : An Official Publication of the Infectious Diseases Society of America*.

24.   Chan, T. C., Ariizumi, T., & Asashima, M. (1999). A model system for organ engineering: transplantation of in vitro induced embryonic kidney. *Die Naturwissenschaften*, *86*(5), 224–227.

25.   Chandrashekar, A., Liu, J., Martino, A. J., McMahan, K., Mercad, N. B., Peter, L., Tostanosk, L. H., Yu, J., Maliga, Z., Nekorchuk, M., Busman-Sahay, K., Terry, M., Wriji, L. M., Ducat, S., Martine, D. R., Atyeo, C., Fischinger, S., Burk, J. S., Slei, M. D., … Barou, D. H. (2020). SARS-CoV-2 infection protects against rechallenge in rhesus macaques. *Science*.

26. Chen, N., Zhou, M., Dong, X., Qu, J., Gong, F., Han, Y., Qiu, Y., Wang, J., Liu, Y., Wei, Y., Xia, J., Yu, T., Zhang, X., & Zhang, L. (2020). Epidemiological and clinical characteristics of 99 cases of 2019 novel coronavirus pneumonia in Wuhan, China: a descriptive study. *Lancet (London, England)*, *395*(10223), 507–513.

27. Cheng, H.-T., Kim, M., Valerius, M. T., Surendran, K., Schuster-Gossler, K., Gossler, A., McMahon, A. P., & Kopan, R. (2007). Notch2, but not Notch1, is required for proximal fate acquisition in the mammalian nephron. *Development (Cambridge, England)*, *134*(4), 801–811.

28. Chow, T., Wong, F. T. M., Monetti, C., Nagy, A., Cox, B., & Rogers, I. M. (2020). Recapitulating kidney development in vitro by priming and differentiating mouse embryonic stem cells in monolayers. *NPJ Regenerative Medicine*, *5*, 7.

29. Costantini, F., & Kopan, R. (2010). Patterning a complex organ: Branching morphogenesis and nephron segmentation in kidney development. *Developmental Cell*, *18*(5), 698–712. https://doi.org/1878-1551 (Electronic) 1534-5807 (Linking)

30. Crackower, M. A., Sarao, R., Oudit, G. Y., Yagil, C., Kozieradzki, I., Scanga, S. E., Oliveira-dos-Santos, A. J., da Costa, J., Zhang, L., Pei, Y., Scholey, J., Ferrario, C. M., Manoukian, A. S., Chappell, M. C., Backx, P. H., Yagil, Y., & Penninger, J. M. (2002). Angiotensin-converting enzyme 2 is an essential regulator of heart function. *Nature*, *417*(6891), 822–828.

31. Danilczyk, U., & Penninger, J. M. (2006). Angiotensin-converting enzyme II in the heart and the kidney. *Circulation*

Research, *98*(4), 463–471.

32. Davidson, A. J. (2008). *Mouse kidney development.*

33. Davies, J A, & Garrod, D. R. (1995). Induction of early stages of kidney tubule differentiation by lithium ions. *Developmental Biology*, *167*(1), 50–60.

34. Davies, Jamie A. (2002). Do different branching epithelia use a conserved developmental mechanism? *BioEssays : News and Reviews in Molecular, Cellular and Developmental Biology*, *24*(10), 937–948.

35. Ding, Y., He, L., Zhang, Q., Huang, Z., Che, X., Hou, J., Wang, H., Shen, H., Qiu, L., Li, Z., Geng, J., Cai, J., Han, H., Li, X., Kang, W., Weng, D., Liang, P., & Jiang, S. (2004). Organ distribution of severe acute respiratory syndrome (SARS) associated coronavirus (SARS-CoV) in SARS patients: implications for pathogenesis and virus transmission pathways. *The Journal of Pathology*, *203*(2), 622–630.

36. Dobbs, L. G. (1989). Pulmonary surfactant. In *Annual Review of Medicine*.

37. Dressler, G R, Deutsch, U., Chowdhury, K., Nornes, H. O., & Gruss, P. (1990). Pax2, a new murine paired-box-containing gene and its expression in the developing excretory system. *Development (Cambridge, England)*, *109*(4), 787–795.

38. Dressler, Gregory R. (2006). The cellular basis of kidney development. *Annual Review of Cell and Developmental Biology*, *22*, 509–529.

39. Drosten, C., Günther, S., Preiser, W., van der Werf, S., Brodt, H.-R., Becker, S., Rabenau, H., Panning, M., Kolesnikova, L., Fouchier, R. A. M., Berger, A., Burguière, A.-M., Cinatl, J.,

Eickmann, M., Escriou, N., Grywna, K., Kramme, S., Manuguerra, J.-C., Müller, S., … Doerr, H. W. (2003). Identification of a Novel Coronavirus in Patients with Severe Acute Respiratory Syndrome. *New England Journal of Medicine*.

40. Drummond, I A, Majumdar, A., Hentschel, H., Elger, M., Solnica-Krezel, L., Schier, A. F., Neuhauss, S. C., Stemple, D. L., Zwartkruis, F., Rangini, Z., Driever, W., & Fishman, M. C. (1998). Early development of the zebrafish pronephros and analysis of mutations affecting pronephric function. *Development (Cambridge, England)*, *125*(23), 4655–4667.

41. Drummond, Iain A. (2005). Kidney development and disease in the zebrafish. *Journal of the American Society of Nephrology : JASN*, *16*(2), 299–304.

42. Dudley, A. T., Godin, R. E., & Robertson, E. J. (1999). Interaction between FGF and BMP signaling pathways regulates development of metanephric mesenchyme. *Genes & Development*, *13*(12), 1601–1613.

43. Eremina, V., Sood, M., Haigh, J., Nagy, A., Lajoie, G., Ferrara, N., Gerber, H.-P., Kikkawa, Y., Miner, J. H., & Quaggin, S. E. (2003). Glomerular-specific alterations of VEGF-A expression lead to distinct congenital and acquired renal diseases. *The Journal of Clinical Investigation*, *111*(5), 707–716.

44. Evans, M. J., & Kaufman, M. H. (1981). Establishment in culture of pluripotential cells from mouse embryos. *Nature*, *292*(5819), 154–156.

45. Fan, Z., Chen, L., Li, J., Cheng, X., Yang, J., Tian, C., Zhang, Y., Huang, S., Liu, Z., & Cheng, J. (2020). Clinical Features of COVID-19-Related Liver Functional Abnormality. *Clinical*

Gastroenterology and Hepatology : The Official Clinical Practice Journal of the American Gastroenterological Association, *18*(7), 1561–1566.

46. Ferrario, C. M., Trask, A. J., & Jessup, J. A. (2005). Advances in biochemical and functional roles of angiotensin-converting enzyme 2 and angiotensin-(1-7) in regulation of cardiovascular function. *American Journal of Physiology. Heart and Circulatory Physiology*, *289*(6), H2281-90.

47. FOX, H. (1963). The amphibian pronephros. *The Quarterly Review of Biology*.

48. Freedman, B. S., Brooks, C. R., Lam, A. Q., Fu, H., Morizane, R., Agrawal, V., Saad, A. F., Li, M. K., Hughes, M. R., Werff, R. Vander, Peters, D. T., Lu, J., Baccei, A., Siedlecki, A. M., Valerius, M. T., Musunuru, K., McNagny, K. M., Steinman, T. I., Zhou, J., … Bonventre, J. V. (2015). Modelling kidney disease with CRISPR-mutant kidney organoids derived from human pluripotent epiblast spheroids. *Nature Communications*, *6*(May), 8715.

49. Friedmann, H. (1960). The Avian Embryo. Structural and functional development. Alexis L. Romanoff. Macmillan, New York, 1960. xvi + 1305 pp. Illus. $35. *Science*.

50. Gabrielli, M. G., & Accili, D. (2010). The chick chorioallantoic membrane: a model of molecular, structural, and functional adaptation to transepithelial ion transport and barrier function during embryonic development. *Journal of Biomedicine & Biotechnology*, *2010*, 940741.

51. Ganeva, V., Unbekandt, M., & Davies, J. A. (2011). An improved kidney dissociation and re-aggregation culture system results in

nephrons arranged organotypically around a single collecting duct system. *Organogenesis*, *7*(2).

52. Garreta, E., Kamm, R. D., Chuva de Sousa Lopes, S. M., Lancaster, M. A., Weiss, R., Trepat, X., Hyun, I., & Montserrat, N. (2020). Rethinking organoid technology through bioengineering. In *Nature Materials*.

53. Garreta, E., Prado, P., Tarantino, C., Oria, R., Fanlo, L., Martí, E., Zalvidea, D., Trepat, X., Roca-Cusachs, P., Gavaldà-Navarro, A., Cozzuto, L., Campistol, J. M., Belmonte, J. C. I., Pozo, C. H. del, & Montserrat, N. (2019). Fine tuning the extracellular environment accelerates the derivation of kidney organoids from human pluripotent stem cells. *Nature Materials*.

54. Georgas, K. M., Chiu, H. S., Lesieur, E., Rumballe, B. A., & Little, M. H. (2011). Expression of metanephric nephron-patterning genes in differentiating mesonephric tubules. *Developmental Dynamics*, *240*(6), 1600–1612.

55. Graves, J. S., Dunn, B. E., & Brown, S. C. (1986). Embryonic chick allantois: functional isolation and development of sodium transport. *The American Journal of Physiology*, *251*(5 Pt 1), C787-94.

56. Grieshammer, U., Cebrián, C., Ilagan, R., Meyers, E., Herzlinger, D., & Martin, G. R. (2005). FGF8 is required for cell survival at distinct stages of nephrogenesis and for regulation of gene expression in nascent nephrons. *Development (Cambridge, England)*, *132*(17), 3847–3857.

57. Grieshammer, U., Ma, L., Plump, A. S., Wang, F., Tessier-Lavigne, M., & Martin, G. R. (2004). SLIT2-mediated ROBO2 signaling restricts kidney induction to a single site.

Developmental Cell, *6*(5), 709–717.

58. GROBSTEIN, C. (1953). Inductive epitheliomesenchymal interaction in cultured organ rudiments of the mouse. *Science (New York, N.Y.)*, *118*(3054), 52–55.

59. GROBSTEIN, C. (1956). Trans-filter induction of tubules in mouse metanephrogenic mesenchyme. *Experimental Cell Research*, *10*(2), 424–440.

60. Grote, D., Souabni, A., Busslinger, M., & Bouchard, M. (2006). Pax 2/8-regulated Gata 3 expression is necessary for morphogenesis and guidance of the nephric duct in the developing kidney. *Development (Cambridge, England)*, *133*(1), 53–61.

61. Gu, J., Gong, E., Zhang, B., Zheng, J., Gao, Z., Zhong, Y., Zou, W., Zhan, J., Wang, S., Xie, Z., Zhuang, H., Wu, B., Zhong, H., Shao, H., Fang, W., Gao, D., Pei, F., Li, X., He, Z., … Leong, A. S.-Y. (2005). Multiple organ infection and the pathogenesis of SARS. *The Journal of Experimental Medicine*, *202*(3), 415–424.

62. Guan, W., Ni, Z., Hu, Y., Liang, W., Ou, C., He, J., Liu, L., Shan, H., Lei, C., Hui, D. S. C., Du, B., Li, L., Zeng, G., Yuen, K.-Y., Chen, R., Tang, C., Wang, T., Chen, P., Xiang, J., … Zhong, N. (2020). Clinical Characteristics of Coronavirus Disease 2019 in China. *New England Journal of Medicine*.

63. Hale, L. J., Howden, S. E., Phipson, B., Lonsdale, A., Er, P. X., Ghobrial, I., Hosawi, S., Wilson, S., Lawlor, K. T., Khan, S., Oshlack, A., Quinlan, C., Lennon, R., & Little, M. H. (2018). 3D organoid-derived human glomeruli for personalised podocyte disease modelling and drug screening. *Nature Communications*, *9*(1).

64. Halt, K., & Vainio, S. (2012). In vitro induction of nephrogenesis in mouse metanephric mesenchyme with lithium introduction and ureteric bud recombination. *Methods in Molecular Biology (Clifton, N.J.)*, *886*, 23–30.

65. Hamming, I., Timens, W., Bulthuis, M. L. C., Lely, A. T., Navis, G. J., & van Goor, H. (2004). Tissue distribution of ACE2 protein, the functional receptor for SARS coronavirus. A first step in understanding SARS pathogenesis. *The Journal of Pathology*, *203*(2), 631–637.

66. Han, Y., Yang, L., Duan, X., Duan, F., Nilsson-Payant, B. E., Yaron, T. M., Wang, P., Tang, X., Zhang, T., Zhao, Z., Bram, Y., Redmond, D., Houghton, S., Nguyen, D., Xu, D., Wang, X., Uhl, S., Huang, Y., Johnson, J. L., … Chen, S. (2020). Identification of Candidate COVID-19 Therapeutics using hPSC-derived Lung Organoids. *BioRxiv*, 2020.05.05.079095.

67. Harcourt, J., Tamin, A., Lu, X., Kamili, S., Sakthivel, S. K., Murray, J., Queen, K., Tao, Y., Paden, C., Zhang, J., Li, Y., Uehara, A., Wang, H., Goldsmith, C., Bullock, H., Wang, L., Whitaker, B., Lynch, B., Gautam, R., … Thornburg, N. (2020). Isolation and characterization of SARS-CoV-2 from the first US COVID-19 patient. *BioRxiv : The Preprint Server for Biology*.

68. Herzlinger, D., Qiao, J., Cohen, D., Ramakrishna, N., & Brown, A. M. (1994). Induction of kidney epithelial morphogenesis by cells expressing Wnt-1. *Developmental Biology*, *166*(2), 815–818.

69. Hochane, M., van den Berg, P. R., Fan, X., Bérenger-Currias, N., Adegeest, E., Bialecka, M., Nieveen, M., Menschaart, M., Chuva de Sousa Lopes, S. M., & Semrau, S. (2019). Single-cell

transcriptomics reveals gene expression dynamics of human fetal kidney development. In *PLoS Biology* (Vol. 17, Issue 2). https://doi.org/1111111111

70. Hoffmann, M., Kleine-Weber, H., Schroeder, S., Krüger, N., Herrler, T., Erichsen, S., Schiergens, T. S., Herrler, G., Wu, N. H., Nitsche, A., Müller, M. A., Drosten, C., & Pöhlmann, S. (2020). SARS-CoV-2 Cell Entry Depends on ACE2 and TMPRSS2 and Is Blocked by a Clinically Proven Protease Inhibitor. *Cell*.

71. Homan, K. A., Gupta, N., Kroll, K. T., Kolesky, D. B., Skylar-Scott, M., Miyoshi, T., Mau, D., Valerius, M. T., Ferrante, T., Bonventre, J. V., Lewis, J. A., & Morizane, R. (2019). Flow-enhanced vascularization and maturation of kidney organoids in vitro. *Nature Methods*, *16*(3), 255–262. https://doi.org/4159201903

72. Huang, C., Wang, Y., Li, X., Ren, L., Zhao, J., Hu, Y., Zhang, L., Fan, G., Xu, J., Gu, X., Cheng, Z., Yu, T., Xia, J., Wei, Y., Wu, W., Xie, X., Yin, W., Li, H., Liu, M., … Cao, B. (2020). Clinical features of patients infected with 2019 novel coronavirus in Wuhan, China. *The Lancet*.

73. Imai, Y., Kuba, K., Rao, S., Huan, Y., Guo, F., Guan, B., Yang, P., Sarao, R., Wada, T., Leong-Poi, H., Crackower, M. A., Fukamizu, A., Hui, C. C., Hein, L., Uhlig, S., Slutsky, A. S., Jiang, C., & Penninger, J. M. (2005). Angiotensin-converting enzyme 2 protects from severe acute lung failure. *Nature*.

74. Imberti, B., Tomasoni, S., Ciampi, O., Pezzotta, A., Derosas, M., Xinaris, C., Rizzo, P., Papadimou, E., Novelli, R., Benigni, A., Remuzzi, G., & Morigi, M. (2015). Renal progenitors derived

from human iPSCs engraft and restore function in a mouse model of acute kidney injury. *Scientific Reports*, *5*, 8826.

75. James, R. G., & Schultheiss, T. M. (2003). Patterning of the avian intermediate mesoderm by lateral plate and axial tissues. *Developmental Biology*, *253*(1), 109–124.

76. James, R. G., & Schultheiss, T. M. (2005). Bmp signaling promotes intermediate mesoderm gene expression in a dose-dependent, cell-autonomous and translation-dependent manner. *Developmental Biology*, *288*(1), 113–125.

77. Junttila, S., Saarela, U., Halt, K., Manninen, A., Pärssinen, H., Lecca, M. R., Brändli, A. W., Sims-Lucas, S., Skovorodkin, I., & Vainio, S. J. (2015). Functional genetic targeting of embryonic kidney progenitor cells ex vivo. *Journal of the American Society of Nephrology : JASN*, *26*(5), 1126–1137.

78. Kim, A. D., Lake, B. B., Chen, S., Wu, Y., Guo, J., Parvez, R. K., Tran, T., Thornton, M. E., Grubbs, B., McMahon, J. A., Zhang, K., & McMahon, A. P. (2019). Cellular Recruitment by Podocyte-Derived Pro-migratory Factors in Assembly of the Human Renal Filter. *IScience*, *20*, 402–414.

79. Kim, D., & Dressler, G. R. (2005). Nephrogenic factors promote differentiation of mouse embryonic stem cells into renal epithelia. *Journal of the American Society of Nephrology : JASN*, *16*(12), 3527–3534.

80. Kim, Y. Il, Kim, S. G., Kim, S. M., Kim, E. H., Park, S. J., Yu, K. M., Chang, J. H., Kim, E. J., Lee, S., Casel, M. A. B., Um, J., Song, M. S., Jeong, H. W., Lai, V. D., Kim, Y., Chin, B. S., Park, J. S., Chung, K. H., Foo, S. S., … Choi, Y. K. (2020). Infection and Rapid Transmission of SARS-CoV-2 in Ferrets. *Cell Host*

and Microbe.

81.   Kim, J. M., Chung, Y. S., Jo, H. J., Lee, N. J., Kim, M. S., Woo, S. H., Park, S., Kim, J. W., Kim, H. M., & Han, M. G. (2020). Identification of coronavirus isolated from a patient in Korea with covid-19. *Osong Public Health and Research Perspectives*.

82.   Kimmel, C. B., Ballard, W. W., Kimmel, S. R., Ullmann, B., & Schilling, T. F. (1995). Stages of embryonic development of the zebrafish. *Developmental Dynamics : An Official Publication of the American Association of Anatomists*, *203*(3), 253–310.

83.   Kishimoto, Y., Lee, K. H., Zon, L., Hammerschmidt, M., & Schulte-Merker, S. (1997). The molecular nature of zebrafish swirl: BMP2 function is essential during early dorsoventral patterning. *Development (Cambridge, England)*, *124*(22), 4457–4466.

84.   Kispert, A., Vainio, S., Shen, L., Rowitch, D. H., & McMahon, A. P. (1996). Proteoglycans are required for maintenance of Wnt-11 expression in the ureter tips. *Development (Cambridge, England)*, *122*(11), 3627–3637.

85.   Kitamoto, Y., Tokunaga, H., & Tomita, K. (1997). Vascular endothelial growth factor is an essential molecule for mouse kidney development: glomerulogenesis and nephrogenesis. *The Journal of Clinical Investigation*, *99*(10), 2351–2357.

86.   KLEINSMITH, L. J., & PIERCE, G. B. J. (1964). MULTIPOTENTIALITY OF SINGLE EMBRYONAL CARCINOMA CELLS. *Cancer Research*, *24*, 1544–1551.

87.   Kobayashi, A., Kwan, K.-M., Carroll, T. J., McMahon, A. P., Mendelsohn, C. L., & Behringer, R. R. (2005). Distinct and sequential tissue-specific activities of the LIM-class homeobox

gene Lim1 for tubular morphogenesis during kidney development. *Development (Cambridge, England)*, *132*(12), 2809–2823.

88. Kreidberg, J. A., Sariola, H., Loring, J. M., Maeda, M., Pelletier, J., Housman, D., & Jaenisch, R. (1993). WT-1 is required for early kidney development. *Cell*, *74*(4), 679–691.

89. Krneta-Stankic, V., DeLay, B. D., & Miller, R. K. (2017). Xenopus: leaping forward in kidney organogenesis. *Pediatric Nephrology (Berlin, Germany)*, *32*(4), 547–555.

90. Kuba, K., Imai, Y., Rao, S., Gao, H., Guo, F., Guan, B., Huan, Y., Yang, P., Zhang, Y., Deng, W., Bao, L., Zhang, B., Liu, G., Wang, Z., Chappell, M., Liu, Y., Zheng, D., Leibbrandt, A., Wada, T., … Penninger, J. M. (2005). A crucial role of angiotensin converting enzyme 2 (ACE2) in SARS coronavirus-induced lung injury. *Nature Medicine*.

91. Kumar Gupta, A., Sarkar, P., Wertheim, J. A., Pan, X., Carroll, T. J., & Oxburgh, L. (2020). Asynchronous mixing of kidney progenitor cells potentiates nephrogenesis in organoids. *Communications Biology*, *3*(1).

92. Kume, T., Deng, K., & Hogan, B. L. (2000). Murine forkhead/winged helix genes Foxc1 (Mf1) and Foxc2 (Mfh1) are required for the early organogenesis of the kidney and urinary tract. *Development (Cambridge, England)*, *127*(7), 1387–1395.

93. Kuure, S., Popsueva, A., Jakobson, M., Sainio, K., & Sariola, H. (2007). Glycogen synthase kinase-3 inactivation and stabilization of beta-catenin induce nephron differentiation in isolated mouse and rat kidney mesenchymes. *Journal of the American Society of Nephrology : JASN*, *18*(4), 1130–1139.

94. Kyuno, J., Massé, K., & Jones, E. A. (2008). A functional screen for genes involved in Xenopus pronephros development. *Mechanisms of Development*, *125*(7), 571–586.

95. Lam, A. Q., Freedman, B. S., Morizane, R., Lerou, P. H., Valerius, M. T., & Bonventre, J. V. (2014). Rapid and efficient differentiation of human pluripotent stem cells into intermediate mesoderm that forms tubules expressing kidney proximal tubular markers. *Journal of the American Society of Nephrology : JASN*, *25*(6), 1211–1225.

96. Lamers, M. M., Beumer, J., van der Vaart, J., Knoops, K., Puschhof, J., Breugem, T. I., Ravelli, R. B. G., Paul van Schayck, J., Mykytyn, A. Z., Duimel, H. Q., van Donselaar, E., Riesebosch, S., Kuijpers, H. J. H., Schipper, D., van de Wetering, W. J., de Graaf, M., Koopmans, M., Cuppen, E., Peters, P. J., … Clevers, H. (2020). SARS-CoV-2 productively infects human gut enterocytes. *Science (New York, N.Y.)*, *369*(6499), 50–54.

97. Lawson, A., Colas, J. F., & Schoenwolf, G. C. (2001). Classification scheme for genes expressed during formation and progression of the avian primitive streak. *The Anatomical Record*, *262*(2), 221–226.

98. Leimeister, C., Schumacher, N., & Gessler, M. (2003). Expression of Notch pathway genes in the embryonic mouse metanephros suggests a role in proximal tubule development. *Gene Expression Patterns : GEP*, *3*(5), 595–598.

99. Letko, M., Marzi, A., & Munster, V. (2020). Functional assessment of cell entry and receptor usage for SARS-CoV-2 and other lineage B betacoronaviruses. *Nature Microbiology*.

100. Li, Q., Guan, X., Wu, P., Wang, X., Zhou, L., Tong, Y., Ren, R.,

Leung, K. S. M., Lau, E. H. Y., Wong, J. Y., Xing, X., Xiang, N., Wu, Y., Li, C., Chen, Q., Li, D., Liu, T., Zhao, J., Liu, M., … Feng, Z. (2020). Early Transmission Dynamics in Wuhan, China, of Novel Coronavirus–Infected Pneumonia. *New England Journal of Medicine*.

101. Li, W., Moore, M. J., Vasllieva, N., Sui, J., Wong, S. K., Berne, M. A., Somasundaran, M., Sullivan, J. L., Luzuriaga, K., Greeneugh, T. C., Choe, H., & Farzan, M. (2003). Angiotensin-converting enzyme 2 is a functional receptor for the SARS coronavirus. *Nature*.

102. Li, Z., Wu, M., Yao, J., Guo, J., Liao, X., Song, S., Li, J., Duan, G., Zhou, Y., Wu, X., Zhou, Z., Wang, T., Hu, M., Chen, X., Fu, Y., Lei, C., Dong, H., Xu, C., Hu, Y., … Yan, J. (2020). Caution on Kidney Dysfunctions of COVID-19 Patients. *MedRxiv*, 2020.02.08.20021212.

103. Lienkamp, S. S., Liu, K., Karner, C. M., Carroll, T. J., Ronneberger, O., Wallingford, J. B., & Walz, G. (2012). Vertebrate kidney tubules elongate using a planar cell polarity-dependent, rosette-based mechanism of convergent extension. *Nature Genetics*, *44*(12), 1382–1387.

104. Lindahl, P., Hellström, M., Kalén, M., Karlsson, L., Pekny, M., Pekna, M., Soriano, P., & Betsholtz, C. (1998). Paracrine PDGF-B/PDGF-Rbeta signaling controls mesangial cell development in kidney glomeruli. *Development (Cambridge, England)*, *125*(17), 3313–3322.

105. Lindström, N. O., De Sena Brandine, G., Tran, T., Ransick, A., Suh, G., Guo, J., Kim, A. D., Parvez, R. K., Ruffins, S. W., Rutledge, E. A., Thornton, M. E., Grubbs, B., McMahon, J. A.,

Smith, A. D., & McMahon, A. P. (2018). Progressive Recruitment of Mesenchymal Progenitors Reveals a Time-Dependent Process of Cell Fate Acquisition in Mouse and Human Nephrogenesis. *Developmental Cell*, *45*(5), 651-660.e4.

106. Lindström, N. O., Tran, T., Guo, J., Rutledge, E., Parvez, R. K., Thornton, M. E., Grubbs, B., McMahon, J. A., & McMahon, A. P. (2018). Conserved and divergent molecular and anatomic features of human and mouse nephron patterning. *Journal of the American Society of Nephrology*, *29*(3), 825–840.

107. Little, M. H., Brennan, J., Georgas, K., Davies, J. A., Davidson, D. R., Baldock, R. A., Beverdam, A., Bertram, J. F., Capel, B., Chiu, H. S., Clements, D., Cullen-McEwen, L., Fleming, J., Gilbert, T., Herzlinger, D., Houghton, D., Kaufman, M. H., Kleymenova, E., Koopman, P. A., … Yu, J. (2007). Corrigendum to "A high-resolution anatomical ontology of the developing murine genitourinary tract" [Gene Expression Patterns 7 (2007) 680–699]. *Gene Expression Patterns*, *8*(1), 47–50.

108. Little, M. H., & Combes, A. N. (2019). Kidney organoids: Accurate models or fortunate accidents. *Genes and Development*, *33*(19–20), 1319–1345.

109. Little, M. H., & McMahon, A. P. (2012). Mammalian kidney development: principles, progress, and projections. *Cold Spring Harbor Perspectives in Biology*, *4*(5).

110. Liu, S., Lu, W., Obara, T., Kuida, S., Lehoczky, J., Dewar, K., Drummond, I. A., & Beier, D. R. (2002). A defect in a novel Nek-family kinase causes cystic kidney disease in the mouse and in zebrafish. *Development (Cambridge, England)*, *129*(24), 5839–5846.

111. Low, J. H., Li, P., Chew, E. G. Y., Zhou, B., Suzuki, K., Zhang, T., Lian, M. M., Liu, M., Aizawa, E., Rodriguez Esteban, C., Yong, K. S. M., Chen, Q., Campistol, J. M., Fang, M., Khor, C. C., Foo, J. N., Izpisua Belmonte, J. C., & Xia, Y. (2019). Generation of Human PSC-Derived Kidney Organoids with Patterned Nephron Segments and a De Novo Vascular Network. *Cell Stem Cell*.

112. Lu, R., Zhao, X., Li, J., Niu, P., Yang, B., Wu, H., Wang, W., Song, H., Huang, B., Zhu, N., Bi, Y., Ma, X., Zhan, F., Wang, L., Hu, T., Zhou, H., Hu, Z., Zhou, W., Zhao, L., … Tan, W. (2020). Genomic characterisation and epidemiology of 2019 novel coronavirus: implications for virus origins and receptor binding. *The Lancet*.

113. Mae, S. I., Shono, A., Shiota, F., Yasuno, T., Kajiwara, M., Gotoda-Nishimura, N., Arai, S., Sato-Otubo, A., Toyoda, T., Takahashi, K., Nakayama, N., Cowan, C. A., Aoi, T., Ogawa, S., McMahon, A. P., Yamanaka, S., & Osafune, K. (2013). Monitoring and robust induction of nephrogenic intermediate mesoderm from human pluripotent stem cells. *Nature Communications*, *4*.

114. Magella, B., Adam, M., Potter, A. S., Venkatasubramanian, M., Chetal, K., Hay, S. B., Salomonis, N., & Potter, S. S. (2018). Cross-platform single cell analysis of kidney development shows stromal cells express Gdnf. *Developmental Biology*, *434*(1), 36–47.

115. Majumdar, A., & Drummond, I. A. (2000). The zebrafish floating head mutant demonstrates podocytes play an important role in directing glomerular differentiation. *Developmental Biology*,

225

222(1), 147–157.

116. Mao, Y., Francis-West, P., & Irvine, K. D. (2015). Fat4/Dchs1 signaling between stromal and cap mesenchyme cells influences nephrogenesis and ureteric bud branching. *Development (Cambridge, England)*, *142*(15), 2574–2585.

117. Matsuyama, S., Nao, N., Shirato, K., Kawase, M., Saito, S., Takayama, I., Nagata, N., Sekizuka, T., Katoh, H., Kato, F., Sakata, M., Tahara, M., Kutsuna, S., Ohmagari, N., Kuroda, M., Suzuki, T., Kageyama, T., & Takeda, M. (2020). Enhanced isolation of SARS-CoV-2 by TMPRSS2- expressing cells. *Proceedings of the National Academy of Sciences of the United States of America*.

118. Mauch, T. J., Yang, G., Wright, M., Smith, D., & Schoenwolf, G. C. (2000). Signals from trunk paraxial mesoderm induce pronephros formation in chick intermediate mesoderm. *Developmental Biology*, *220*(1), 62–75.

119. McLaughlin, K. A., Rones, M. S., & Mercola, M. (2000). Notch regulates cell fate in the developing pronephros. *Developmental Biology*, *227*(2), 567–580.

120. Menon, R., Otto, E. A., Kokoruda, A., Zhou, J., Zhang, Z., Yoon, E., Chen, Y. C., Troyanskaya, O., Spence, J. R., Kretzler, M., & Cebrián, C. (2018). Single-cell analysis of progenitor cell dynamics and lineage specification in the human fetal kidney. *Development (Cambridge)*, *145*(16 Special Issue). https://doi.org/0000000178693

121. Merlet-Bénichou, C., Gilbert, T., Vilar, J., Moreau, E., Freund, N., & Lelièvre-Pégorier, M. (1999). Nephron number: variability is the rule. Causes and consequences. *Laboratory Investigation;*

a Journal of Technical Methods and Pathology, *79*(5), 515–527.

122. Meyer, T. N., Schwesinger, C., Bush, K. T., Stuart, R. O., Rose, D. W., Shah, M. M., Vaughn, D. A., Steer, D. L., & Nigam, S. K. (2004). Spatiotemporal regulation of morphogenetic molecules during in vitro branching of the isolated ureteric bud: toward a model of branching through budding in the developing kidney. *Developmental Biology*, *275*(1), 44–67.

123. Miyazaki, Y., Oshima, K., Fogo, A., Hogan, B. L., & Ichikawa, I. (2000). Bone morphogenetic protein 4 regulates the budding site and elongation of the mouse ureter. *The Journal of Clinical Investigation*, *105*(7), 863–873.

124. Monteil, V., Dyczynski, M., Lauschke, V. M., Kwon, H., Wirnsberger, G., Youhanna, S., Zhang, H., S.Slutsky, A., Hurtado del Pozo, C., Horn, M., Montserrat, N., Penninger, J. M., & Mirazimi, A. (2020). Human soluble ACE2 improves the effect of remdesivir in SARS-CoV-2 infection. *EMBO Molecular Medicine*.

125. Monteil, V., Kwon, H., Prado, P., Hagelkrüys, A., Wimmer, R. A., Stahl, M., Leopoldi, A., Garreta, E., Hurtado Del Pozo, C., Prosper, F., Romero, J. P., Wirnsberger, G., Zhang, H., Slutsky, A. S., Conder, R., Montserrat, N., Mirazimi, A., & Penninger, J. M. (2020). Inhibition of SARS-CoV-2 Infections in Engineered Human Tissues Using Clinical-Grade Soluble Human ACE2. *Cell*, *181*(4), 905-913.e7.

126. Moriya, N., Uchiyama, H., & Asashima, M. (1993). Induction of Pronephric Tubules by Activin and Retinoic Acid in Presumptive Ectoderm of Xenopus laevis (RA/kidney/mesoderm induction/Xenopus laevis). *Development, Growth &*

Differentiation.

127. Morizane, R., Lam, A. Q., Freedman, B. S., Kishi, S., Valerius, M. T., & Bonventre, J. V. (2015). Nephron organoids derived from human pluripotent stem cells model kidney development and injury. *Nature Biotechnology*, *33*(11), 1193–1200.

128. Morizane, R., Monkawa, T., & Itoh, H. (2009). Differentiation of murine embryonic stem and induced pluripotent stem cells to renal lineage in vitro. *Biochemical and Biophysical Research Communications*, *390*(4), 1334–1339.

129. MOSCONA, A., & MOSCONA, H. (1952). The dissociation and aggregation of cells from organ rudiments of the early chick embryo. *Journal of Anatomy*, *86*(3), 287–301.

130. Mugford, J. W., Yu, J., Kobayashi, A., & McMahon, A. P. (2009). High-resolution gene expression analysis of the developing mouse kidney defines novel cellular compartments within the nephron progenitor population. *Developmental Biology*, *333*(2), 312–323.

131. Nakai, S., Sugitani, Y., Sato, H., Ito, S., Miura, Y., Ogawa, M., Nishi, M., Jishage, K., Minowa, O., & Noda, T. (2003). Crucial roles of Brn1 in distal tubule formation and function in mouse kidney. *Development (Cambridge, England)*, *130*(19), 4751–4759.

132. Narayanan, K., Schumacher, K. M., Tasnim, F., Kandasamy, K., Schumacher, A., Ni, M., Gao, S., Gopalan, B., Zink, D., & Ying, J. Y. (2013). Human embryonic stem cells differentiate into functional renal proximal tubular-like cells. *Kidney International*, *83*(4), 593–603.

133. Narbaitz, R., & Kacew, S. (1978). Ultrastructural and

biochemical observations on the metanephros of normal and cultured chick embryos. *Anatomy and Embryology*, *155*(1), 95–105.

134. Nauli, S. M., Alenghat, F. J., Luo, Y., Williams, E., Vassilev, P., Li, X., Elia, A. E. H., Lu, W., Brown, E. M., Quinn, S. J., Ingber, D. E., & Zhou, J. (2003). Polycystins 1 and 2 mediate mechanosensation in the primary cilium of kidney cells. *Nature Genetics*, *33*(2), 129–137.

135. Nishinakamura, R., Matsumoto, Y., Nakao, K., Nakamura, K., Sato, A., Copeland, N. G., Gilbert, D. J., Jenkins, N. A., Scully, S., Lacey, D. L., Katsuki, M., Asashima, M., & Yokota, T. (2001a). Murine homolog of SALL1 is essential for ureteric bud invasion in kidney development. *Development*.

136. Nishinakamura, R., Matsumoto, Y., Nakao, K., Nakamura, K., Sato, A., Copeland, N. G., Gilbert, D. J., Jenkins, N. A., Scully, S., Lacey, D. L., Katsuki, M., Asashima, M., & Yokota, T. (2001b). Murine homolog of SALL1 is essential for ureteric bud invasion in kidney development. *Development (Cambridge, England)*, *128*(16), 3105–3115.

137. O'Keefe, L. C. (2016). Middle east respiratory syndrome coronavirus. *Workplace Health and Safety*.

138. O'Toole, J. F., & Sedor, J. R. (2014). Kidney disease: new technologies translate mechanisms to cure. *The Journal of Clinical Investigation*, *124*(6), 2294–2298.

139. Obara-Ishihara, T., Kuhlman, J., Niswander, L., & Herzlinger, D. (1999). The surface ectoderm is essential for nephric duct formation in intermediate mesoderm. *Development (Cambridge, England)*, *126*(6), 1103–1108.

140. Osafune, K., Nishinakamura, R., Komazaki, S., & Asashima, M. (2002). In vitro induction of the pronephric duct in Xenopus explants. *Development, Growth & Differentiation*, *44*(2), 161–167.

141. Osafune, K., Takasato, M., Kispert, A., Asashima, M., & Nishinakamura, R. (2006). Identification of multipotent progenitors in the embryonic mouse kidney by a novel colony-forming assay. *Development (Cambridge, England)*, *133*(1), 151–161.

142. Otto, E. A., Schermer, B., Obara, T., O'Toole, J. F., Hiller, K. S., Mueller, A. M., Ruf, R. G., Hoefele, J., Beekmann, F., Landau, D., Foreman, J. W., Goodship, J. A., Strachan, T., Kispert, A., Wolf, M. T., Gagnadoux, M. F., Nivet, H., Antignac, C., Walz, G., … Hildebrandt, F. (2003). Mutations in INVS encoding inversin cause nephronophthisis type 2, linking renal cystic disease to the function of primary cilia and left-right axis determination. *Nature Genetics*, *34*(4), 413–420.

143. Ou, X., Liu, Y., Lei, X., Li, P., Mi, D., Ren, L., Guo, L., Guo, R., Chen, T., Hu, J., Xiang, Z., Mu, Z., Chen, X., Chen, J., Hu, K., Jin, Q., Wang, J., & Qian, Z. (2020). Characterization of spike glycoprotein of SARS-CoV-2 on virus entry and its immune cross-reactivity with SARS-CoV. *Nature Communications*.

144. Panopoulos, A. D., Yanes, O., Ruiz, S., Kida, Y. S., Diep, D., Tautenhahn, R., Herrerías, A., Batchelder, E. M., Plongthongkum, N., Lutz, M., Berggren, W. T., Zhang, K., Evans, R. M., Siuzdak, G., & Belmonte, J. C. I. (2012). The metabolome of induced pluripotent stem cells reveals metabolic changes occurring in somatic cell reprogramming. *Cell Research*.

145. Park, J.-S., Valerius, M. T., & McMahon, A. P. (2007). Wnt/beta-catenin signaling regulates nephron induction during mouse kidney development. *Development (Cambridge, England)*, *134*(13), 2533–2539.

146. Park, J., Shrestha, R., Qiu, C., Kondo, A., Huang, S., Werth, M., Li, M., Barasch, J., & Suszták, K. (2018). Single-cell transcriptomics of the mouse kidney reveals potential cellular targets of kidney disease. *Science (New York, N.Y.)*, *360*(6390), 758–763.

147. Poladia, D. P., Kish, K., Kutay, B., Hains, D., Kegg, H., Zhao, H., & Bates, C. M. (2006). Role of fibroblast growth factor receptors 1 and 2 in the metanephric mesenchyme. *Developmental Biology*, *291*(2), 325–339.

148. Quaggin, S. E., & Kreidberg, J. A. (2008). Development of the renal glomerulus: good neighbors and good fences. *Development (Cambridge, England)*, *135*(4), 609–620.

149. Rak-Raszewska, A., Hauser, P. V, & Vainio, S. (2015). Organ In Vitro Culture: What Have We Learned about Early Kidney Development? *Stem Cells International*, *2015*, 959807.

150. Reggiani, L., Raciti, D., Airik, R., Kispert, A., & Brändli, A. W. (2007). The prepattern transcription factor Irx3 directs nephron segment identity. *Genes & Development*, *21*(18), 2358–2370.

151. Reiser, J., Kriz, W., Kretzler, M., & Mundel, P. (2000). The glomerular slit diaphragm is a modified adherens junction. *Journal of the American Society of Nephrology : JASN*, *11*(1), 1–8.

152. Rimoin, D. L., Pyeritz, R. E., & Korf, B. (2013). Emery and Rimoin's principles and practice of medical genetics. In *Emery*

and Rimoin's Principles and Practice of Medical Genetics. https://doi.org/9780123838346

153. Rockx, B., Kuiken, T., Herfst, S., Bestebroer, T., Lamers, M. M., Munnink, B. B. O., De Meulder, D., Van Amerongen, G., Van Den Brand, J., Okba, N. M. A., Schipper, D., Van Run, P., Leijten, L., Sikkema, R., Verschoor, E., Verstrepen, B., Bogers, W., Langermans, J., Langermans, J., … Haagmans, B. L. (2020). Comparative pathogenesis of COVID-19, MERS, and SARS in a nonhuman primate model. *Science*.

154. Romagnani, P., & Anders, H. J. (2013). What can tubular progenitor cultures teach us about kidney regeneration? *Kidney International*, *83*(3), 351–353.

155. Romagnani, P., Lasagni, L., & Remuzzi, G. (2013). Renal progenitors: An evolutionary conserved strategy for kidney regeneration. *Nature Reviews Nephrology*, *9*(3), 137–146.

156. Roost, M. S., Van Iperen, L., Ariyurek, Y., Buermans, H. P., Arindrarto, W., Devalla, H. D., Passier, R., Mummery, C. L., Carlotti, F., De Koning, E. J. P., Van Zwet, E. W., Goeman, J. J., & Chuva De Sousa Lopes, S. M. (2015). KeyGenes, a Tool to Probe Tissue Differentiation Using a Human Fetal Transcriptional Atlas. *Stem Cell Reports*, *4*(6), 1112–1124.

157. Roselli, S., Gribouval, O., Boute, N., Sich, M., Benessy, F., Attié, T., Gubler, M.-C., & Antignac, C. (2002). Podocin localizes in the kidney to the slit diaphragm area. *The American Journal of Pathology*, *160*(1), 131–139.

158. Rosselot, C., Spraggon, L., Chia, I., Batourina, E., Riccio, P., Lu, B., Niederreither, K., Dolle, P., Duester, G., Chambon, P., Costantini, F., Gilbert, T., Molotkov, A., & Mendelsohn, C.

(2010). Non-cell-autonomous retinoid signaling is crucial for renal development. *Development*, *137*(2), 283–292.

159. Rothenpieler, U. W., & Dressler, G. R. (1993). Pax-2 is required for mesenchyme-to-epithelium conversion during kidney development. *Development (Cambridge, England)*, *119*(3), 711–720.

160. RUDNICK, D. (1946). Regulation and localization in the hind limb bud of the chick embryo. *The Anatomical Record*.

161. Ruotsalainen, V., Ljungberg, P., Wartiovaara, J., Lenkkeri, U., Kestilä, M., Jalanko, H., Holmberg, C., & Tryggvason, K. (1999). Nephrin is specifically located at the slit diaphragm of glomerular podocytes. *Proceedings of the National Academy of Sciences of the United States of America*, *96*(14), 7962–7967.

162. Ryan, G., Steele-Perkins, V., Morris, J. F., Rauscher, F. J. 3rd, & Dressler, G. R. (1995). Repression of Pax-2 by WT1 during normal kidney development. *Development (Cambridge, England)*, *121*(3), 867–875.

163. SAUNDERS, J. W. J. (1947). An experimental study of the distribution, orientation, and tract specificity of feather germs in the wing of the chick embryo. *The Anatomical Record*, *99*(4), 647.

164. Saxén, L., & Sariola, H. (1987). Early organogenesis of the kidney. *Pediatric Nephrology (Berlin, Germany)*, *1*(3), 385–392.

165. Schedl, A. (2007). Renal abnormalities and their developmental origin. *Nature Reviews. Genetics*, *8*(10), 791–802.

166. Schell, C., Wanner, N., & Huber, T. B. (2014). Glomerular development--shaping the multi-cellular filtration unit. *Seminars in Cell & Developmental Biology*, *36*, 39–49.

167. Schmitt, S. M., Gull, M., & Brändli, A. W. (2014). Engineering Xenopus embryos for phenotypic drug discovery screening. *Advanced Drug Delivery Reviews*, *69–70*, 225–246.

168. Self, M., Lagutin, O. V, Bowling, B., Hendrix, J., Cai, Y., Dressler, G. R., & Oliver, G. (2006). Six2 is required for suppression of nephrogenesis and progenitor renewal in the developing kidney. *The EMBO Journal*, *25*(21), 5214–5228.

169. Serluca, F. C., Drummond, I. A., & Fishman, M. C. (2002). Endothelial signaling in kidney morphogenesis: a role for hemodynamic forces. *Current Biology : CB*, *12*(6), 492–497.

170. Shakya, R., Watanabe, T., & Costantini, F. (2005). The role of GDNF/Ret signaling in ureteric bud cell fate and branching morphogenesis. *Developmental Cell*, *8*(1), 65–74.

171. Shan, J., Jokela, T., Skovorodkin, I., & Vainio, S. (2010). Mapping of the fate of cell lineages generated from cells that express the Wnt4 gene by time-lapse during kidney development. *Differentiation; Research in Biological Diversity*, *79*(1), 57–64.

172. Shankland, S. J., Pippin, J. W., Reiser, J., & Mundel, P. (2007). Podocytes in culture: Past, present, and future. *Kidney International*, *72*(1), 26–36.

173. Sharmin, S., Taguchi, A., Kaku, Y., Yoshimura, Y., Ohmori, T., Sakuma, T., Mukoyama, M., Yamamoto, T., Kurihara, H., & Nishinakamura, R. (2016). Human induced pluripotent stem cell-derived podocytes mature into vascularized glomeruli upon experimental transplantation. *Journal of the American Society of Nephrology*, *27*(6), 1778–1791.

174. Shi, J., Wen, Z., Zhong, G., Yang, H., Wang, C., Huang, B., Liu,

R., He, X., Shuai, L., Sun, Z., Zhao, Y., Liu, P., Liang, L., Cui, P., Wang, J., Zhang, X., Guan, Y., Tan, W., Wu, G., … Bu, Z. (2020). Susceptibility of ferrets, cats, dogs, and other domesticated animals to SARS-coronavirus 2. *Science*.

175. Shih, N. Y., Li, J., Karpitskii, V., Nguyen, A., Dustin, M. L., Kanagawa, O., Miner, J. H., & Shaw, A. S. (1999). Congenital nephrotic syndrome in mice lacking CD2-associated protein. *Science (New York, N.Y.)*, *286*(5438), 312–315.

176. Sison, K., Eremina, V., Baelde, H., Min, W., Hirashima, M., Fantus, I. G., & Quaggin, S. E. (2010). Glomerular structure and function require paracrine, not autocrine, VEGF-VEGFR-2 signaling. *Journal of the American Society of Nephrology : JASN*, *21*(10), 1691–1701.

177. Smith, H. W. (2011). From fish to philosopher; the story of our internal environment. Supplement with collaboration of CIBA Pharmaceutical Products Inc. In *From fish to philosopher; the story of our internal environment. Supplement with collaboration of CIBA Pharmaceutical Products Inc.*

178. Smith, J., Ladi, E., Mayer-Pröschel, M., & Noble, M. (2000). Redox state is a central modulator of the balance between self-renewal and differentiation in a dividing glial precursor cell. *Proceedings of the National Academy of Sciences of the United States of America*.

179. Smith, R. D. (2006). Responding to global infectious disease outbreaks: Lessons from SARS on the role of risk perception, communication and management. *Social Science and Medicine*.

180. Song, B., Smink, A. M., Jones, C. V., Callaghan, J. M., Firth, S. D., Bernard, C. A., Laslett, A. L., Kerr, P. G., & Ricardo, S. D.

(2012). The Directed Differentiation of Human iPS Cells into Kidney Podocytes. *PLoS ONE*, *7*(9), 1–9.

181. Sun, Z., & Hopkins, N. (2001). vhnf1, the MODY5 and familial GCKD-associated gene, regulates regional specification of the zebrafish gut, pronephros, and hindbrain. *Genes & Development*, *15*(23), 3217–3229.

182. Suzuki, T., Itoh, Y., Sakai, Y., Saito, A., Okuzaki, D., Motooka, D., Minami, S., Kobayashi, T., Yamamoto, T., Okamoto, T., & Takayama, K. (2020). Generation of human bronchial organoids for SARS-CoV-2 research. *BioRxiv*, 2020.05.25.115600.

183. Taguchi, A., Kaku, Y., Ohmori, T., Sharmin, S., Ogawa, M., Sasaki, H., & Nishinakamura, R. (2014). Redefining the in vivo origin of metanephric nephron progenitors enables generation of complex kidney structures from pluripotent stem cells. *Cell Stem Cell*, *14*(1), 53–67.

184. Taguchi, A., & Nishinakamura, R. (2017). Higher-Order Kidney Organogenesis from Pluripotent Stem Cells. *Cell Stem Cell*, *21*(6), 730-746.e6.

185. Takasato, M., Er, P. X., Becroft, M., Vanslambrouck, J. M., Stanley, E. G., Elefanty, A. G., & Little, M. H. (2014). Directing human embryonic stem cell differentiation towards a renal lineage generates a self-organizing kidney. *Nature Cell Biology*, *16*(1), 118–126.

186. Takasato, Minoru, Er, P. X., Chiu, H. S., Maier, B., Baillie, G. J., Ferguson, C., Parton, R. G., Wolvetang, E. J., Roost, M. S., Chuva de Sousa Lopes, S. M., & Little, M. H. (2015). Kidney organoids from human iPS cells contain multiple lineages and model human nephrogenesis. *Nature*, *526*(7574), 564–568.

https://doi.org/0028-0836

187. Takasato, Minoru, Er, P. X., Chiu, H. S., Maier, B., Baillie, G. J., Ferguson, C., Parton, R. G., Wolvetang, E. J., Roost, M. S., De Sousa Lopes, S. M. C., & Little, M. H. (2015). Kidney organoids from human iPS cells contain multiple lineages and model human nephrogenesis. *Nature*, *526*(7574), 564–568.

188. Takasato, Minoru, & Little, M. H. (2015). The origin of the mammalian kidney: Implications for recreating the kidney in vitro. *Development (Cambridge)*, *142*(11), 1937–1947.

189. Tanigawa, S., Islam, M., Sharmin, S., Naganuma, H., Yoshimura, Y., Haque, F., Era, T., Nakazato, H., Nakanishi, K., Sakuma, T., Yamamoto, T., Kurihara, H., Taguchi, A., & Nishinakamura, R. (2018). Organoids from Nephrotic Disease-Derived iPSCs Identify Impaired NEPHRIN Localization and Slit Diaphragm Formation in Kidney Podocytes. *Stem Cell Reports*, *11*(3), 727–740.

190. Tikellis, C., & Thomas, M. C. (2012). Angiotensin-converting enzyme 2 (ACE2) is a key modulator of the renin angiotensin system in health and disease. In *International Journal of Peptides*.

191. Tomlinson, M. L., Hendry, A. E., & Wheeler, G. N. (2012). Chemical genetics and drug discovery in Xenopus. *Methods in Molecular Biology (Clifton, N.J.)*, *917*, 155–166.

192. Torres, M., Gómez-Pardo, E., Dressler, G. R., & Gruss, P. (1995). Pax-2 controls multiple steps of urogenital development. *Development (Cambridge, England)*, *121*(12), 4057–4065.

193. Tsang, T. E., Shawlot, W., Kinder, S. J., Kobayashi, A., Kwan, K. M., Schughart, K., Kania, A., Jessell, T. M., Behringer, R. R.,

& Tam, P. P. (2000). Lim1 activity is required for intermediate mesoderm differentiation in the mouse embryo. *Developmental Biology*, *223*(1), 77–90.

194. Unbekandt, M., & Davies, J. A. (2010). Dissociation of embryonic kidneys followed by reaggregation allows the formation of renal tissues. *Kidney International*, *77*(5), 407–416.

195. van den Berg, C. W., Ritsma, L., Avramut, M. C., Wiersma, L. E., van den Berg, B. M., Leuning, D. G., Lievers, E., Koning, M., Vanslambrouck, J. M., Koster, A. J., Howden, S. E., Takasato, M., Little, M. H., & Rabelink, T. J. (2018). Renal Subcapsular Transplantation of PSC-Derived Kidney Organoids Induces Neo-vasculogenesis and Significant Glomerular and Tubular Maturation In Vivo. *Stem Cell Reports*, *10*(3), 751–765.

196. van Doremalen, N., Lambe, T., Spencer, A., Belij-Rammerstorfer, S., Purushotham, J., Port, J., Avanzato, V., Bushmaker, T., Flaxman, A., Ulaszewska, M., Feldmann, F., Allen, E., Sharpe, H., Schulz, J., Holbrook, M., Okumura, A., Meade-White, K., Pérez-Pérez, L., Bissett, C., … Munster, V. (2020). ChAdOx1 nCoV-19 vaccination prevents SARS-CoV-2 pneumonia in rhesus macaques. *BioRxiv : The Preprint Server for Biology*.

197. Varga, Z., Flammer, A. J., Steiger, P., Haberecker, M., Andermatt, R., Zinkernagel, A. S., Mehra, M. R., Schuepbach, R. A., Ruschitzka, F., & Moch, H. (2020). Endothelial cell infection and endotheliitis in COVID-19. In *Lancet (London, England)* (Vol. 395, Issue 10234, pp. 1417–1418).

198. Vize, P. D., Jones, E. A., & Pfister, R. (1995). Development of the Xenopus pronephric system. *Developmental Biology*, *171*(2),

531–540.

199. Vize, P. D., Seufert, D. W., Carroll, T. J., & Wallingford, J. B. (1997). Model systems for the study of kidney development: use of the pronephros in the analysis of organ induction and patterning. *Developmental Biology*, *188*(2), 189–204.

200. Voronkov, A., & Krauss, S. (2013). Wnt/beta-catenin signaling and small molecule inhibitors. *Current Pharmaceutical Design*, *19*(4), 634–664.

201. Walls, A. C., Park, Y. J., Tortorici, M. A., Wall, A., McGuire, A. T., & Veesler, D. (2020). Structure, Function, and Antigenicity of the SARS-CoV-2 Spike Glycoprotein. *Cell*.

202. Wan, Y., Shang, J., Graham, R., Baric, R. S., & Li, F. (2020). Receptor Recognition by the Novel Coronavirus from Wuhan: an Analysis Based on Decade-Long Structural Studies of SARS Coronavirus. *Journal of Virology*.

203. Wanet, A., Arnould, T., Najimi, M., & Renard, P. (2015). Connecting Mitochondria, Metabolism, and Stem Cell Fate. *Stem Cells and Development*.

204. Weiss, P., & Taylor, A. C. (1960). RECONSTITUTION OF COMPLETE ORGANS FROM SINGLE-CELL SUSPENSIONS OF CHICK EMBRYOS IN ADVANCED STAGES OF DIFFERENTIATION. *Proceedings of the National Academy of Sciences of the United States of America*, *46*(9), 1177–1185.

205. Wellik, D. M., Hawkes, P. J., & Capecchi, M. R. (2002). Hox11 paralogous genes are essential for metanephric kidney induction. *Genes & Development*, *16*(11), 1423–1432.

206. Wessely, O., & Tran, U. (2011). Xenopus pronephros

development-past, present, and future. *Pediatric Nephrology*.

207. Williamson, B. N., Feldmann, F., Schwarz, B., Meade-White, K., Porter, D. P., Schulz, J., van Doremalen, N., Leighton, I., Yinda, C. K., Pérez-Pérez, L., Okumura, A., Lovaglio, J., Hanley, P. W., Saturday, G., Bosio, C. M., Anzick, S., Barbian, K., Cihlar, T., Martens, C., … de Wit, E. (2020). Clinical benefit of remdesivir in rhesus macaques infected with SARS-CoV-2. *Nature*.

208. Wouters, O. J., O'Donoghue, D. J., Ritchie, J., Kanavos, P. G., & Narva, A. S. (2015). Early chronic kidney disease: diagnosis, management and models of care. *Nature Reviews. Nephrology*, *11*(8), 491–502.

209. Wrapp, D., Wang, N., Corbett, K. S., Goldsmith, J. A., Hsieh, C. L., Abiona, O., Graham, B. S., & McLellan, J. S. (2020). Cryo-EM structure of the 2019-nCoV spike in the prefusion conformation. *Science*.

210. Xia, Y., Nivet, E., Sancho-Martinez, I., Gallegos, T., Suzuki, K., Okamura, D., Wu, M.-Z., Dubova, I., Esteban, C. R., Montserrat, N., Campistol, J. M., & Belmonte, J. C. I. (2013). Directed differentiation of human pluripotent cells to ureteric bud kidney progenitor-like cells. *Nature Cell Biology*, *15*(12), 1507–1515. https://doi.org/1476-4679 (Electronic)r1465-7392 (Linking)

211. Xu, P.-X., Zheng, W., Huang, L., Maire, P., Laclef, C., & Silvius, D. (2003). Six1 is required for the early organogenesis of mammalian kidney. *Development (Cambridge, England)*, *130*(14), 3085–3094.

212. Xu, P. X., Adams, J., Peters, H., Brown, M. C., Heaney, S., & Maas, R. (1999). Eya1-deficient mice lack ears and kidneys and show abnormal apoptosis of organ primordia. *Nature Genetics*,

23(1), 113–117.

213. Yanes, O., Clark, J., Wong, D. M., Patti, G. J., Sánchez-Ruiz, A., Benton, H. P., Trauger, S. A., Desponts, C., Ding, S., & Siuzdak, G. (2010). Metabolic oxidation regulates embryonic stem cell differentiation. *Nature Chemical Biology*.

214. Ye, S., Tan, L., Yang, R., Fang, B., Qu, S., Schulze, E. N., Song, H., Ying, Q., & Li, P. (2012). Pleiotropy of glycogen synthase kinase-3 inhibition by CHIR99021 promotes self-renewal of embryonic stem cells from refractory mouse strains. *PloS One*, *7*(4), e35892.

215. Yoshimura, Y., Taguchi, A., Tanigawa, S., Yatsuda, J., Kamba, T., Takahashi, S., Kurihara, H., Mukoyama, M., & Nishinakamura, R. (2019). Manipulation of nephron-patterning signals enables selective induction of podocytes from human pluripotent stem cells. *Journal of the American Society of Nephrology*, *30*(2), 304–321.

216. Yu, J., Tostanosk, L. H., Peter, L., Mercad, N. B., McMahan, K., Mahrokhia, S. H., Nkolol, J. P., Liu, J., Li, Z., Chandrashekar, A., Martine, D. R., Loos, C., Atyeo, C., Fischinger, S., Burk, J. S., Slei, M. D., Chen, Y., Zuiani, A., Lelis, F. J. N., … Barou, D. H. (2020). DNA vaccine protection against SARS-CoV-2 in rhesus macaques. *Science*.

217. Zeisberg, M., & Kalluri, R. (2015). Physiology of the Renal Interstitium. *Clinical Journal of the American Society of Nephrology : CJASN*, *10*(10), 1831–1840.

218. Zhang, H., Penninger, J. M., Li, Y., Zhong, N., & Slutsky, A. S. (2020). Angiotensin-converting enzyme 2 (ACE2) as a SARS-CoV-2 receptor: molecular mechanisms and potential

therapeutic target. *Intensive Care Medicine*, *46*(4), 586–590.

219. Zhao, B., Ni, C., Gao, R., Wang, Y., Yang, L., Wei, J., Lv, T., Liang, J., Zhang, Q., Xu, W., Xie, Y., Wang, X., Yuan, Z., Liang, J., Zhang, R., & Lin, X. (2020). Recapitulation of SARS-CoV-2 infection and cholangiocyte damage with human liver ductal organoids. In *Protein & cell* (Vol. 11, Issue 10, pp. 771–775).

220. Zhao, Y., Zhao, Z., Wang, Y., Zhou, Y., Ma, Y., & Zuo, W. (2020). Single-cell RNA expression profiling of ACE2, the putative receptor of Wuhan 2019-nCov. In *bioRxiv*.

221. Zheng, Y.-Y., Ma, Y.-T., Zhang, J.-Y., & Xie, X. (2020). COVID-19 and the cardiovascular system. *Nature Reviews. Cardiology*, *17*(5), 259–260.

222. Zhou, J., Li, C., Liu, X., Chiu, M. C., Zhao, X., Wang, D., Wei, Y., Lee, A., Zhang, A. J., Chu, H., Cai, J.-P., Yip, C. C.-Y., Chan, I. H.-Y., Wong, K. K.-Y., Tsang, O. T.-Y., Chan, K.-H., Chan, J. F.-W., To, K. K.-W., Chen, H., & Yuen, K. Y. (2020a). Infection of bat and human intestinal organoids by SARS-CoV-2. *Nature Medicine*, *26*(7), 1077–1083.

223. Zhou, J., Li, C., Liu, X., Chiu, M. C., Zhao, X., Wang, D., Wei, Y., Lee, A., Zhang, A. J., Chu, H., Cai, J. P., Yip, C. C. Y., Chan, I. H. Y., Wong, K. K. Y., Tsang, O. T. Y., Chan, K. H., Chan, J. F. W., To, K. K. W., Chen, H., & Yuen, K. Y. (2020b). Infection of bat and human intestinal organoids by SARS-CoV-2. *Nature Medicine*.

224. Zhou, P., Yang, X. Lou, Wang, X. G., Hu, B., Zhang, L., Zhang, W., Si, H. R., Zhu, Y., Li, B., Huang, C. L., Chen, H. D., Chen, J., Luo, Y., Guo, H., Jiang, R. Di, Liu, M. Q., Chen, Y., Shen, X. R., Wang, X., … Shi, Z. L. (2020). A pneumonia outbreak

associated with a new coronavirus of probable bat origin. *Nature*.

225. Zhou, Z., Zhao, N., Shu, Y., Han, S., Chen, B., & Shu, X. (2020). Effect of Gastrointestinal Symptoms in Patients With COVID-19. *Gastroenterology*, *158*(8), 2294–2297.

226. Zhu, N., Zhang, D., Wang, W., Li, X., Yang, B., Song, J., Zhao, X., Huang, B., Shi, W., Lu, R., Niu, P., Zhan, F., Ma, X., Wang, D., Xu, W., Wu, G., Gao, G. F., & Tan, W. (2020). A Novel Coronavirus from Patients with Pneumonia in China, 2019. *New England Journal of Medicine*.

227. Zoccali, C., Arici, M., Blankestijn, P. J., Bruchfeld, A., Capasso, G., Fliser, D., Fouque, D., Goumenos, D., Ketteler, M., Malyszko, J., Massy, Z., Rychlík, I., & Spasovski, G. (2018). The ERA-EDTA today and tomorrow: A progress document by the ERA-EDTA Council. *Nephrology Dialysis Transplantation*.

VII. ANNEXES

VII. ANNEXES

Co-authored reviews

Garreta E, Oria R, Tarantino C, Pla-Roca M, Prado P, Fernández-Avilés F, Campistol JM, Samitier J, Montserrat N. **Tissue engineering by decellularization and 3D bioprinting.** Materials Today. 2017, 20(4):166–178.

Marco A, Hurtado Del Pozo, C, Prado P, Garreta E, Montserrat N. **Understanding kidney development and disease through the generation of kidney organoids and CRISPR/Cas9 engineering**. Biology of the Cell *(under revision).*

Co-authored book chapter

Garreta E, Prado P, Izpisua Belmonte JC, Montserrat N. Non-coding microRNAs for cardiac regeneration: **Exploring novel alternatives to induce heart healing. Non-coding RNA** Research. 2017.

Awards

Best poster prize at **Summer School 2016 - Regenerative Nano-Medicine: From Advanced Delivery Systems to Electronic-Based Devices** (Tel Aviv University, Israel)

Best poster prize at **9th IBEC Symposium "Bioengineering for active aging"** (Barcelona)

International research mobility

Granted with **Severo Ochoa Triple-I mobility programme** for performing a three-month stay at Dr. Jamie Davies research group at the University of Edinburgh.

Dr Jamie Davies' group has been pioneering in the establishment of dissagregation-reaggregation methods to allow the reconstruction of mouse kidney rudiments. This stay was a unique opportunity to combine their knowledge with our experiment in the derivation of hPSCs-derived kidney organoids and their implantation onto the chick CAM. We could assess the kidney identity of hPSCs-derived NPCs co-culturing them with mouse embryonic UB rudiments. Overall, this stay was so valuable for learning knew techniques and to exchange complementary methodologies between the two groups.

Institutional and outreach activities

Member of the IBEC PhD Committee for 1 year and participation in several institutional activities

Participation in the organization of the 1st IBEC PhD Symposium, held in Barcelona, Spain, in October 2018.

Participation in two editions of "Bojos i Bojes per la Bioenginyeria" organized by Fundación de Catalunya la Pedrera.

Media attention

Paper I and Paper III received important media attention. Some examples of the headlines.

Investigadores del IBEC generan minirriñones vascularizados a partir de células madre humanas

⊘ febrero 18, 2019   ▣ Noticias de investigación
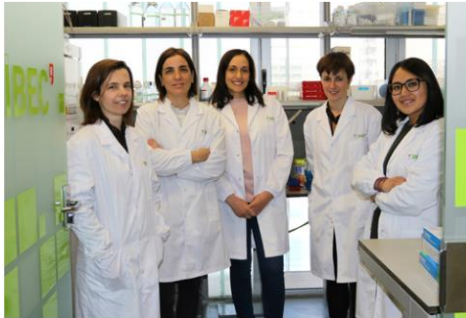
Investigadores del IBEC han creado por primera vez cultivos tridimensionales -organoides- a partir de células madre pluripotentes, que se asemejan a tejido embrionario de riñón humano durante el segundo trimestre de gestación.

Mediante el uso de biomateriales que mimetizan el microambiente embrionario los investigadores también han logrado que estos minirriñones presenten características relevantes para su uso inmediato en el modelado de patologías renales. En un estudio publicado ayer en la revista Nature Materials se describe cómo investigadores del IBEC han generado organoides, o miniórganos, que se asemejan al riñón embrionario humano

durante el segundo trimestre

IBEC researchers generate mini-kidneys vascularized from stem cells

18.02.2019

Researchers from the Institute for Bioengineering of Catalonia (IBEC) at the Barcelona science park, have created, for the first time, 3D organoid cultures from pluripotent stem cells, which resemble human embryonic kidney tissue during the second trimester of pregnancy. Using biomaterials that mimic the embryonic microenvironment, scientifics have also achieved mini-kidneys with relevant features for immediate use in renal disease modeling.
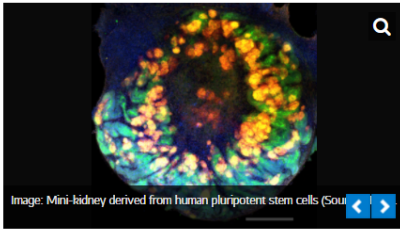
Image: Mini-kidney derived from human pluripotent stem cells (Sou...

A study published today in Nature Materials reports how researchers from IBEC have created organoids, or mini-organs, that resemble the human embryonic kidney, and how these 3D cultures mimic essential aspects during the formation of the kidney, such as distribution, functionality and specific organization of cells.

The research, led by Dr. Núria Montserrat, ICREA principal investigator at IBEC, with the collaboration of the Hospital Clinic in Barcelona, the Spanish National Research Council, the University of Barcelona and the Salk Institute for Biological Studies in the United States, generates fundamental knowledge about how this organ develops and, in turn, facilitates the design of experiments focused on narrowing down therapeutic compounds for renal regeneration.

To carry out this process, researchers have used pluripotent stem cells, with which they have been able to recapitulate the embryonic development of the kidney – until the second trimester of pregnancy – and have created mini-kidneys by simulating the features of the embryonic microenvironment with the use of biomaterials.

"Minirriñones" creados en el IBEC contribuyen a identificar un fármaco en fase clínica que bloquea los efectos del SARS-Co-V2
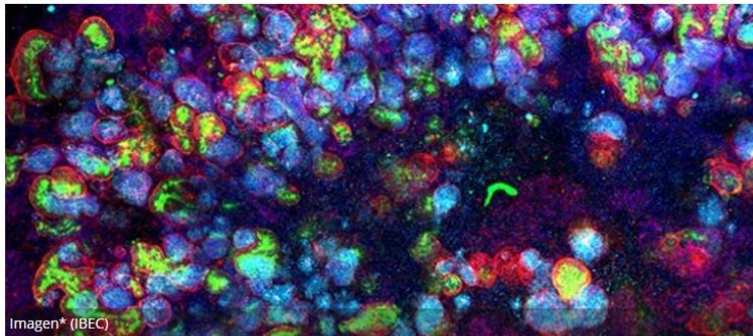
Imagen* (IBEC)

IBEC | viernes, 3 de abril de 2020

Tissue engineering by decellularization and 3D bioprinting

Elena Garreta[1], Roger Oria[2], Carolina Tarantino[1], Mateu Pla-Roca[3], Patricia Prado[1], Francisco Fernández-Avilés[4], Josep Maria Campistol[5], Josep Samitier[6,7,8] and Nuria Montserrat[1,8,*]

[1] Pluripotent Stem Cells and Activation of Endogenous Tissue Programs for Organ Regeneration, Institute for Bioengineering of Catalonia (IBEC), c/ Baldiri Reixac 15-21, 08028 Barcelona, Spain
[2] Institute for Bioengineering of Catalonia (IBEC), c/ Baldiri Reixac 15-21, 08028 Barcelona, Spain; University of Barcelona, Spain
[3] Nanotechnology Platform, Institute for Bioengineering of Catalonia (IBEC), c/ Baldiri Reixac 15-21, 08028 Barcelona, Spain
[4] Department of Cardiology, Hospital General Universitario Gregorio Marañón, Instituto de Investigación Sanitaria Gregorio Marañón, Universidad Complutense-Facultad de Medicina, c/ Dr Esquerdo 46, 28007 Madrid, Spain
[5] Hospital Clinic, University of Barcelona, IDIBAPS, 08036 Barcelona, Spain
[6] Nanobioengineering Group, Institute for Bioengineering of Catalonia (IBEC), c/ Baldiri Reixac 15-21, 08028 Barcelona, Spain
[7] Department of Engineering: Electronics, University of Barcelona, 08028 Barcelona, Spain
[8] Networking Biomedical Research Center in Bioengineering, Biomaterials and Nanomedicine (CIBER-BBN), Madrid, Spain

Discarded human donor organs have been shown to provide decellularized extracellular matrix (dECM) scaffolds suitable for organ engineering. The quest for appropriate cell sources to satisfy the need of multiple cells types in order to fully repopulate human organ-derived dECM scaffolds has opened new venues for the use of human pluripotent stem cells (hPSCs) for recellularization. In addition, three-dimensional (3D) bioprinting techniques are advancing towards the fabrication of biomimetic cell-laden biomaterial constructs. Here, we review recent progress in decellularization/recellularization and 3D bioprinting technologies, aiming to fabricate autologous tissue grafts and organs with an impact in regenerative medicine.

Introduction

Regenerative medicine holds the promise to replace or regenerate human cells, tissue or organs in order to restore or establish the normal function lost due to disease or damage [1]. By the combination of novel biomaterials with cells, one of the aims of regenerative medicine is to create autologous tissue grafts for future replacement therapies [2,3]. In the last three years, discarded human donor organs, such as kidney [4,5], lung [6], heart [7], and liver [8], have been used to obtain decellularized extracellular matrix (dECM) scaffolds, proving their potential application in tissue engineering. Despite the translational value of these advances, we are still far to generate relevant tissues for immediate clinical applications.

The use of organ-derived dECM scaffolds for bioengineering of human-scale patient-specific organs using hPSCs is envisioned as a major platform for therapeutic applications (reviewed in [9]). Interestingly, the concept of organ printing has lately taken center stage due to recent three-dimensional (3D) bioprinting advancements (reviewed in [10–13]). Current 3D bioprinting techniques have shown to simultaneously deposit combinations of different cell types encapsulated within biomimetic hydrogels via a layer-by-layer process, leading to the generation of 3D bioinspired tissue constructs (reviewed in [10,12,14,15]) [16–20]. Such approach could offer new venues when translating hPSCs-related technologies to a high-throughput 3D setup (e.g., patient induced pluripotent stem cells (iPSCs)-derived organoid screening platforms) (reviewed in [21]).

*Corresponding author:. Montserrat, N. (nmontserrat@ibecbarcelona.eu)

So far, different laboratories have shown that it is possible to build up tissue- and organ-like structures either by the use of organ-derived dECM scaffolds (reviewed in [22–27]) or 3D bio-printing techniques (reviewed in [10,12,14,15]) [16–20]. However, the bioengineering of vascularized human-scale organ analogues with optimal functional activity still requires much effort from multidisciplinary research groups before this can become a reality.

Here, we review the latest advancements in the application of decellularization/recellularization technology for the generation of autologous tissue grafts taking advantage of hPSCs. We also examine how 3D bioprinting technologies may benefit from hPSCs derivatives to fabricate human organ analogues.

The advent of decellularization technology
Tissue-specific extracellular matrix (ECM) through decellularization of tissues and organs

Pioneer findings on the production of tissue-specific ECM were first reported in the 1970s and 1980s [28,29]. Despite these major steps, it was not until 10 years later that Badylak and coworkers generated intact acellular small intestinal submucosa matrices by mechanically removing all mesenteric tissues while leaving the trilaminate connective tissue layers intact [30]. Indeed, such matrices demonstrated healing capacity in a dog model for Achille's tendon repair [30]. Soon, different works on decellularization of other simple tissues such as skin [31], vascular tissue [32], heart valves [33] and bladder [34] showed promising results on the generation of biological scaffolds for biomedical applications, representing a realistic alternative to the use of synthetic biomaterial scaffolds. From that moment, further works began to apply decellularization methodologies for the fabrication of dECM slices from complex organs such as liver [35].

In 2008, the seminal work by Ott and coworkers, who successfully generated whole rat acellular hearts by means of perfusion decellularization, represented a breakthrough in the field of tissue engineering and the beginning of the era of whole organ decellularization technology [36]. Over the last years, different research groups following similar approaches have reported the possibility to derive full-scale dECM scaffolds from different organs including liver, heart, lungs, and kidneys; and multiple species including mouse, rat, pig, rhesus monkey, and human (reviewed in [22,23]) [37]. The main milestones on decellularization technology are summarized in Fig. 1.

In vivo the composition and ultrastructure of ECM is in constant remodeling by the resident cells depending on the metabolic and mechanical demands of the tissue, a concept called 'dynamic reciprocity' [38]. Such dynamic remodeling may be altered during injury or disease, leading to modifications in the composition and biophysical properties of the ECM, and ultimately, compromising organ function. Accordingly, it has been suggested that 'organ specificity', may determine why cells belonging to a specific organ exhibit an innate preference towards dECM scaffolds derived from the organ of origin [39,40]. Along this line, Nakayama and co-workers showed that human embryonic stem cells (hESCs) differentiated into renal-like cells when seeded onto rhesus monkey kidney dECM, but this was not the case when lung dECM was used instead [40]. The main hypothesis supporting such findings relies on the idea that specific ECM proteins are distinctively distributed along the different compartments of the organ as footprints from
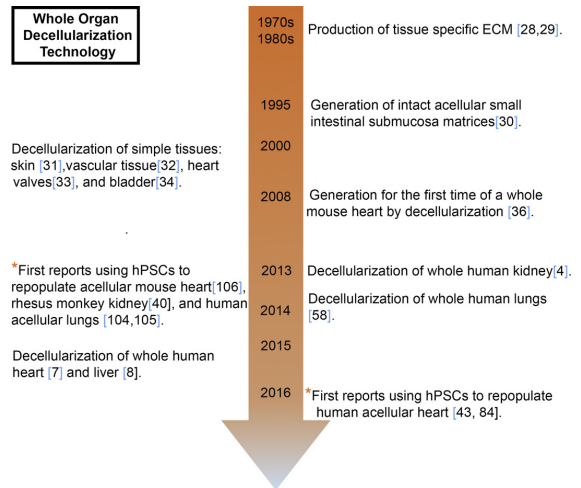

FIGURE 1

Timeline of key events leading to whole organ decellularization methodologies and major milestones using hPSC-derived cells to repopulate organ-derived dECM scaffolds (*).

resident cells. Interestingly, site-specific ECM micromechanical properties have been described to delimitate different tissue regions [41].

Overall, dECM scaffolds provide a complex site-specific combination of biochemical and mechanical cues, which have been hypothesized to guide cell adhesion, proliferation and differentiation during recellularization and further tissue formation (reviewed in [42]) [39–41,43–45]. The main advantages using dECM scaffolds for the de novo biofabrication of tissues and organs are summarized in Box 1.

Methods of decellularization

Decellularization techniques aim to remove all the cells from a tissue or organ while preserving the native ECM composition and architecture integrity. As such, tissue and organ decellularization, can lead to the production of 3D dECM scaffolds retaining their biological activity and mechanical properties. If effective, dECM scaffolds should not elicit immune-mediated rejection after im-

---

BOX 1
Potential of dECM scaffolds to recapitulate tissues and organs

• Preservation of dECM ultrastructure and composition induce favorable tissue organization and remodeling (reviewed in [23,24,36]).
• dECM can modulate cell behavior: attachment, migration and differentiation (reviewed in [23,24,36]) [39,40,43,44].
• dECM do not elicit immune-mediated rejection, since ECM components are largely and highly conserved across species [46,47].
• dECM exhibit suitable mechanical performance, similar to that of their native counterparts (reviewed in [23,24,36]) [41].
• dECM promote constructive remodeling response, as shown for a variety of tissues in both pre-clinical and clinical studies (reviewed in [42]) [45].
• The potential advantage of dECM organ specificity ensures the maintenance of selected cell functions and phenotypes (reviewed in [38]) [39].

RESEARCH: Review

plantation [46,47]. Extensive research has shown the mode of action and peculiarities of each kind of decellularization agents employed, as widely discussed elsewhere (reviewed in [48–50]). In general, the optimal decellularization protocol will generate a DNA-free dECM scaffold by finding the right compromise between the duration and complexity of the treatment and the conservation of the desired compositional, structural and mechanical properties of the generated dECM construct.

With respect to the techniques used to infuse the decellularization agents within all regions of the organ, perfusion through the vasculature and immersion/agitation are nowadays the most employed, though others techniques have been also described (e.g., pressure gradient [51,52], supercritical fluid [53]). Perfusion decellularization takes advantage of the innate vasculature of the organ to deliver the decellularization agents across the entire organ. Such approach is often performed in organs in which its main artery can be cannulated for perfusion with decellularization solutions under physiologic perfusion pressures. In their seminal work, Ott and coworkers developed a protocol for whole rat heart decellularization using a homemade bioreactor to perfuse 1% sodium dodecyl sulfate (SDS) through the coronary vasculature, showing that 12 hours perfusion at a physiological pressure sufficed to yield a fully decellularized rat heart [36]. The same research group subsequently applied a similar approach to decellularize whole rat lungs [54] and kidneys [55]. For lung decellularization, both the airway and vascular compartments were investigated to deliver the decellularization solutions, rendering in all cases acellular organ scaffolds with preserved ECM composition, microstructure and 3D architecture [54,56–59]. Overall, perfusion decellularization is the preferred technique to decellularize whole organs, especially in large animals or humans [4–8,58,60–63].

On another hand, in immersion-based decellularization protocols, the tissue or organ of interest is submerged into the decellularization solutions while being subjected to agitation. In this way, decellularization agents enter through the tissue by diffusion.

The duration of the protocol will then depend on the initial tissue thickness and cell density. Such approach is mainly used on tissue samples that do not have easy access to the vascular network (e.g., skeletal muscle, skin) [64–66], as well as on organ slices typically obtained from a segmental resection. Box 2 summarizes the advantages and disadvantages of the different methods of decellularization discussed in this review.

Due to the large diversity of decellularization protocols and tissue sources reported so far, there has been the necessity to establish common criteria to evaluate the effectiveness of any decellularization process. Decellularization requirements and associated methodologies are summarized in Box 3.

Although successful decellularization was achieved for many organs, still much effort should be directed on the definition of standardized decellularization protocols with the final goal to advance in the creation of biocompatible and personalized organ scaffolds for clinical applications. For that, issues including biodegradation, cytocompatibility, pathogenicity and immunogenicity should also be further studied (reviewed in [67]).

Recellularization of whole organ dECM scaffolds

One of the major issues in the field of organ bioengineering is the precise positioning of specific cell types inside their corresponding specific organ compartment. Methods of cell seeding into whole organ-derived dECM scaffolds will largely depend on the organ itself and usually will require the use of bioreactors. Complex organs including kidney, heart, lung, and liver entail the development of challenging cell seeding and culture methods to promote tissue formation and maturation. Oxygen diffusion across an engineered tissue is limited to a maximum tissue thickness of 200 micrometers (reviewed in [68]), meaning that higher tissue thicknesses must require functional vasculature to supply the cells with oxygen and nutrients as well as facilitate the removal of metabolic waste products. In this regard, bioreactor technology for whole organ engineering still needs to overcome many issues:

BOX 2
Methods of decellularization

	Perfusion	Immersion/agitation
Mode of action	• Infusion of the decellularization agents through the organ vasculature • Preferred when decellularizing large animal or human organs	• Immersion of the tissue or organ into the decellularization solutions while shaking • Used when the access to the vasculature is difficult or absent
Advantages	• Facilitates homogeneous exposure to the decellularization reagents and removal of cellular content • The possibility to apply physiological perfusion pressures would favor preservation of tissue ECM composition and architecture • Controlled perfusion conditions by the use of bioreactors enhances the robustness and efficiency of the process	• Mechanical agitation facilitates cellular content removal • Easy and fast procedure when decellularizing small animal organs or tissues, and human tissues obtained from segmental resections • Does not need overly specific bioreactor equipment
Disadvantages	• Unappropriate perfusion pressures can disrupt ECM and impact on the viscoelastic behavior of the dECM scaffold. Optimization is required for each tissue/organ • Needs cannulation of the main organ artery • This method usually needs the use of specific perfusion bioreactors	• Decellularization conditions (e.g., agitation, reagents' exposure time) have to be optimized depending on the tissue thickness. Excessive agitation can disrupt ECM • It is an unreliable method when decellularizing large animal or human whole organs • This method usually needs increasing times of exposure to the decellularization agents when compared to perfusion
References	[4–8,54,56–63]	[39,64–66]

BOX 3

Established criteria for effective decellularization

Requirement	Methodology	Outcome for effective decellularization	References
Removal of cells and DNA content	● Decellularized tissues should accomplish (i) <50 ng of double-stranded DNA (dsDNA) per mg of dry weight dECM, as quantified by commercially available dsDNA intercalators such as PicoGreen and gel electrophoresis (ii) <200 bp DNA fragment length, analyzed by gel electrophoresis ● Histological stainings (Hematoxylin and Eosin, Masson's Trichome, Movat's Pentachrome, or Safrin O) or immunohistochemistry analysis in dECM should denote the lack of visible nuclei (as stained DAPI or Hoechst). These can be used to qualitatively detect if nuclei content, cytoplasmic proteins or some extracellular components are still present after decellularization	● Avoid adverse cell and host response as well as negative tissue remodeling and inflammation responses after implantation	[34] (reviewed in [48])
Quantification of residual detergents	● Quantification of remnant SDS can be determined using Stains-All reagent ● Similarly residual Triton X-100 can be quantified by using derivative spectrophotometry. ● Undetectable amounts of such components are desired	● Avoid toxic effects form these decellularization agents, ensuring cell viability during dECM scaffold recellularization.	[67]
Preservation of ECM components	● Qualitative evaluation by immunohistochemistry analysis of the main ECM proteins including collagens, laminin, fibronectin and elastin ● Quantitative colorimetric assays are employed to determine the amount of collagen, elastin and glycosaminoglycans using commercially available Sircol, Fastin and Blyscan kits, respectively ● Mass spectrometry-based proteomics allows precise identification of matrisome proteins and other tissue-specific proteins	● Retention of the main basement membrane components and structural ECM proteins as compared to their native counterparts	[8,43,56,84]
Maintenance of 3D architecture and vascular integrity	● Micro- and nano-architecture of relevant parenchymal structures of each organ can be assessed by scanning electron microscopy (SEM) ● Conservation of the hierarchical vascular bed of the organ after decellularization can be evaluated by MicroCT, dye or microbeads perfusion assays, angiography or corrosion casting	● Conservation of the main structural features specific of each organ, which will facilitate tissue organization and maintenance of specific cell phenotypes ● Conservation of the hierarchical vascular bed of the organ, which is essential to further achieve an effective recellularization outcome	[4,5] (reviewed in [22,36])
Biomechanical performance	● Traditional material science and engineering techniques including uni- or bi-axial mechanical testing and atomic force microscopy (AFM) have been mainly used for mechanical testing on produced decellularized scaffolds ● Lung mechanics has been assessed using pressure-volume curves and measuring force tension relationships in linear strips of decellularized lungs	● Optimal dECM scaffold mechanical properties (mechanical strength and viscoelastic behavior), that following recellularization should be similar to those of their native counterparts	[4,41,56,63]

BOX 4

Bioreactor requirements for recellulatization of whole organ dECM scaffolds

- Include independent access lines for cell seeding through vascular and non-vascular routes
- Integrate pressure transducers to control flow/volume-based pressure
- Allow continuous or pulsatile perfusion through the vasculature to provide nutrients while removing metabolic waste products
- Monitoring and maintenance of physiological vascular pressure
- Monitoring and maintenance of proper gases supply
- Monitoring organ mechanics during repopulation
- Can include organ-specific biophysical stimuli (e.g. provide mechanical ventilation in lung, provide mechanical stretch and electrical stimulation in heart)
- Allow non-invasive or minimally invasive monitoring of relevant biochemical and biophysical markers indicative of organ maturation and function
- Allow automation of critical parameters
- Maintain sterility (disposable or easily sterilized components)
- Good manufacturing practices (GMP) amenable/Clinical grade bioreactors

from the definition of optimal cell seeding methodologies to the possibility to monitor biochemical and biophysical markers indicative of organ maturation and function in a non-invasive manner. Other issues are related to the application of physiological relevant stimuli that can enhance tissue formation and functionality. The principle bioreactor requirements for whole organ culture are listed in Box 4. Extensive discussion on recent bioreactor developments is reported elsewhere (reviewed in [69] [70–77].

Vascular and non-vascular routes have been employed to deliver cells into whole organ-derived dECM scaffolds, mostly following dynamic seeding procedures, which consist of introducing cells at a specific concentration into the vascular perfusion line. Following this methodology, researchers have recellularized the vasculature and parenchyma of liver, heart, lung and kidney (reviewed in [22–27]). Cells introduced into the vascular flow may traverse the vascular lining through pores produced during decellularization, then reaching the organ parenchyma. In this regard, it has been proposed that the proper adjustment of flow rates may reduce shear stress on cells, while minimizing the potential damage on the dECM scaffold. Moreover, multiple inoculations of cells are preferable than a unique one with the same total cell number. Performing multiple cell infusions directly into the liver vascular circuit in a step-wise manner led to more than 85% cell engraftment [77–79], also showing a more efficient distribution of cells across all regions of the organ-derived dECM scaffold. Alternatively, direct injection of cells with a small gauge needle by performing multiple injections throughout different areas of organ parenchyma has shown less success [80]. Other non-vascular routes commonly used to reintroduce cells are the trachea in lungs [54,56–59] or the ureter in kidney [55,81–83].

So far, the large body of work regarding recellularization of whole organ dECM scaffolds has been performed in small animal models using different bioreactor settings, cell types and seeding conditions (reviewed in [22–27]). The main problems encountered during recellularization were the uncomplete re-endothelization of the organ vasculature, and the insufficient repopulation of the organ parenchyma [55,56,60]. Notably, recently this year, Guyette and coworkers have partially repopulated whole decellularized human

hearts using a custom human heart bioreactor capable of providing coronary perfusion and left ventricle wall mechanical stimulation, showing metabolically active repopulated myocardial segments after 14 days of organ culture [84]. Also Nichols and coworkers have reported, for the first time, the development of a bioreactor system to support recellularization of whole human paediatric lung dECM scaffolds, identifying the main conditions and cell requirements necessary for bioengineering whole human lungs [85].

Moreover, many different cell types and sources have been reported for recellularization strategies of different organs (reviewed in [22–27]). Initial works made use of neonatal or fetal cells derived from the organ of interest, showing retention of their tissue-specific phenotype after seeding into the organ-derived dECM scaffold together with relevant organ-specific functionality. Overall, these works served as a proof-of-concept of the fabrication of whole organs *de novo* by decellularization/recellularization techniques. However, those findings also highlighted the necessity to find more amenable cell sources that could be easily expanded and differentiated into functional and multiple cell lineages. In this regard, hPSCs have been proposed as promising candidates due to their self-renewal capacity and the potential to give rise to any cell type in the body [86–88]. The use of hPSCs as a cell source for the development of bioengineered organs based on dECM scaffolds is further discussed in the following section.

Pluripotent stem cells: a long-standing cell source for regenerative medicine

Pluripotent stem cells

Pluripotency is defined as the ability of a single cell to divide and produce differentiated cells from the three germ layers of the embryo [86–88]. The idea to generate functional tissues and organs from pluripotent stem cells (PSCs) has been a long-standing goal in stem cell biology, representing an unprecedented opportunity to study development and even to heal degenerative diseases and aging-related disorders. In this regard, the possibility to capture and culture indefinitely hESCs from the pluripotent inner cell mass (ICM) of the blastocyst has been a major breakthrough in the area of regenerative medicine [86].

Before hESCs were first derived, seminal studies already tried to answer how shape and pattern emerge from the simple beginnings of an embryo, and even how specialized cells differentiate during embryo development becoming organized into a 3D architectural context (reviewed in [89]) [90]. Pursuing the idea to reprogram differentiated cells to an 'embryonic' state, Takahashi and Yamanaka in 2006 discovered that the pluripotent state found in hESCs derived from the ICM could be artificially induced in a somatic cell through the overexpression of just four transcription factors (OCT4, SOX2, cMYC, and KLF4-OSKM) [87] (reviewed in [91]). The produced cells, so called iPSCs, exhibited all the molecular and functional features of ESCs. Importantly, in the last years human iPSCs (hiPSCs) have shown to become instrumental platforms for the study of human development and disease with the identification, in some cases, of molecular and cellular mechanisms responsible for disease gestation and progression (reviewed in [92]).

Overall, one major limitation in the field of hiPSC disease modeling is the lack of a systemic context and disease-related environmental cues [e.g., disorganized ECM, insufficient biochemical signals from the niche, among others], opening new

RESEARCH: Review

BOX 5
Extracellular matrix components used in hPSCs culture and differentiation

ECM components	References
• **Collagens** are the most abundant ECM macromolecules found in our body. Among the 28 types of collagen that exist, collagen IV and I have been widely used in hPSCs differentiation studies demonstrating to be implicated in mesodermal differentiation. In addition, collagen's ability to self-aggregate and crosslink makes it an attractive macromolecule for biomaterial science	[97]
• **Laminin** is a trimeric protein found in the basement membrane, which has been largely investigated for its influence in hPSCs differentiation towards ectodermal tissues	[98]
• **Fibronectin** is an ECM protein highly expressed during the early stages of embryonic development, being essential for proper development of the mesoderm and the neural tube. Generally, it is widely used as cell adhesion protein due to the presence of the peptide sequence arginine-serine-aspartic acid (RGD) in its structure, which is implicated in integrin-mediated cell adhesion	[99,100]
• **Matrigel** is generated from the basement membrane of mouse sarcoma cells thereby containing a variety of ECM molecules and growth factors. Laminin is the major constituent although collagen IV and proteoglycans also take part in its composition. Since it is derived form basement membrane it provides a rich environment that has been largely used for the maintenance of hPSCs as well as differentiation to many lineages including cells from the three germ layers, mesoderm, endoderm and ectoderm	Reviewed in [94–96]
• **Cell-deposited ECM** can be extracted from different cell types by first allowing the cells to produce their own ECM and then removing them without disturbing the newly synthesized ECM structure and biochemical composition. Such cell-deposited ECM has been then used as a coating for stem cell stemness and differentiation studies	[101]

challenges when integrating biomaterials mimicking disease pathology. In this regard, it has been recently shown that the proper fine-tuning of 3D scaffolds recapitulated the abnormal contractility in hiPSC-derived cardiomyocytes from patients with long QT syndrome type 3, and not when healthy counterparts were used. Such platform also allowed for the screening of cardiotoxic compounds in different 3D settings, highlighting the potential application of these approaches for human disease modeling [93].

Differentiation strategies: from pluripotent colonies to organoids/organogenesis in a dish

One of the major areas of research in the field of hPSCs has been the development of protocols for the generation of functional cell types suitable for disease modeling and cell replacement therapies. Until recently, most protocols of differentiation relayed on the generation of single cell populations rather than complete tissues. However, in the last three years pivotal studies have demonstrated
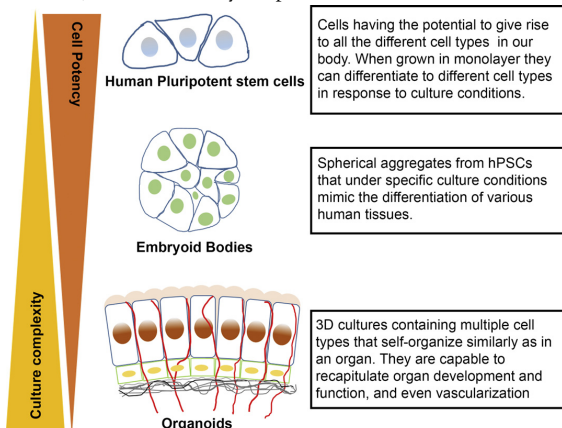

FIGURE 2

The main strategies used for hPSCs differentiation include guided differentiation in 2D monolayer cultures, the formation of embryoid bodies and the induction of 3D self-organization giving rise to organoids. The generation of organoids needs a higher cell culture complexity than the other two approaches.

that it is possible to generate 3D cultures of developing tissues named organoids (reviewed in [94,95]).

After the first derivation of hESCs [86], different laboratories worldwide explored hESCs capacity to undergo controlled differentiation either in monolayer, by seeding cells in the presence of different ECM protein coatings (major matrices used for the culture of hPSCs are described in Box 5) (reviewed in [94–96]) [97–101], or as spheroid-like structures named embryoid bodies (EBs) (Fig. 2). Although EBs can recapitulate several aspects of early development (reviewed in [94]), as any other methodology, EB formation still hampers the translation of this approach into a clinical setting (e.g., low reproducibility and scalability). Nevertheless, all these advances have been fundamental for the proper instruction of hPSCs to form self-organized tissue-specific organoids including the optic cup, brain, intestine, liver and kidney (reviewed in [94]).

Organoids are similar to *in vitro* derived EBs, but they can recapitulate a large number of biological processes related with spatial and temporal organization of heterogeneous tissue-specific cells within the 3D structures (Fig. 2). Even in some cases, organoids have proved to exhibit physiological functions being close to the *in vivo* setting. In this regard, kidney organoids derived from hiPSCs have been recently shown to contain multiple nephron segments surrounded by nascent blood vessels, being able to respond in front of nephrotoxic compounds [102]. Despite these findings, most hPSC-derived organoid models only represented single or partial components of a tissue, hindering the proper control of cell-cell interactions, cell-matrix interplay, and cell organization. Moreover, common hurdles in organoid technologies are being related to incomplete maturation of hPSC-derived cell types and the lack of vascularization.

Bioengineering approaches for hPSCs differentiation: dECMs as biomimetic platforms for generating tissues on-demand

Bioengineering approaches can be used to overcome major issues associated with hPSCs differentiation as maturation and functionality. In this regard, matrigel has been a fundamental matrix for organoid methodologies, including cerebral, optic cup and intestinal organoids from hPSCs (reviewed in [94,95]). However, matrigel

BOX 6
3D bioprinting techniques

Bioprinting techniques	Additive unit	Actuation method	Cell viability	Commercial bioprinter	Bioink viscosity	Disadvantages	Advantages	References
Inkjet printing	Drop	• Piezoelectric pulse • Thermal induced pulse	>85%	Yes	Low	• Microvalves for inkjet are fragile • Requires fast material gelation/stabilization • Height of 3D constructs limited due to low bioink viscosity	• High control on the amount of material deposited (1 pL to 0.1 nL per drop)	Reviewed in [12]
Laser assisted bioprinting	Drop	• Laser induced pulse	>95%	No	Medium-high	• High cost of future commercial bioprinters • Long fabrication time • Long preparation time of material ribbons • Low diversity of bioink for ribbon preparation	• High printing resolution • Single cell deposition	Reviewed in [12]
Micro extrusion	Material strain	• Pneumatic pressure • Mechanical pressure	40–95%	Yes	Medium-high	*Pneumatic pressure* • Cells may suffer important shear stress • Medium printing accuracy • Low printing resolution *Mechanical pressure* • Cells may suffer important shear stress • Medium printing accuracy • Low printing resolution • Mechanical parts make this system more fragile • Screw based system require cleaning of mechanical parts	*Pneumatic pressure* • Abrasive materials can be used • Disposable cartridge that avoids cross-contamination • Non mechanical parts • Used by most of commercial bioprinters due to its robustness and simplicity • Allows printing cell high density *Mechanical pressure* • Abrasive materials can be used • Piston based systems uses disposable syringes • Allows printing cell high density	Reviewed in [10,12]
Stereolithography (SLA)	Cured bioink voxel	• Laser based curing • UV and visible light projection curing	>85%	Yes	Medium	• Only can be used with light crosslinkable bioinks • Multicellular structures are challenging • Printer are not specifically designed for biofabrication	• Affordable • High printing velocity	Reviewed in [10,123,127,128]

composition is not well defined and batch-to-batch differences may lead to important differences in experimental outcomes [103].

Along this line, biomaterials can be used to create stem-cell-like niches providing key elements to control the regulation of stem cell fate and function. Indeed, material properties have been often designed to mimic physiologically relevant ECM stiffness, topography, and adhesion-ligand type, density and affinity. These features, when combined with hPSCs have led to the derivation of protocols for hPSCs differentiation building personalized tissue constructs using human organ-derived dECM scaffolds [43,84,104,105], and even for partially or totally reconstructing mouse [106] and human whole organs [84,105].

Ott and coworkers recently reported for the first time the whole repopulation of decellularized human hearts with hiPSCs-derived cardiomyocytes [84]. In the same line, our group developed a rapid protocol for the generation of human heart grafts by co-culturing hPSC-derived cardiomyocytes on top of 400 micrometers-thick slices of human ventricular dECM scaffolds [43].

Importantly, rat and human lung dECM scaffolds have been also recently shown to be repopulated with endothelial and perivascular cells differentiated from hiPSCs [105]. Concerning kidney, only two works have investigated the role of rhesus monkey kidney dECM scaffolds on hPSCs renal differentiation [40,107].

Alternatively, 3D bioprinting technology have opened new venues for the bottom-up generation of tissue and organ analogues by the deposition in an additive layer-to-layer approach of differentiated hPSCs and biomaterials, specifically arranged to reproduce native 3D architectures (reviewed in [11,12,95]). Nevertheless, attempts to generate hPSCs derived bioprinted constructs are still in its infancy, with only one report on the generation of mini livers from hPSCs [16].

Tissue engineering of human organ analogues by 3D bioprinting

3D bioprinting techniques

Bioprinting techniques aim to perform simultaneous deposition of single or multiple combinations of living cells together with supportive matrices containing biochemical and biophysical cues (altogether termed as bioink). In this manner, organs or tissue analogues are constructed following a predefined architecture in 3D (reviewed in [12–14]). These methodologies are generally classified based on the technology used to generate the structures of the cell-laden material as follows:

Inkjet bioprinting, also referred as 'drop-on-demand printers' appeared early in 2003 [108]. Firstly developed inkjet printers modified commercially available two-dimensional (2D) ink-based printers by replacing the ink in the cartridge by a biological material, and the paper, by an electric-controlled elevator that moves on the *z* direction providing three-dimensionality (reviewed in [12] [109]). Nowadays, inkjet printers make use of nozzles that generate isolated droplets of cell-laden material by means of piezoelectric [110] or thermal (reviewed in [111]) actuation systems. In this manner, by means of either acoustic waves or thermal forces, respectively, liquid drops are ejected onto a substrate. In the last years, inkjet bioprinting has allowed for the efficient introduction of gradients of cells or growth factors along the 3D constructs by the modification of drop densities and size [17,112,113]. Despite this major advances, one common drawback

in inkjet printing is the need to work with biological materials in liquid forms, which in most of the cases demand a fast polymerization procedure post-printing (e.g., by either chemical, pH or ultraviolet mechanisms, among others). All these procedures directly affect the bioprinting process, compromising the chemical and mechanical properties of ECM-derived materials. As reviewed elsewhere, other disadvantages are related to the impediment of building 3D cell-laden constructs with general tissue size, nozzle clogging when using solutions with high cell densities, and cell viability constraints (related to the use of cross-linkers) (reviewed in [12]). Nevertheless, inkjet-based bioprinters have become a massive used technology reducing costs and facilitating the use of free designs and softwares worldwide. Current research is now focused in the development of novel technologies allowing the use of multiple cell types and materials.

Microextrusion systems appeared as a modification of inkjet printers. Here the extrusion of the material takes place through micrometric apertures (usually a needle with inner diameters that range from few to hundred micrometers). By applying a continuous force, this technique allows to print uninterrupted cylindrical lines. Commonly, these systems robotically extrude biological materials by pneumatic or mechanical dispensing systems onto a substrate. It has been reported that almost all kind of hydrogels with varying viscosities, as well as aggregates with high cell density can be printed with this approach (reviewed in [10,12]). Compared to inkjet printing, microextrusion printing enables the deposition of large amount of cells, allowing the generation of constructs with general tissue size. So far, high concentrations of hydrogels such as alginate, fibrin and Pluronic F-127, among others, have proved to be effective when producing stable 3D cell-laden structures [114–120]. Importantly, microextrusion systems have been particularly effective when printing multicellular tissue spheroids that further self-assemble into the desired 3D structure (reviewed in [15]). Although all the advantages described here, one of the major limitations of this technique is the decreased cell viability resulting from the shear stress when cells are in viscous fluids during the extrusion process [121]. Thus, one of the main challenges consists in the retention of cell viability and printing speed without decreasing pressure or reducing nozzle size. Several tissues have been fabricated using this system, including branched vascular trees, aortic valves, and *in vitro* tumor models (reviewed in [12]). Recently, Atala and coworkers have lead the first work on the fabrication of bioprinted tissue functional constructs *in vitro* and *in vivo* for mandible bone, ear-shaped cartilage and organized skeletal muscle at human-scale [18].

In *laser-assisted bioprinting (LABP)* drops of cell-laden biomaterials are generated after laser pulses. The falling bioink droplet is further collected on the substrate and crosslinked, avoiding shear stress and resulting in high cell viabilities, even when using highly viscous materials. This recent methodology relies on the use of a laser pulse that creates a high-pressure bubble on a ribbon containing the material to be printed, thereby generating a bioink droplet. LABP is nozzle-free, thus minimizing clogging-related issues. Moreover, the achieved resolution allows the delivery of single-cells on each drop. Since this system generates scaffold-free 3D cell constructs through a layer-by-layer manner, lately LABP is becoming used for the deposition of different living cells and biomaterials in a well-defined 3D structure. Besides these advantages, still possible side

effects of laser exposure to cells remain elusive. Other limitations are related to the preparation of cell-laden ribbons (specific for each cell type and hydrogel, hindering scaling-up procedures) and the deposition of metallic residues in the final bioprinted construct. Similarly, targeting and positioning cells becomes difficult because of the nature of the ribbon cell coating (reviewed in [12]). To date, few works took advantage of this system in regenerative medicine [19,122], and the high cost of LABP precludes their use for many researchers worldwide.

Stereolithography (SLA) was initially used to create cell-free scaffolds but the increasing development in the formulations of new cross-linkable materials allowed the use of SLA for 3D bioprinting (reviewed in [123]) [124]. In SLA, the laser focusing point moves on the X/Y axes along the uncured bioink, while the stage where the material is polymerized lowers allowing polymerization. Lately, *direct light projection (DLP)* has emerged as an affordable and versatile variant of SLA. In DLP, the light from a digital micro mirror device or projector is used for curing photocrosslinkable hydrogels in a layer-by-layer approach. By curing the structures plane-by-plane, DLP offers enormous advantages in front of SLA (e.g., printing time is not depending on the design complexity of each plane). DLP has been recently used for generating biocompatible

scaffolds [125–127], and more recently Wang and coworkers demonstrated that DLP enabled for the fabrication of 3D cell-laden structures with resolutions of 50 micrometers, and reaching 85% cell viability when encapsulating human fibroblasts [128]. DLP and SLA offer new alternatives for the fabrication of 3D bioconstructs with precise micro- and nano-architecture, being affordable systems in terms of costs.

A summary of the aforementioned bioprinting techniques is presented in Box 6.

3D bioprinting of cell-laden hydrogels

Since 2000, when rapid prototyping technologies were first adapted for the deposition of cell-laden hydrogel 3D structures in cell-compatible printing conditions, researchers all over the world have tried to produce biological tissue-like constructs using different cell types and hydrogel formulations. The basic 3D bioprinting equipment needs when aiming to fabricate cell-laden 3D structures are described in Box 7.

Current efforts are devoted to develop novel biomaterial formulations that can mimic the complexity of the native ECM–a concept called biomimicry – with an impact for bioprinting applications. ECM composition and rigidity have proved to dictate cell

---

BOX 7
3D bioprinting of cell-laden tissue constructs

3D bioprinter needs	● Allow combination of micro-extrusion, fused deposition and inkjet printing at the same time during a printing procedure ● Have at least two hydrogel-compatible printing heads, which facilitates deposition of different cell types in the same printed construct ● Possess temperature control systems for printing heads and substrate ● Allow optical monitoring of the printing process ● Allow the interchange of material cartridges during the printing procedure ● Precise control of the pressure applied during the printing process ● Allow the use of different substrates to print the desired 3D tissue construct (e.g. petri dish, multiwall plates) ● Posses an accurate calibration system for needle tip positioning ● Posses a source of light (UV, blue light) for light-crosslinking hydrogels ● Work under sterile conditions
Key material properties for 3D bioprinting	● *Printability* defines the suitability of a material for a specific printing process and largely depends on the material physicochemical properties (viscosity, shear thinning, yield stress, hydrogel crosslinking mechanism) under the conditions provided by the bioprinting instrument ● *Biocompatibility* refers to the ability to perform as a material that will support the appropriate cellular activity, including the facilitation of molecular and mechanical signaling systems, in order to optimize tissue regeneration, without eliciting any undesirable host responses ● *Biodegradability* describes the biological processes inside the body that cause a gradual breakdown of a material. Degradation kinetics should be matched to the novo tissue formation and the byproducts generated should be nontoxic ● *Biomechanical properties* of the material should provide sufficient structural integrity to the printed construct and match tissue specific biomechanic requirements ● *Biomimicry* refers to the ability of reproduce tissue-specific endogenous material compositions
3D bioprinting processing parameters	● The four main variables that need to be balanced to optimize the printing procedure and ensure the design fidelity are: the needle/tip size, the distance from the tip to the surface, the material flow rate and the linear write speed ● These variables are balanced when the leading edge of the printed bioink is continual with the needle, being possible to dispense a uniform strand ● These aforementioned variables need to be optimized for every different material used ● Changes on environmental conditions such as humidity and temperature may influence printing fidelity ● As printed structures increase in complexity, the incorporation of support structures within the fabricated pattern is necessary ● The printing time should be considered, since extended periods of time at non-optimal temperature, humidity or material biocompatibility will affect both material properties and cell viability

fate and function (reviewed in [129]). In the human body, tissue rigidity ranges from 0.2–5 kPa in soft tissues as brain, to 15,000 kPa in bone, being an important parameter to be considered when aiming to design 3D tissue and organ analogues.

Besides the need to be biocompatible and biodegradable, a biomaterial formulation for bioprinting must possess suitable physicochemical properties in order to fabricate 3D constructs with high resolution and printing fidelity – a characteristic named printability (Box 7) (reviewed in [130–132]). In addition, it must also be optimized in order to minimize stress-induced damage to the cells and biological components, which occur during the deposition process (reviewed in [130–132]). The ideal hydrogel formulation should reach a compromise between preserving cell viability and matching optimal printability.

Viscosity, shear thinning and yield stress of a defined bioink will directly affect printing fidelity during the biofabrication process. Similarly, the specific processing parameters will define the shear stress that cells will suffer during the deposition and the time required for the fabrication of a given 3D construct (e.g., tip size, flow rate, temperature; Box 7). Another important outcome is the maintenance of sufficient structural integrity by the bioprinted 3D construct, which will be mainly dependent on the gelation of the

hydrogel formulation. Natural and synthetic hydrogels applied to 3D bioprinting and their correspondent gelation mechanism are further reviewed elsewhere (reviewed in [130–133]).

Elegant works have demonstrated the feasibility of 3D bioprinting for the generation of several tissues, including bone [18], skin [19], vascular grafts [118,120,134], tracheal supports [135], heart [20,117,136] and cartilage [18,20] tissue structures, using several cell sources such as human umbilical vein endothelial cells, mesenchymal stem cells, human meniscus cells and fibroblasts (reviewed in [10,12]). However, the fabrication of human size organ analogues with complex architectures requires a more elaborate 3D bioprinting strategy, usually involving the co-deposition of other material components (such as supportive and sacrificial materials), together with cell-laden hydrogels, ensuring sufficient structural integrity to the printed construct while maintaining an internal porosity (Fig. 3). In this regard, the recent work by Atala and coworkers provides a 3D bioprinting platform for the production of tissues for human applications, paving the way for future building of solid organs [137].

Acellular organ-specific dECM hydrogels for 3D bioprinting

As decellularization protocols emerged, hydrogels made from decellularized tissues including urinary bladder [138], heart [139], liver [140], dermis [141], adipose tissue [142], bone [143], and lung [144], among others, were developed and reported to support growth and function of different cell types. However, it is not until very recently that tissue-specific dECM hydrogels have been envisioned as a new class of hydrogels for 3D bioprinting [20,145–147]. Nowadays, one of the main hurdles when using dECM hydrogels as bioinks relies on their low viscosity, which inevitably compromise shape fidelity of the bioprinted 3D construct, worsening printing resolution.

To date, only few studies have used dECM hydrogels for 3D bioprinting, applying different strategies to improve their printability [20,145–147]. Pati and coworkers were the first to successfully apply dECM hydrogels for 3D bioprinting. Their strategy consisted on the co-deposition of an open porous structure of polycaprolactone (PCL) as a supportive material, together with the cell-laden dECM hydrogel made from cartilage, heart or adipose porcine tissues [20]. Recently, the same group used skeletal muscle-derived dECM hydrogels for 3D printing of muscle constructs [147].

Following a different strategy, Skardal and coworkers elegantly developed modular hyaluronic acid and gelatin-based hydrogels supplemented with porcine liver, cardiac and skeletal muscle dECM solutions. Following a two-step crosslinking procedure, the authors achieved printable bioinks with different stiffness ranging from 100 Pa to 20 kPa, thus allowing the possibility to mimic the mechanical characteristics of different tissues in the body [145]. Other recent work by Jang and coworkers took advantage of pig heart dECM to prepare cardiac-specific hydrogels that in combination with human cardiac progenitor cells were used to fabricate 3D bioprinted cardiac constructs. The gelation of cardiac dECM hydrogels was based on thermal and chemical crosslinking using vitamin B2 via UVA activation [146].

Future outlook

A major limitation when generating artificial organs on demand stands in the development of techniques to properly reintroduce
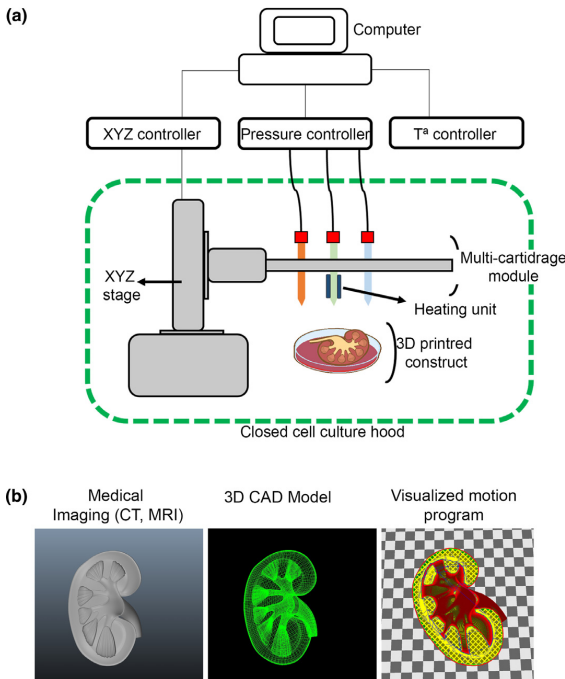
(a)

(b)

FIGURE 3

Schematic representation of a 3D bioprinting system consisting of a computer aided 3-axis stage controller and a deposition module including three different print heads connected to a pressure controller (a). Computer aided design and computer aided manufacturing (CAD/CAM) process for 3D bioprinting of a human size kidney. A 3D CAD model generated from medical imaging data (CT: computed tomography; MRI: magnetic resonance imaging) produces a visualized motion program which dictates the XYZ stage movements to generate the 3D bioprinted kidney prototype (b).

RESEARCH: Review

cells into the organ-specific dECM scaffolds, assessing both complete organ re-endothelization and functional activity. Due to their intrinsic characteristics, hPSCs have been envisioned as an optimal cell source for the generation of complex tissue structures like the organ parenchyma and the vascular system, offering major advantages when compared with adult somatic or stem cells for the same purposes. Moreover, targeted genome editing, as CRISPR platform, is a powerful tool to manipulate and correct disease related genes in patient-derived hiPSCs, allowing for the generation of autologous-corrected cells suitable for disease modeling and drug screening [148]. We believe that targeted genome editing approaches combined with recent progress in the formation of patient-specific hiPSCs-derived organoids could provide an unprecedented source of organ-specific cell types suitable for cell replacement therapies. In this regard, common efforts on the definition of chemically defined conditions to culture hPSC-derived organ-specific cells has led to the examination of novel approaches guiding hPSCs maturation. Following these questions, different works have relayed on the use of human dECM scaffolds together with hPSCs in order to generate human tissue grafts [43,84,104], and even to reconstruct whole organs [84,105], revealing the impact of organ-derived dECMs on the proper instruction of hPSCs fate and function [40,43,84].

Alternatively, 3D bioprinting represents a formidable technology for artificial organ generation. Besides the different limitations of this nascent technology (e.g., printing resolution and time, combination of different bioinks simultaneously, among others), the possibility to print human-scale tissues has been recently demonstrated [18]. In this regard, seminal studies have already proved the feasibility to print 3D tissue constructs using organ-specific dECM hydrogels as biomimetic bioinks [20,145–147], opening the door to the fabrication of novel bioink formulations matching cytocompatibility and mechanical strength requirements for 3D bioprinting.

Overall, we believe that recent advancements in the fields of hPSCs differentiation together with organ-derived dECM scaffolds or novel dECM-based hydrogels aimed for 3D bioprinting represent a step forward in the fabrication of autologous functional tissues on-demand (Fig. 4 and Box 8). To this end, multidisciplinary research in the field of engineering, biomaterials science, stem
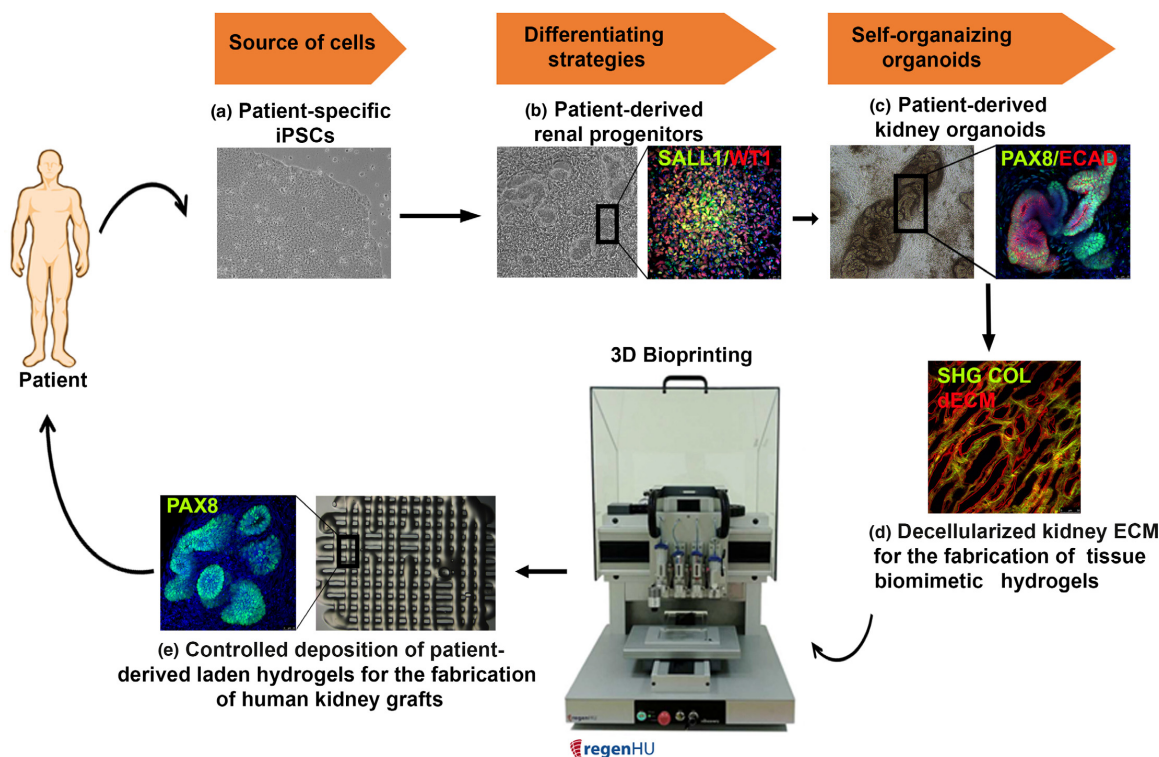

FIGURE 4

3D bioprinting approach for the development of patient-specific organ analogues such as kidney. Patient-specific iPSCs (a) are differentiated into renal progenitor cells in 2D monolayer cultures (representative image for SALL1 and WT1 double positive renal progenitors by immunofluorescence) (b) that are further induced to develop into kidney organoids (representative image for PAX8 and E-cadherin positive 3D renal-like structures by immunofluorescence) (c). The combination of kidney dECM-based hydrogels (d) with patient iPSC-derived renal progenitor cells could be used for the biofabrication of specialized 3D renal constructs (representative image for PAX8 renal structures developed into printed kidney dECM-based hydrogels) (e). This approach renders to the generation of tissue and organ analogues suitable for regenerative medicine applications (e.g., disease modeling, drug screening, cell replacement therapies, among others).

BOX 8
Challenges and future perspectives

Research area	Specific challenges	Future outcomes
Decellularization	• Standardization of decellularization protocols for each specific organ • Systematic evaluation of immunologic response and the possibility of using dECM scaffolds from different species	• Robust production of organ-derived dECM scaffolds • Determination of the need of immunosuppressive drugs after transplantation. Increase the tissue source, overcoming donor shortage
Recellularization	• Improved seeding methodologies for complete re-endothelization of the organ vascular bed and parenchyma recellularization • Novel bioreactor systems with optimal control over the culture conditions (oxygen delivery, biophysical stimulation, continuous monitoring of functional parameters)	• Optimal vascularization • Determination of organ biochemical/biophysical parameters during recellularization, and end-points for each organ • Definition of common guidelines for the assessment of organ mechanics Preservation of bioengineered organs before transplantation • Functional evaluation in large animal models
Human pluripotent stem cells	• Standardized protocols for expansion and differentiation to large cell numbers • Purification of hPSC-differentiated cells and identification of optimal cell culture conditions (growth factors, cytokines) for cell phenotype maintenance • Identification of hPSC-derived progenitor cell types suitable for engraftment and maturation into dECM scaffolds	• Repopulation of organ-derived dECM scaffolds with multiple hPSC-derived progenitor cell types specific for each organ compartment, and in sufficient cell number to achieve comparable native organ cell densities • Generation of personalized human bioengineered organ equivalents with optimal functional activity
3D bioprinting	• Development of novel cell-compatible hydrogels with tailored viscosity and biochemical composition • Monitoring of bioink flow rate with automatic adjustment of printing conditions • Present alignment capability on previously printed constructs • Improve bioprinting full automation • Development of bioreactors for tissue/organ growth and maturation post-processing	• Bioprinting of cell-laden structures with increased mechanical strength, bioactivity and cell viability • Increased printing fidelity • Step-wise fabrication of complex multicellular structures • Rapid production of 3D printed constructs, thereby improving cell viability • Generation of functional tissue/organs

cell biology and medicine will be essential to further succeed in the biofabrication of autologous organs for future clinical replacement strategies.

References
[1] C. Mason, Regen. Med. 3 (2008) 1–5.
[2] P. Bajaj, et al. Annu. Rev. Biomed. Eng. 16 (2014) 247–276.
[3] A.S. Mao, Proc. Natl. Acad. Sci. U. S. A. 112 (2015) 14452–14459.
[4] G. Orlando, et al. Biomaterials 34 (2013) 5915–5925.
[5] A. Peloso, et al. Transplantation (2015) 1–10.
[6] S.E. Gilpin, et al. J. Heart Lung Transplant. 33 (2014) 298–308.
[7] P.L. Sánchez, et al. Biomaterials 61 (2015) 279–289.
[8] G. Mazza, et al. Sci. Rep. 7 (2015) 13079.
[9] P.T. Moser, H.C. Ott, Curr. Opin. Organ Transplant. 19 (2014) 603–609.
[10] D.-H.K. Christian Mandrycky, Z. Wang, K. Kim, Biotechnol. Adv. (2015)[Epub ahead].
[11] D.Y.C. Cheung, B. Duan, J.T. Butcher, Essent. 3D Biofabrication Transl. (2015) 351–370.
[12] S.V. Murphy, A. Atala, Nat. Biotechnol. 32 (2014) 773–785.
[13] J. Groll, et al. Biofabrication 8 (2016) 013001.
[14] B. Derby, Science (80-.) 338 (2012) 921–926.
[15] F. Marga, et al. Biofabrication 4 (2012) 022001.
[16] J.K. Alan Faulkner-Jones, et al. Biofabrication 7 (2015) 044102.
[17] J.A. Phillippi, et al. Stem Cells 26 (2008) 127–134.
[18] H.-W. Kang, et al. Nat. Biotechnol. 34 (2016) 312–319.
[19] S. Michael, et al. PLoS ONE 8 (2013).
[20] F. Pati, et al. Nat. Commun. 5 (2014) 3935.

[21] W. Peng, U. Derya, I.T. Ozbolat, Trends Biotechnol. 34 (2016) 722–732.
[22] M.E. Scarritt, N.C. Pashos, B.A. Bunnell, Front. Bioeng. Biotechnol. 3 (2015) 43.
[23] S.F. Badylak, D. Taylor, K. Uygun, Annu. Rev. Biomed. Eng. 13 (2011) 27–53.
[24] J.J. Song, H.C. Ott, Trends Mol. Med. 17 (2011) 424–432.
[25] A.A. Khan, et al. J. Artif. Organs 17 (2014) 291–300.
[26] D. Rana, et al. J. Tissue Eng. Regen. Med. (2015).
[27] N. Montserrat, E. Garreta, J.C. Izpisua Belmonte, FEBS J. (2016).
[28] J.T. Hjelle, E.C. Carlson, K. Brendel, Kidney Int. 15 (1979) 20–32.
[29] M. Rojkind, et al. J. Cell Biol. 87 (1980) 255–263.
[30] S.F. Badylak, et al. J. Biomed. Mater. Res. 29 (1995) 977–985.
[31] R-N. Chen, et al. Biomaterials 25 (2004) 2679–2686.
[32] C.E. Schmidt, J.M. Baier, Biomaterials 21 (2000) 2215–2231.
[33] R.C. Elkins, et al. Ann. Thorac. Surg. (2001).
[34] D. Schultheiss, et al. J. Urol. 173 (2005) 276–280.
[35] T.W. Gilbert, T.L. Sellaro, S.F. Badylak, Biomaterials 27 (2006) 3675–3683.
[36] H.C. Ott, et al. Nat. Med. 14 (2008) 213–221.
[37] J.P. Guyette, et al. Nat. Protoc. 9 (2014) 1451–1468.
[38] M.J. Bissell, J. Aggeler, Prog. Clin. Biol. Res. 249 (1987) 251–262.
[39] J. Cortiella, et al. Tissue Eng. Part A 16 (2010) 2565–2580.
[40] K.H. Nakayama, et al. PLoS ONE 8 (2013).
[41] T. Luque, et al. Acta Biomater. 9 (2013) 6852–6859.
[42] R. Londono, S.F. Badylak, Ann. Biomed. Eng. 43 (2015) 577–592.
[43] E. Garreta, et al. Biomaterials 98 (2016) 64–78.
[44] G. Yang, et al. Biomaterials 34 (2013) 9295–9306.
[45] S.F. Badylak, et al. Biomaterials 103 (2016) 128–136.
[46] M.P. Bernard, et al. Biochemistry 22 (1983) 5213–5223.
[47] M.I.S. Chung, et al. Matrix Biol. 25 (2006) 492–504.
[48] P.M. Crapo, T.W. Gilbert, S.F. Badylak, Biomaterials 32 (2011) 3233–3243.
[49] M. He, A. Callanan, Tissue Eng. Part B: Rev. 19 (2013) 194–208.
[50] T.J. Keane, I. Swinehart, S.F. Badylak, Methods (2015).
[51] C.V. Montoya, P.S. McFetridge, Tissue Eng. Part C. Methods 15 (2009) 191–200.
[52] L.N. Sierad, et al. Tissue Eng. Part C: Methods 21 (2015) 1284–1296.
[53] K. Sawada, et al. J. Chem. Technol. Biotechnol. 83 (2008) 943–949.
[54] H.C. Ott, et al. Nat. Med. 16 (2010) 927–933.
[55] J.J. Song, et al. Nat. Med. 19 (2013) 646–651.
[56] T.H. Petersen, et al. Cell Transplant. 20 (2011) 1117–1126.
[57] A.P. Price, et al. Tissue Eng. Part A 16 (2010) 2581–2591.
[58] J.E. Nichols, et al. Tissue Eng. Part A 19 (2013) 2045–2062.
[59] J. Niles, et al. Tissue Eng. Part A 16 (2010) 2565–2580.
[60] G. Orlando, et al. Ann. Surg. 256 (2012) 363–370.
[61] R. Katari, et al. Nephron Exp. Nephrol. 126 (2014) 119–124.
[62] P.M. Baptista, et al. Methods Mol. Biol. 1001 (2013) 289–298.
[63] D.E. Wagner, et al. Biomaterials 35 (2014) 2664–2679.
[64] A.R. Gillies, et al. Tissue Eng. Part C: Methods 17 (2011) 383–389.
[65] J.E. Reing, et al. Biomaterials 31 (2010) 8626–8633.
[66] B.D. Elder, D.H. Kim, K.A. Athanasiou, Neurosurgery 66 (2010) 722–727.
[67] K.H. Hussein, K.M. Park, K.S. Kang, Mater. Sci. Eng. C: Mater. Biol. Appl. 67 (2016) 766–778.
[68] J. Folkman, M. Hochberg, J. Exp. Med. 138 (1973) 745–753.
[69] B.M. Bijonowski, W.M. Miller, J.A. Wertheim, Curr. Opin. Chem. Eng. 2 (2013) 32–40.
[70] J.S. Uzarski, et al. Tissue Eng. Part C: Methods 21 (2015) 1032–1043.
[71] J. Hülsmann, et al. J. Artif. Organs 16 (2013) 294–304.
[72] Y. Barash, et al. Tissue Eng. Part C: Methods 16 (2010) 1417–1426.
[73] J. Hulsmann, et al. Methods Mol. Biol. (2016) 257–284.
[74] M.S. Raredon, et al. Biores Open Access 5 (2016) 72–83.
[75] J.M. Charest, et al. Biomaterials 52 (2015) 79–87.
[76] M.R. Ebrahimkhani, et al. Adv. Drug Deliv. Rev. 69–70 (2014) 132–157.
[77] H. Yagi, et al. Cell Transplant. 22 (2013) 231–242.
[78] A. Soto-Gutierrez, et al. Tissue Eng. Part C: Methods 17 (2011) 677–686.
[79] B.E. Uygun, et al. Nat. Med. 16 (2010) 814–820.
[80] N. Shirakigawa, T. Takei, H. Ijima, J. Biosci. Bioeng. 116 (2013) 740–745.
[81] B. Bonandrini, et al. Tissue Eng. Part A 20 (2014) 1486–1498.
[82] M. Caralt, et al. Am. J. Transplant. (2014) 64–75.
[83] E.A. Ross, et al. Organogenesis 8 (2012) 49–55.
[84] J.P. Guyette, et al. Circ. Res. (2015).
[85] J.E. Nichols, et al. J. Tissue Eng. Regen. Med. (2016).
[86] J.A. Thomson, et al. Science 282 (1998) 1145–1147.
[87] K. Takahashi, et al. Cell 131 (2007) 861–872.
[88] J. Yu, et al. Science 318 (2007) 1917–1920.
[89] P.B. Armstrong, Crit. Rev. Biochem. Mol. Biol. 24 (1989) 119–149.
[90] P. Weiss, A.C. Taylor, Proc. Natl. Acad. Sci. U. S. A. 46 (1960) 1177–1185.
[91] S. Yamanaka, Philos. Trans. R. Soc. Lond. B: Biol. Sci. 363 (2008) 2079–2087.
[92] G. Tiscornia, E.L. Vivas, J.C. Izpisúa Belmonte, Nat. Med. 17 (2011) 1570–1576.
[93] Z. Ma, et al. Biomaterials 35 (2014) 1367–1377.
[94] M.A. Lancaster, J.A. Knoblich, Science 345 (2014) 1247125.
[95] X. Yin, et al. Cell Stem Cell 18 (2016) 25–38.
[96] L.G. Villa-Diaz, et al. Stem Cells 31 (2013) 1–7.
[97] Y. Liu, et al. PLoS ONE 7 (2012).
[98] J.S. Meyer, et al. Stem Cells 29 (2011) 1206–1218.
[99] E.L. George, et al. Development 119 (1993) 1079–1091.
[100] R.A. Oldershaw, et al. Nat. Biotechnol. 28 (2010) 1187–1194.
[101] Y. Yan, et al. Biomaterials 73 (2015) 231–242.
[102] M. Takasato, et al. Nature 526 (2015) 564–568.
[103] H.K. Kleinman, et al. Biochemistry 21 (1982) 6188–6193.
[104] S.E. Gilpin, et al. Ann. Thorac. Surg. 98 (2014) 1721–1729.
[105] X. Ren, et al. Nat. Biotechnol. 33 (2015) 1097–1102.
[106] T.-Y. Lu, et al. Nat. Commun. 4 (2013) 2307.
[107] C.A. Batchelder, M.L. Martinez, A.F. Tarantal, PLOS ONE 10 (2015).
[108] R.S. Tuan, G. Boland, R. Tuli, Arthritis Res. Ther. 5 (2003) 32–45.
[109] J.P. Mattimore, et al. Conf. Proc. IEEE SOUTHEASTCON, 2010, 510–513.
[110] Y. Fang, et al. Tissue Eng. Part C: Methods 18 (2012) 647–657.
[111] X. Cui, et al. Recent Pat. Drug Deliv. Formul. 6 (2012) 149–155.
[112] E.D.F. Ker, et al. Biomaterials 32 (2011) 8097–8107.
[113] P.G. Campbell, et al. Biomaterials 26 (2005) 6762–6770.
[114] N.E. Fedorovich, et al. Tissue Eng. Part A 14 (2008) 127–133.
[115] K. Jakab, et al. Proc. Natl. Acad. Sci. 101 (2004) 2864–2869.
[116] R. Landers, et al. Biomaterials 23 (2002) 4437–4447.
[117] Y.S. Zhang, et al. Biomaterials 110 (2016) 45–59.
[118] W. Jia, et al. Biomaterials 106 (2016) 58–68.
[119] K.A. Homan, et al. Sci. Rep. 6 (2016) 34845.
[120] D.B. Kolesky, et al. Proc. Natl. Acad. Sci. U. S. A. 113 (2016) 3179–3184.
[121] R. Chang, J. Nam, W. Sun, Tissue Eng. Part A 14 (2008) 41–48.
[122] V. Keriquel, et al. Biofabrication 2 (2010) 014101.
[123] K.C. Hribar, et al. Lab Chip 14 (2014) 268–275.
[124] V. Chan, et al. Lab Chip 10 (2010) 2062–2070.
[125] G. Mapili, et al. J. Biomed. Mater. Res. Part B: Appl. Biomater. 75 (2005) 414–424.
[126] A.P. Zhang, et al. Adv. Mater. 24 (2012) 4266–4270.
[127] S.P. Grogan, et al. Acta Biomater. 9 (2013) 7218–7226.
[128] Z. Wang, et al. Biofabrication 7 (2015) 1–29.
[129] W.L. Murphy, T.C. McDevitt, A.J. Engler, Nat. Mater. 13 (2014) 547–557.
[130] J. Malda, et al. Adv. Mater. 25 (2013) 5011–5028.
[131] D.L.K. Rod, et al. ACS Biomater. Sci. Eng. (2016).
[132] A. Skardal, A. Atala, Ann. Biomed. Eng. 43 (2015) 730–746.
[133] T.L. Panwar, Molecules 21 (2016).
[134] D.B. Kolesky, et al. Adv. Mater. 26 (2014) 3124–3130.
[135] D.A. Zopf, et al. N. Engl. J. Med. 368 (2013) 2043–2045.
[136] R. Gaetani, et al. Biomaterials 33 (2012) 1782–1790.
[137] H.W. Kang, et al. Nat. Biotechnol. 34 (2016) 312–319.
[138] A.L. Brown, et al. Macromol. Biosci. 6 (2006) 648–657.
[139] R.M. Wang, K.L. Christman, Adv. Drug Deliv. Rev. 96 (2016) 77–82.
[140] A. Skardal, et al. Biomaterials 33 (2012) 4565–4575.
[141] M.T. Wolf, et al. Biomaterials 33 (2012) 7028–7038.
[142] D.A. Young, et al. Acta Biomater. 7 (2011) 1040–1049.
[143] M.J. Sawkins, et al. Acta Biomater. 9 (2013) 7865–7873.
[144] R.A. Pouliot, et al. J. Biomed. Mater. Res. Part A (2016).
[145] A. Skardal, et al. Acta Biomater. 25 (2015) 24–34.
[146] J. Jang, et al. Acta Biomater. 33 (2016) 88–95.
[147] Y.J. Choi, et al. Adv Healthc. Mater. (2016).
[148] F. Gonzalez, Dev. Dyn. Off. Publ. Am. Assoc. Anat. (2016).

Review Article

Non-coding microRNAs for cardiac regeneration: Exploring novel alternatives to induce heart healing

Elena Garreta [a], Patricia Prado [a], Juan Carlos Izpisua Belmonte [b, *], Nuria Montserrat [a, **]

[a] Pluripotent Stem Cells and Activation of Endogenous Tissue Programs for Organ Regeneration, Institute for Bioengineering of Catalonia (IBEC), Barcelona, Spain
[b] Gene Expression Laboratory, Salk Institute for Biological Studies, La Jolla, CA, USA

ARTICLE INFO

ABSTRACT

In recent years, different studies have revealed that adult mammalian cardiomyocytes have the capacity to self-renew under homeostatic conditions and after myocardial injury. Interestingly, data from animal models capable of regeneration, such as the adult zebrafish and neonatal mice, have identified different non-coding RNAs (ncRNAs) as functional RNA molecules driving cardiac regeneration and repair. In this review, we summarize the current knowledge of the roles that a specific subset of ncRNAs, namely microRNAs (miRNA), plays in these animal models. We also emphasize the importance of characterizing and manipulating miRNAs as a novel approach to awaken the dormant regenerative potential of the adult mammalian heart by the administration of miRNA mimics or inhibitors. Overall, the use of these strategies alone or in combination with current cardiac therapies may represent new avenues to pursue for cardiac regeneration.

1. Introduction

Cardiovascular diseases (CVDs) represent a leading cause of death worldwide [1,2]. Among them, coronary artery disease is the most frequent cardiovascular disorder leading to acute myocardial infarction (MI). In the best cases, patients who survive an MI episode face progressive deterioration of their condition over the years, ultimately resulting in heart failure. During the last decades, many efforts have been focused on improving treatments during the acute phase of MI and enhancing the contraction of the surviving myocardium (i.e., β-blockers, angiotensin-converting enzyme inhibitors, and mineralocorticoid receptor blockers, among others). However, none of these approaches are aimed at inducing the formation of new functional cardiac tissue. Since transplantation remains the only therapeutic option for end-stage heart failure, extraordinary efforts have been devoted towards the identification of novel approaches to induce heart regeneration, including: (i) the activation of resident cardiac progenitor cells with proliferative competence and their differentiation into mature cardiomyocytes, (ii) the transplantation of cardiac precursor cells to the damaged myocardium, and (iii) improving the proliferation of pre-existing cardiomyocytes by the administration of compounds [3,4]. While the two first approaches have not proved successful enough to restore the cardiomyocytes lost after injury, the third approach involving the activation of endogenous cardiac regeneration by manipulating cardiomyocyte proliferation has recently demonstrated promising outcomes.

Certain non-mammalian vertebrates, such as some fish and amphibians are able to regenerate their heart throughout their entire life [5—7]. For example, adult zebrafish have been shown to elicit a primitive regenerative response upon injuries such as cryoinjury [8—10], ventricular resection [6], genetic ablation of cardiomyocytes [11] and hypoxia-reoxygenation injury [12]. Recently, lineage tracing approaches in this species have shown that dedifferentiated cardiomyocytes re-enter the cell cycle through increased expression of polo-kinase 1 (plk1) to replenish the lost myocardium [7]. Despite these findings, endogenous mammalian cardiomyocyte dedifferentiation upon injury was

unexplored until 2011, when Porrello and colleagues observed a remarkably similar regenerative response in neonatal murine hearts to that seen in the adult zebrafish [13]. In particular, the authors showed that amputating 10%–15% of the ventricular mass in newborn mice elicited a regenerative response during the early days of life (up to 7 days). These newly generated cardiomyocytes restored heart function after approximately 30 days, and arose from pre-existing cardiomyocytes, as demonstrated by Cre/lox genetic lineage-tracing [13]. Supporting this notion, Senyo and colleagues later provided conclusive observations implicating pre-existing cardiomyocytes as the main cellular source of new cardiomyocytes in aging mice and after MI [14]. Altogether, these findings suggest that the mammalian heart possesses all the required elements for regeneration, and that the identification of the molecular pathways sustaining these responses may represent an attracting area to complement existing approaches for repairing the human heart [15].

Currently, regenerative strategies for heart healing rely on developing efficient approaches linked to proliferation, differentiation, and reprogramming. Although these methods have different characteristics and outcomes, they all depend on gene regulatory networks responsible for specialized biological processes during cardiac development and disease [1]. Globally, non-coding RNAs (ncRNAs) refer to those RNAs with no protein-coding potential but control different aspects of gene regulatory network activity, including transcriptional and epigenetic control, post-transcriptional gene regulation, and nuclear genome organization [1]. The different RNAs produced by the noncoding genome are rich and diverse in terms of biogenesis, structure, and function [16]. To date, hundreds of thousands of ncRNAs have been described in humans, however, the precise role of a great majority remains largely unknown. Traditionally, ncRNAs are classified based on their size into two categories: small (<200 nt), which include microRNAs (miRNAs), transfer RNAs, and small nucleolar RNAs; and longer RNAs (>200 nt), which include ribosomal RNAs, natural antisense transcripts and other long ncRNAs (lnRNAs) [17]. Recently, the incorporation of ncRNAs within cardiac gene regulatory networks represents a novel venue for therapeutic intervention in the heart. Mounting evidence highlight the role of lncRNA in cardiac development [18–23] and cardiovascular diseases [21–27]. The reader may refer to the following reviews summarizing the effects of lncRNAs on cardiac biology and regeneration [1,2,28,29], and cardiac disease [30]. In this regard, the development of next generation sequencing techniques has allowed the characterization of newly discovered lncRNAs in cardiac homeostasis and disease, which will allow their use in diagnosis, disease progression monitoring and targeted therapies [30].

miRNAs represent the most extensively studied class of small regulatory ncRNAs in the field of cardiac regeneration. These 21–22 nucleotide-long single-stranded ncRNAs guide RNA-inducing silencing complexes to their target messenger RNAs (mRNAs) for degradation or translational repression. Importantly, miRNAs are known to control embryonic development, tissue homeostasis and pathological processes, such as MI [31]. Recent studies highlight that the activation of endogenous cardiac regeneration may be possible by manipulating cardiomyocyte proliferation. Alternatively, another approach to cardiac regeneration that has attracted much attention is the direct reprogramming of fibroblasts into functional cardiomyocytes, raising the possibility of *in vivo* conversion of cardiac fibroblasts into cardiomyocytes within the injured zone. This review will focus on highlighting the characteristics and biological roles of miRNAs in these processes by paying specific attention to the studies addressing the use of miRNAs that could be targeted for inducing *in situ* myocardial repair after cardiac injury in a clinical setting.

2. miRNAs controlling cardiomyocyte proliferation after cardiac damage: lessons from animal models

Regardless of the injury model used, cardiac regenerative responses in adult zebrafish are mediated by the proliferation of pre-existing cardiomyocytes, which undergo de-differentiation and re-enter the cell cycle. All these events drive cardiomyocyte migration into the damaged area to restore the ventricular mass lost after injury [7,32,33]. Indeed, genetic lineage tracing studies have revealed that existing cardiomyocytes, and not stem cells, are the major source of regenerating cardiac muscle in these species [7,33,34]. In this regard, it has been demonstrated that cardiomyocyte de-differentiation and proliferation after damage in the adult zebrafish heart takes place as a major consequence to sarcomere disassembly, which is required for DNA synthesis and cell division to occur. Along this line, a recent study using proteomic analyses has revealed that the zebrafish heart, similar to neonatal mouse hearts, is characterized by an immature myofilament composition, lacking many of the structural proteins present in mature mouse cardiomyocytes [35]. However, such cardiac regeneration capacity found in the adult zebrafish is largely impeded in the adult mammalian heart.

Within the last few years, alternative approaches attempting to recapitulate innate mechanisms of cardiac regeneration as those found in adult zebrafish or neonatal mice have attracted a lot of attention. The inability of the adult mammalian heart to regenerate reflects the postnatal loss of cardiomyocyte proliferative capacity, which occurs during the first few weeks after birth in mice. Indeed, the molecular mechanisms sustaining postnatal cardiomyocyte binucleation and mitotic arrest remain unknown and are currently some of the most challenging questions to answer in cardiac biology. In an attempt to identify miRNAs involved in these processes, Porrello and colleagues performed microarray analyses to profile miRNAs involved in postnatal cardiomyocyte mitotic arrest in 1- and 10- day old mouse hearts. Using this approach, the authors observed that miR-195 expression was upregulated during this period, and that its overexpression in developing cardiomyocytes correlated with premature cell cycle arrest and a predisposition to congenital abnormalities, including ventricular septal defects [36]. On the contrary, postnatal inhibition of the entire miR-15 family (miR-15a, miR-15b, miR-16-1, miR-16-2, miR-195, and miR-497) using locked nucleic acid (LNA)-modified anti-miRs extended the proliferative capacity of neonatal cardiomyocytes beyond the normal window of postnatal cell cycle arrest, resulting in increasing numbers of mitotic cardiomyocytes and the de-repression of checkpoint kinase 1 [36]. Similarly, the same group demonstrated that 1-day old miR-195 transgenic mice failed to regenerate after an infarct, and that cardiac function was severely impaired due to the formation of large fibrotic scars soon after the infarct [37]. Accordingly, inhibition of the miR-15 family in postnatal stages increased cardiomyocyte proliferation and improved left ventricular function after ischemia-reperfusion (I/R) injury in mice [37]. The same group observed similar results after acute inhibition of the miR-15 family in mice and pig models [38]. Overall, these findings suggest that upregulation of the miR-15 family during the neonatal period is an important regulatory mechanism that controls cardiomyocyte cell cycle arrest and highlights its potential use as a therapeutic target for the manipulation of cardiac remodeling and function. Nevertheless, further studies are needed in order to ascertain its effects in cardiac proliferation in adult stages [37].

Of interest, in a work by Yin and colleagues, miR-133, a miRNA that induces defects in cardiac looping and chamber formation in *Xenopus* [39], which also has known roles in cardiac proliferation [40] and disease [41], was found to diminish its expression during

zebrafish heart regeneration [42]. Accordingly, the authors engineered a miR-133 sponge construct encoding an EGFP cDNA followed by triplicate perfect binding sites for miR-133. In this manner, by transgenic miR-133 depletion, authors achieved an enhanced regenerative response seven days after ventricular amputation compared with wild type controls. Remarkably, one of the miR133 targets is Mps1 (monopolar spindle protein 1), a mitotic checkpoint kinase that when mutated hampers zebrafish heart regeneration leading to scar formation after damage [6].

Importantly, a genomic-scale screening performed by Eulalio and colleagues has described several individual miRNAs and miRNA families able to reduce or stimulate cardiomyocyte proliferation when delivered exogenously to neonatal rodent cardiomyocytes [43]. Besides the miR-15 family, another family identified by the authors to largely inhibit cardiac proliferation was the let-7 family, a highly conserved miRNA family that has previously been shown to play important roles during development and stem cell differentiation [44]. Notably, recent findings from our laboratory have identified that the miRNA (miR) clusters miR99/Let-7c and miR-100/Let-7a are down regulated during the early stages of zebrafish regeneration, resulting in increased expression of their protein targets: smarca 5 (SWI/SNF-related matrix-associated actin-dependent regulator of chromatin subfamily a, member 5) and fntb (beta subunit of farnesyl-transferase) [15]. Interestingly, our results also showed that both human and murine hearts failed to downregulate these miRs after injury, and that the delivery of anti-miRs using adeno-associated virus (AAVs) in a mouse model of MI improved cardiac function and was correlated with increases in the levels of FNTB and SMARCA5 expression. Using this approach we also demonstrated that experimental downregulation of miR-99/100 and/or let-7a/c in vitro (in primary cultures of neonatal cardiomyocytes) and ex vivo (murine heart organotypic slices) resulted in the expression of increased amount of GATA4, a marker associated with dedifferentiated cardiomyocytes, together with markers of proliferation (PCNA, or phosphorylated H3, respectively) [15]. Importantly, it has been shown that both miR99a and Let-7c act as key regulators of cardiomyogenesis during embryonic development [45], and that the manipulation of the let-7-a/c miRNAs by Lin28a allows for the induction of regenerative responses in several adult mouse tissues [46].

Of note, in the above mentioned work by Eulalio and colleagues, at least 40 miRNAs with previously unknown roles in stimulating cardiomyocyte proliferation were also identified, including miR-199a and miR-590, as well as the miR-17/92 and the miR-302/367 clusters [43]. The authors elegantly manipulate miRNA expression in order to evaluate cardiomyocyte proliferation in vivo. Specifically, they made use of high-throughput analyses and high-content microscopy systems to methodically identify proliferation-competent cardiomyocytes using a library of 875 miRNA mimics. The study was focused on the identification of miRNAs that promote expression of proliferative markers (Ki67, H3S10ph) and incorporation of DNA analogs indicative of DNA synthesis. Using this approach, the authors found over 204 miRNAs that enhanced cardiomyocyte proliferation more than 2-fold in both neonatal rats and adult mice. Subsequently, they selected two inducers with the highest potential of cardiomyocyte proliferation, namely miR-199a and miR-590, to be delivered into uninjured and infarcted adult mice using adeno-associated virus serotype 9 (AAV9) transduction. Interestingly, the overexpression of the two miRNAs increased cardiomyocyte proliferation rates, cardiac regeneration and improved cardiac function [43].

As stated above, the miR-17-92 cluster has also been recognized as a critical regulator of cardiac proliferation [43]. Interestingly, this same cluster was previously identified as a human oncogene [47] and a regulator of cardiac function during embryonic heart development [48]. Recently, Chen and colleagues have also demonstrated that transgenic overexpression of the miR-17-92 cluster in the murine heart induces cardiomyocyte proliferation in embryonic, postnatal and adult stages through the inhibition of phosphatase and tensin homolog (PTEN) [49]. Moreover, Chen and colleagues also showed that its overexpression was associated with enhanced cardiac function after MI, highlighting its potential use for the induction of cardiomyocyte proliferation and regeneration in adult stages [49].

In addition to miRNAs that can act by suppressing or enhancing cardiomyocyte proliferation, also several miRNAs have been described to play a role in regulating cardiomyocyte survival. Among them, the miR-34 family is induced after MI and promotes cardiomyocyte cell death [17,50—52]. Specifically, miR-34a has been described to be upregulated over time in both endothelial cells and cardiomyocytes [53,54], after cardiac injury [31,52,54], and in patients with heart failure [55]. Moreover, recent findings indicate a cardioprotective effect for miR-34a during cardiac aging [54]. Interestingly, miR-34a targets SIRT1, a deacetylase with cardiac and vasculoprotective functions, which upon de-repression contributes to the antiapoptotic effects of miR-34a inhibition. Moreover, miR-34a represses the protein phosphatase 1 regulator PNUTS (or serine/threonine protein phosphatase 1 regulatory subunit 10 [PPP1R10]), which is involved in mediating DNA damage response and telomere shortening [51,54]. Similarly, it has been demonstrated that cardiac miR-34a levels are low in the early postnatal period and will rise to adult levels within one week after birth. Accordingly, overexpression of miR-34a in early postnatal mice was found to limit cardiomyocyte proliferation and cardiac regeneration following injury. Conversely, intravenous antagonism of miR-34a using LNA improved cardiac function after MI in adult mice through the modulation of genes previously linked to cellular proliferation and/or survival, such as Bcl2, Cyclin D1 and Sirt1 [54].

Overall, mounting evidence highlights that manipulation of cardiomyocyte proliferation is feasible and represents an effective approach for cardiac regeneration. Nevertheless, the molecular mechanisms promoting cardiomyocyte re-entry into the cell cycle still remain largely unknown. In this regard, it has been recently demonstrated that the miR302/367 cluster stimulates cardiomyocyte proliferation during early heart development by inhibiting the Hippo pathway, and that transient treatment with miR302/367 mimics in mice after MI promotes cardiac regeneration [56]. Interestingly, miR302/367 gain of function led to cardiomegaly in fetal and juvenile hearts, which show a more undifferentiated phenotype, similar to that seen in developing hearts with disrupted Hippo signaling [57]. Conversely, the deletion of Hippo signaling extends the heart's regenerative capacity beyond the first week of postnatal life and sustains cardiomyocyte generation with functional recovery after MI in adult mice [57,58]. Similarly, deletion of Yap in the embryonic mouse heart causes myocardial hypoplasia, which causes early embryonic lethality [59,60], whereas in the postnatal heart it induces progressive dilated cardiomyopathy, which is associated with a reduced number of mitotic cardiomyocytes during the neonatal stage [61]. Interestingly, when LAD ligation was performed in 7 day-old transgenic mice overexpressing a constitutively active mutation of Yap (YapS112A) under the control of an αMHC promoter, transgenic mouse hearts could regenerate with almost no fibrosis and showed increased cardiac tissue formation [61]. Importantly, overexpression of the constitutively active YapS112A mutation in cultured cardiomyocytes was associated with the induction of cardiomyocyte proliferation through activation of the insulin growth factor (IGF) signaling pathway and the inactivation of Glycogen synthase kinase 3 beta (GSK3β) [61], highlighting the importance of Hippo and IGF-Wnt/β-catenin crosstalk for

cardiomyocyte proliferation during heart development [60,62].

Research of the Hippo pathway in *Drosophila* has provided important hints for understanding cell proliferation regulation and organ size in mammals. In the developing mouse heart, many key Hippo pathway components are functionally preserved throughout evolution [63,64]. In mammals the most downstream Hippo pathway components are the transcriptional coactivators Yap (Yki in *Drosophila*) and Taz, which promote transcription of pro-proliferative genes. Yap is inactivated by a kinase cascade that includes Mst1/Mst2 (Hippo in Drosophila) and the Lats kinases (Lats1/2), which act together with the Mob1 complex to promote Yap exclusion from the nucleus. Indeed, the work by Tian and colleagues identified that one of the possible mechanisms of action of the miR302/367 cluster is through the repression of Mst1, Mst2 and Mob1b [56]. Recently, Yang and colleagues conducted micro-array analyses and observed that miR-206 expression was upregulated by Yap in cardiomyocytes, and that cardiac-specific overexpression of miR-206 in mice induced hypertrophy and

protected the heart from I/R injury, whereas its suppression exacerbated I/R injury and prevented pressure overload-induced cardiac hypertrophy. Overall, the authors also identified FoxP1 as a functional target of miR-206, which when overexpressed, attenuated miR-206-induced cardiac hypertrophy and survival [65].

Fig. 1 summarizes the different miRNAs controlling post-natal cardiomyocyte proliferation after injury in different animal models.

3. miRNAs controlling cardiomyocyte (re)programming

The possibility to isolate and expand cardiac progenitor cells (CPCs) capable of differentiation into cardiomyocytes and vascular cells has encouraged the field of cardiac regeneration with hopes of future uses in regenerative medicine. Several CPC populations have been identified in the developing and adult heart including c-Kit + CPCs [66,67], cardiosphere-derived cells (CDCs) [68], epicardium derived cells, cardiac side population cells [69], Sca-1+ CPCs [70], Isl-1+ CPCs [71], and PDGRα+ CPCs [72], (further reviewed in
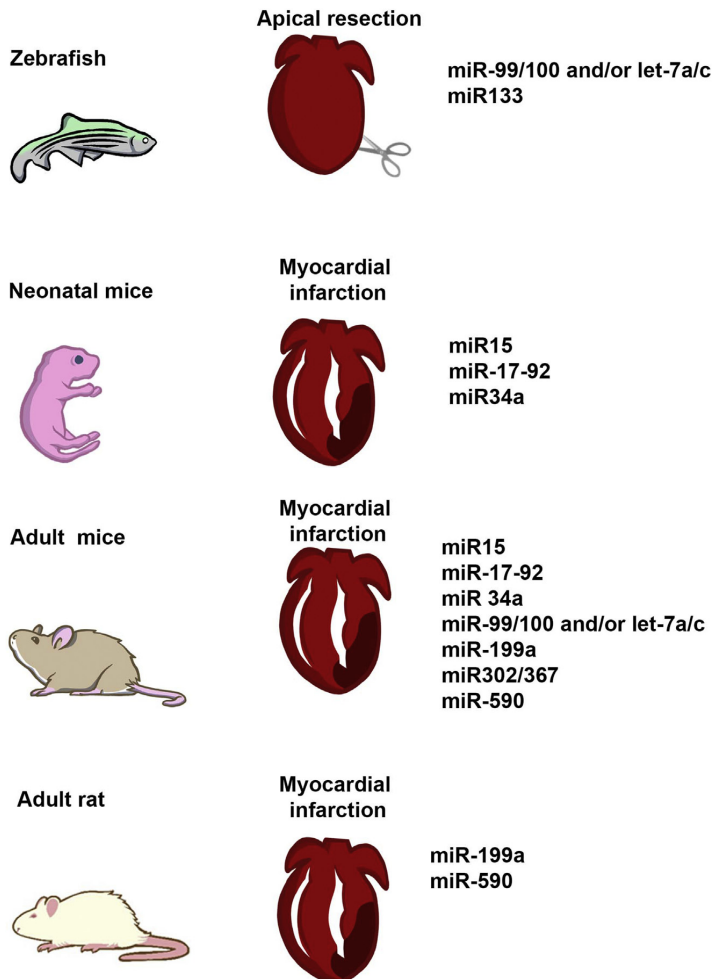

Fig. 1. microRNAs controlling post-natal cardiomyocyte proliferation. The use of different animal models has allowed for the identification of miRNAs driving cardiac endogenous repair by the induction of proliferative responses in cardiomyocytes.

Refs. [73,74]). Despite all the progress, the actual function of these cell populations is still controversial and further studies are needed in order to define their regenerative potential in a clinical setting [4]. Other cell types, such as human embryonic stem cells (hESCs) or induced pluripotent stem cells (iPSCs) have been recently evaluated. However, specification and differentiation towards cardiac cell types must be tightly controlled in order to produce mature cell types and avoid adverse events (i.e., tumor formation after transplantation, among others). In addition, a robust protocol for their derivation into cardiomyocytes has yet to be established, and the generation of mature and functional cardiomyocytes from human pluripotent stem cells still remains a major challenge in the field (Fig. 2).

To date several miRNAs have been shown to promote cardiac differentiation from hESCs. Wilson and colleagues reported the first miRNA profiling of cardiomyocytes derived from hESCs and identified that the expression of several miRNAs, including miR-1, miR-133, miR-208 was upregulated during the time course of differentiation. The authors also defined a novel role for miR-499 in cardiac differentiation, since its overexpression caused upregulation of the cardiac transcription factor MEF2C [75]. Interestingly, both miR-499 and miR-208 are also known to affect cardiac function. miR-499 and miR-208 are encoded by an intron of MYH7 and MYH6, respectively, and they share many predicted targets, though miR-208 has been previously shown to play a crucial role in stress adaptation of the adult heart [76]. In recent years, further studies

have tried to dissect the functional role of different miRNAs previously shown to be related to cardiac differentiation in stem cells, and identified that whereas miR-499 promotes ventricular specification of hESCs, miR-1 facilitates electrophysiological maturation [77].

In an effort to bypass the use of pluripotent stem cell sources as the initial population for the derivation of cardiac cells, several strategies are being devised to eliminate the risk of teratomas and eventually allow for in vivo reprogramming of resident cardiac cells (Fig. 2). Along this line, a recent report has demonstrated the direct conversion of mouse fibroblasts to a cardiomyocyte-like phenotype using a single transient transfection with a combination of miRNAs with known roles in cardiac development and differentiation (miR-1, miR-133, miR-208, and miR-499) [78]. Interestingly, the reprogrammed cells expressed specific markers for cardiac-like cells and exhibited electrophysiological characteristics related to cardiomyocytes. More importantly, direct administration of these miRNAs into injured myocardia resulted in direct conversion of cardiac fibroblasts to cardiomyocyte-like cells in vivo, as confirmed by genetic tracing using Fsp1Cre-mice [78]. In parallel to these findings, Nam and colleagues found that different human cardiac transcription factors, including GATA binding protein 4, Hand2, T-box5, and myocardin, together with two microRNAs, miR-1 and miR-133, activated cardiac marker expression in neonatal and adult human fibroblasts. Importantly, long-term culture of transduced cells showed that human fibroblasts reprogrammed with these
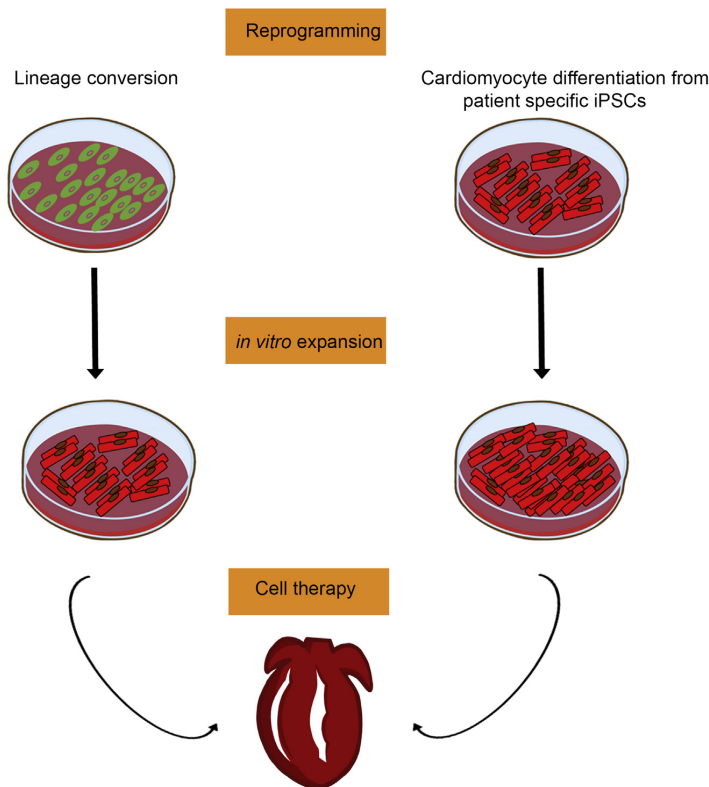

Fig. 2. **Cellular reprogramming for heart repair**. To date reprogramming strategies as lineage conversion and/or guided differentiation from patient-specific iPSCs represent attractive strategies for the treatment of cardiovascular diseases. The possibility to work with unlimited amounts of starting cell populations (either patient fibroblasts or patient-specific iPSCs) would allow for their generation and expansion on demand.

factors exhibited sarcomere-like structures and calcium transients, and that a small subset of reprogrammed cardiac cells showed spontaneous contractility. Interestingly, those changes were in agreement with the acquisition of the expression of cardiac genes and suppression of non-myocyte genes [79].

4. Conclusion

Though the ability to induce organ regeneration has fascinated humanity for centuries, the cellular and molecular events driving the generation of new tissue structures or parts of organs after damage are still unknown. With respect to the heart, early studies in amphibian, axolotls, and newts described the intrinsic capabilities of those organisms to regenerate their hearts after damage [80—82]. This potential has been believed to be absent in mammals until the recent years, when independent studies highlighted the observation that adult mammalian cardiomyocyte renewal occurs under biological conditions [14,83,84]. Identifying the intrinsic repair capacity of the mammalian heart has encouraged the scientific community to develop therapeutic strategies to enhance this residual potential. In this regard, comparative analyses between cardiac repair and regeneration in different animal models and at different stages of development have identified the existence of conserved pathways driving heart regeneration. In this review, we highlight different studies that provide convincing evidence that miRNAs might represent an attractive approach when developing novel strategies for heart healing. Despite these encouraging results, important issues need to be addressed before translating these findings into the clinic. For instance, our understanding of miRNA biology in cardiac tissue is still in its infancy, requiring further studies in order to achieve a full perspective on cardiac regulatory networks under miRNA control. Such information will also benefit the development of effective and safe methods of miRNA-targeting molecules and the avoidance of unwanted off-target effects. Eventually, these advances will result in novel therapeutic approaches targeting cardiac failure, a major unmet need in the clinic.

Acknowledgements

References

[1] S. Ounzain, T. Pedrazzini, The promise of enhancer-associated long noncoding RNAs in cardiac regeneration, Trends cardiovasc. Med. 25 (7) (2015) 592—602.
[2] S. Frank, A. Aguirre, J. Hescheler, L. Kurian, A lncRNA perspective into (Re) Building the heart, Front. Cell Dev. Biol. 4 (2016) 128.
[3] A. Aguirre, I. Sancho-Martinez, J.C. Izpisua Belmont, Reprogramming toward heart regeneration: stem cells and beyond, Cell Stem Cell (2013) 275—284.
[4] M. Giacca, S. Zacchigna, Harnessing the microRNA pathway for cardiac regeneration, J. Mol. Cell. Cardiol. (2015) 68—74.
[5] J. Itou, H. Kawakami, T. Burgoyne, Y. Kawakami, Life-long preservation of the regenerative capacity in the fin and heart in zebrafish, Biol. Open 1 (2012) 739—746.
[6] K.D. Poss, L.G. Wilson, M.T. Keating, Heart regeneration in zebrafish, Science (80-.) 298 (2002) 2188—2190.
[7] C. Jopling, E. Sleep, M. Raya, M. Martí, A. Raya, J.C. Izpisúa Belmonte, Zebrafish heart regeneration occurs by cardiomyocyte dedifferentiation and proliferation, Nature 464 (2010) 606—609.
[8] F. Chablais, J. Veit, G. Rainer, A. Jaźwińska, The zebrafish heart regenerates after cryoinjury-induced myocardial infarction, BMC Dev. Biol. 11 (2011) 21.
[9] J.M. González-Rosa, V. Martín, M. Peralta, M. Torres, N. Mercader, Extensive scar formation and regression during heart regeneration after cryoinjury in zebrafish, Development 138 (2011) 1663—1674.
[10] K. Schnabel, C.C. Wu, T. Kurth, G. Weidinger, Regeneration of cryoinjury induced necrotic heart lesions in zebrafish is associated with epicardial activation and cardiomyocyte proliferation, PLoS One (2011) 6.
[11] J. Wang, D. Panáková, K. Kikuchi, J.E. Holdway, M. Gemberling, J.S. Burris, et al., The regenerative capacity of zebrafish reverses cardiac failure caused by genetic cardiomyocyte depletion, Development 138 (2011) 3421—3430.
[12] V. Parente, S. Balasso, G. Pompilio, L. Verduci, G.I. Colombo, G. Milano, et al., Hypoxia/reoxygenation cardiac injury and regeneration in zebrafish adult heart, PLoS One 8 (2013).
[13] E.R. Porrello, A.I. Mahmoud, E. Simpson, J a Hill, J a Richardson, E.N. Olson, et al., Transient regenerative potential of the neonatal mouse heart, Science 331 (2011) 1078—1080.
[14] S.E. Senyo, M.L. Steinhauser, C.L. Pizzimenti, V.K. Yang, L. Cai, M. Wang, et al., Mammalian heart renewal by pre-existing cardiomyocytes, Nature 493 (2012) 433—436.
[15] A. Aguirre, N. Montserrat, S. Zacchigna, E. Nivet, T. Hishida, M.N. Krause, et al., In vivo activation of a conserved microRNA program induces mammalian heart regeneration, Cell Stem Cell. 15 (2014) 589—604.
[16] T.R. Mercer, J.S. Mattick, Structure and function of long noncoding RNAs in epigenetic regulation, Nat. Struct. Mol. Biol. 20 (2013) 300—307.
[17] F.H. Seeger, A.M. Zeiher, S. Dimmeler, MicroRNAs in stem cell function and regenerative therapy of the heart, Arter. Thromb. Vasc. Biol. 33 (2013) 1739—1746.
[18] Phillip Grote, Lars Wittler, Sandra Währisch, David Hendrix, Arica Beisaw, K. Macura, Gaby Bläss, Manolis Kellis, Martin Werber, BGH, The tissue-specific lncRNA Fendrr is an essential regulator of heart and body wall development in the mouse, Dev. Cell. 24 (2014) 206—214.
[19] C.A. Klattenhoff, J.C. Scheuermann, LE. Surface, R.K. Bradley, P.A. Fields, M.L. Steinhauser, et al., Braveheart, a long noncoding RNA required for cardiovascular lineage commitment, Cell 152 (2013) 570—583.
[20] L. Kurian, A. Aguirre, I. Sancho-Martinez, C. Benner, T. Hishida, T.B. Nguyen, et al., Identification of novel long noncoding RNAs underlying vertebrate cardiovascular development, Circulation 131 (2015) 1278—1290.
[21] S. Ounzain, R. Micheletti, C. Arnan, I. Plaisance, D. Cecchi, B. Schroen, et al., CARMEN, a human super enhancer-associated long noncoding RNA controlling cardiac specification, differentiation and homeostasis, J. Mol. Cell. Cardiol. 89 (2015) 98—112.
[22] S. Ounzain, R. Micheletti, T. Beckmann, B. Schroen, M. Alexanian, I. Pezzuto, et al., Genome-wide profiling of the cardiac transcriptome after myocardial infarction identifies novel heart-specific long non-coding RNAs, Eur. Heart J. 36 (2015) 353—368.
[23] S. Ounzain, I. Pezzuto, R. Micheletti, F. Burdet, R. Sheta, M. Nemir, et al., Functional importance of cardiac enhancer-associated noncoding RNAs in heart development and disease, J. Mol. Cell. Cardiol. 76 (2014) 55—70.
[24] P. Han, W. Li, C.-H. Lin, J. Yang, C. Shang, S.T. Nurnberg, et al., A long noncoding RNA protects the heart from pathological hypertrophy, Nature 514 (2014) 102—106.
[25] K.M. Michalik, X. You, Y. Manavski, A. Doddaballapur, M. Zörnig, T. Braun, et al., Long noncoding RNA MALAT1 regulates endothelial cell function and vessel growth, Circ. Res. 114 (2014) 1389—1397.
[26] K.L. Yap, S. Li, A.M. Muñoz-Cabello, S. Raguz, L. Zeng, S. Mujtaba, et al., Molecular interplay of the noncoding RNA ANRIL and methylated histone H3 lysine 27 by polycomb CBX7 in transcriptional silencing of INK4a, Mol. Cell. 38 (2010) 662—674.
[27] K. Wang, B. Long, L.-Y. Zhou, F. Liu, Q.-Y. Zhou, C.-Y. Liu, et al., CARL lncRNA inhibits anoxia-induced mitochondrial fission and apoptosis in cardiomyocytes by impairing miR-539-dependent PHB2 downregulation, Nat. Commun. 5 (2014) 3596.
[28] Y. Devaux, J. Zangrando, B. Schroen, E.E. Creemers, T. Pedrazzini, C.-P. Chang, et al., Long noncoding RNAs in cardiac development and ageing, Nat. Rev. Cardiol. 12 (2015) 415—425.
[29] S. Ounzain, S. Crippa, T. Pedrazzini, Small and long non-coding RNAs in cardiac homeostasis and regeneration, Biochim. Biophys. Acta - Mol. Cell Res. (2013) 923—933.
[30] S. Uchida, S. Dimmeler, Long noncoding RNAs in cardiovascular diseases, Circ. Res. (2015) 737—750.
[31] E. Van Rooij, L.B. Sutherland, J.E. Thatcher, J.M. DiMaio, R.H. Naseem, W.S. Marshall, et al., Dysregulation of microRNAs after myocardial infarction reveals a role of miR-29 in cardiac fibrosis, Proc. Natl. Acad. Sci. U. S. A. 105 (2008) 13027—13032.
[32] K. Kikuchi, Dedifferentiation, transdifferentiation, and proliferation: mechanisms underlying cardiac muscle regeneration in zebrafish, Curr. Pathobiol. Rep. 3 (2015) 81—88.

[33] K. Kikuchi, J.E. Holdway, A.A. Werdich, R.M. Anderson, Y. Fang, G.F. Egnaczyk, et al., Primary contribution to zebrafish heart regeneration by gata4(+) cardiomyocytes, Nature 464 (2010) 601—605.

[34] K. Kikuchi, V. Gupta, J. Wang, J.E. Holdway, A. Wills, Y. Fang, et al., Tcf21+ epicardial cells adopt non-myocardial fates during zebrafish heart development and regeneration, Development 138 (2011) 2895—2902.

[35] R.S.M. Gomes, P. Skroblin, A.B. Munster, H. Tomlins, S.R. Langley, A. Zampetaki, et al., "Young at heart": regenerative potential linked to immature cardiac phenotypes, J. Mol. Cell. Cardiol. Authors 92 (2016) 105—108.

[36] E.R. Porrello, B.A. Johnson, A.B. Aurora, E. Simpson, Y.-J. Nam, S.J. Matkovich, et al., MiR-15 family regulates postnatal mitotic arrest of cardiomyocytes, Circ. Res. 109 (2011) 670—679.

[37] E.R. Porrello, A.I. Mahmoud, E. Simpson, B.A. Johnson, D. Grinsfelder, D. Canseco, et al., Regulation of neonatal and adult mammalian heart regeneration by the miR-15 family, Proc. Natl. Acad. Sci. U. S. A. 110 (2013) 187—192.

[38] T.G. Hullinger, R.L. Montgomery, A.G. Seto, B.A. Dickinson, H.M. Semus, J.M. Lynch, et al., Inhibition of miR-15 protects against cardiac ischemic injury, Circ. Res. 110 (2012) 71—81.

[39] J.-F. Chen, E.M. Mandel, J.M. Thomson, Q. Wu, T.E. Callis, S.M. Hammond, et al., The role of microRNA-1 and microRNA-133 in skeletal muscle proliferation and differentiation, Nat. Genet. 38 (2006) 228—233.

[40] N. Liu, S. Bezprozvannaya, A.H. Williams, X. Qi, J.A. Richardson, R. Bassel-Duby, et al., microRNA-133a regulates cardiomyocyte proliferation and suppresses smooth muscle gene expression in the heart, Genes Dev. 22 (2008) 3242—3254.

[41] A. Carè, D. Catalucci, F. Felicetti, D. Bonci, A. Addario, P. Gallo, et al., microRNA-133 controls cardiac hypertrophy, Nat. Med. 13 (2007) 613—618.

[42] V.P. Yin, A. Lepilina, A. Smith, K.D. Poss, Regulation of zebrafish heart regeneration by miR-133, Dev. Biol. 365 (2012) 319—327.

[43] A. Eulalio, M. Mano, M. Dal Ferro, L. Zentilin, G. Sinagra, S. Zacchigna, et al., Functional screening identifies miRNAs inducing cardiac regeneration, Nature 492 (2012) 376—381.

[44] S. Roush, F.J. Slack, The let-7 family of microRNAs, Trends Cell Biol. (2008) 505—516.

[45] A. Coppola, A. Romito, C. Borel, C. Gehrig, M. Gagnebin, E. Falconnet, et al., Cardiomyogenesis is controlled by the miR-99a/let-7c cluster and epigenetic modifications, Stem Cell Res. Authors 12 (2014) 323—337.

[46] N. Shyh-Chang, H. Zhu, T. Yvanka De Soysa, G. Shinoda, M.T. Seligson, K.M. Tsanov, et al., XLin28 enhances tissue repair by reprogramming cellular metabolism, Cell (2013) 155.

[47] A. Ventura, A.G. Young, M.M. Winslow, L. Lintault, A. Meissner, S.J. Erkeland, et al., Targeted deletion reveals essential and overlapping functions of the miR-17-92 family of miRNA clusters, Cell 132 (2008) 875—886.

[48] J. Wang, S.B. Greene, M. Bonilla-Claudio, Y. Tao, J. Zhang, Y. Bai, et al., Bmp signaling regulates myocardial differentiation from cardiac progenitors through a MicroRNA-mediated mechanism, Dev. Cell. 19 (2010) 903—912.

[49] J. Chen, Z.P. Huang, H.Y. Seok, J. Ding, M. Kataoka, Z. Zhang, et al., Mir-17-92 cluster is required for and sufficient to induce cardiomyocyte proliferation in postnatal and adult hearts, Circ. Res. 112 (2013) 1557—1566.

[50] K. Ikeushi, F. Seeger, B. Assmus, A.M. Zeiher, S. Dimmeler, Regulation of cardiac MicroRNAs by bone marrow mononuclear cell therapy in myocardial infarction, Circulation 125 (2012) 1765—1773.

[51] M. Yamakuchi, M. Ferlito, C.J. Lowenstein, miR-34a repression of SIRT1 regulates apoptosis, Proc. Natl. Acad. Sci. U. S. A. 105 (2008) 13421—13426.

[52] B.C. Bernardo, X.-M. Gao, C.E. Winbanks, E.J.H. Boey, Y.K. Tham, H. Kiriazis, et al., Therapeutic inhibition of the miR-34 family attenuates pathological cardiac remodeling and improves heart function, Proc. Natl. Acad. Sci. U. S. A. 109 (2012) 17615—17620.

[53] T. Ito, S. Yagi, M. Yamakuchi, microRNA-34a regulation of endothelial senescence, Biochem. Biophys. Res. Commun. 398 (2010) 735—740.

[54] R a Boon, K. Iekushi, S. Lechner, T. Seeger, A. Fischer, S. Heydt, et al., MicroRNA-34a regulates cardiac ageing and function, Nature 495 (2013) 107—110.

[55] S. Matsumoto, Y. Sakata, S. Suna, D. Nakatani, M. Usami, M. Hara, et al., Circulating p53-responsive MicroRNAs are predictive indicators of heart failure after acute myocardial infarction, Circ. Res. 113 (2013) 322—326.

[56] Y. Tian, Y. Liu, T. Wang, N. Zhou, J. Kong, L. Chen, et al., A microRNA-Hippo pathway that promotes cardiomyocyte proliferation and cardiac regeneration in mice, Sci. Transl. Med. 7 (2015), 279ra38.

[57] T. Heallen, Y. Morikawa, J. Leach, G. Tao, J.T. Willerson, R.L. Johnson, et al., Hippo signaling impedes adult heart regeneration, Development 140 (2013) 4683—4690.

[58] H. Wackerhage, D.P. Del Re, R.N. Judson, M. Sudol, J. Sadoshima, The Hippo signal transduction network in skeletal and cardiac muscle, Sci. Signal 7 (2014) re4—re4.

[59] A. Von Gise, Z. Lin, K. Schlegelmilch, L.B. Honor, G.M. Pan, J.N. Buck, et al., YAP1, the nuclear target of Hippo signaling, stimulates heart growth through cardiomyocyte proliferation but not hypertrophy, Proc. Natl. Acad. Sci. U. S. A. 109 (2012) 2394—2399.

[60] M. Xin, Y. Kim, L.B. Sutherland, X. Qi, J. McAnally, R.J. Schwartz, et al., Regulation of insulin-like growth factor signaling by Yap governs cardiomyocyte proliferation and embryonic heart size, Sci. Signal 4 (2011) ra70.

[61] M. Xin, Y. Kim, L.B. Sutherland, M. Murakami, X. Qi, J. McAnally, et al., Hippo pathway effector Yap promotes cardiac regeneration, Proc. Natl. Acad. Sci. 110 (2013) 13839—13844.

[62] T. Heallen, M. Zhang, J. Wang, M. Bonilla-Claudio, E. Klysik, R.L. Johnson, et al., Hippo pathway inhibits Wnt signaling to restrain cardiomyocyte proliferation and heart size, Science (80-.) 332 (2011) 458—461.

[63] D. Pan, The hippo signaling pathway in development and cancer, Dev. Cell (2010) 491—505.

[64] G. Tao, J. Wang, J.F. Martin, Small RNA: from development to regeneration, Sci. Transl. Med. 7 (2015), 279fs12.

[65] Y. Yang, D.P. Del Re, N. Nakano, S. Sciarretta, P. Zhai, J. Park, et al., MIR-206 mediates YAP-induced cardiac hypertrophy and survival, Circ. Res. 117 (2015) 891—904.

[66] A.P. Beltrami, L. Barlucchi, D. Torella, M. Baker, F. Limana, S. Chimenti, et al., Adult cardiac stem cells are multipotent and support myocardial regeneration, Cell 114 (2003) 763—776.

[67] C. Bearzi, M. Rota, T. Hosoda, J. Tillmanns, A. Nascimbene, A. De Angelis, et al., Human cardiac stem cells, Proc. Natl. Acad. Sci. U. S. A. 104 (2007) 14068—14073.

[68] E. Messina, L. De Angelis, G. Frati, S. Morrone, S. Chimenti, F. Fiordaliso, et al., Isolation and expansion of adult cardiac stem cells from human and murine heart, Circ. Res. 95 (2004) 911—921.

[69] C.M. Martin, A.P. Meeson, S.M. Robertson, T.J. Hawke, J.A. Richardson, S. Bates, et al., Persistent expression of the ATP-binding cassette transporter, Abcg2, identifies cardiac SP cells in the developing and adult heart, Dev. Biol. 265 (2004) 262—275.

[70] H. Oh, S.B. Bradfute, T.D. Gallardo, T. Nakamura, V. Gaussin, Y. Mishina, et al., Cardiac progenitor cells from adult myocardium: homing, differentiation, and fusion after infarction, Proc. Natl. Acad. Sci. U. S. A. 100 (2003) 12313—12318.

[71] K.-L. Laugwitz, A. Moretti, J. Lam, P. Gruber, Y. Chen, S. Woodard, et al., Postnatal isl1+ cardioblasts enter fully differentiated cardiomyocyte lineages, Nature 433 (2005) 647—653.

[72] J.J.H. Chong, H. Reinecke, M. Iwata, B. Torok-Storb, A. Stempien-Otero, C.E. Murry, Progenitor cells identified by PDGFR-alpha expression in the developing and diseased human heart, Stem Cells Dev. 22 (2013) 1932—1943.

[73] M.P. Santini, E. Forte, R.P. Harvey, J.C. Kovacic, Developmental origin and lineage plasticity of endogenous cardiac stem cells, Development 143 (2016) 1242—1258.

[74] M.C.B.R. Keith, "String theory" of c-kit(pos) cardiac cells: a new paradigm regarding the nature of these cells that may reconcile apparently discrepant results, Circ. Res. 116 (2015) 1216—1230.

[75] K.D. Wilson, S. Hu, S. Venkatasubrahmanyam, J.-D. Fu, N. Sun, O.J. Abilez, et al., Dynamic microRNA expression programs during cardiac differentiation of human embryonic stem cells: role for miR-499, Circ. Cardiovasc. Genet. 3 (2010) 426—435.

[76] E. Van Rooij, L.B. Sutherland, X. Qi, J A Richardson, J. Hill, E.N. Olson, Control of stress-dependent cardiac growth and gene expression by a microRNA, Science (80-.) 316 (2007) 575—579.

[77] J.-D. Fu, S.N. Rushing, D.K. Lieu, C.W. Chan, C.-W. Kong, L. Geng, et al., Distinct roles of microRNA-1 and -499 in ventricular specification and functional maturation of human embryonic stem cell-derived cardiomyocytes, PLoS One 6 (2011) e27417.

[78] T.M. Jayawardena, B. Egemnazarov, E.A. Finch, L. Zhang, J. Alan Payne, K. Pandya, et al., MicroRNA-mediated in vitro and in vivo direct reprogramming of cardiac fibroblasts to cardiomyocytes, Circ. Res. 110 (2012) 1465—1473.

[79] Y.-J. Nam, K. Song, X. Luo, E. Daniel, K. Lambeth, K. West, et al., Reprogramming of human fibroblasts toward a cardiac fate, Proc. Natl. Acad. Sci. U. S. A. 110 (2013) 5588—5593.

[80] Rumyantsev, Autoradiographic study on the synthesis of DNA, RNA, and proteins in normal cardiac muscle cells and those changed by experimental injury, Folia Histochen Cytochem 4 (1966) 397—424.

[81] Sulima, On the regeneration of the myocardium in various injuries to the cardiac wall of reptiles, Arkh Anat. Gistol. Embriol 55 (1968) 56—63.

[82] Rumyantsev, Post-injury DNA synthesis, mitosis and ultrastructural reorganization of adult frog cardiac myocytes. An electron microscopic-autoradiographic study, Z Zellforsch Mikrosk Anat. 139 (1973) 431—450.

[83] O. Bergmann, R.D. Bhardwaj, S. Bernard, S. Zdunek, F. Barnabé-Heider, S. Walsh, et al., Evidence for cardiomyocyte renewal in humans, Science 324 (2009) 98—102.

[84] A.P. Beltrami, K. Urbanek, J. Kajstura, S.-M. Yan, N. Finato, R. Bussani, et al., Evidence that human cardiac myocytes divide after myocardial infarction, N. Engl. J. Med. 344 (2001) 1750—1757.